UCRL--53120
DE82 005607

Summary of Results from the Tandem Mirror Experiment (TMX)

TMX Group

February 26, 1981

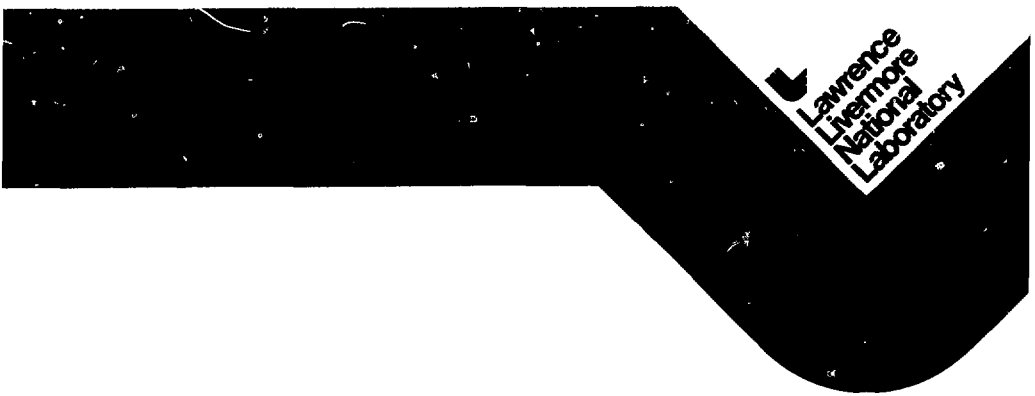

UCRL-53120
Distribution Category UC-20,20f,20g

Summary of Results from the Tandem Mirror Experiment (TMX)

TMX Group
T. C. Simonen, Editor

Manuscript date: February 26, 1981

LAWRENCE LIVERMORE LABORATORY
University of California • Livermore, California • 94550

Available from: National Technical Information Service • U.S. Department of Commerce
5285 Port Royal Road • Springfield, VA 22161 • $16.00 per copy • (Microfiche $3.50)

CONTRIBUTORS

TMX Experimental Physicists, LLNL

S. L. Allen, T. A. Casper, J. F. Clauser, F. H. Coensgen, W. Condit, D. L. Correll, W. C. Cummins, J. C. Davis, R. P. Drake, J. H. Foote, A. H. Futch, R. K. Goodman, D. P. Grubb, E. B. Hooper, R. S. Hornady, A. L. Hunt, C. V. Karmendy, A. W. Molvik, W. E. Nexsen, W. L. Pickles, P. Poulsen, T. C. Simonen, B. W. Stallard

M Division Experimental and Computational Physicists, LLNL

W. L. Barr, J. M. Gilmore, G. E. Gryczkowski, G. W. Leppelmeier, A. A. Mirin, M. E. Rensink, G. D. Porter

I. Division X-Ray/Optics Diagnostics Team, LLNL

C. A. Anderson, G. A. Burginyan, R. Crabb, A. M. Frank, C. E. Frerking, H. Koehler, M. E. McGee, L. B. Olk, H. D. Snyder, J. P. Stoering, A. Toor

E Division Spectroscopy and Neutron Diagnostic Teams, LLNL

D. D. Dietrich, R. J. Fortner, D. R. Slaughter

Surface Studies Team, Sandia National Laboratories

M. J. Baskes, R. Bastasz, W. Bauer, L. G. Haggmark, A. E. Pontau, W. R. Wampler, K. L. Wilson

Department of Applied Science, UC Davis—Livermore Campus

S. Fallabella, T. J. Nash

Rensselaer Polytechnic Institute

G. A. Hallock

Johns Hopkins University

O. T. Strand

University of Iowa

P. Coakley

Participating Scientists

D. Boyd, University of Maryland; A. L. Gardner, Brigham Young University; W. Getty, University of Michigan; N. Hershkowitz, University of Iowa; R. L. Hickock, Rensselaer Polytechnic Institute; T. Kawabe, Tsukuba University, Japan; H. W. Moos, Johns Hopkins University; M. P. Paul, Alcorn State University; M. Siedel, Stevens Institute of Technology; R. S. Post, University of Wisconsin; K. Yatsu, Tsukuba University, Japan.

CONTENTS

ACKNOWLEDGEMENTS

It is a pleasure for the authors of this report to acknowledge the many contributions to various phases of the TMX project. T. K. Fowler and B. G. Logan of the Lawrence Livermore National Laboratory invented the tandem mirror concept, and they gave us guidance during TMX design and during analysis of TMX results.

The success of TMX was due to contributions from many well-coordinated teams generating ideas, solving problems and working long hours. The design of the TMX machine was carried out by the LLNL Mechanical and Electrical Engineering Groups assisted by the M Division Theory Group. TMX was built on a fast-paced schedule by several specialized engineering and technical teams who also brought TMX into operation. The Lawrence Berkeley National Laboratory's Neutral Beam Group helped us with the beam system.

Dedicated and skilled physics, electronic, and mechanical technicians operated the TMX facility to demonstrate the tandem mirror concept. The data described in this report resulted from many innovative contributions to diagnostic designs, to instrument construction and operation, and to computer programming. Close cooperation with the Theoretical and Computational Groups advanced our understanding to the level described here. Our secretarial and technical editing staff helped publish the results.

We benefited from contributions of other laboratories, especially our tandem mirror colleagues at the University of Wisconsin, the University of Tsukuba in Japan, and at the Siberian Institute of Nuclear Physics in the Soviet Union where the tandem mirror concept was invented during the same period.

To all these groups and to the many individual contributors, we express our thanks.

1. Summary of TMX Results—Executive Summary

1.1 INTRODUCTION

This report summarizes results from the successful experimental operation of the Tandem Mirror Experiment (TMX) over the period October 1978 through September 1980. The experimental program, summarized by the DOE milestones given in Table 1-1, had three basic phases: (1) an 8-month checkout period, October 1978 through May 1979, (2) a 6-month initial period of operation, June through November 1979, during which the basic principles of the tandem configuration were demonstrated (i.e., plasma confinement was improved over that of a single-cell mirror), and (3) a 10-month period, December 1979 through September 1980, during which the initial TMX results were corroborated by additional diagnostic measurements and many detailed physics investigations were carried out. This report summarizes the early results, presents results of recent data analysis, and outlines areas of ongoing research and data analysis which will be reported in future journal publications.

The TMX experiments demonstrated the fundamental tandem mirror principles, as summarized in Table 1-2. Table 1-3 lists the maximum plasma parameters achieved in TMX. The main result was that TMX generated electrostatic confining potentials that significantly improved central-cell plasma confinement. These data established a new scaling of ion confinement by ambipolar potential in magnetic mirror systems and provided the impetus for the initiation of both TMX Upgrade, a tandem mirror in which potential confinement is increased through the use of thermal barriers, and MFTF-B, a larger tandem mirror that will extend the TMX Upgrade results to thermonuclear temperatures.

TABLE 1-1. Summary of TMX milestones.

	Milestones	Date achieved	Reference
1.	Begin TMX checkout.	Oct 1978	Direct communication to DOE
2.	Begin plasma-buildup experiments.	Jul 1979	Direct communication to DOE
3.	Determine density and beta of plug and solenoid.	Sep 1979	Direct communication to DOE
4.	Demonstrate electrostatic plugging of solenoid ions in a measured well.	Sep 1979	Direct communication to DOE
5.	Submit draft report evaluating initial TMX performance.	Oct 1979	*Phys. Rev. Letters* 44, 1132 (1980)
6.	Begin neutral-beam heating experiments in solenoid with two beams.	Nov 1979	Section 8[a]
7.	Submit final report evaluating initial TMX performance.	Jan 1980	UCID-18496
8.	Submit a plan for modification of TMX, based on TMX data, that will address issues most appropriate to MFTF-B.	Jan 1980	Mirror Senior Review Panel
9.	Begin plug-optimization experiments.	May 1980	Section 10[a]
10.	Submit report on measurements of initial electron-beam experiments in TMX.	May 1980	Section 10,[a] UCID-18725
11.	Submit report evaluating impurities in TMX including types and origins of impurities.	Oct 1980	Section 13,[a] UCID-18883
12.	Obtain Thomson-scattering measurements of TMX solenoid electron temperature.	Sep 1980	Section 3[a]
13.	Initiate procurement of hardware to improve TMX performance.	Aug 1980	Initiation of TMX Upgrade construction
14.	Submit report summarizing TMX results.	Feb 1981	UCRL-53120
15.	Submit report on radial transport of plasma in the solenoid of TMX.	Feb 1981	Section 9[a]
16.	Submit report on initial TMX central-cell ICRH experiments.	Dec 1980	UCID-18566

[a]Section of this report (UCRL-53120).

TABLE 1-2. Summary of TMX results.

- Generated tandem mirror configuration:
  - —Configuration sustained for full 25-ms shot duration.
  - —Plug microstability maintained with solenoid outflow.
  - —Central-cell MHD stability (40% maximum beta with neutral-beam injection).
- Demonstrated central-cell electrostatic plugging:
  - —Measured electrostatic potential well.
  - —Direct evidence by measurements made when one end plug was turned off.
  - —Measured factor-of-9 electrostatic enhancement.
  - —Radial confinement exceeds axial confinement.
- Improved electron confinement:
  - —Electron temperature higher than in 2XIIB.
  - —Low density at end wall.
  - —Dominant power loss to end walls.
  - —Low levels of impurities.

TABLE 1-3. Maximum plasma parameters achieved in TMX with deuterium and a central-cell magnetic field strength of 0.1 T. These parameters were not achieved simultaneously on the same shot.

Plug density	4×10^{13} cm^{-3}
Plug ion energy	13 keV
Plug electron temperature	0.26 keV
Plug radius	10 cm
Central-cell density	3×10^{13} cm^{-3}
Central-cell ion energy	0.25 keV
Central-cell radius	30 cm
Plug plasma potential	1 kV
Central-cell confining potential	0.3 kV
Central-cell axial-confinement parameter	10^{11} cm^{-3}·s
Electrostatic enhancement in confinement	9
Central-cell beta (0.07 without central-cell neutral-beam injection)	0.40

1.2 INITIAL TMX RESULTS

1.2.1 Tandem Mirror Configuration

● One of the expected tandem mirror characteristics verified by TMX was that the density of the plasma in the end plug could be sustained at a higher level than that of the central-cell plasma, and that this produced higher electric potentials in the end plugs than in the central cell. These densities were controlled by varying the end-plug neutral-beam current and the central-cell gas-feed current. The density peaks generate potential peaks, as shown in Fig. 1-1, which also shows that relatively small end-plug plasmas can electrostatically confine a much larger central-cell plasma.

● The density and temperature of the TMX plasma are within a factor of 2 of those predicted by theoretical codes. Calorimeter measurements showed that most of the neutral-beam power deposited on the axis is carried to the end walls by ions.

● Gross MHD stability and microstability were achieved. Finite-beta plasma was confined in the central cell with minimum-B end-plugs. The outflow of central-cell plasma provided end-plug microstability.

1.2.2 Improved Plasma Confinement

● The TMX end plugs improve confinement of the central-cell plasma by up to a factor of 9 over that which would have been attained if the end-plug plasmas had not been present. Typical enhancements were in the range of 3 to 7 times. Central-cell axial confinement of ions is near that predicted by our theoretical models.

● TMX plasma confinement can be explained by classical Coulomb theoretical models, over a certain range of parameters. However, there must be sufficient warm plasma to stabilize the plugs. If insufficient low-energy plasma flows through the end plug, then fluctuating electric fields develop at the end-plug ion-cyclotron frequency and confinement of central-cell ions is reduced. Theoretical models describing TMX performance over a wide range of operation have been developed on the basis of these experiments.

● A second measure of improvement in the tandem mirror over the single mirror is the electron temperature that can be achieved with a given amount of input neutral-beam power. TMX end plugs achieved electron temperatures up to 260 eV, three to four times higher than the electron temperatures of the similar single-cell mirror machine 2XIIB when operated with comparable neutral-beam input power. Since TMX has such a large central-cell plasma, this electron temperature increase indicates a hundred-fold improvement in electron energy confinement. This improvement arises from the fact that the low-energy plasma required for end-plug microstability is supplied from the TMX central cell rather than from the ends, as

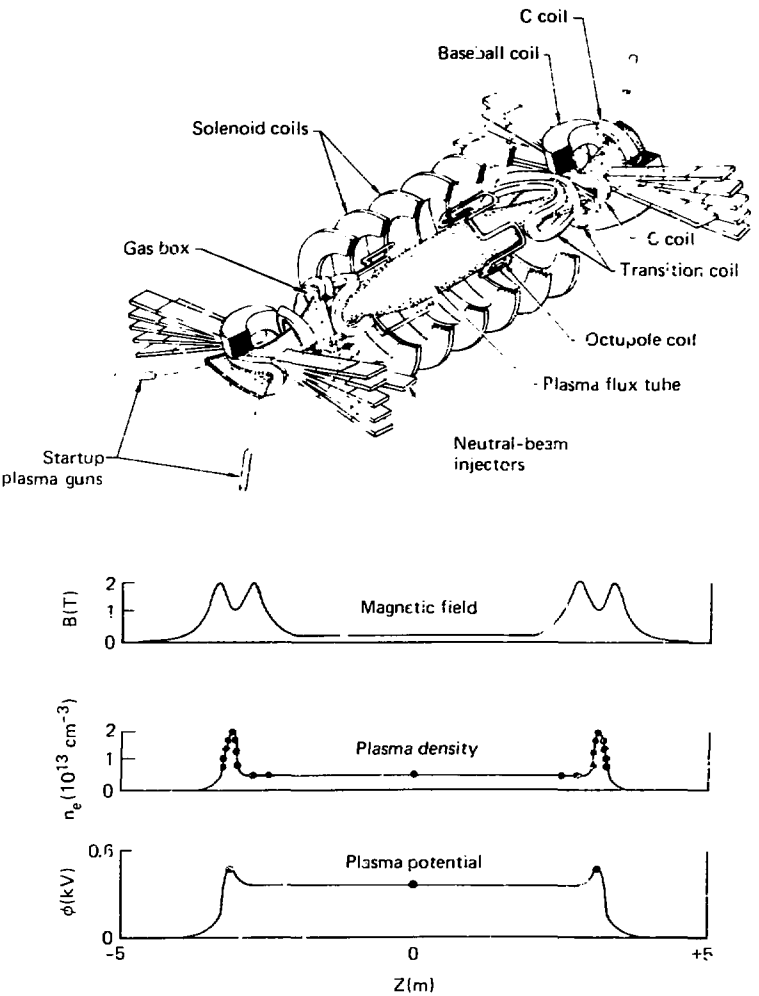

FIG. 1-1. TMX magnet geometry and measured axial plasma profiles.

in 2XIIB, thus reducing the electron energy loss to the end walls.

1.3 NEW RESULTS PRESENTED IN THIS REPORT

During much of the last period of TMX operation (December 1979 through September 1980), poor vacuum conditions caused lower electron temperatures than had been achieved earlier (although sometimes temperatures above 200 eV were still observed). Therefore, our progress during the later phases of TMX operation was in physics understanding rather than in increasing plasma parameters. This increase in understanding resulted from more extensive diagnostic instrumentation, new data analysis, and improved theoretical understanding. Highlights of these recent results are summarized below.

1.3.1 Tandem Configuration

- Plasma potential measurements carried out as a function of radius have shown that the electrostatic potential well is not just localized near the axis but extends across the central cell. The well diagnosed plasmas had 150-V well depths, as expected for the measured electron temperature and densities. Other cases had well depths about twice as high.
- End-plug potentials exceeding 1 kV have been generated and maintained in TMX.
- Methods for controlling the radial profiles have been demonstrated. Operation of TMX over a wide range of central-cell gas feeds has shown that . . adial density profiles can be changed from peak on-axis to inverted profiles peaked off-axis. Additional diagnostic channels allowed us to measure these radial density profiles in more detail than was previously possible.

1.3.2 Plasma Confinement

- Under proper operating conditions, the confinement of the central-cell plasma is in agreement with the theoretical Coulomb values. The highest confinement parameter achieved was $n\tau = 10^{11}$ cm^{-3} · s. When end-plug fluctuation levels are significant, confinement is degraded in agreement with Monte-Carlo calculations. These fluctuations limited the range over which TMX could be operated but did not prevent us from demonstrating the basic features of tandem mirrors.

1.3.3 Power Balance

- We have been able to account for the neutral-beam power input by using multiple diagnostic arrays.
- Near the axis, most of the trapped neutral-beam power is lost axially, indicating good radial confinement. Near the edge, more power is lost radially. Radial arrays of calorimeters on the TMX end wall show that the power is more concentrated on the axis than was previously assumed. Radial end-loss analyzer measurements indicate that this concentration is due to the radial profiles of both the end-loss current and the plasma potential.

1.3.4 Plasma Beta Measurements

- After TMX was shut down, an extensive calibration of the diamagnetic loops was carried out. With this new calibration, we determined that a maximum central-cell beta of 0.4 was achieved with neutral-beam injection.
- This calibration has also enabled us to conclude that the central-cell ion distribution has a non-Maxwellian component, as we had expected, because of ion-cyclotron heating by plug fluctuations.

1.3.5 Radial Transport

- In TMX, radial particle confinement exceeds axial confinement near the axis. Near the edge, radial transport processes are more important.
- Resonant-neoclassical-ion-transport theory is consistent with the experimental measurements, but the measurements cannot resolve factor-of-3 uncertainties in the theory nor can we resolve comparable amounts of ambipolar radial transport.

1.3.6 Radio-Frequency Measurements

- Wavelength and polarization measurements of the end-plug ion-cyclotron fluctuations indicate wave properties more similar to the Alfven ion-cyclotron (AIC) mode than to the drift-cyclotron loss-cone (DCLC) mode. In comparison to 2XIIB, the AIC mode is theoretically more unstable in TMX, while the DCLC mode is less unstable. Theoretically, the AIC mode is expected to be much more stable in the low-ion-beta end plugs of TMX Upgrade and MFTF-B, as is the DCLC mode.
- Turbulent noncoherent central-cell fluctuations extending up to 0.5 MHz, possibly

associated with drift waves, have been detected in the central cell. No correlation with plasma confinement has been identified.

- Coherent low-frequency 7 kHz (m = 1) and 12 kHz (m = 0) oscillations have been observed in the central cell. The m = 0 mode is correlated with bursting of end-plug ion-cyclotron fluctuations and thus would not be expected in TMX Upgrade with microstable sloshing-ion end plugs. The m = 1 mode exists at large amplitude near the edge when sufficient central-cell gas input causes large density gradients near the edge. The m = 1 mode can be controlled by modifying central-cell radial profiles by controlled central-cell fueling and heating.

1.3.7 Impurity Studies

- Further analysis continues to indicate remarkably low central-cell impurity levels (0.5%), resulting in less than 10% power loss by impurity radiation. Recent data analysis shows that the lower ionization states of the prevalent oxygen impurity are localized near the edge and the higher ionization states near the axis, as expected.
- High-resolution spectroscopy has provided Doppler-broadening measurements of impurity radiation that corroborate the 100-to-200-eV diamagnetic-loop measurements of central-cell ion temperature.

1.3.8 Sandia Surface-Probe Studies

- Surface probes have been employed to characterize plasma-wall interactions and to determine TMX plasma properties. Passive solid-state probe measurements of particle fluxes and energies at the central-cell walls corroborate other central-cell diagnostic measurements.
- The probes collected the expected number of particles on the end walls. The major component of end losses comes from the central cell. The end-plug contribution is also in agreement with theoretical calculations.

1.3.9 End-Wall Plasma Characteristics

- We have succeeded in decoupling the TMX plasma from the end walls. This was a necessary accomplishment for future higher-temperature machines. A very low density (2×10^9 cm^{-3}) and cool (5 eV) plasma exists near the end wall. This density is four orders of magnitude less and this electron temperature 40 times cooler than the density and electron temperature of the end plug plasmas.
- Secondary electrons emitted from the end wall are detected but the power losses are small, consistent with a model developed for MFTF-B end-wall processes.

MAJOR TMX PUBLICATIONS

1. F. H. Coensgen, *TMX Major Project Proposal*, Lawrence Livermore National Laboratory, Livermore, CA, LLL-PROP-148 (1977).
2. F. H. Coensgen, C. A. Anderson, T. A. Casper, J. F. Clauser, W. C. Condit, D. L. Correll, W. F. Cummins, J. C. Davis, R. P. Drake, J. H. Foote, A. H. Futch, R. K. Goodman, D. P. Grubb, G. A. Hallock, R. S. Hornady, A. L. Hunt, B. G. Logan, R. H. Munger, W. E. Nexsen, T. C. Simonen, D. R. Slaughter, B. W. Stallard, and O. T. Strand, "Electrostatic Plasma-Confinement Experiments in a Tandem Mirror System," *Phys. Rev. Lett.* 44, 1132-35 (1980).
3. Papers presented at the session on the TMX experiment at the 21st Annual Meeting of the Division Plasma Physics of the American Physical Society, *Bull. Am. Phys. Soc.* 24, 1017 (1979).
4. D. P. Grubb, T. A. Casper, J. F. Clauser, F. H. Coensgen, D. L. Correll, W. C. Cummins, R. P. Drake, J. H. Foote, A. H. Futch, R. K. Goodman, R. S. Hornady, W. E. Nexsen, P. Poulsen, T. D. Rognlien, T. C. Simonen, G. R. Smith, and B. W. Stallard, "Effects of End-Cell Ion Cyclotron Fluctuations on Central-Cell Ion Confinement in the Tandem Mirror Experiment (TMX)," in *Proc. Intl. Symp. Physics in Open-Ended Fusion Systems, University of Tsukuba, Japan, April 15-18, 1980* (University of Tsukuba, Ibakari, Japan, 1980); also Lawrence Livermore National Laboratory, Livermore, CA, UCRL-84236 (1980).
5. D. E. Baldwin, B. G. Logan, and T. C. Simonen, Eds., *Physics Basis for MFTF-B*, Lawrence Livermore National Laboratory, Livermore, CA, UCID-18496 (1980).
6. T. C. Simonen, C. A. Anderson, T. A. Casper, J. F. Clauser, F. J. Coensgen, W. C. Condit, D. L. Correll, W. F. Cummins, J. C. Davis, R. P. Drake, J. H. Foote, R. J. Fortner, A. H. Futch, R. K. Goodman, D. P. Grubb, E. B. Hooper, R. S. Hornady, A. L. Hunt, C. V. Karmendy, B. G. Logan, R. H. Munger, W. E. Nexsen, W. L. Pickles, P. Poulsen, D. R. Slaughter, B. W. Stallard, G. A. Hallock, and O. T. Strand, "Plasma Confinement Experiments in the TMX Tandem Mirror," in *Proc. Intl. Conf. Plasma Physics and Controlled Nucl. Fusion Research, 8th, Brussels, 1980* (IAEA-CN-35/F-1, Vienna, 1981).
7. R. P. Drake, G. Deis, M. Richardson, and T. C. Simonen, "Gas Control and Wall Conditioning in TMX," *J. Nucl. Mat.* 93/94, 291 (1980).
8. R. P. Drake, T. A. Casper, J. F. Clauser, F. H. Coensgen, D. L. Correll, W. F. Cummins, J. C. Davis, J. H. Foote, A. H. Futch, R. K. Goodman, D. P. Grubb, R. S. Hornady, W. E. Nexsen, T. C. Simonen, and B. W. Stallard, "The Effect of End-Cell Stability on the Confinement of the Central-Cell Plasma in TMX," *Nucl. Fusion* 21, 359 (1981).
9. T. D. Rognlien and Y. Matsuda, "Tandem Mirror Confinement in the Presence of Ion Cyclotron Fluctuations," *Nucl. Fusion* 21, 345 (1981).
10. Papers presented at the session on TMX experiments at the Annual Meeting of the Division of Plasma Physics of the American Physical Society, *Bull. Am. Phys. Soc.* 25, 878 (1980) and 26, 925 (1981).
11. D. L. Correll and R. P. Drake, Eds., *Results of TMX Operations: January-July 1980*, Lawrence Livermore National Laboratory, Livermore, CA, UCID-18803 (1980).
12. T. C. Simonen, "Experimental Progress in Magnetic Mirror Fusion Research," Lawrence Livermore National Laboratory, Livermore, CA, UCRL-85494 (1981); *Proc. IEEE* 69, 935 (1981).
13. T. C. Simonen, "Comparison of Tandem Mirror Confinement with Single Mirror Experiments," Lawrence Livermore National Laboratory, Livermore, CA, UCRL-85834, (1981); to be published in *Nucl. Fusion*.

2. Introduction

2.1 TANDEM MIRROR CONCEPT

The tandem mirror configuration suggested by Fowler and Logan[1] and by Dimov[2] utilizes previously demonstrated mirror physics principles. Figure 2-1 shows the essential parts and the axial plasma profiles of a tandem mirror machine. Two single-cell mirror machines are placed at the ends of a longer solenoid. The mirror-machine end plugs provide a minimum-B magnetic field that contains a high-temperature plasma. The end plugs develop a positive electric potential that confines electrons. This positive end-plug potential, together with the high magnetic mirror ratio, confines the solenoid ions.

In the tandem mirror reactor, most of the fusion power would be produced in the solenoid. Despite the fact that the end plugs are not efficient power producers, the overall Q of the tandem system can be high because the solenoid volume can be much larger than the end-plug volume. The relative advantages of the tandem mirror configuration are shown in Fig. 2-2, which compares TMX results to results from previous single mirror experiments. Confinement of both single and tandem mirrors increases with ion temperature ($T_i^{3/2}$).

In the tandem mirror configuration sketched in Fig. 2-1, high-energy-neutral-beams maintain dense mirror plasmas in the end cells. The ions lost from the central solenoid are replaced by gas ionized and heated by the electrons. The electrons are heated by the energetic plug ions. Thus, the system is characterized by $E_p > T_{ep} > T_{ec} > T_{ic}$, where E_p is the average ion energy of the plug, T_{ep} is the plug electron temperature, T_{ec} the central-cell electron temperature, and T_{ic} is the ion temperature in the central cell.

If the plug density n_p exceeds the solenoid density n_c, the requirement of quasi-neutrality establishes a potential difference ϕ_c between the two regions,

$$\phi = T_e \ln\left(\frac{n_p}{n_c}\right). \qquad (1)$$

Central-cell ions with average energy T_{ic} (less than ϕ_c) are confined in this axial potential well for the time τ_c required for them to diffuse by

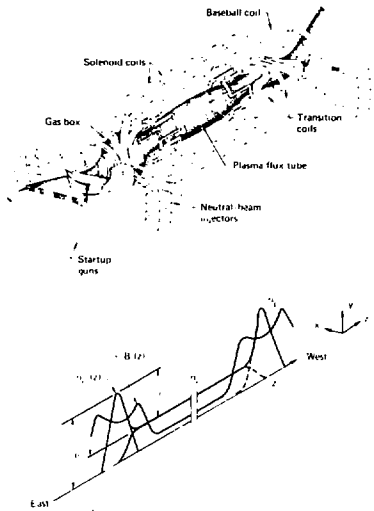

FIG. 2-1. Schematic diagram of the TMX device together with axial profiles of magnetic field B, plasma density n, and plasma potential.

Coulomb collisions upward in energy above the barrier height,

$$n\tau_c = \left[5 \times 10^{10}\, M_i^{1/2} T_{ic}^{1/2} \phi_c + 2 \times 10^{-8} \times n_c L_c R_c\, (M_i/T_{ic})^{1/2}\right] \exp \phi_c/T_{ic} \qquad (2)$$

where L_c is the central cell length and R_c is the central-cell mirror ratio R_c = B(mirror)/B(solenoid). Equation (2) includes contributions from both collisionless and collisional effects. It does not include effects of rf fluctuations. Tandem mirror confinement is enhanced over basic mirror confinement by a factor of $5\,(\phi_c/T_{ic})\ \exp(\phi_c/T_{ic})$; a hundred-fold improvement if $\phi_c/T_{ic} = 2.2$.

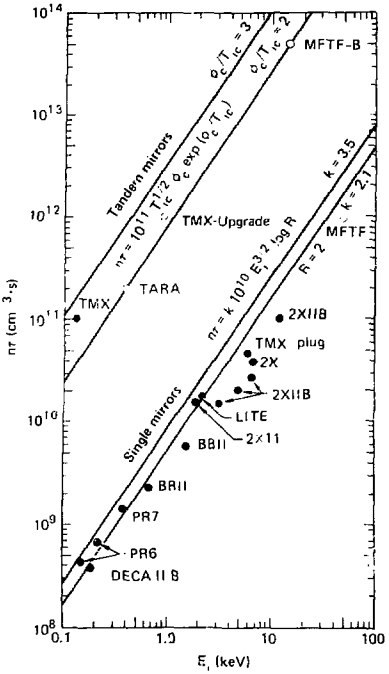

FIG. 2-2. Comparison of confinement scaling shows advantage of tandem mirror over single mirror systems. Best TMX operating point is compared with earlier single mirror experiments all normalized to mirror ratio R = 2 and deuterium ion mass. Both systems increase with ion temperatures as $T_i^{3/2}$ and depend on other parameters.

There are three tandem mirror experiments in operation and a fourth near completion. Their characteristics are given in Table 2-1. Gamma 6 at Tsukuba University in Japan began operation in early 1983, followed by TMX in 1979. Phaedrus, at the University of Wisconsin, has recently begun operation and AMBAL-1, at Novosibirsk USSR, is nearing completion of construction.

The Gamma 6 experiment gave the first indications of the promise of the tandem mirror geometry. This experiment showed that a macroscopically stable density distribution could be created in the tandem mirror magnetic field configuration. Langmuir probe measurements also showed that the potential difference between the end plug and central cell was in agreement with calculations based on Eq. (1).

2.2 THE TMX TANDEM MIRROR EXPERIMENT

The TMX device is described in detail in Appendix A and in Refs. 3 to 9. Figure 2-3 is a photo of TMX which shows the large vacuum tanks, diagnostics above the machine and, on the sides, the neutral beams and power supplies. The TMX neutral-beam system has the most neutral-beam power of any fusion experiment in the world. Twenty-four neutral beams provided up to 5 MW of power for 25-ms pulses to heat the TMX end-plug plasmas up to 13 keV.

A simplified illustration of the TMX magnets and plasma shape is shown in Fig. 2-1. The magnets are turned on for a few seconds for each plasma shot and are water-cooled between shots. The magnet system has three regions: two small high-field-strength end plugs at the end of a much larger and lower magnetic field central solenoid. The end-plug baseball coils produce a minimum-B magnetic field for MHD stability. By electrical plasma contact, the end-plug plasmas hold the central-cell plasma centered on axis. That the end plugs can hold a high-pressure central-cell plasma was one of the important tandem mirror results demonstrated in TMX.

Startup plasma guns located at both ends of TMX create the initial target plasma required to begin the trapping of the neutral-beam atoms. The ions and electrons deposited by the beams help to ionize additional neutral-beam atoms. As shown in Fig. 2-4, once end-plug plasma buildup is initiated, the central-cell gas-feed is used to increase the central-cell density. After 5 ms, when the plasma has been established, the startup guns are turned off; thereafter, the plasma is sustained without plasma feed from the startup guns. Thus the plasma is isolated from contact with end walls and electron heat loss along magnetic field lines is reduced.

Figure 2-5 shows the diagnostic instruments employed on TMX. These instruments are

TABLE 2-1. Summary of operating design parameters of tandem mirror experiments in operation or construction.

	Gamma 6	TMX	Phaedrus	AMBAL-1
Plug:				
B_0 (T)	0.4	1.0	0.4	1.2
B_{mirror} (T)	1.0	2.0	—	—
R_p (cm)	4	10	7	12
L_m mirror-mirror (cm)	—	75	105	—
Heating method	Beam, RF, REB	Beam	ICRF, Beam	Beam
Heating power (MW)	*0.5*	*7*	*0.1*	*1.0*
Duration (ms)	2.5	25	1	—
n (cm^{-3})	5×10^{13}	4×10^{13} max	5×10^{12}	3×10^{13}
W_i (keV)	0.4–10	13	2	20
T_e (eV)	20–2000	260 max	40	1000
Solenoid:				
B (T)	0.15	0.05–0.2	0.05	0.2
$L_{plug\text{-}to\text{-}plug}$ (cm)	315	640	390	—
R_p (cm)	2×20	30	30	30
n (cm^{-3})	$1.0 \times 1.0 \times 10^{13}$	3×10^{13} max	2×10^{12}	1×10^{13}
W_i (eV)	—	250 max	15	500–1000

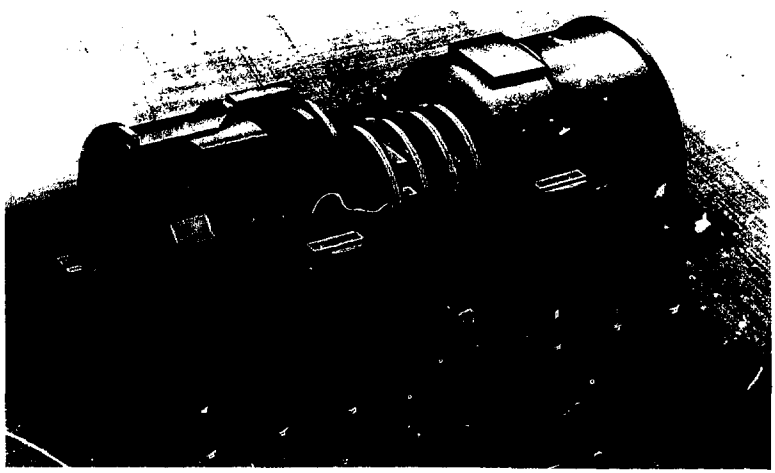

FIG. 2-3. Drawing of the major components of the TMX device.

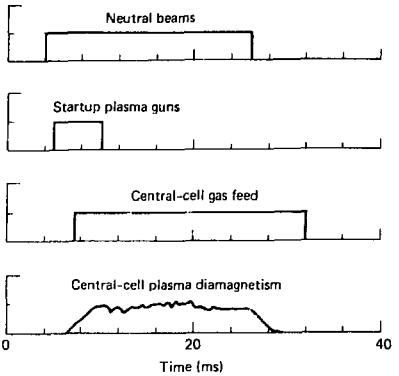

FIG. 2-4. Typical TMX startup sequence.

described in Appendix B. More than 350 diagnostic channels from these instruments provide measurements of such phenomena as plasma density, temperature, shape, impurities, and potentials. Over a million points of data are acquired on each shot.

2.3 OUTLINE OF THIS REPORT

This report summarizes results from the TMX experiments in several subsections of Section III as follows:

Section 3. A description of the tandem mirror configuration of density, temperature potential, and confinement. Extensive diagnostic measurements indicate that the electrostatic potential well improves the central-cell confinement

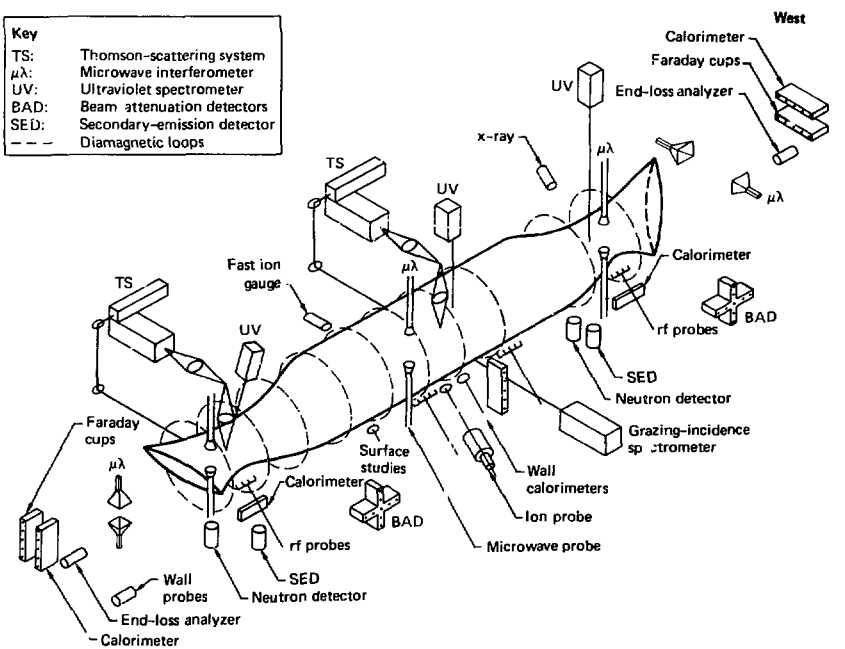

FIG. 2-5. Schematic diagram of diagnostic instrumentation employed on TMX.

over that which could be achieved with magnetic mirrors alone.

Section 4. A description of the effect of the end-cell stability on the confinement of the central-cell plasmas in TMX. The section shows that confinement near the Coulomb value is achieved when end-cell ion-cyclotron fluctuation levels are low, but that higher levels of fluctuations degrade central-cell confinement.

Section 5. The scaling of end-cell confinement is shown to depend on central-cell plasma properties. With sufficient central-cell fueling (density), near-Coulomb end-plug densities are achieved.

Section 6. A discussion of a model for the interaction between the end-cell plasma and the ion flow associated with a stability requirement. Data from a gas fueling scan and two beam current scans show that a correlation exists.

Section 7. An analysis of power balance for several days of operation under different conditions. These results show that near the axis of the central cell the predominant power loss is out the ends by escaping central-cell ions. At the edges of the plasma the power loss is mainly radial by plug charge-exchange and central-cell transport.

Section 8. A report of beta studies that describe measurements of central-cell betas with and without central-cell neutral-beam injection.

Section 9. A description of radial transport studies. These measurements are consistent with resonant neoclassical transport theory.

Section 10. A description of several end-plug optimization experiments. These include an end-plug and central-cell fluctuations.

Section 11. A description of rf studies of end-plug and central-cell fluctuations.

Section 12. Analysis of the data from TMX reveals that the end loss measurements combine with the measurements of the plug-plasma length and beta to provide important clues about the nature of the plug instability.

Section 13. A description of spatial and temporal measurements of low levels of impurities.

Section 14. A description of solid-state plasma-surface probe studies carried out by the Sandia group.

Section 15. A description of end-wall plasma studies and how they indicate low plasma density and electron temperature near the end wall. The density is consistent with theoretical models.

REFERENCES

1. T. K. Fowler and B. G. Logan, "Tandem Mirror Reactor," *Comments Plasma Phys. Controlled Fusion* **2**, 167 (1977).
2. G. I. Dimov, V. V. Zakaidakhov, and M. E. Kishinevskii, "Thermonuclear Confinement System with Turn Mirror Systems," *Fiz. Plazmy* **2**, 597 (1976); [*Sov. Plasma Phys.* **2**, 326 (1976)].
3. F. H. Coensgen, "TMX Major Project Proposal," Lawrence Livermore National Laboratory, Livermore, CA, LLL-Prop-148 (1977).
4. F. H. Coensgen et al., *Phys. Rev. Lett.* **43**, 626 (1979).
5. D. P. Grubb, T. A. Casper, J. F. Clauser, F. H. Coensgen, D. L. Correll, W. C. Cummins, R. P. Drake, J. H. Foote, A. H. Futch, R. K. Goodman, R. S. Hornady, W. E. Nexsen, P. Poulsen, T. D. Rognlien, T. C. Simonen, G. R. Smith, and B. W. Stallard, "Effects of End Cell Ion Cyclotron Fluctuations on Central-Cell Ion Confinement in the Tandem Mirror Experiment (TMX)*," in *Proc. Intl. Symp. on Physics of Open-Ended Fusion Systems, April 15–18, 1980, University of Tsukuba, Japan* (University of Tsukuba, Ibakari, Japan, 1980); also Lawrence Livermore National Laboratory, Livermore, CA, UCRL-84236 (1980).

6. D. L. baldwin, B. G. Logan, and T. C. Simonen, Eds., *Physics Basis for MFTF-B*, Lawrence Livermore National Laboratory, Livermore, CA, UCID-18496 (1980).*
7. R. P. Drake, T. A. Casper, J. F. Clauser, F. H. Coensgen, D. L. Correll, W. F. Cummins, J. C. Davis, J. H. Foote, A. H. Futch, R. K. Goodman, D. P. Grubb, R. S. Hornady, W. E. Nexsen, T. C. Simonen, and B. W. Stallard, "The Effect of End-Cell Stability on the Confinement of the Central-Cell Plasma in TMX," *Nucl. Fusion* **21**, 359 (1981).
8. D. L. Correll and R. P. Drake, Eds., *Results of TMX Operations: January–July 1980*, Lawrence Livermore National Laboratory, Livermore, CA, UCID-18803 (1980).
9. T. C. Simonen et al., in *Proc. Intl. Conf. Plasma Physics and Controlled Nucl. Fusion Research, 8th, Brussels, 1980;* (IAEA-CN-38/F-1, Vienna, Austria, 1981).
10. K. Yatsu et al., "Experimental Observation of Enhancement of the Ambipolar Potential by Injection of Neutral Beams in a Tandem Mirror," *Phys. Rev. Letters* **43**, 627-630 (1979).

3. Ambipolar Potential Formation and Axial Confinement in TMX

3.1 INTRODUCTION

The tandem mirror configuration[1,2] uses three mirror cells: two hot, dense plasmas confined within minimum-B mirrors (end plugs), which provide both MHD stability and electrostatic stoppering for a warm Maxwellian plasma of lower density within a longer, solenoidal mirror (central cell). The TMX group has reported creating the tandem mirror configuration of axial density and potential profiles which were sustained by central-cell gas fueling and end-cell neutral-beam injection.[3] Axial central-cell particle confinement improved because of the confining ambipolar potential. In a subsequent publication[4] (also see Sec. 4), end-cell stability requirements (rising from microinstabilities near the plug ion-cyclotron frequencies) were shown to affect central-cell confinement.

This paper expands the data set supporting these original conclusions, documents measurements of the radial dependence of the ambipolar potentials, and demonstrates that for low, constant values of ion-cyclotron fluctuations, the central-cell axial confinement scaled with end-cell neutral-beam injection energy according to implied values of the confining potential. Enhancement of axial confinement of central-cell ions scaled from 4 to 8 as the neutral-beam injection voltage was increased. We measured central-cell confining potentials of 150 V, which are in good agreement with density and electron temperature data within the radial core of the central-cell plasma.

In the following sections we briefly describe the experimental hardware and timing sequence of events (Sec. 3.2), discuss the data and diagnostics associated with the measurements of axial and radial profiles (Sec. 3.3), compare radial potential measurements with theoretical predictions based on the Boltzmann relation (Sec. 3.4), evaluate the axial confinement of central-cell ions and compare it to the predicted amount of enhancement due to electrostatic confinement (Sec. 3.5), and finally summarize our observations and conclusions (Sec. 3.6).

3.2 EXPERIMENTAL ARRANGEMENT

Figure 3-1 shows the TMX magnet and neutral-beam injector systems. A detailed description of the experimental facility is given in Appendix A. The four deuterium-loaded titanium-washer startup guns supply a plasma target for neutral-beam buildup within the plugs. Those guns are turned off after 5 ms, and the central cell is fueled either by gas injection into two gas boxes in the transition regions between the plugs and central cell or by feeding gas into the central region of the solenoid vacuum vessel (gas puffing). Steady-state density conditions are reached within 10 ms and are sustained for the entire 25-ms pulse length of the neutral beams. The expected axial plasma density, potential, and magnetic field profiles are shown in Fig. 3-1. The inside mirror and the outside mirror at each end are 265 cm and 375 cm respectively from the midplane of the central cell. The plug midplane is 320 cm from the central-cell midplane. The plug and central-cell densities, n_p and n_c, are controlled predominantly by the amount of neutral-beam current and central-cell gas fueling; however, day-to-day variations in other key plasma parameters such as electron temperature, T_e, can have a minor effect. The value of the central-cell potential, ϕ_e, is established by the required equality of electron and ion losses. The plug potential, ϕ_p, is higher than ϕ_e for a Maxwellian distribution of electrons by an amount $\phi_c = T_e \ln(n_p/n_c)$ (for T_e constant along field lines). This positive electrostatic potential, ϕ_c, augments the central-cell magnetic confinement by turning back ions of parallel energy less than ϕ_c.

Figure 3-2 shows the time histories from 0 to 30 ms of key plasma parameters for a typical shot. This shot is representative of a 29-shot group required to increment diagnostics from one radial position to another. The plug magnetic field had a midplane strength of 1 T with a 2-to-1 mirror ratio. The central-cell field strength, which could be set between 0.05 to 0.2 T, was at 0.1 T. The neutral-beam injection current per plug averaged 150 A

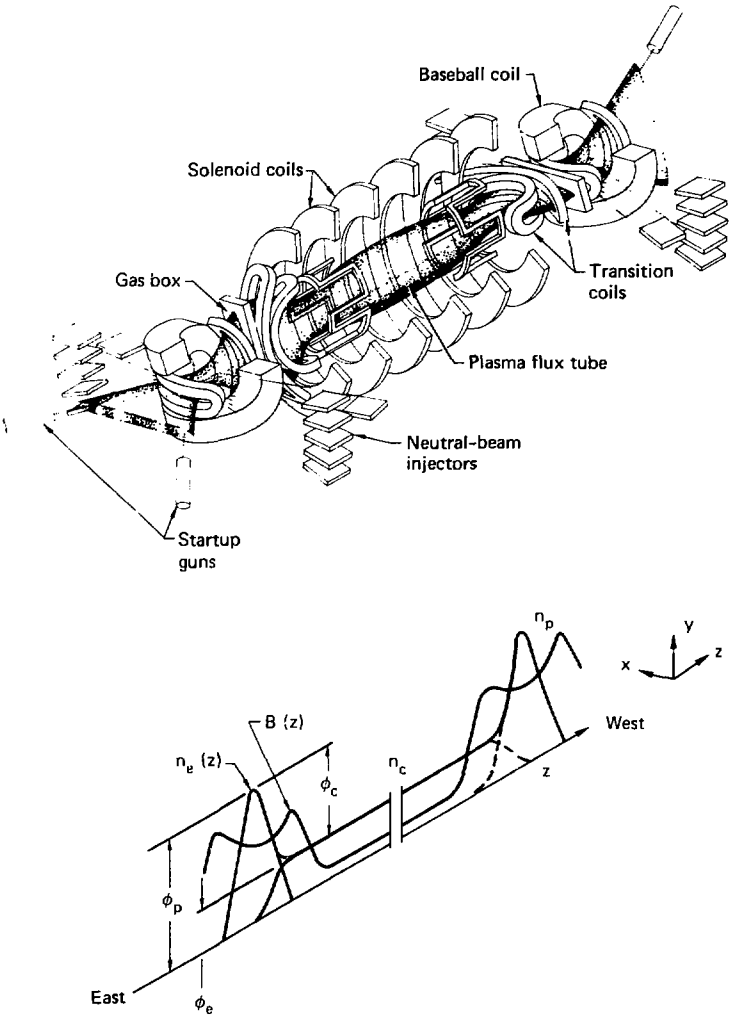

FIG. 3-1. TMX magnet geometry and expected axial plasma profiles.

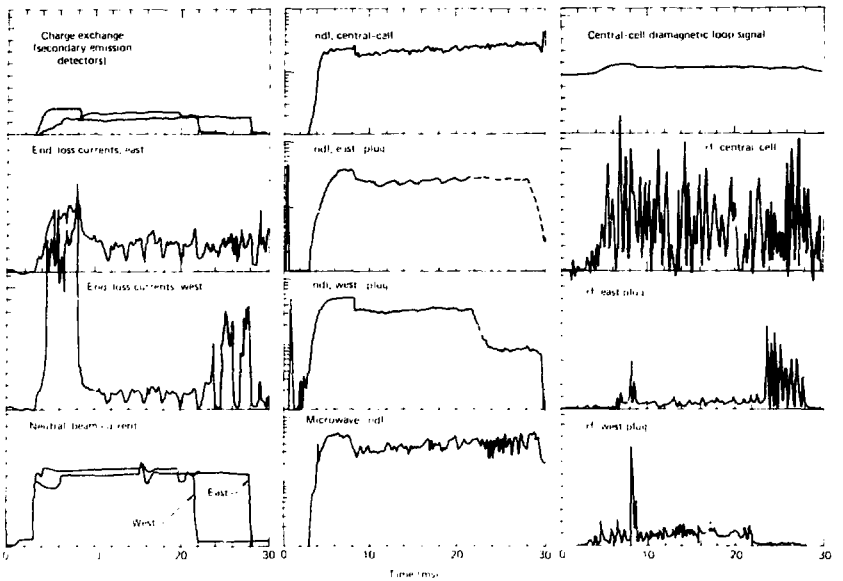

FIG. 3-2. Time histories (0 to 30 ms) of key plasma parameters for a typical shot. The vertical scales are: charge exchange, 0 to 2 mA; end-loss current, east, 0 to 70 mA/cm^2; end-loss current, west, 0 to 140 mA/cm^2; neutral-beam current, 0 to 250 A; ∫ndl, central cell, east plug, and west plug, 10^{13} to 10^{15} cm^{-2}; microwave ∫ndl, 10^{12} to 10^{14} cm^{-2}; central-cell diamagnetic loop signal, −8 to 8 A·m^2·cm^{-1}; rf, central-cell, 0 to 7.7 V_{pp}; rf, east-plug, 0 to 33 V_{pp}; rf, west-plug, 0 to 24 V_{pp}.

equivalent of atomic deuterium and varied from shot to shot between 130 and 165 A. To fuel the central cell, we used a standard LBL neutral-beam gas valve on the middle bottom port of the central cell. The neutral gas input was 790 molecular A of deuterium or 1580 equivalent atomic A. The selection criteria were that the neutral-beam current was near 150 A and that the on-axis potential was reproducible. All plasma parameters of this shot are within 20% of the mean of the group except the plug electron temperature, which is 30% below the mean. Reading from top to bottom, the first column of Fig. 3-2 shows the charge-exchange signal from secondary emission detectors in the east and west plug, the east and west ion end-loss currents, and finally the amount of injected neutral-beam current in each plug. The second column shows the central chord line density in the central cell and in the east and west plugs, respectively. The dashed line in the east measurement beginning at 22 ms represents data from a similar shot. The last measurement of line density was made at z = 285 cm which is 2/3 of the way between the midplane of the east plug and its inside mirror towards the central cell. The last column shows the central-cell diamagnetic loop signal and wide-band rf measurements of oscillations in the central cell and in the east and west plugs.

As can be seen by the line-density and ion end-loss current measurements, steady-state plasma values are reached within 10 ms and are maintained for the entire length of neutral-beam injection. The high end losses from 3 to 8 ms are caused by stream plasma from the startup guns being reflected from the plasma being built up within the plugs. After a sufficiently dense, hot, mirror-

confined plasma is reached within the plugs, the startup guns are turned off and the central cell is fueled by gas injection and the end plugs by the neutral beams. A steady state is established with comparable end losses out both ends of the machine. If we turn off the neutral beams in one plug before the other, as we did with the west plug for this shot, we find that the measured end losses out that end of the machine increase dramatically as the density drops, and with it the plug potential. That the current measured at the west end is higher than that at the east end is qualitative evidence of electrostatic stoppering. The central-cell losses dominate over the end-plug losses because the central-cell plasma is approximately 10 times longer.

3.3 DENSITY, ELECTRON TEMPERATURE, AND POTENTIAL PROFILES

3.3.1 Density Profiles

Spatial profiles of line-integral densities, $\int ndl$, are measured in TMX with extensive arrays of beam-attenuation detectors (BAD's) and with microwave interferometers (both are described in Appendix B). The beam-attenuation detectors are located on the vacuum chamber wall opposite a selected neutral beam in each of the three mirror cells. They measure secondary electron emission and are used to determine the neutral current of each beam, with and without the plasma present. The plasma line density along the detector line of sight is then unfolded from the total cross section and the measured loss of neutral beam particles. This calculation is not sensitive to observed background gas conditions because ionization and charge-exchange events dominate over collisions between neutrals. For the plasma conditions in the plugs, one holding of attenuation of the detected neutral-beam current requires a line density of ionized deuterium of approximately 6.5×10^{14} cm^{-2}. We determined the radial and axial line-density profile of each plug from the particle attenuation of one of the heating and fueling neutral beams, measured by cross-shaped arrays of beam-attenuation detectors. We determined the radial plasma profiles of the larger-radius central cell from the particle attenuation of a neutral beam mounted with the major axis of its footprint vertical. Because the magnetic field in the central cell is lower than that in the end cells, the ionized particles from the central-cell beam have gyroradii too large to be magnetically trapped. Axial measurements of the central cell were not possible because the beam footprint was too narrow.

Figure 3-3 shows the radial and axial profiles of $\int ndl$ for the plugs and the radial profile of $\int ndl$ for the central cell. We selected the time of 16 ms, within the 25-ms neutral-beam pulse, to display data representative of steady-state conditions, and have averaged 29 constant-condition shots.

Figure 3-3(a) shows average line densities measured at various positions along the magnetic axis (the horizontal or z direction). An additional data point measured by microwave attenuation, located at $z = -220$ cm, has a normalized value about 37% greater than the data point at $z = -286$ cm. The magnetic field runs east to west ($+z$) with vertical displacement being in the $+y$ direction according to the right-hand rule. The left-to-right orientation of the $\int ndl$ data in this figure is the same as for the schematic shown in Fig. 3-1; for example, the axial line density at $z = -330$ cm is in the east half of the east end cell of the machine. This measurement would be near the horizontal fan of the left plug of Fig. 3-1.

Many of the qualitative features of the axial plasma-density profiles of Fig. 3-1 are reproduced in the experimental data of Fig. 3-3(a). The plug line density is observed to decline smoothly to the central-cell value. As we will prove later, using radial-profile measurements, the plug density is several times that of the central-cell density. Gaussian curves with a dependence in z given by $\exp(-z^2/L^2)$ have been drawn through the axial variation of the plug data. We have allowed the plugs to have different e-folding lengths. In Fig. 3-3(a), as in most of our data, we find that the axial lengths in the west plug are larger than in the east plug. We have come to believe that the central-cell density which leans towards the plug is the source of this difference. The west transition fan, which is horizontal and parallel to the beam injection, is a better target for trapping neutral-beam particles at positions off of the plug midplane than the east transition fan, which is vertical. The west and east fans are oriented perpendicular to each other in order to ensure that the central-cell drift surfaces are approximately circular. Better trapping in the west plug can also explain why line densities in the west

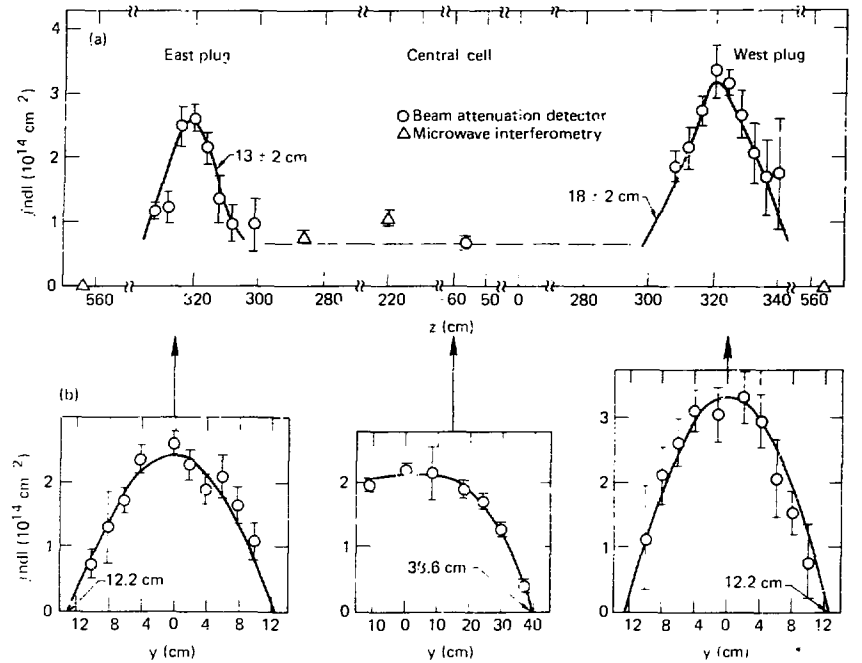

FIG. 3-3. Plasma line-density profile experimental results: (a) Variation along the magnetic axis (z). All data points have been normalized to the same path length through the plasma as at the center of the plugs. The data indicated by open circles are from the beam-attenuation diagnostic, and the data indicated by the triangles are from microwave interferometry. (b) Vertical (radial) profiles at the centers of the east and west plugs and near the center of the central cell.

plug are usually higher than in the east plug for comparable beam currents. The axial e-folding lengths, L, are typically from 10 to 20 cm and asymmetric, with the west-plug L as much as 50% longer than the east-plug L. We also find that L tends to be more sensitive than the radial scale lengths to plasma conditions such as electron temperature, central-cell density, and neutral gas pressure.

Figure 3-3(b) shows the variations in vertical line density in the midplane of both plugs and near the midplane of the central cell. We have used parabolic profiles to draw smooth curves through the plug data and second-order polynomials through the central-cell data. Figure 3-4 gives the radial profile inversions, n(r), of the line density data, ∫ndl, of Fig. 3-3(b). The solid lines of Fig. 3-3(b) are polynomial fits of the form

$$\int ndl = A[1 - (r/R_c)^2] + B[1 - (r/R_c)^4]$$

which are inverted in Fig. 3-4 to give

$$n(r) = \frac{2}{\pi R_c}[A + 2/3\,B + 4/3\,B(r/R_c)^2] \times [1 - (r/R_c)^2]^{1/2}$$

The constants A and B in the east plug, west plug, and central cell were $A_E = 2.4 \times 10^{14}$ cm^{-2}, $B_E = 0$, $A_W = 3.3 \times 10^{14}$ cm^{-2}, $B_W = 0$, $A_c = 0.7 \times 10^{14}$ cm^{-2}, and $B_c = 1.4 \times 10^{14}$ cm^{-2}. We found that the cut-off radius, R_c, was the same for both east and west plugs, $R_{cE} = R_{cW} \equiv R_{cp} = 12.2$ cm, and that the central-cell value was $R_{cc} = 38.6$ cm. As in many other experimental running conditions, the experimentally determined values of R_{cp} and R_{cc} are related by flux conservation $B_p \pi R_{cp}^2 = B_c \pi R_{cc}^2$, where B_p and B_c are the midplane magnetic field values of the plugs and central cell respectively. Two electrically grounded limiters with radii of 38.6 cm were located in the central cell at $z = \pm 54$ cm. The gas-box limiters mapped to a central-cell midplane radius of 47.4 cm and the central-cell getters and diagnostics were at a radius of 39 cm or more.

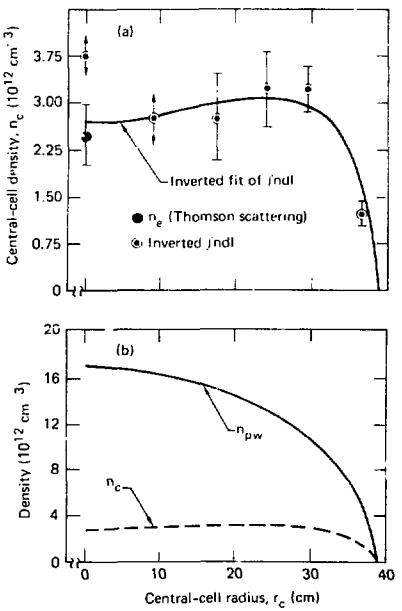

FIG. 3-4. Radial density profiles. (a) Inverted central-cell line-density data compared with the inverted polynomial fit to the data, and with the electron density at zero radius measured by Thomson scattering. (b) Density profiles of the west plug and the central cell.

Figure 3-4(a) compares the continuously inverted central-cell density, $n_c(r)$, with the matrix inversion of the line-density data points (open circles) and with the Thomson-scattering measurement of the electron density, n_e, at zero radius (solid circle). The large error bars for n_c at 0 and 9 cm result from propagating errors at the edge to the central core when inverting chord values of ∫ndl. The data point for n_e at zero radius gives added support to the inverted profile, $n_c(r_c) = 3.5 \times 10^{12} [1 - (r_c/38.6)^2]^{1/2} \times [0.8 + 0.9 (r_c/38.6)^2]$ cm^{-3}. In Fig. 3-4(b), the same analysis was used to generate the density profile for the west plug, $n_{pW}(r_c) = 1.7 \times 10^{13} \times [1 - (r_c/38.6)^2]^{1/2}$ cm^{-3}. We have again used flux conservation to convert plug radii values, r_p, to central-cell radii values, $r_c = r_p (B_p/B_c)^{1/2}$. For comparison, we replotted $n_c(r_c)$ in Fig. 3-4(b) on the same scale as was used for $n_{pW}(r_c)$.

3.3.2 Electron Temperature Profiles

The electron density, n_e, and electron temperature, T_e, for the east plug (subscript p) and central cell (subscript c) are plotted in Fig 3-5 for the entire 29-shot radial scan group. As with the line-density profiles, the data was taken at 16 ms. The Thomson-scattering system, which is described in detail in Appendix B, comprised two separate ruby lasers and viewing optics located axially at the midplanes of the east plug and central cell. The electron temperature is inferred from the Doppler profile of the scattered light and the plasma density from the total amount of scattered light. The east-cell optics could view three different radii, 0, 5, and 10 cm. The central-cell system was fixed at zero radius. The radial positions of the magnetic lines of force in the central cell are related to their position within the plug by $r_c = r_p (B_p/B_c)^{1/2}$, with B_p and B_c being the midplane field strengths of 1.0 and 0.1 T respectively. The data at each radial position is separated in Fig. 3-5 for purposes of clarity. There is no data for plug electron density, n_{ep}, at 10-cm radius. Only the positions at 0- and 5-cm radius were calibrated by scattering light from a known amount of nitrogen. The values of n_{ep} in Fig. 3-5 are the same, within

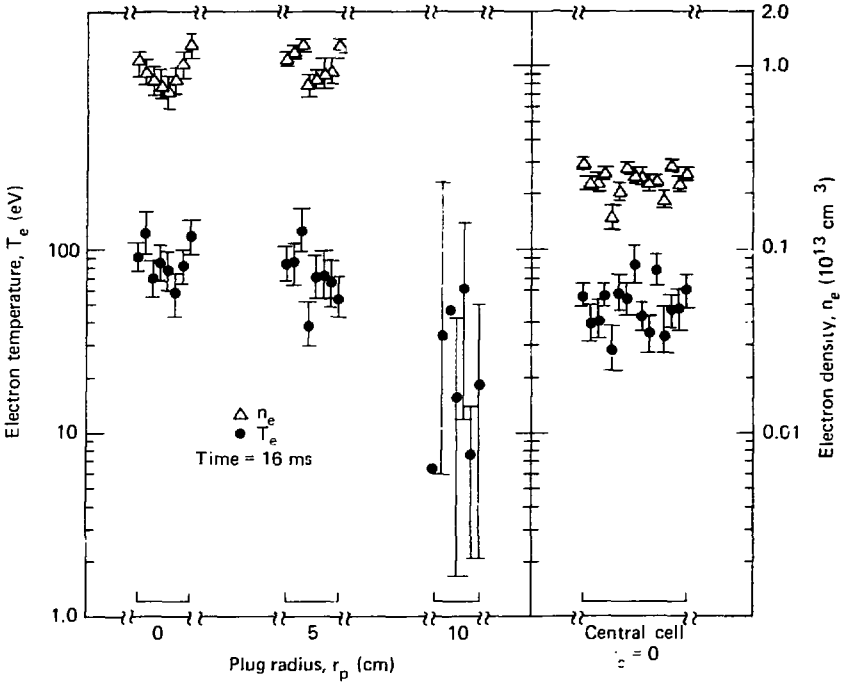

FIG. 3-5. Electron temperatures and densities in the east plug (at r_p = 0, 5, and 10 cm) and the central cell (at r_c = 0), as measured by Thomson scattering.

the accuracy of each measurement, as the values given by the polynomial inversions to the line-density data shown in Fig. 3-3.

As Fig. 3-5 shows, the average electron temperature, T_e, at zero radius was 87 eV in the east plug and 49 eV in the central cell. In several earlier experimental days of running, before we had the capability of taking central-cell electron-temperature measurements, we found the mean value of T_{ep} to be 150 eV. Data that supported the conclusion that variations in T_{ep} are due to vacuum conditions (static and dynamic) is discussed in Appendix A. What we have seen on several occasions is that the measured values of the end-cell (plug) potential, ϕ_p, and central-cell potential, ϕ_c, adjust to changes in T_{ep} and T_{ec} according to the physics of electron confinement.

This observation can be supported by the data of Fig. 3-6, where we have plotted T_{ec} and ϕ_p against T_{ep}. These shots are separate from the group of 29 presently under evaluation. The data of Fig. 3-6 represent a day's run where machine conditions were not constant because two vacuum leaks (in a vacuum feed-through and in a magnet-cover case) occurred during the experiment. In this run, the plug potential and central-cell electron temperature decreased as the plug electron temperature decreased. We therefore feel confident in continuing with the discussion of the data of interest generated when the machine conditions and electron temperature were constant for enough shots to generate profile information.

In Fig. 3-5, the average value of T_{ep} for the constant condition shots at 5-cm radius is very

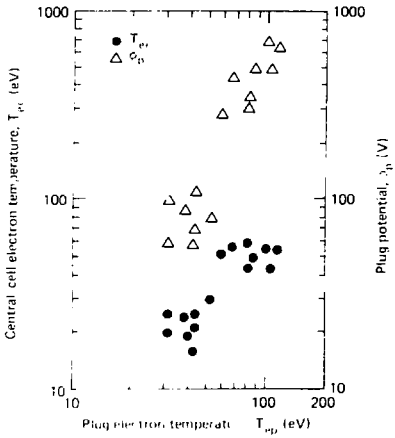

FIG. 3-6. Variation of the central-cell electron temperature and the plug potential with changes in the plug electron temperature, for a separate experimental run with known vacuum problems.

close to the zero-radius average. The lower plasma density at 5-cm radius accounts for the increase in scatter of the data points. The average value of T_{ep} at 10-cm radius is approximately $[n(r = 10)/n(r = 0)]^2$ less than the value at zero radius. The profile of T_{ep} is approximated by the same radial dependency as n_p^2. Because no data exist for T_{ec} for central-cell radii other than zero, we assume that T_{ec} has the same radial dependence as n_c^2. There is also no direct measurement of T_{ep} in the west end cell. The electron temperature in the west plug was estimated as $T_{eW}(\phi_{pW}/\phi_{pE})$.

3.3.3 Potential Profiles

In this section we discuss direct measurements of the plug potential, ϕ_p, and central-cell potential, ϕ_c.

The value of ϕ_p is determined by the four swept-voltage end-loss analyzers (two per end-cell with one movable on the west plug). These electrostatic end-loss ion analyzers (ELA's), described in detail in Appendix B, can have their ion-repeller grids biased positively with respect to ground. Then ions with energies less than the ion-repeller grid voltage do not reach the collector plate. Because the ELA's are located in the escaping plasma fan regions at the end wall where the magnetic field strength is 0.007 T, the ion end-loss current has most of its energy converted to parallel motion. Since all the escaping ions either come from the plug or must pass through it to leave the central cell, the flux of end-loss current will not be attenuated until the ion-repeller voltage exceeds the potential drop from the plug to the end wall, ϕ_p.

The ion repeller voltage on all four ELA's was ramped on and off 10 times during each shot. The sawtooth characteristics every 2 ms in the second and third plots of the first column of Fig. 3-2 are caused by this biasing of the ion repeller grid on and off to voltages of +1500 V above ground. Note how, after 22 ms, when the west neutral beams are turned off and the plasma density in the west plug begins to decay, the propeller voltage ramp is able to turn away all the escaping ion flux to the west end wall. This is not the case for the east end-loss current, which is continuing to pass through a plug of high-density plasma. The secondary emission detector signal in the east plug indicates that steady-state density conditions still exist. The beam-attenuation diagnostic happened to fail temporarily right after 22 ms, as is seen in the east fndl plot.

Figure 3-7(a) shows the west-plug ion end-loss current density, j, after computer processing of the data to determine ϕ_p. The current density in mA/cm^2 is referenced to the central-cell midplane. The current spike near 8 ms is due to stream plasma from the startup guns being reflected from the plug. Turning the west neutral beams off before the east neutral beams resulted in a dramatic increase in measured west-end losses at 22 ms. Figures 7(c) and (d) show the current-voltage characteristics of the ion end-loss current density, j, measured by the west ELA at two different repeller sweep times, one near 10 ms (representative of steady-state operation) and one near 25 ms (representative of a single-plug tandem). The ion end-loss current is not reduced until the ion repeller voltage exceeds ϕ_p. At higher repeller voltages, the curvature of the current voltage curve is a measure of the energy distribution of the ion end losses. During steady-state operation the shot-to-shot average value for ϕ_p at $r_c = 0$ was 480 V for the west plug and 540 V for the east plug. When either plug is turned off before the other (as the west plug

was for the data in Fig. 3-7) the measured value of ϕ_p is near that of ϕ_e; that is, only one end of the machine has any electrostatic stoppering. These points are illustrated in Fig. 3-7(b), where measured values of ϕ_p are plotted versus time, including the 16 and 25 ms data of Fig. 3-7(c) and (d).

To measure the dependence of ϕ_p on radius, the movable ELA on the west plug was scanned across the thin dimension of the west end fan. Because of the machine geometry (ports and liner configuration), movable ELA measurements could be made only for the west plug. The second ELA on the west end, fixed at zero radius, monitored shot-to-shot variations in ϕ_p to aid in analyzing the data. It was necessary to allow the ϕ_p radial profile to shift by roughly an ion-gyro diameter (4 cm at the plug midplane) to bring the ELA ion-current profile, as well as the end-loss current measurements made by a fixed array of Faraday cups, into agreement with the mechanical machine axis.

The thallium heavy-ion beam probe (HIBP) described in Appendix B was used to measure the central-cell space potential, ϕ_e. The potential is determined from the energy of doubly ionized thallium ions. The energy of injected ions, which undergo a change in charge state through electron impact ionization, increases above the injection voltage by an amount equal to the product of ϕ_e at the collision point and the change in charge. The measured ϕ_e at a central-cell radius of zero and the experimental time sequence are given in Fig. 3-8. The plasma guns were turned off at 8 ms, and the

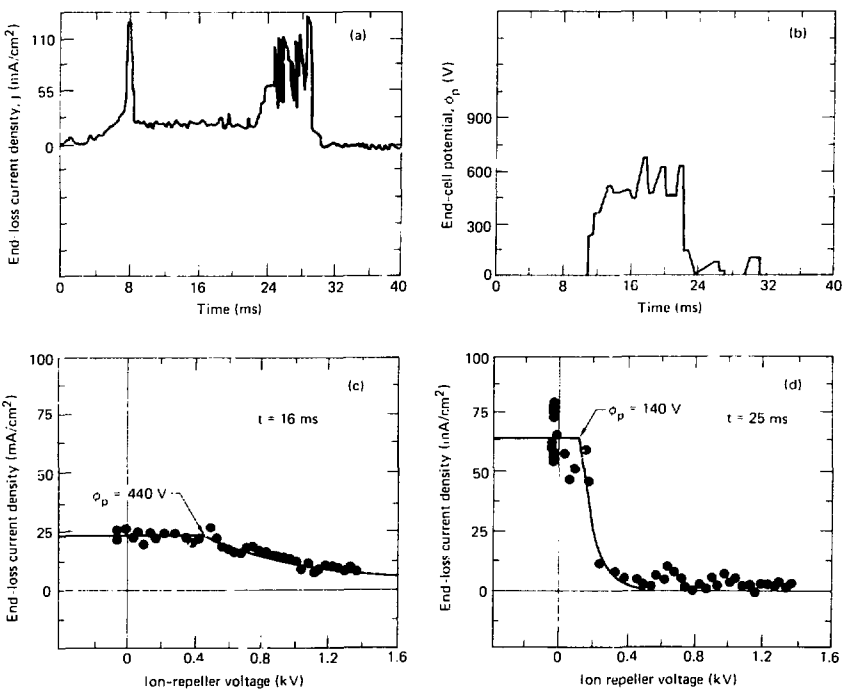

FIG. 3-7. The end-loss current density and end-cell potential versus time. The current-voltage characteristics of the end-loss analyzer (ELA) at 16 and 25 ms are given to illustrate ϕ_p measurements.

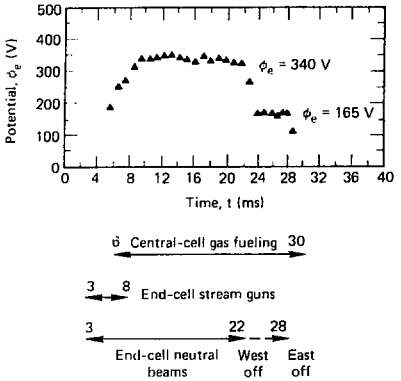

FIG. 3-8. **The central-cell space potential on-axis (measured by HIBP) versus time. The timing sequence for plasma fueling and heating is shown as well.**

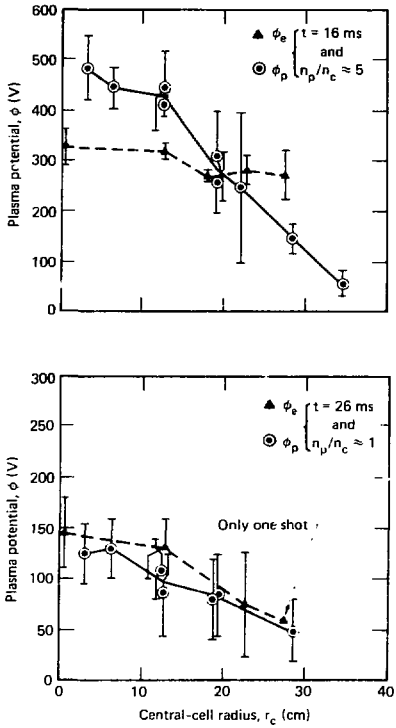

FIG. 3-9. **Plug potential and central-cell space potential versus central-cell radius at 16 ms ($n_p/n_c \approx 5$) and 26 ms ($n_p/n_c \approx 1$). The data was averaged about 16 ± 2 and 26 ± 1 ms. The data for $n_p/n_c \approx 1$ is used to check the calibration of the HIBP and ELA against each other.**

central cell was fueled by gas injection and the end plugs by the neutral beams. Steady-state values of ϕ_e were reached within 10 ms and maintained for the entire length of neutral-beam injection. When the neutral beams in the west plug were turned off (at 22 ms), ϕ_e fell to a lower steady-state value because of the reduction in the central-cell electron temperature, T_{ec}, and in ion particle confinement. When the remaining (east-plug) neutral beams were turned off, we observed that the central-cell potential dropped continually until it reached the lower sensitivity limit of the HIBP. To measure the radial dependence of ϕ_e, the HIBP could be radially incremented shot-to-shot by adjusting the beam voltage or, if there was sufficient signal-to-noise, a single-shot radial scan could be accomplished by using a set of beam-deflection plates.

The central-cell and plug potentials at 16 and 26 ms are plotted in Fig. 3-9 as functions of the central-cell radius. These measurements were taken under constant machine conditions of magnetic field strength, neutral-beam injection current, and central-cell fueling. The plug magnetic field had a midplane strength of 1 T with a 2-to-1 mirror ratio and the central-cell field strength was 0.1 T. The neutral-beam injection current per plug was 150 ± 20 A equivalent of atomic deuterium. We used a standard LBL neutral-beam gas valve located on the middle bottom port to fuel the central cell. The deuterium gas input was 1580 equivalent atomic A. The selection criteria were that the neutral-beam current was near 150 A and that the on-axis potential was reproducible.

That the two diagnostics (HIPB and ELA) measured similar potentials at 26 ms when $n_p \approx n_c$ testifies that there is no obvious systematic offset in the determination of ϕ_c and ϕ_p. Therefore, we

conclude that the data in Fig. 3-9 at 16 ms, when $n_p/n_c \approx 5$, can be used to give the central-cell confining potential by simple subtraction, $\phi_c = \phi_p - \phi_e$. The error bars represent the statistical fluctuations from shot to shot. We have estimated the systematic error in the HIBP and the ELA to be ±20 V and ±30 V, respectively.

At 16 ms, the largest radial measurement of ϕ_p falls below ϕ_e, according to our present calibrations and error analysis. From a diagnostic viewpoint, the ELA should determine the highest potential within the plasma, whether it is ϕ_p or ϕ_e, unless the axial central-cell losses become mirror-trapped within the end cells or undergo charge-exchange events before reaching the end wall. (These additional changes to central-cell end losses are discussed in detail in Section 6.) Although no experimental evidence exists for significant azimuthal asymmetries, such asymmetries could alter our interpretation of the data. The radial dependence of ϕ_p had to be measured horizontally while the radial dependence of ϕ_e had to be measured vertically. We are investigating how thermal-barrier effects,[5] non-Maxwellian electron distributions, edge fueling of neutrals, and radial losses of electrons might modify theoretical predictions for ϕ_p and ϕ_e. These effects are discussed in the following section in the comparison of experimentally determined and theoretically predicted central-cell confining potentials.

3.4 CONSISTENCY AMONG PLASMA PROFILES

We will use the profiles of plasma density and electron temperature discussed in Section 3.3 to compare the experimentally determined confining potential, $\phi_c = \phi_p - \phi_e$, to the predicted value, $\phi_c = T_e \ln (n_p/n_c)$, as a function of radius.

Figure 3-10 shows that the central-cell confining potential is 150 V on-axis, and that it remains near the on-axis value to a radius of 15 cm. Between 0 and 20 cm, there is agreement between the measured values of ϕ_c and the predicted values on the basis of the ambipolar potential well established by quasi-neutrality in the absence of any electron temperature differences between the plug and the central cell,

$$\phi_c(r) = T_{ep}(r) \ln[n_p(r)/n_c(r)] \quad . \qquad (1)$$

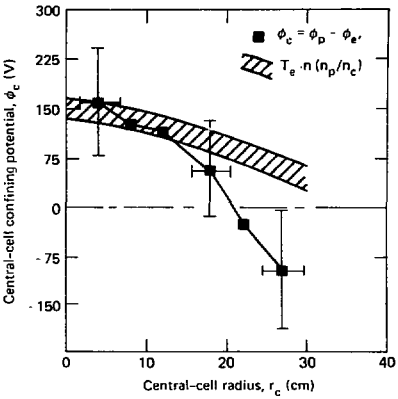

FIG. 3-10. The central-cell confining potentials determined experimentally compared with the potentials predicted from density and electron temperature measurements by T_e ln(n_p/n_c), both as functions of radius.

The range of predicted values of ϕ_c represents the uncertainty in determining the values of electron temperature, T_e, plug plasma density, n_p, and central-cell density, n_c. The electron temperature in the east plug, T_{eE}, was measured by Thomson-scattering techniques at three radii that map into central-cell radii of 0, 15.8, and 31.6 cm by flux conservation [$r_c = r_p (B_p/B_c)^{1/2}$], and was found to scale radially as $n_{pE}^2(r)$. As discussed in Section 3.3.2, the electron temperature in the west plug was estimated as $T_{eW} = T_{eE}\, \phi_{pW}/\phi_{pE}$. We used the radial values of n_p and n_c shown in Fig. 3-4.

Beyond a central-cell radius of 20 cm, the experimental data of Fig. 3-10 fall below the predicted value. (We will discuss the sign of ϕ_c later.) One way to investigate this phenomenon is to assume a thermal barrier between the plug and the central cell.[5] In the presence of a thermal barrier, ϕ_c is given by

$$\phi_c(r) = T_{ep}(r) \ln\left\{\frac{n_p(r)}{n_b(r)}\left[\frac{T_{ec}(r)}{T_{ep}(r)}\right]^{1/2}\right\} - T_{ec}(r) \ln\left[\frac{n_c(r)}{n_b(r)}\right] \qquad (2)$$

where n_b in the thermal-barrier region is lower than either n_p or n_c. A thermal barrier allows an electron temperature difference to exist between plug and central cell ($T_{ep} \neq T_{ec}$) by reducing the electron-electron collision frequency.[5] Note that as n_b approaches n_c, and hence as T_{ec} approaches T_{ep}, the value of ϕ_c obtained from Eq. (2) approaches the same value as obtained from Eq. (1). As shown in Fig. 3-5, we found that the average central-cell electron temperature was 60% of the average east-plug electron temperature (49 eV vs 87 eV). The microwave interferometry density measurements of Section 3.3.1 did not show a density depression (thermal barrier) between the east plug and the central cell. These measurements had to be taken on either side of the plug–central-cell transition region because of magnetic coil interference. It is not unreasonable to ask how large the density depression must be to explain the observed differences in T_{ep} and T_{ec}. Equating Eq. (2) to the experimental value of ϕ_c at $r_c = 0$, using the experimental values of n and T_e, gives $n_b \approx 0.5\ n_c$. Electron power flow calculations in Section 7 find n_b/n_c equal to 0.3 to 0.5. We can only speculate that radial variations of density in a barrier region might have a stronger gradient than in the central cell, so that the term $T_{ec}\ln[n_c/n_b]$ in Eq. (2) became larger at increasing r_c. This effect would lower the predicted value of ϕ_c near the radial edge.

Using either Eqs. (1) or (2) to substantiate a negative ϕ_c, ($\phi_p < \phi_e$) would require, for a Maxwellian electron population, that either the electron temperature and/or density in the central cell exceed that of the plug. This was not what we observed experimentally. We firmly believe that the negative values of ϕ_c at radii greater than 20 cm are an artifact of the measurement of ϕ_p and/or ϕ_e. This conclusion is also supported by the measured radial dependence of the central-cell axial ion-loss current. Central-cell axial ion losses were measured by Faraday cups mounted in arrays across the narrow dimension of the magnetic flux bundle at both ends of the machine. The total current of central-cell axial ion losses from both ends is plotted versus central-cell radius in Fig. 3-11. The Faraday-cup measurements were integrated assuming axisymmetric profiles with symmetry points at the peak of the plug potential. If, as the measurements leading to Fig. 3-10 indicate, ϕ_c were to change from a positive confining potential to a negative repelling potential beyond the 20-cm radius, one would expect some kind of discontinuity in the data of Fig. 3-11. Such a discontinuity is not observed.

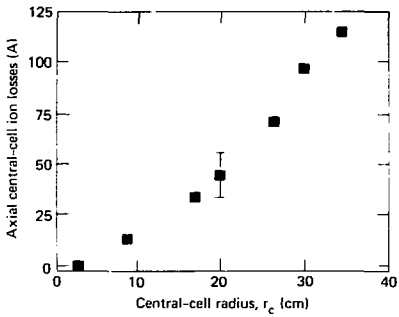

FIG. 3-11. The experimentally determined central-cell axial ion-loss current versus r_c.

3.5 ELECTROSTATIC CONFINEMENT

We limit our discussion of electrostatic confinement of the central cell to the core of the central cell (radius less than 15 cm), where we have both confidence and correlation between measured and predicted ϕ_c. We have found that radial ion losses from the central cell are an insignificant fraction of the axial losses within a radius of 20 cm. The radial loss data are presented in detail in Section 9.

To quantify the amount of enhanced electrostatic confinement of the central cell, the experimental value of the axial particle-confinement parameter of the central cell, $n\tau_c$, is compared to the mirror confinement parameter for $\phi_c = 0$, $n\tau_0$. The classical Coulomb expression for the predicted central-cell confinement in the presence of a confining potential, $n\tau_\phi$ is then evaluated and checked for agreement with $n\tau_c$. Besides looking at the central core $n\tau$'s for the radial profile data associated with Figs. 4, 10, and 11, we will also discuss scaling of the central-cell axial confinement.

We determine the ion-confinement parameter $n\tau_c(cm^{-3}\cdot s)$ during steady-state operation by evaluating the expression

$$n\tau_c = en_c^2\, L_c/j_c \qquad (3)$$

where e is the electronic Coulomb charge (1.6×10^{-19}), n_c is again the central-cell density in cm^{-3}, L_c is the effective length of the solenoid (314 cm), and j_c is the total central-cell loss-current density out both ends in A/cm^2 (evaluated at the central-cell midplane).

The unstoppered mirror confinement ($\phi_c = 0$) of the central cell predicted by theory is given by

$$n\tau_0 = n_c\tau_{ii}\log R + 2n_cL_c\left(\frac{\pi m}{3T_c}\right)^{1/2} R \,, \qquad (4)$$

where T_c is the central-cell ion temperature. The two terms are: (1) the ion-ion scattering time for an empty loss cone with mirror ratio R (mean free path >> RL_c), and (2) the product of the density and flux from a Maxwellian distribution out both ends of a magnetic bottle with mirror ratio R for a filled loss cone (mean free path << RL_c).[6] The two terms add directly, not inversely, because they represent collisionality limits of ion-ion scattering losses, not individual competing losses.

The Coulomb confinement of the central-cell $n\tau_\phi$ in the presence of a potential $\phi_c = T_e \ln(n_p/n_c)$ is increased according to the following expression:

$$n\tau_\phi = \left[n_c\tau_{ii}g(R)\frac{\phi_c}{T_c} + 2n_cL_c\left(\frac{\pi m}{8T_c}\right)^{1/2}\frac{R}{2}\right]\exp\left(\frac{\phi_c}{T_c}\right) \qquad (5)$$

where for $\phi_c \gtrsim T_c$, $g(20) \approx 3$. Both terms of Eq. (5) are enhanced over Eq. (4) by $\exp(\phi_c/T_c)$ because only ions with energy exceeding the confining potential ϕ_c can escape axially. The additional enhancement of the first term by ϕ_c/T_c can qualitatively be explained by the modification of the ion-ion collision frequency term due to collisions among particles with energy less than ϕ_c in determining the rate of diffusion into the loss cone. The function g(R) takes into account that the confining potential is peaked at the end-cell midplane, not at the mirror point of the central cell. This same effect changes the mirror-ratio dependence of the flow term from R to R/2 for an end-cell midplane field strength half that of the mirror point.

The central-cell ion temperature was not measured directly. However, from diamagnetic loop measurements within the central cell, we know that the average value of the sum of T_{ec} and T_c was 100 eV, given that the electrons and ions have the same radial dependence. Therefore, the T_{ec} of 49 eV measured by Thomson scattering would imply a T_c of 51 eV. Using the central-cell density from Fig. 3-4, the axial end-loss current data from Fig. 3-11, and a central-cell core average T_c of 51 eV and ϕ_c of 130 eV, we obtain $n\tau_c = 1 \times 10^{10}\ cm^{-3} \cdot s$, $n\tau_0 = 0.4 \times 10^{10}\ cm^{-3} \cdot s$, and $n\tau_\phi = 5 \times 10^{10}\ cm^{-3} \cdot s$ from Eqs. (3) through (5). The fact that the experimental value of the electrostatic enhancement factor, $n\tau_c/n\tau_0$, is only 2.5 while the predicted enhancement from Coulomb confinement in the presence of ϕ_c, $n\tau_\phi/n\tau_0$, is 12 can be explained by the equation

$$n\tau_{rf} = n\tau_\phi\left(1 + \frac{E^2}{E_c^2}\right)^{-1} \qquad (6)$$

Equation 6 describes the degradation of central-cell ion confinement by the distortion of the ion-velocity distribution (assumed initially to be Maxwellian) due to oscillating electric fields E at the ion-cyclotron frequencies of the end cells. Because of the magnetic geometry (see Fig. 3-1), 10-kG zones resonant with the plug midplanes exist within the central cell. We have observed that as the magnitude of the rf fluctuations within the central cell (at the end-cell ion-cyclotron frequencies) increased, the experimental $n\tau_c$ degraded.[4] At low levels of rf fluctuations, there was good agreement between $n\tau_c$ and the Coulomb value $n\tau_0$. At the higher levels of rf fluctuations, the measured enhancement of $n\tau_c$ over $n\tau_0$ decreased. The critical electric field, E_c, can be taken as a one-point fit between $n\tau_c$ and $n\tau_{rf}$; however, Rognlien and Matsuda,[7] who developed the theory that led to Eq. (4), have also discussed models that predict the critical electric field strength required for such effects to occur.

We found that we could observe the scaling of the electrostatic enhancement of the central-cell axial confinement if the central-cell fluctuations were less than 10 volts peak-to-peak, V_{pp}, which normally required $n_p/n_c \leq 3$, and if we varied the energy of the injected neutral-beam current. Our results are shown in Table 3-1. We varied the neutral-beam injection voltage on the east plug without changing the total injected-beam current by operating 20-kV and 40-kV neutral-beam injectors at various levels (cases A, B, and C in Table

TABLE 3-1. Central-cell ion confinement for three cases of end-cell neutral-beam injection voltage compared to implied ϕ_c enhancement (case A: 11 kV; case B: 16 kV; and case C: 27.5 kV).

Parameter	Case A	Case B	Case C
East plug			
V_{inj} (kV)	11	16	27.5
I_{inj} (A)	70	70	70
E_p (keV)	5.7	9.2	14.6
T_e (eV)	96	121	133
n_p (10^{13} cm^{-3})	1.1	1	0.84
Central cell			
J_c (mA/cm^2)	32	28	14
n_c (10^{12} cm^{-3})	3.9	4.8	3.7
T_c (eV)	62	44	48
rf (V_{pp})	7.0	9.5	8.5
$\frac{n\tau_c}{n\tau_{flow}} = \frac{en_c^2 L_c (2/CE)^{-1}}{2n_c L_c (\pi m/8T_c)^{1/2} (R/2)}$	4	5	8
$\frac{n\tau_\phi}{n\tau_{flow}} = \exp(\phi_c/T_c) = \left(\frac{n_p}{n_c}\right)^{T_e/T_c}$	5	8	10

3-1). The west plug was operated with a constant neutral-beam injection level similar to case B; its parameters were quite similar to the case-B parameters of the east plug shown in Table 3-1. The ion energy, E, was determined from the plasma diamagnetism and total number of particles. The entries in Table 3-1 are mean values of the parameters, averaged over six to eight experimental shots. The experimental conditions were constant for each of the cases. The shot-to-shot variation in plasma parameters was within ±20% of the mean. The main result shown in Table 3-1 was that central-cell ion end-loss current flowing out the east plug was reduced by more than a factor of 2 for relatively constant central-cell density, central-cell ion temperature, and rf fluctuation levels within the central cell at the end-plug ion-cyclotron frequency. The value of ϕ_c was determined from $T_e \ln(n_p/n_c)$. The HIBP used to evaluate ϕ_e was at an early stage of its development and was not able to make accurate enough measurements to verify the scaling phenomenon. Our data from Fig. 3-10, where we could use the HIBP to measure ϕ_e, supports our using $\phi_c = T_e \ln(n_p/n_c)$ along the magnetic axis. In all three cases we have normalized the experimental value for $n\tau_c$ to the "flow" term of Eq. (5). The values of n_c and T_c justify this approximation. For the conditions of cases A, B, and C, we find that the normalized experimental value of the central-cell ion confinement, $n\tau_c/n\tau_{flow}$, agrees with the theoretically implied scaling one would describe for mirror confinement enhanced by a confining electrostatic potential, $n\tau_\phi/n\tau_{flow}$.

3.6. SUMMARY

The experimental data of this section verifies the formation and control of ambipolar potentials in TMX and the accompanying electrostatic enhancement of the central-cell ion confinement. In Fig. 3-10, we expanded upon earlier on-axis measurements[3] of ϕ_c and discussed its dependence on radius. In the core of the central cell (radius 0 to 15 cm), the experimentally determined value of ϕ_c, 150 V, is in good agreement with the expected value, $T_e \ln(n_p/n_c)$. Near the edge (radius from 20 to 30 cm), ϕ_c is lower, and although it seems to reverse at the edge, other indirect measurements imply that ϕ_c is positive at all radii.

Table 3-1 shows that under conditions where rf effects on central-cell ion confinement (discussed in Section 4) can be ignored, the on-axis $n\tau_c$ scaled according to the implied values of ϕ_c. The electrostatic confinement associated with $\phi_c > 0$ was enhanced from 4 to 8 above the confinement for $\phi_c = 0$ as the end-cell neutral-beam injection voltage was increased from 11 to 27.5 kV.

The data generated by TMX demonstrated that electrostatic confining potentials in magnetic mirror systems can significantly improve central-cell plasma confinement.

4. The Effect of End-Cell Stability on the Confinement of the Central-Cell Plasma in TMX

4.1 INTRODUCTION

The Tandem Mirror Experiment (TMX) has demonstrated improved plasma confinement over that of a single-mirror system.[1–3] TMX employs three connected magnetic-mirror cells. The plasma density in the two end cells is controlled by neutral beams; the larger—but lower density—central-cell plasma is fueled by a gas feed. The two end cells establish an electrostatic potential well which confines all but the most energetic central-cell ions. When the electron temperature is axially uniform, this confining potential,

$$\phi_c = T_e \ln(n_p/n_c) \quad , \tag{1}$$

depends on the temperature, T_e, the end-cell plasma density, n_p, and the central-cell plasma density n_c. This paper describes experimental results, in agreement with theory, that show the limitations *on the central-cell confinement* due to end-cell microinstabilities.

A certain quantity of warm, unconfined plasma must flow through the end cells to control microinstabilities. The central-cell losses provide this warm plasma. If the potential well that confines the central-cell ions becomes too large, the supply of warm plasma to the end cells becomes insufficient. The experiments reported in this paper show that under these conditions the end-cell ion-cyclotron-frequency plasma fluctuations increase. These fluctuations degrade the central-cell confinement as described below. This increases the quantity of warm, unconfined plasma flowing through the end cells, which presumably allows the end-cell plasmas to maintain a marginally stable steady state. The plan of the paper is as follows: (1) the theoretical stability limit is derived; (2) an experiment is described in which the stability limit is substantially exceeded and a large increase of the amplitude of the plasma fluctuations is measured; and (3) the relation of the central-cell confinement to the plasma fluctuations is shown to agree with the theory developed in a companion paper.[4]

4.2 IMPLICATIONS OF END-CELL STABILITY

TMX was designed to satisfy end-cell microstability criteria.[5] In the end cells, low energy ions are unconfined because of the positive electrostatic potential of the end-cell plasmas. The complete absence of low-energy ions, together with the radial density gradient, would result in the drift-cyclotron-loss cone instability. This instability can be limited to low levels if a sufficient density of warm, unconfined ions is present in the end cells.[6] In TMX these ions are supplied by the central-cell losses. Thus, the stability of the end-cell plasmas is controlled by the central-cell losses. This imposes a stability limit upon the confinement of the central-cell plasma. If this plasma is confined too well, insufficient warm plasma will be supplied to the end cells, and unstable behavior is predicted.

The required warm plasma density is a certain fraction of the end-cell plasma density. The fraction depends upon the plasma potential, the mean ion energy of the end cell, and the radial density gradient. The warm plasma has a characteristic velocity, so the stability requirement corresponds to a central-cell loss current. The required loss current for TMX at the end-cell midplane (in A·cm^{-2} per end) is[7,8]

$$j_c = \frac{3.8 \times 10^{-12} n_p \phi_{pm}^{3/2}}{E_p (R_p - 1) M_i^{1/2}} \left(\frac{r_p}{a_i}\right)^{4.3} \tag{2}$$

In this expression, n_p (cm^{-3}), is the density of the end-cell plasma, ϕ_{pm} (keV), is the potential drop from the midplane to the outer magnetic mirror of the end cell, E_p (keV), R_p(=2), and M_i (AMU) are the ion energy, mirror ratio, and ion mass in the end cell, and r_p/a_i is the ratio of end-cell plasma radius to ion gyroradius.

To supply this required loss current in the absence of plasma fluctuations, the central-cell loss current due to Coulomb collisions alone, j_{coul}, must satisfy

$$j_{coul} \geq j_c \tag{3}$$

The loss rate ($cm^{-3} \cdot s^{-1}$) due to Coulomb collisions is proportional to the square of the central-cell density divided by the confinement, $(n\tau)_{coul}$, for this process. The current per unit area flowing through the end-cell midplane is provided by a flux tube of volume $L_c R_c / R_p$ per unit area, in which the central-cell length and mirror ratio are L_c (314 cm) and R_c (20). Thus, the loss current j_{coul} (in $A \cdot cm^{-2}$ at each end-cell midplane) is

$$j_{coul} = \frac{e n_c^2 L_c}{2 (n\tau)_{coul}} \left(\frac{R_c}{R_p} \right) \qquad (4)$$

Here the central-cell density is n_c (cm^{-3}), and $e = 1.6 \times 10^{-19}$ coulombs.

If Coulomb collisions determine the central-cell confinement this confinement, $(n\tau)_{coul}$ ($cm^{-3} \cdot s^{-1}$), is[9]

$$(n\tau)_{coul} = \left(0.4 \times 10^{10} \; T_{ic}^{3/2} \; \frac{\phi_c}{T_{ic}} + 10^{-8} \frac{2 n_c L_c R_c}{\sqrt{T_{ic}} \sqrt{m_i}} \right) \exp \left(\frac{\phi_c}{T_{ic}} \right) \qquad (5)$$

in which the central-cell ion temperature and mass are T_{ic} (keV) and m_i (AMU). In the long-mean-free-path limit, Eq. (5) is dominated by the first term. The confinement is then determined by the ion-ion scattering time (proportional to $T_{ic}^{3/2}$) times an exponential function of the plasma potential. The coefficient 0.4×10^{10}, is a weak function of mirror ratio and potential well depth. The given value is appropriate for the experiment described below. The second term in Eq. (5) provides an accurate transition for the short-mean-free-path limit.[9] In this limit a completely Maxwellian plasma is flowing over a potential barrier of height ϕ_c.

The required condition for end-cell microstability is given by Eq. (3). It can be interpreted as a limit on the plasma densities in TMX, to help interpret the experiment described below. The central-cell loss current due to Coulomb collisions, j_{coul}, is a decreasing function of end-cell density n_p. However, the required loss current, j_s, is an increasing function of n_p. Therefore, Eq. (3) cannot be satisfied for an indefinite increase of n_p. To estimate the limiting value of n_p/n_c we use Eqs. (1)–(5) to obtain

$$\frac{n_p}{n_c} \leq \left[0.53 \; \frac{E_p \, T_{ic}^{1.2} \, (r_p/a_i)^{4.3}}{\phi_{pm}^{3/2} \left(\frac{2.3 \times 10^{18} T_{ic} \, \phi_c}{n_c R_c L_c} + 1 \right)} \right]^{\frac{1}{1 + T_e/T_{ic}}} \qquad (o)$$

for $R_p = 2$, $M_i = m_i = 2$. By substituting TMX parameters into Eq. (o), we estimate $n_p/n_c > 3$ for stable operation. The parameters were chosen for the experiment described below, but are also typical of much of TMX operation ($E_p = 10$ keV, $T_{ic} = 0.08$ keV, $\phi_{pm} = 0.5$ kV, $T_e/T_{ic} = 2$, $n_c = 5 \times 10^{13}$ cm^{-3}, $r_p/a_i = 5$ and $\phi_c = 0.16$ keV). Thus, the theory of TMX confinement and microstability predicts that increased plasma fluctuations should be observed when $n_p/n_c > 3$.

4.3 THE EXPERIMENT

An experiment was performed that tests these predictions. The gas feed into the central-cell vacuum chamber was held fixed at 120 Torr liters per second. The neutral-beam current fueling the end-cell plasmas was increased from 80 equivalent amperes of deuterium per end to 225 A per end. The total central-cell plasma losses were limited by the fixed gas feed. The measured losses along the axis, which we identify with the current required for stabilization, could vary depending upon the penetration of the gas. As we shall see, the measured end losses did vary. For this experiment, the magnetic fields and other control settings were held constant, and the central-cell plasma radius was within the range 38 ± 5 cm.

As the neutral-beam current fueling the end-cell plasmas was increased, the plasma fluctuations increased more than a factor of 10. Figure 4-1 shows the floating potential fluctuations as a function of neutral-beam current, as measured using a high-impedance probe at the boundary of the central-cell plasma. The probe is located at a radius of 41 cm. The plasma fluctuations were also measured using microwave scattering in the central cell and by a probe in the east end cell. The microwave scattering measures plasma density fluctuations in the core of the central-cell plasma.

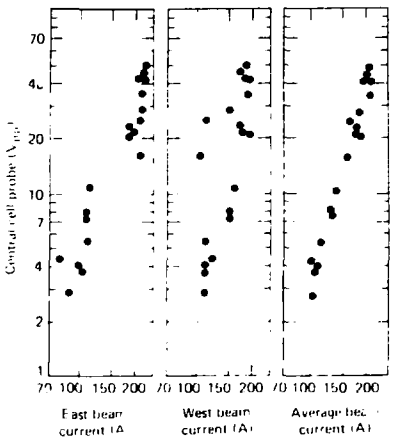

FIG. 4-1 Floating-potential fluctuations, measured in the TMX central cell, are shown as a function of the injected neutral-beam current. The central-cell gas feed was held constant.

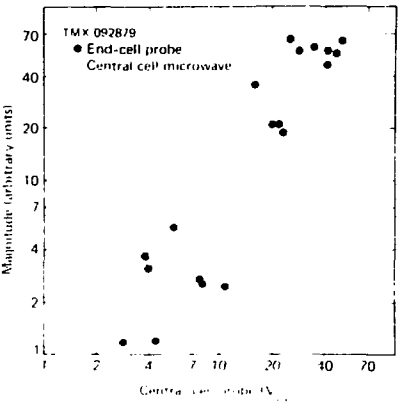

FIG. 4-2. Three diagnostics detected the increase of plasma fluctuations. The end-cell probe (●) and central-cell microwave scattering (O) are compared to the central-cell probe.

The high-impedance probe in the east end cell is located at a radius of 30 cm. These two diagnostics measured fluctuations that were proportional to the fluctuations measured by the central-cell probe, as is shown in Fig. 4-2. Thus, the large increase in plasma fluctuations was detected by three diagnostics.

The spectrum of the plasma fluctuations was measured. The fluctuations at the end-cell ion cyclotron frequency and its harmonics were as large as many times stronger than the fluctuations at other frequencies. No distinct fluctuations are observed at the ion-cyclotron frequency of the central cell. These results are consistent with measurements made on many operating days.[10] In more recent experiments the wave number of the ion-cyclotron-frequency fluctuations has been measured in the end cell.[11] Fluctuations characteristic of the drift-cyclotron-loss-cone instability have been observed. These fluctuations have an azimuthal mode number, $m \lesssim 20$ and propagate in the ion-diamagnetic-drift direction as expected. In addition, fluctuations characteristic of an Alfvén ion-cyclotron-type instability are measured. These fluctuations have $m \approx 2$-7 and propagate in either direction. As is shown below, the theory of the drift-cyclotron loss-cone instability appears sufficient to explain the results reported here. Whether the theory of the Alfvén ion-cyclotron instability provides an alternative explanation is a subject of current research.

The changes in the plasma parameters were measured as the neutral beam current was increased. Some of the results are plotted as a function of detected plasma fluctuations in Fig. 4-3. The diagnostics used for these measurements have been described previously.[7] As the neutral beam current and plasma fluctuations increased, the end-cell plasma density increased slightly, the central-cell plasma density decreased, and the measured end losses increased. The electron temperature in the east end cell was nearly constant. The central-cell ion temperature was estimated on the basis of diamagnetic loop measurements. These were normalized to ion temperatures obtained from similar plasmas by measurements of Doppler broadening.[12]

The analysis of the data described above is presented in Fig. 4-4. At low neutral-beam currents the density ratio n_p/n_c was about 3 and low levels of plasma fluctuations were observed (Fig. 4-4a). As the neutral-beam current increased, n_p/n_c increased. The increase in plasma fluctuations as n_p/n_c increased is predicted by the theory presented above. Thus, this experiment supports

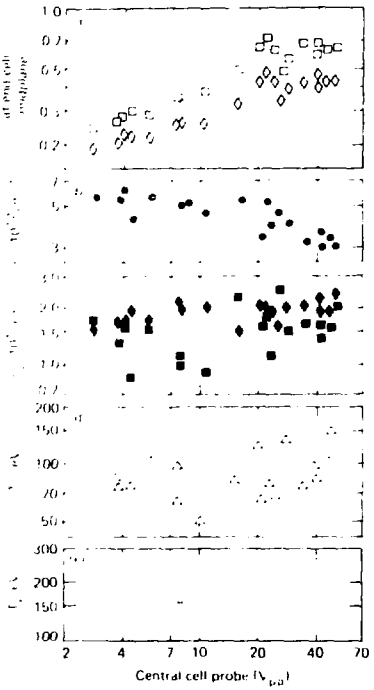

FIG. 4-3. Plasma parameters measured during the beam current scan and plotted against the observed fluctuation level: (a) end losses, j_E and j_W (east-□, west-◇); (b) central-cell density, n_c, (●); (c) end-cell density, n_E and n_W (east-■, west-◆); (d) central-cell ion temperature, T_{ic} (△); and (e) east end-cell electron temperature, T_e (○).

the end cell stability theory based on the drift-cyclotron loss-cone instability. It appears that central cell losses are necessary to maintain the stability of the end cells.

The performance of TMX changed as the end-cells became more unstable. The end-cell plasma is expected to enhance the axial confinement of the central-cell plasma by electrostatic end-plugging. The end-plugging effect of the end-cell plasma may be judged by comparing the central-cell axial confinement to the confinement the central cell would provide without any end-plugging. The confinement parameter without an electrostatic well is

$$(n\tau)_m = 4.4 \times 10^{10}\, T_{ic}^{3.2} \log R_c + 4.1 \times 10^{8} \frac{n_c R_c L_c}{\sqrt{T_{ic}/m_i}} \,. \qquad (7)$$

The right-hand side of this equation is similar to the factor in parenthesis in Eq. (5). The first term reflects the long-mean-free-path confinement of a mirror confined plasma, and the second term evaluates the loss of a (short-mean-free-path) collisional plasma through a magnetic nozzle. The measured axial confinement parameter is

$$(n\tau)_c = \frac{en_c^2 L_c}{j_c} \frac{R_c}{R_p} \,, \qquad (8)$$

in which j_c is the total loss-current from the central cell in A/cm^2 evaluated at the end-cell midplanes. When the plasma fluctuations were small, the central-cell confinement was several times the value expected without end-plugging, as determined from the data and Eq. (7). Figure 4-4a shows this result. As the plasma fluctuations increased, the central-cell confinement decreased. In addition the end-plugging effect of the end-cell plasmas appears to have been eliminated. We believe this was a direct consequence of the increasing plasma fluctuations, as is described below.

4.4 EFFECT OF FLUCTUATIONS

The effect of end-cell ion-cyclotron-frequency fluctuations on the central-cell confinement has been studied.[4] These fluctuations are expected to resonantly heat the central-cell ions near the magnetic mirror where the ion-cyclotron frequency equals that of the fluctuations. The central-cell ions heated by this mechanism can escape the plasma by scattering a small angular distance into the loss cone. The predicted effect of the plasma fluctuations depends on the magnitude of the fluctuating electric field. For small electric fields ($E < 10$ V/cm), the central-cell confinement is not substantially reduced, although there is some heating of the central-cell ions. As the electric field increases, central-cell ions are lost by the mechanism

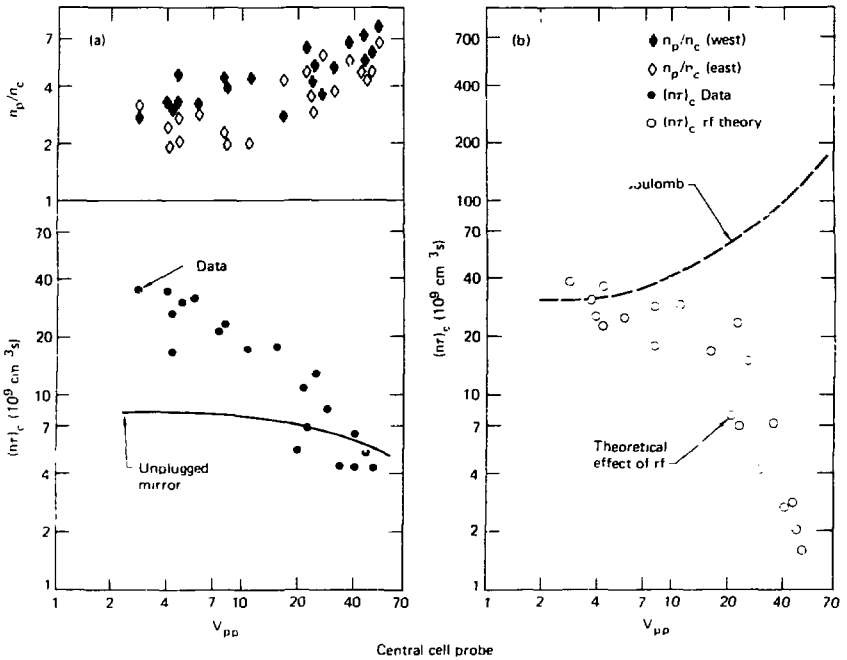

FIG. 4-4. Analysis of the data. (a) As the end-plug-to-central-cell density ratio (♦) increased above 3, the plasma fluctuations increased. The measured central-cell axial confinement (●) decreased from several times the single-mirror value (–). (b) The predicted axial confinement (○) includes the reduction of the confinement due to Coulomb collisions (---) by the plasma fluctuations.

described above. The central-cell confinement decreases until the fluctuating electric field becomes so large that substantial ion heating occurs. At very large electric fields ($E > 40$ V/cm for TMX) the confinement may begin to increase as a result of the ion heating. For moderate electric fields ($E \gtrsim 40$ V/cm), the effect of the fluctuating electric field on central-cell ion confinement is predicted to be

$$(n\tau)_c = (n\tau)_{coul}(1 + E^2/E_c^2)^{-1} \quad . \qquad (9)$$

in which E is the peak fluctuation level in V/cm at the core of the central-cell plasma. This electric field is normalized to E_c, where

$$E_c^2 = 5.4 \times 10^{-11}\, n_c\, T_\kappa^{-1}\, \ell^2 \left(\frac{T_\kappa}{\phi_c}\right)^{3/2} \quad . \qquad (10)$$

To compare this theory with the data, one must evaluate E, E_c, and $(n\tau)_{c,ul}$. The critical electric field E_c is evaluated using Eq. (10) and the data. The Coulomb confinement is determined by Eq. (5) if the end-cell densities are equal. For unequal end-cell densities, the following relation was used:

$$(n\tau)_{coul} = 6.4 \times 10^{10} T_{ic}^{1/2} \phi_c \exp(\phi_c/T_{ic}) \Big|_{min} + 10^{-8} \frac{4 n_c L_c R_c}{\sqrt{T_{ic}/m_i}} \left[\exp(-\phi_c/T_{ic} \Big|_{min} + \exp(-\phi_c/T_{ic}) \Big|_{max} \right]^{-1} , \quad (11)$$

in which $\phi_c = T_e \ln(n_p/n_c)$ was assumed, the electron temperatures were taken to be 160 eV, "min" designates the end cell with smaller density, and "max" designates the end cell with larger density. To evaluate the fluctuating electric field at the core of the plasma (E), a relation must be assumed between E and the peak-to-peak fluctuations of the floating potential (ϕ_{pp}) measured at the plasma boundary. The relation $E = 1.5\, \phi_{pp}$ was used, based on a theoretical estimate of the wave number k for the drift-cyclotron-loss-cone instability in TMX. Equating the phase velocity of the instability to the ambipolar hole velocity gives $k \sim 3\ cm^{-1}$.[6] Then we have $E \sim k\phi_{pp}/2 \sim 1.5\, \phi_{pp}$. This estimate ignores spatial variations of the plasma fluctuations and effects due to the ellipticity of the magnetic field. As a result, the comparison of theory and data described below is essentially a one-parameter fit. We have just shown that the fit parameter required to obtain agreement is a plausible one.

The results of these calculations are shown in Fig. 4-4b. The observed central-cell confinement equals the Coulomb-dominated value when the measured fluctuations are small. As the plasma fluctuations increase, the observed axial central-cell ion confinement becomes significantly less than the Coulomb-dominated value. Within the experimental uncertainties, the theory just described reproduces the shape and magnitude of the decreasing confinement. The greatest disagreement between theory and experiment is at very large fluctuation levels. As is described in Reference 4, Eq. (9) is expected to fail for very large electric fields. Thus, the data supports the hypothesis that the plasma fluctuations degrade the confinement of the central-cell plasma. This effect, which results in increased central-cell losses (Fig. 4-3), is believed to provide the additional stabilizing warm plasma needed by the end-cell plasmas. A steady state is reached at which the enhanced central-cell losses and other effects of the plasma fluctuations produce marginally stable end-cell plasmas.

In summary, the ion-cyclotron-frequency plasma fluctuations are observed to increase in TMX as the drift-cyclotron loss-cone mode becomes theoretically more unstable. The effect of these fluctuations is to decrease the axial confinement of the central-cell plasma. We expect to extend the stable operating range of TMX and future mirror machines by creating end-cell plasmas which confine low-energy ions without requiring central-cell losses. One method we will use is to employ sloshing-ion end cells.[13]

5. Scaling of End-Cell Confinement in TMX

5.1 INTRODUCTION

A Tandem Mirror machine[1,2] uses three (or more) magnetic-mirror cells to confine a central-cell plasma between two end-cell plasmas. The positively-charged end-cell plasmas act as electrostatic end plugs which reduce the end losses from the central-cell plasma. The central-cell plasma becomes Maxwellian, and ion microinstabilities do not easily arise there. The end-cell plasmas can and do become unstable to microinstabilities. Warm plasma can stabilize the end-cell plasmas, if low-energy ions are supplied to the end-cell.[3] Central-cell losses provide the low-energy ions needed by the end cells. Thus, if the central-cell end losses are sufficient to stabilize the end-cell plasmas, such a device should be stable. Otherwise, instabilities will arise and will change the behavior of the plasma. With sufficient central-cell losses, the end-cell density in TMX is close to the limit set by Coulomb collisions. As the central-cell losses are reduced by reducing the gas feed to the central-cell plasma, the end-cell plasma cannot be stabilized and the end-cell density drops. The first section of this paper describes how we expect (TMX)[4] to operate. The bulk of the paper describes the scaling of end-cell ion confinement in TMX, in which end-cell stability plays a crucial role.

To be stable, the end-cell plasmas must contain a minimum density of low-energy ions. If the central-cell losses that result from Coulomb collisions do not provide the required low-energy ions, plasma fluctuations will arise. These plasma fluctuations may have two effects. They may increase the end losses from the central-cell by heating the central-cell ions.[5] This effect was observed by means of an end-cell neutral-beam-current scan and has been reported previously.[6] Sec. 4. In addition, the plasma fluctuations may reduce the confinement of the end-cell ions and reduce the end-cell plasma density,[7] thereby reducing the required amount of low-energy ions. A central-cell gas-feed scan produced significant changes of end-cell density, as is described below. As the density of low-energy stabilizing plasma in the end cell increased, the end-cell density approached the limit determined by Coulomb collisions.

Based on these mechanisms, TMX operates as follows: The end-cell reaches marginal stability through the balancing of two effects. The neutral-beam fueling attempts to increase the density toward the Coulomb limit. This tends to reduce the central-cell losses as the electrostatic potential well becomes deeper. If the central-cell losses are too small, plasma fluctuations arise. These plasma fluctuations increase the central-cell losses and decrease the end-cell density until a marginally stable steady-state is reached. In steady state, the central-cell losses supply enough low-energy plasma to stabilize the end-cells in the presence of the fluctuations.

Thus, if TMX is not stable two effects compete to determine the operating point. The plasma fluctuations both reduce the end-cell density and increase the central-cell losses. To completely understand the steady-state plasmas obtained in TMX, one must understand what determines the relative magnitude of these two effects. This may depend upon many factors, including electron temperature, plasma density and magnetic field. This section focuses on the evidence supporting the importance of warm plasma stabilization and does not attempt a complete description of the steady-state plasmas obtained in TMX.

This section describes experimental results that indicate the importance of end-cell stability to the end-cell-ion confinement in TMX. The results of a gas-feed scan show that the end cell density responds to changes in stabilization. A variety of data supports this conclusion. In addition, certain specific experiments could improve the performance of TMX. Our plan is as follows. Section 5.2 describes the theory of end-cell-ion confinement in TMX. We discuss the significant processes and the end-cell stability requirements. The results of an experiment that tests this theory are presented in Sec. 5.3, and we discuss the implications of these and other data in Sec. 5.4. Section 5.5 is the conclusion. A more detailed publication is in preparation; it will include additional data and a more accurate treatment of radial profiles.

5.2 THEORETICAL CONSIDERATIONS

5.2.1 End-Cell Rate Equation

This section focuses on the theory of ion confinement in the TMX end-cells. A rate equation summarizes the processes that determine the ion density. Then, we consider these processes in more detail. The most important processes are neutral-beam trapping, Coulomb collisions, and the effects of plasma fluctuations. As is well known, the ion confinement determines the plasma density, and the electrons are electrostatically confined to maintain quasineutrality. We focus on the ion confinement in the plasma core—the region within three Larmor radii (o cm) of the plasma centerline.

The end-cell density is determined by a balance between neutral-beam trapping and various loss processes. The end-cell plasmas are short, the rates of fueling and loss vary significantly along a given flux tube. Hence, an average of these processes over the plasma length determines the equilibrium. To simplify this discussion, we will evaluate the fueling and loss processes at the plasma midplane, and include the averaging by means of weighting coefficients. These coefficients are discussed in the Appendix D. The fueling and loss processes affect the end-cell density, n_p (cm^{-3}) as follows:

$$\frac{dn_p}{dt} = f_1 \langle \sigma v \rangle_{ion} n_b n_p \quad f_2 c_\perp n_b n_p - f_3 \frac{n_p}{\tau_{loss}} - f_4 \Gamma_g \qquad (1)$$

This equation contains one source term and three loss terms. Ionization of the neutral-beam atoms fuels the plasma. The loss terms include radial transport due to charge-exchange with neutral-beam atoms, losses produced by Coulomb collisions and plasma fluctuations, and losses which result from charge-exchange between plasma ions and low-energy neutral atoms or molecules that strike the plasma ("background gas"). The average density of neutral-beam atoms within the plasma core is n_b (cm^{-3}). The rate coefficient for ionization of these atoms (by both electrons and deuterons) is $\langle \sigma v \rangle_{ion}$ (cm^3 s^{-1}). The rate coefficient for radial transport out of the plasma core by charge-exchange with neutral-beam atoms is $c_\perp$ (cm^3 s^{-1}) (see below). The rate of loss of plasma ions by means of Coulomb collisions and as a result of plasma instabilities is τ_{loss}(s). Finally, the flux of low-energy neutral atoms to the plasma is Γ_g (cm^{-2} s^{-1}). The weighting coefficients f_1 through f_4 are described in Appendix D.

In addition to the processes included in Eq. (1), charge-exchange events exchange plasma ions and neutral beam atoms. This process alters the ion velocity distribution and affects the loss rates caused by other processes.[8] An ion must lose most of its energy or scatter through a large pitch angle in velocity space to become unconfined. Charge-exchange processes tend to replace plasma ions with new ions of higher energy and smaller pitch angle. Thus, charge-exchange tends to decrease the loss of ions due to various loss processes. If the lifetime for charge-exchange is τ_{cx} and the characteristic lifetime for the loss processes at work is τ_p, then the loss rate of ions in the actual plasma is n_p/τ_{loss}, where

$$\tau_{loss} = \tau_{cx}[\exp(\tau_p/\tau_{cx}) - 1] \quad . \qquad (2)$$

The lifetime for charge-exchange depends on the neutral-beam-atom density and the charge-exchange rate coefficient $\langle \sigma v \rangle_{cx}$(cm^{+3} s^{-1}):

$$\tau_{cx} = \frac{1}{n_b \langle \sigma v \rangle_{cx}} \qquad (3)$$

Equation (1) has several limits. If the gas load on the plasma becomes too high, the final loss term will lower the plasma density and eventually destroy the plasma. Most of the data described below was obtained with a beam current at least twice the minimum required to sustain plasma and this term will be ignored. Assuming a small gas load, Eqs. (1), (2), and (3) can be solved for steady-state to obtain

$$\tau_p = \tau_{cx} \ln \left[1 + \frac{f_3 \langle \sigma v \rangle_{cx}}{f_1 \langle \sigma v \rangle_{ion} - f_2 c_\perp} \right] \quad . \qquad (4)$$

If the loss processes are understood, τ_p can be expressed as a function of the plasma parameters and Eq. (4) determines the steady-state. For example, if the plasma fluctuations are unimportant, the

plasma density rises until the Coulomb loss rate equals the net source by ionization less the beam-driven radial transport. The resulting density limit is derived below. As the plasma fluctuations increase, the density will drop. Thus, improved plasma stability will cause the measured plasma density to increase until it approaches the Coulomb limit.

5.2.2 Neutral Beam Trapping

The neutral beams inject energetic atoms which are ionized by the plasma and cause radial transport by means of charge-exchange. The electrons and ions within the plasma ionize the neutral-beam atoms. The source due to this process is $f_1 \langle\sigma v\rangle_{ion} n_b n_p$. A certain fraction of this ionized source is lost because neutral-beam injection produces an unavoidable radial transport.[9] Charge-exchange events replace plasma ions with new ions having a different gyrocenter. This radial step, which occurs on a charge-exchange time scale, causes radial transport. The transport depends upon the rate of charge-exchange (which is proportional to the rate of ionization) and on the amount of radial motion that results. We have used a radial Fokker-Planck computer code[10] to evaluate this radial motion. The code determines the actual gyrocenter motion for plasmas similar to those produced in TMX. These calculations show that

$$c_\perp = 0.41 \langle\sigma v\rangle_{ion} \quad . \tag{5}$$

In addition, because the rates of ionization and charge-exchange-driven radial transport depend on the same variables, they have the same axial weighting coefficient. That is,

$$f_2 = f_1 \tag{6}$$

5.2.3 Coulomb Density Limit

The limits imposed by Coulomb collisions are an important yardstick to be compared with the data, because plasma losses due to Coulomb collisions are inescapable. Coulomb collisions cause losses by several mechanisms. Electron-ion collisions cool the energetic ions and cause them to be lost.[11] This process, known as Spitzer drag, is the only significant process in the TMX end-cells. In addition, ion-ion collisions produce pitch-angle scattering and electron-ion or impurity-ion collisions cause radial transport; but these processes are insignificant. In the absence of charge-exchange, the ion lifetime due to Spitzer drag is[11]

$$\tau_D = \frac{10^{13}\ M\ T_e^{3/2}}{n_p\ Z^2\ \ln \lambda_{ei}} \ln\left(\frac{E_{INJ}}{E_L}\right) \tag{7}$$

In this equation, T_e (keV) is the electron temperature, M(AMU) and Z are the mass and charge numbers and $\ln \lambda_{ei}$ is the appropriate Coulomb logarithm. The energetic ions are injected by the neutral beams with energy E_{INJ} (keV) and are lost with energy E_L (keV). Fokker-Planck studies indicate that $E_L \sim 1$ keV for ions lost by Coulomb collisions from TMX.[12]

If Coulomb collisions are the only significant loss process, the plasma density rises to the Coulomb density limit. Equation (4) determines this limit, with τ_p replaced by τ_D from Eq. (7). If we evaluate this density limit for typical TMX parameters ($M = 2$, $Z = 1$, $\ln \lambda_{ei} = 14$, $E_{INJ} = 12$ keV, $E_L = 1$ keV, $\langle\sigma v\rangle_{cx} = 1.4 \times 10^{-7}$ cm^3 s^{-1}) we obtain

$$n_p = n_b\ T_e^{3/2}\ \frac{5.0 \times 10^{-5}}{\ln\left(1 + \frac{f_3 \langle\sigma v\rangle_{cx}}{f_1 0.59 \langle\sigma v\rangle_{ion}}\right)} \tag{8}$$

Equation (8) was used to determine the Coulomb density limit for the experiments described below. This density limit depends primarily on the neutral-beam current and the electron temperature.

5.2.4 End-Cell Stability

Under certain conditions, ion micro-instabilities may arise in the TMX end cells. The most serious such instability has been thought to be the drift-cyclotron-loss-cone (DCLC) instability. This subsection summarizes the DCLC instability, how it may be stabilized, and the effects it may have on end-cell confinement. At the present time, there is not a quasilinear description of the Alfvén-Ion-Cyclotron instability and other similar instabilities.

The DCLC instability is a loss-cone instability driven by two sources of free energy.[3,11,13] One source of free energy is the absence of low-energy ions in the end-cell, which is caused by the positive plasma potential; the plasma-density gradient is the

other. This instability can be stabilized by the presence of a sufficient density of low-energy ions at the end-cell midplane. To avoid the two-component instability, the low-energy ions must be sufficiently warm. Because these ions are unconfined they flow out of the end-cell. This means that a steady current of low-energy ions must be supplied to the end-cell to maintain stability. In TMX, this current is supplied by the central-cell losses.

Several factors determine the required minimum loss current. In this paper, we express the loss current which must flow through a given end cell to maintain stability, j_s, in $A \cdot cm^{-2}$ evaluated at the end-cell midplane, as[13,14]:

$$j_s = \frac{3.8 \times 10^{-12}}{E_p (R_p - 1) M_i^{1/2}} n_p \phi_{pm}^{3/2} \left(\frac{r_p}{a_i}\right)^{-4/3} \quad . \quad (9)$$

In this expression, n_p (cm^{-3}), is the density of the end-cell plasma, ϕ_{pm} (keV), is the potential drop from the midplane to the outer magnetic mirror of the end cell, E_p (keV), R_p, and M(AMU) are the ion energy, mirror ratio, and ion mass in the end cell, and r_p/a_i is the ratio of end-cell plasma radius to ion gyroradius. The required density of low-energy ions is some fraction of the end-cell density n_p times the relative size of the plasma potential, ϕ_{pm}/E_p. These ions flow out of the end cell with a velocity proportional to $\phi_{pm}^{1/2}$. Equation (9) is expected to describe the total ion current flowing out of each end cell. The end-cell losses may supply some or all of this current.[13] The central-cell losses supply the remainder. In practice in TMX, the central-cell losses often supply one-half to nearly all the required loss current.

There are several uncertainties associated with Eq. (9). They include the effective velocity of the flowing ions, the precise value of the numerical coefficient, and the presence of the factor, $(r_p/a_i)^{-4/3}$. In Eq. (9) the velocity of the flowing ions is taken to be proportional to $\phi_{pm}^{1/2}$. Depending on the source of these ions, the mechanism which supplies them, and on how well-localized the instability is, the correct dependence might be $T_{ic}^{1/2}$ or some other factor (where T_{ic} is the temperature of the central-cell ions). Secondly, the numerical coefficient, 3.8×10^{-12}, was derived assuming that a stable velocity distribution was obtained with the minimum possible number of unconfined ions. Depending on the distribution function of the low-energy ions, a larger density of such ions, and hence a larger loss current, may be required to obtain stability.[15] If the low-energy ions are too cold, the two-component instability may arise. Finally, the required loss current is expected to decrease as the plasma becomes larger, because the density gradient becomes smaller.[13,16] This effect is represented by the factor $(r_p/a_i)^{-4/3}$ in Eq. (9). If the velocity distribution of the low-energy ions departs significantly from the optimum described above, this effect may become smaller and the required loss current may increase. Some of these detailed considerations will be addressed in future publications.[17] For our purposes here, Eq. (9) provides a useful indication of the end-cell stability requirements.

If the end losses do not stabilize the end-cell plasmas, several effects may result. As was discussed in the introduction, the end-cell density may decrease and the central-cell losses may increase. The less stable plasma will produce plasma fluctuations. As the fluctuations in the plasma core increase, the signals detected by probes at the plasma boundary probably will increase, but this does depend on how the plasma parameters and the propagation of the unstable waves change. In addition, if the hot end-cell ions are heating the cool central-cell ions by means of the instability, the mean energy of the end-cell ions may decrease.

5.3 EXPERIMENTAL EVIDENCE

This section describes a gas-box scan experiment in TMX. To avoid instabilities, the central cell must be able to supply the unconfined, low-energy plasma required by the end cell. In TMX we can decrease the maximum central-cell end losses by reducing the gas feed to the central-cell plasma. In response, the end-cell density should decrease because the amount of end-cell density that the central-cell losses can stabilize will decrease.

We used TMX to perform the experiment just described. The neutral-beam current fueling the end-cell was held constant at 150 A per end. We fueled the central cell using the two gas boxes that surround the plasma at each end of the central cell. Three piezoelectric valves injected gas into each gas box. The gas-pressure change in the plenum chamber (of volume 1.0 liters) that supplied the valves was measured using a capacitance manometer. The

pressure drop during each shot determined the flow rate of gas into the gas boxes. During this experiment, we changed the gas feed to the central cell by more than an order of magnitude on a shot to shot basis.

We varied the measured end-loss current by changing the gas feed into the gas boxes. Figure 5-1 shows the observed end losses as a function of the pressure drop in the plenum chamber that supplies the gas. The end losses increased as the flow rate of gas into the gas boxes increased. The end losses were measured using an array of Faraday cups on each end of TMX.[18] Each Faraday cup has a suppressor plate that repels the electron flux and a deep cup which collects the ions. The data points in Fig. 5-1 represent the ion-end-loss current per unit area at the end-cell midplane; this value is an average over a circular area with a radius of 6 cm, obtained using data from three or four cups on each end of TMX. Figure 5-1 shows that we obtained a significant variation of the end losses from TMX. As is shown below, this resulted in a significant increase of the end-cell density.

During this experiment, we measured several plasma parameters. Figure 5-2 shows some of these results. As the gas feed and the end losses increased, so did the density and diamagnetism of the central-cell plasma. These measurements were obtained using the neutral-beam-attenuation diagnostic and a diamagnetic loop, described in Appendix B. The central-cell and east-end-cell electron temperatures (measured by Thomson scattering) may have decreased somewhat as the end losses increased. However the scatter in the electron-temperature data is significant compared to any trends. For analysis, the electron temperature may be taken as 50 eV with an uncertainty of ±20 eV throughout this experiment. The central-cell diamagnetism increased as much as the central-cell density, indicating that the sum of the central-cell electron and ion temperatures did not change significantly either. Although the data is not shown in Fig. 5-2, the plasma fluctuations were also measured at the plasma boundary during this experiment. As the end losses increased above 0.4 $A \cdot cm^{-2}$, the magnitude of the detected fluctuations decreased in both end cells and the central cell.

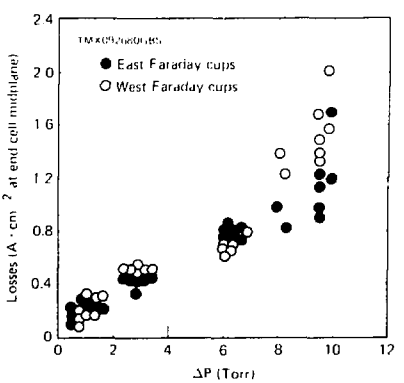

FIG. 5-1. The end losses, measured by two arrays of Faraday cups, increased as the gas fueling of the central cell increased. The gas fueling was measured by the pressure drop, ΔP, in the plenum. The end losses shown are averaged over a 6-cm radius at the end-cell midplane.

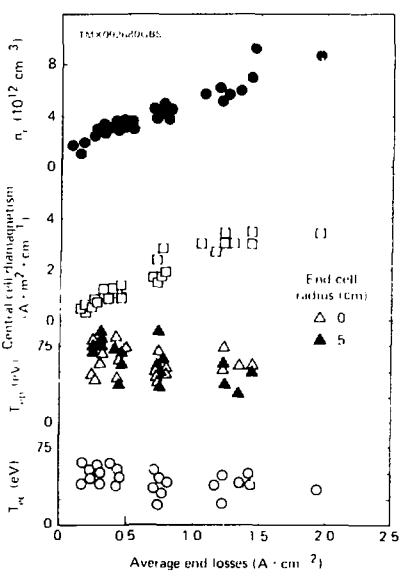

FIG. 5-2. Plasma parameters are shown as a function of end-loss current. The central-cell density (●) and diamagnetism (□) increased while the end-cell (△,▲) and central-cell (○) electron temperature did not.

The electron temperatures obtained during this experiment are quite low compared to those reported previously.[4,6] This does not fundamentally affect the argument stated here. The low-electron temperature is not due to a large-electron power loss to the end wall along the magnetic field lines.[19-21] Two possibilities which have not been eliminated are:

1. The vacuum conditions in the end-cell may have worsened (as described in Appendix A). This could have removed a substantial amount of power from the plasma boundaries by means of charge-exchange between hot plasma ions and cold neutral atoms.

2. The moderate-Z impurities (principally titanium) were not closely monitored and might have increased to significant levels; although there is no evidence supporting a high titanium concentration.

During this experiment, the plasma densities increased. The line density profiles measured by the neutral-beam-attenuation diagnostics are shown in Figs. 5-3, 5-4, and 5-5. The figures show line density profiles measured in the east end cell (Fig. 5-3), in the west end cell (Fig. 5-4), and in the central cell (Fig. 5-5). As the gas feed increased, the line densities increased everywhere. In the end cells, the plasma shape did not change substantially. The data from the east end cell has a 20% systematic experimental uncertainty on certain channels. Thus, the actual line density profile is probably much smoother than the data suggests. We improved the grounding of the electronics on the west end, and the west end cell diagnostic gave smoother data.

The most significant difference between the two end cells is at the plasma edge. For high gas feed rates, the east-end-cell line density is twice as large as the line density in the west end cell at a diameter of 20 cm (3×10^{14} cm^{-2} vs 1.5×10^{14} cm^{-2}). Thus, at this radius the end-plugging effect of the end-cell plasmas should be larger at the east end of the central cell. At large radii, most of the end losses should flow out through the west end cell. (They do: see below. However, the difference between the line-density profiles is not certain due to the uncertainties in the data.)

The central-cell line density also increased as the gas feed was increased (Fig. 5-5). The central-cell line densities were almost equal to the end-cell values. Thus, the central-cell density was several times less than the end-cell density, because the central-cell radius was several times the end-cell radius. In addition, as the gas feed increased the central-cell line-density profile increased more rapidly near the plasma edge than along the central chord. This shows that the radial density profile in the central cell was changing; it was becoming broader and developing a shell near the plasma edge.

The line-density data does not indicate the precise radial density profile within the plasma. In the core of the end-cell plasmas (within a 6-cm radius), the density profile may be flat, peaked, or inverted. To interpret this data we determined the average plasma density within a radius of 6 cm. Let the line density be I(y), as a function of height, y. Also assume azimuthal symmetry. Then, by integrating the Abel inversion we can determine the number of particles per unit length within a radius b. If this is N(b), we find

$$N(b) = \int_{-\infty}^{\infty} I(y)dy - \int_{b}^{\infty} I(\sqrt{u^2 + b^2})\, du$$

$$- \int_{-\infty}^{b} I(\sqrt{u^2 + b^2})\, du \quad . \qquad (10)$$

Equation (10) can be evaluated from the data, but is insensitive to the derivative of the data unless b becomes small. Using b = ±6 cm (six detector spacings), we integrated Eq. (10) trapezoidally to obtain the number of particles per unit length in the plasma core. The average density in the plasma core is $N(b)/\pi b^2$. This is what we have plotted below.

The radial profiles of the ion-end-loss currents are shown in Figs. 5-6 (west) and Fig. 5-7 (east). The Faraday-cup arrays, located at each end of TMX, measured these profiles. The ion-loss current is determined in A·cm^{-2} flowing through the end-cell midplane, and the detector position has been mapped to the end-cell midplanes along the intended vacuum-magnetic-field lines. We have two comments. First, the center of the end-loss profile appears to be shifted at both ends of the machine relative to the intended machine centerline. The profiles are shifted roughly one detector spacing at low gas feeds and two detector spacings at higher gas feeds. This shift is not well understood but is not the subject here. We believe it

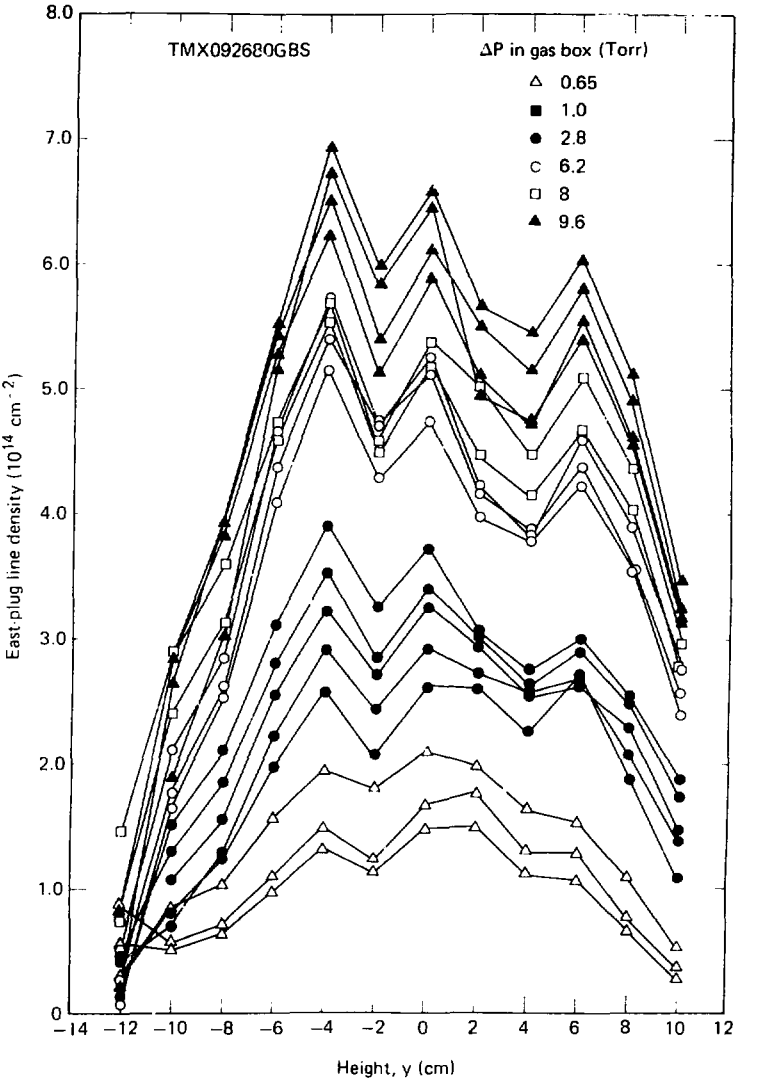

FIG. 5-3. Line density profiles in the east end cell measured for many shots. The data from each shot are connected by a line. The variation of gas feed is indicated by the symbols. As the gas feed increased, the entire line density profile increased.

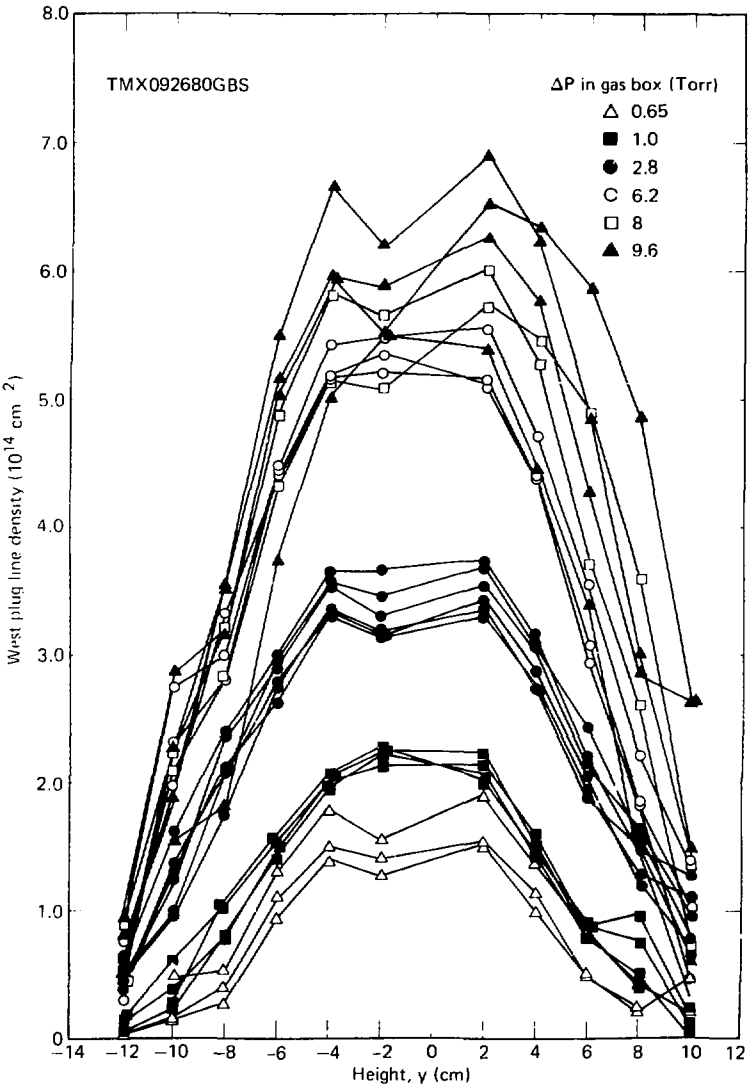

FIG. 5-4. Line density profiles in the west end cell measured for many shots. The data from each shot are connected by a line. The variation of gas feed is indicated by the symbols. As the gas feed increased, the entire line density profile increased.

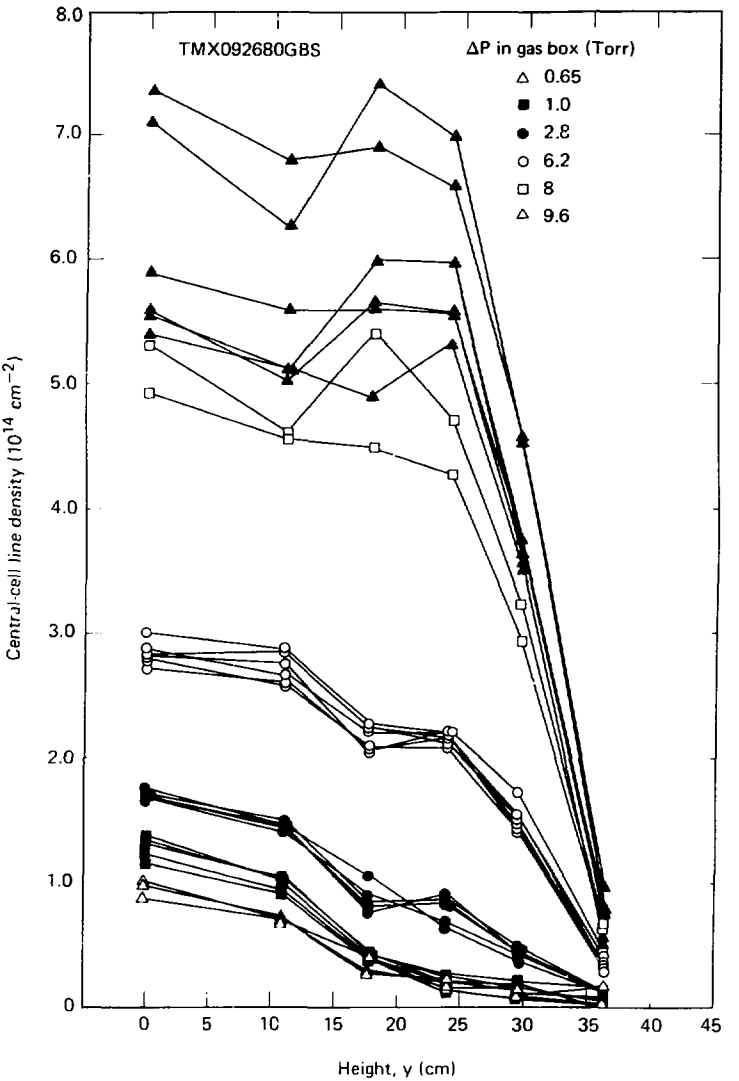

FIG. 5-5. Central-cell line density profiles as a function of gas feed. The central-cell density increased and the profile became flatter as gas feed increased. Data from each shot are connected by lines.

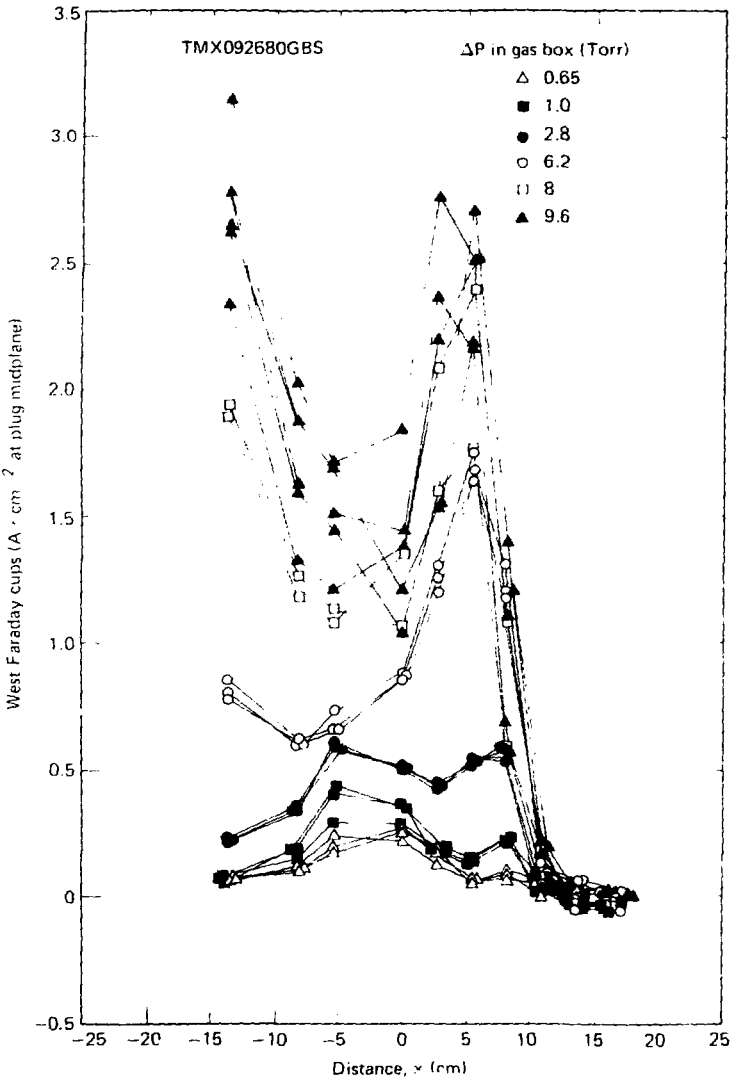

FIG. 5-6. An array of Faraday cups at the west end wall measured the profile of ion end losses as a function of gas feed. Data from each shot are connected by lines.

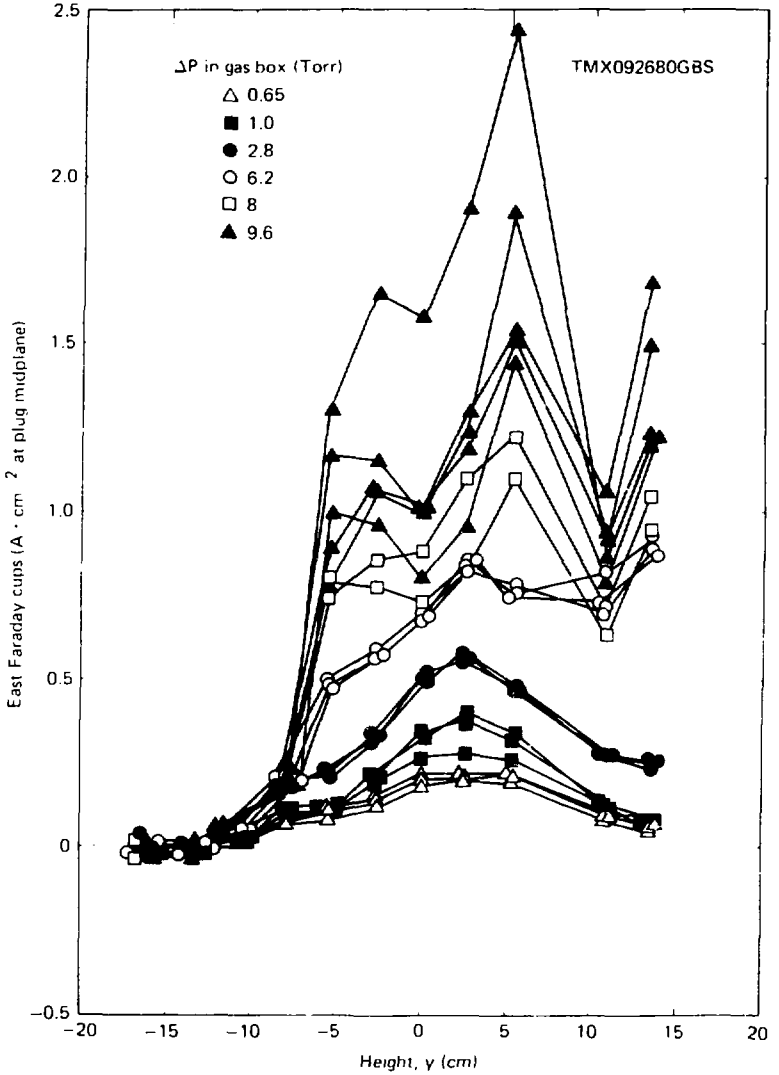

FIG. 5-7. An array of Faraday cups at the east end wall measured the profile of ion end losses as a function of gas feed. Data from each shot are connected by lines.

may result from a combination of magnet alignment errors and plasma effects. The end-loss currents plotted in other figures are radially weighted averages of the data in Figs. 5-6 and 5-7. The average was taken about the symmetry points of the observed end loss profiles. The uncertainties in these numbers are small compared to the changes observed in the course of the experiment.

Second, at large gas feed it is clear that more ions are lost *through the west end cell than through the east end cell*. Figure 5-6 shows large gradients in the plasma edge at high gas feed. Figure 5-7 shows what we expected based on the end loss profiles. In the plasma core, where the densities are comparable, the losses out of the two end cells are comparable.

The principal result of this experiment is shown in Fig. 5-8. As the end losses increased, the end cell density increased from below 10^{11}/cm^3 to about 3×10^{12}/cm^3. The density of unconfined plasma in the end cells was always small compared to the central cell density. The end cells exhibit the behavior predicted at the beginning of this section. At low gas feed, the end cell densities are low and insensitive to the end losses. Thus this experiment provides a qualitative verification of the theory presented in Sec. 5.3. The quantitative details are considered below.

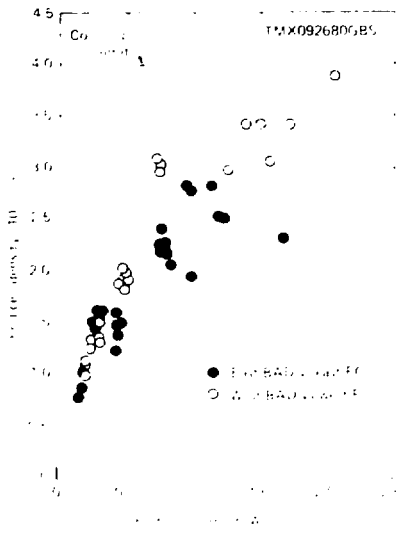

FIG. 5-8. The end-cell density averaged over a 6-cm-radius circle as described in the text, increased and approached the Coulomb limit as the measured end-loss current increased.

5.4 DISCUSSION

5.4.1 Warm-Plasma Stabilization

Coulomb collisions limit the end cell density. In addition to the central cell losses must stabilize ion microinstabilities. The end-cell density was expected to decrease if the central cell gas feed was reduced. We performed this experiment and observed this effect. This section compares data and theory in more detail.

Two limits are indicated in Fig. 5-8: a Coulomb limit and a stability limit. The Coulomb limit was calculated using Eq. (81) and the measured plasma parameters. The evaluation of n_p, E_i, and I_e is summarized in Appendix D. Because the neutral-beam current and electron temperature changed little during this experiment, this limit applies to all the data. The uncertainty in the Coulomb limit due principally to uncertainties in n_p and I_e is of order ±40%. If the end-loss current was sufficient, the end-cell density was within a factor of two of this limit. Under these conditions any end cell losses caused by the instability or other factors were smaller than the Coulomb losses.

The stability limit in Fig. 5-8 is based on Eq. (91). It was evaluated for the data obtained with a low gas feed. Within the uncertainties, the data should lie to the right of this line. If the data is far from the line, this indicates that the central cell losses are far from the optimum low-energy distribution function needed by the end cell for an error in the stability requirements. As the end-cell density reached the Coulomb limit and I_e were unchanged, the end loss could increase substantially without changing n_c. The data moves from the stability limit toward the Coulomb limit as the end losses increase. This is reasonable asymptotic behavior and supports the model presented above.

One other effect is quantitatively too small to cause the observed behavior. Some fraction of the neutral-beam flux extends axially beyond the hot

plasma. On the side of the end cell toward the central cell, these neutral atoms may become trapped by ionization or by charge-exchange with cold ions. If this effect were large enough, the end-cell density would increase in response to an increase of the central-cell density. However, we have evaluated this effect and it is small. In addition, it does not significantly change the Coulomb density limit or explain why the plasma density changes as much as it does.

We have examined how the end cell density responds to changing end losses (Fig. 5.8). These analyses show that adequate fueling of the central cell was required to obtain good results from TMX. In TMX, the fueling of the central cell core was very inefficient. In order to obtain a highly peaked ion density profile, end losses were flowing out of both end cells with a radius of 6 cm. We had to supply a gas flow to the gas boxes equivalent to 1500 A of deuterons. In this case, the total measured end losses were as large as 1700 A, and it seems reasonable to infer that a significant fraction of the initial 1500 A is deposited in the gas box walls and released after the shot. The details of this process, [illegible] and [illegible] transport are beyond the scope of this section and will be addressed in future publications.

5.4.2 Comparison to DCLC Theory

The data in Fig. 5.8 show that the end cell plasma requires adequate central cell losses to approach the Coulomb density limit. This indicates that a microinstability is present which is stabilized by low energy uncontained ions. The containment data can be compared to the DCLC stability requirement expressed by Eq. (9). The required loss current was compared to the observed loss current for a variety of experiments.

For most of the data, the measured end losses are no more than a factor of three above the minimum loss current. The spread of the data points is consistent with the experimental uncertainty in their evaluation (±50%). The observed end losses are somewhat higher than Eq. (9) predicts, but the difference is within the range of the uncertainties described in Sec. 5.2. For shots with end losses greater than 0.7 A/cm^2, the end cell density approached the Coulomb limit. However, for these shots the central cell losses are significantly larger than the Coulomb minimum and are significantly larger than the stability limit of Eq. (9). In the neutral-beam-current scan reported in Sec. 5, the required end losses were reduced until the central cell could easily supply them but only because the end-cell density was significantly below the Coulomb limit. In the experiment described above, the central-cell losses remained large. The plasma should have been stable to the DCLC instability. The data might be explained by the Two-Component instability or by the AIC instability. TMX is predicted to be unstable to the Two-Component instability because the central cell ions are too cold. The end losses are much more energetic than the central cell ions which supports this possibility. On the other hand, the plasma fluctuation data is most consistent with the AIC instability, which can be damped by warm plasma. We are still investigating these possibilities.

5.5 CONCLUSION

The TMX end cell plasma requires low energy ions to stabilize the microinstabilities in the end cells. We have shown that the central cell losses responded to changes in the central cell fueling. If enough central cell losses were supplied, the end cell density approached the Coulomb limit. In previous papers,[1] we reported an experiment in which the central cell losses approached the minimum determined by Coulomb collisions as this minimum became adequate to supply the low energy ions required by the end cells. Both of these experiments provide strong evidence that warm plasma stabilization is important, and in some respects they suggest that the DCLC instability determines plasma stability requirements. However, the picture is complicated by the nature of the observed plasma fluctuations, which do not appear to be the DCLC mode.

Several possible experiments could have produced better performance from TMX. Pellets, low energy beams, or further inventions could improve the central cell fueling. Central-cell heating might improve the electron temperature and the ability of the central cell to supply the optimum distribution of low-energy ions to the end cells. In addition, experiments using programmed beam current or gas feed might first establish an unstable plasma, then either reduce the end-cell density limit or increase the available end losses, in order to obtain stable plasmas. These experiments would focus on improving the ability of the central cell to stabilize the end cells.

REFERENCES

1. T.K. Fowler, B.G. Logan, "The Tandem Mirror Reactor," *Comments Plasma Phys. Cont. Fusion* **2**, 167 (1977).
2. G.I. Dimov, V.V. Zakaidakov, M.E. Kishinevsley, "Thermonuclear Confinement System with Twin Mirror Systems," *Fiz. plazmy* **2**, 597 (1977).
3. D.E. Baldwin, H.L. Berk, L.D. Pearlstein, "Turbulent Lifetimes in Mirror Machines," *Phys. Rev. Lett.* **36**, 1051 (1976).
4. F.H. Coensgen, C.A. Anderson, T.A. Casper, J.F. Clauser, W.C. Condit, et al., *Phys. Rev. Lett.* **44**, 1132 (1980).
5. T.D. Rognlien and Y. Matsuda, "Tandem Mirror Confinement in the Presence of Ion Cyclotron Fluctuations," *Nucl Fusion* **21**, 345 (1981).
6. R.P. Drake, T.A. Casper, J.F. Clauser, F.H. Coensgen, D.L. Correll, W.F. Cummins, J.C. Davis, J.H. Foote, A.H. Futch, R.K. Goodman, D.P. Grubb, R.S. Hornady, W.E. Nexsen, T.C. Simonen, B.W. Stallard, "The Effect of End-Cell Stability on the Confinement of the Central-Cell Plasma in TMX," *Nucl. Fusion* **21**, 359 (1981).
7. H.L. Berk and J.J. Stewart, "Quasi-Linear Transport Model for Mirror Machines," *Phys. Fluids* **20**, 1080 (1976).
8. W.C. Turner, J.F. Clauser, F.H. Coensgen, D.L. Correll, W.F. Cummins, R.P. Freis, R.K. Goodman, A.L. Hunt, T.B. Kaiser, G.M. Melin, W.E. Nexsen, T.C. Simonen, B.W. Stallard, "Field-Reversal Experiments in a Neutral-Beam-Injected Mirror Machine," *Nucl. Fusion* **19**, 1011 (1979).
9. J.T. Woo, *Nucl. Fusion* **17**, 1373 (1977).
10. M. Campbell and A.H. Futch, "Radial Fokker-Planck," Appendix C2 this report.
11. D.E. Baldwin, "End-Loss Processes from Mirror Machines," *Rev. Mod. Phys.* **29**, 317 (1977).
12. B.G. Logan, A.A. Mirin, M.E. Rensink, *Nucl. Fusion* **20**, 1613 (1980).
13. D.L. Correll, J.F. Clauser, F.H. Coensgen, W.F. Cummins, R.P. Drake, J.H. Foote, A.H. Futch, R.K. Goodman, D.P. Grubb, G.M. Melin, W.E. Nexsen, T.C. Simonen, B.W. Stallard, W.C. Turner, "Production of Large-Radius, High-Beta Confined Mirror Plasmas," *Nucl. Fusion* **20**, 655 (1980).
14. D.L. Correll, Lawrence Livermore National Laboratory, private communication (March, 1980).
15. M.J. Gerver, "Stabilization of Drift Cyclotron Loss Cone Instability with Additions of Small Amounts of Cool Plasma," *Phys Fluids* **19**, 1581 (1976).
16. R.F. Post, Varenna School, UCRL-82882.
17. D.P. Grubb, Publication in preparation, Lawrence Livermore National Laboratory, January, 1981.
18. S. L. Allen, C. A. Anderson, W. L. Barr et al., Appendix B of this report.
19. R.P. Drake, G. Deis, M. Richardson and T.C. Simonen, "Gas Control and Wall Conditioning in TMX," *J. Nuc. Mat.* **93** and **94**, 291 (1980).
20. P. Coakely, "End Wall Studies," this report.
21. D.P. Grubb, "TMX Power Balance," this report.
22. R.P. Drake, M.I. Baskes, K.L. Wilson, "Appendix 5D, Particle Storage in the Gas Box Walls," *Results Of TMX Operations: January-July 1980*, UCID-18803, Ed. D.L. Correll and R.P. Drake, Lawrence Livermore National Laboratory, Livermore, Calif.

6. A Model and Correlation of TMX Stability Requirements

6.1 INTRODUCTION

It has been observed in both the 2XIIB and the TMX experiments that a current of ions flowing from the mirror-confined plasma is associated with a stability requirement of the plasma.[1,2] The drift-cyclotron loss-cone (DCLC) mode which requires a population of "warm," unconfined ions in the loss cone of ion velocity space has received considerable attention. A second instability, the Alfvén ion-cyclotron (AIC) mode, driven by β and anisotropy, is also predicted to be unstable. It appears that in TMX we have been successful in stabilizing the DCLC mode since the characteristics of the rf fluctuations usually measured in TMX are not those of the DCLC instability. The measurements, discussed in detail in Sec. 11, show that the wave numbers and polarizations are usually consistent with the AIC instability and that the mode can propagate in the electron diamagnetic direction, inconsistent with the DCLC mode.

These observations have led to both theoretical and experimental work on the interaction of the instability-generated rf fluctuation with the warm stabilizing ions in the plasma. Recent theoretical work by Smith and Nevins[3] shows that warm ions mirror-trapped by the rf heating can stabilize the AIC instability. Though the theory pertains to an infinite medium and predicts a fraction of warm ions too large for TMX, it raises the possibility that a similar mechanism for the finite geometry of TMX could stabilize the plasma with less warm-ion density. Experimental work, discussed below, has led to a scaling relation between end cell plasma parameters and the axial ion current that is lost from the end cell. The scaling relation is based on the AIC instability and valid over a wide range of TMX operating parameters.

Our present view of TMX microstability picture is that the end-cell plasmas are susceptible to both the AIC and the DCLC instabilities. Examination of the data and comparison with the respective models indicates that TMX has operated in regimes where either AIC or DCLC has been dominant. The relative instability drives of the two modes changed as the plasma parameters were varied from experiment to experiment. Our present view is that both modes can be stabilized by warm ions that pass through the end cell plasma. Though the velocity distribution of the warm ions required for stability by the two modes is not the same, it is plausible that it is the instability that requires the greater flow of warm ions that dominates the behavior of the plasma in terms of the rf characteristics and the plasma scaling. It appears that DCLC is present at low injected neutral-beam currents ($\sim$70 A). An instance of DCLC scaling is the beam voltage scan described in Sec. 10. Another candidate is the operation reported in Ref. 4 in which quiet rf periods were observed as the end losses exceed the DCLC stream requirement. The majority of TMX operation appears to have been in a regime in which the DCLC mode is stabilized and the remaining instability was consistent with the AIC mode. The data employed in the correlation discussed below is representative of the majority of TMX data.

A model of the interaction between the end-cell plasma, the central-cell plasma, and the rf fluctuations has evolved. Though still in its formative stages, the model is consistent with representative TMX data. In this model, the rf generated by the plug heats ions in the Yushmanov region on the central-cell side of the plug. Some of these ions subsequently become mirror trapped in the end cell and serve to stabilize the end cell plasma by decreasing the anisotropy of the ion velocity distribution. These ions constitute a part of the end-loss current as they are lost from the end cell. This mechanism of ion loss from the central cell is different from the Rognlien-Matsuda model discussed previously.[2,5]

In this section, we discuss a model for the interaction between the end-cell plasma and the ion flow associated with a stability requirement; data from a gas-fueling scan and two beam-current scans show that a correlation exists that is consistent with the model. The correlation is a relation between the end-cell plasma diamagnetism M and the end-loss current j and is of the form $M \propto j^p$, with $p = 0.84 \pm 0.08$. We discuss the consequences of this model on the ion confinement and heating in the central cell.

6.2 A CORRELATION BETWEEN PLUG DIAMAGNETISM AND ION END LOSS

The causes of the AMX end cell instability are the plasma β and the anisotropy ($E_\perp - E_\parallel$) of the hot ion energy distribution [6]. In particular, a measure of the instability drive is the product $\beta (E_\perp - E_\parallel)$. The instability generates rf fluctuations that cause enhanced velocity diffusion of the ions beyond the limit set by Spitzer electron drag. We view the plasma as operating at a state of marginal stability in which the losses caused by the diffusion processes are just balanced by the fueling to maintain a steady state plasma.

6.3 A MODEL

We present the following model of the interaction between the rf and the low-energy plasma ions to produce a stabilizing stream. The rf that is generated as a result of the instability propagates out of the hot ion region. A part of the warm central cell ions is located between the dense hot-ion population and the inside mirror point of the end cell. A portion of these ions can absorb energy from the rf wave by the cyclotron resonance $k_\parallel V_\parallel = \omega - \omega_{c_i}$. Here $k_\parallel$ (along B) is the wave number of the wave, $V_\parallel$ is the parallel velocity of the ion, ω is the frequency of the rf fluctuations, and ω_{c_i} is the local ion cyclotron velocity. The ions that gain energy can become Yushmanov trapped between the potential of the dense end cell plasma and the magnetic field of the inside mirror. A further gain in energy can produce ions that are mirror confined in the end cell plasma with the energetic ions that originate from beam-injected neutrals. Because of the neutral beam injection the energetic ion population is highly anisotropic, with $E_\perp - E_\parallel \cong 14$ as a typical value. The damping of the rf fluctuations by the central cell ions in the Yushmanov region thus results in mirror-confined ions that aid in reducing the instability drive. The ions that are mirror confined through rf heating are not expected to be strongly anisotropic. First, the energy of the ions is such that ion-ion scattering contributes to the spreading of the ions in velocity space and thus to their loss from the plasma. A second source of parallel energy gain is $(V_\perp \times \tilde{B})_\parallel$ interaction between the ion and the rf. The warm ions are not well confined and constitute a part of the ion end-loss current as they are lost from the end-cell plasma.

The neutral-beam fueling of the end-cell plasma consisted of injection of neutrals nearly perpendicular to the magnetic axis of the machine. Hence, the energetic ion population of the end cell was highly anisotropic. The volume of the end cell did not change greatly as the plasma parameters were varied. As a consequence, the perpendicular ion energy, associated with the instability drive, can be represented by the diamagnetism of the plasma. According to the model presented above, the quantity of warm ions that become mirror confined and then stream out of the end cell affects the average parallel energy of the mirror confined ion population and thus affects the instability drive. A plot of the diamagnetism of the end-cell plasma as a function of the ion current streaming from the plasma would represent the balance between the instability drive and the damping of the instability by the interaction of the rf with the ions in the Yushmanov region. We will show data that indicates that such a relation holds over a wide range of TMX operating parameters.

6.4 THE DATA

The data that we have examined is the beam-current scan of 9-28-79 and the gas and beam-current scan of 9-2e-80. Though the data set covers only two days of operation it includes virtually the whole operating spectrum of TMX, namely a gas-current scan, two beam-current scans, puffer operation, gas-box operation, high T_e ($\gtrsim 175$ eV) operation and low T_e ($\lesssim 60$ eV) operation. Thus, if the correlations that are found hold true for this data, the probability is good that it is true for all data. We show first the individual sets of data, pointing out items of interest, and then show all the data on a plot of M (the plug diamagnetism) vs j (the end-loss current density on plug centerline).

The gas scan of 9-2e-80 is shown in Fig. 6-1. The east-plug diamagnetism and the east-plug line density are plotted as a function of the end-loss current density. We note three items: 1. T_e is near constant and ~ 60 eV for the data. 2. the line density appears to increase more rapidly than the diamagnetism, indicating a decrease in hot ion energy. 3. the magnitude of the rf level in the plug

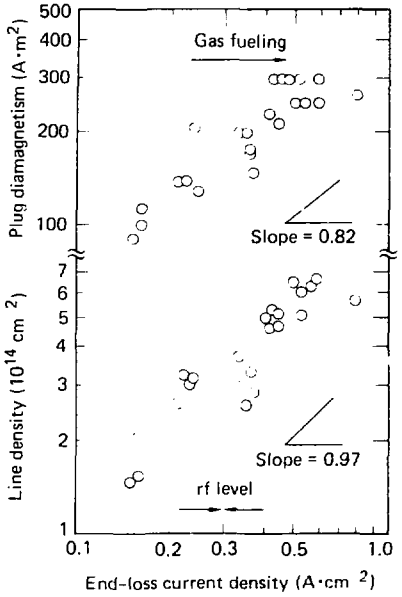

FIG. 6-1. East end-cell diamagnetism and line density vs end-loss current for the gas-box scan of 9-26-80, $T_e \simeq 60$ eV.

first increased and then decreased with increasing fueling and end losses (see Fig. 6-2a).

We now look at the beam-current scan from the same day (Fig. 6-3) and compare: 1. T_e is 60 eV, 2. the line density appears to stay nearly constant as the diamagnetism increases with increased injected neutral beam current, 3. the rf level increases with increasing diamagnetism (see Fig. 6-2b). We note the difference in the behavior of the hot ion energy and the rf turbulence between the two types of scans.

The last set of data (Fig. 6-4) is the beam scan of 9-28-79, analyzed previously in terms of DCLC and the Rognlien-Matsuda model of central-cell ion loss.[3,4] The data shows 1. $T_e \sim 175$ eV and apparently constant for the beam scan, 2. the diamagnetism increases more rapidly than the line density. The open circles (O) are shots #28 through #53, with shots #27 and #45 as background shots. The filled-in points are shots #54 through #60 with shot #61 as background shot. The rf increases with increasing diamagnetism, in agreement with the other beam scan and opposite to the gas scan at high diamagnetism. This feature is discussed later in this section.

We now plot all the data on the same graph (Fig. 6-5) showing the diamagnetism as a function of the end-loss current density. The correlation appears to be about as good, ±25% or so, as the errors in the loop data. The plot confirms the earlier hypothesis that the diamagnetism and the end-loss current should be related. The scaling is not what would be expected from the DCLC instability. For similar densities and ion energies, the $(\omega_{pm}/\omega_{ci})T_e^{3/2}$ factor in the DCLC quasilinear current requirement[2] would correspond to an end-loss requirement ~5 times greater for the $T_e \sim 175$ eV data than the $T_e \sim 60$ eV data $[(175/60)^{3/2} = 5.0]$. The data clearly does not indicate such a difference; rather, the data shows a scaling that is independent of the electron temperature and thus independent of the ambipolar hole in ion velocity space. This feature of the data contradicts the DCLC theory. We therefore conclude that a mechanism other than DCLC determines the operating characteristics of TMX.

The data presented here shows that a wide spectrum of TMX data can be correlated by a relation between the plug diamagnetism M and the end loss current density j. The correlation is of the form $M \propto j^p$, where p has to have the value $p = 0.84 \pm 0.08$. This correlation is, from the discussion above, consistent with the behavior of a plasma dominated by the AIC instability and existing in a state of marginal stability in which the losses due to rf diffusion are balanced[4] by fueling.

6.5 DISCUSSION OF SCALING RELATION, $M \propto j^p$

To find a scaling relation for the plug plasma, we return to the view of marginal stability: the rf generated by the instability causes sufficient velocity diffusion that the instability drive is reduced to a level where the plasma can be supported by the available neutral-beam injection. A state of marginal instability can be described as a constant level of the instability drive, which for the AIC mode can be approximated by a simple

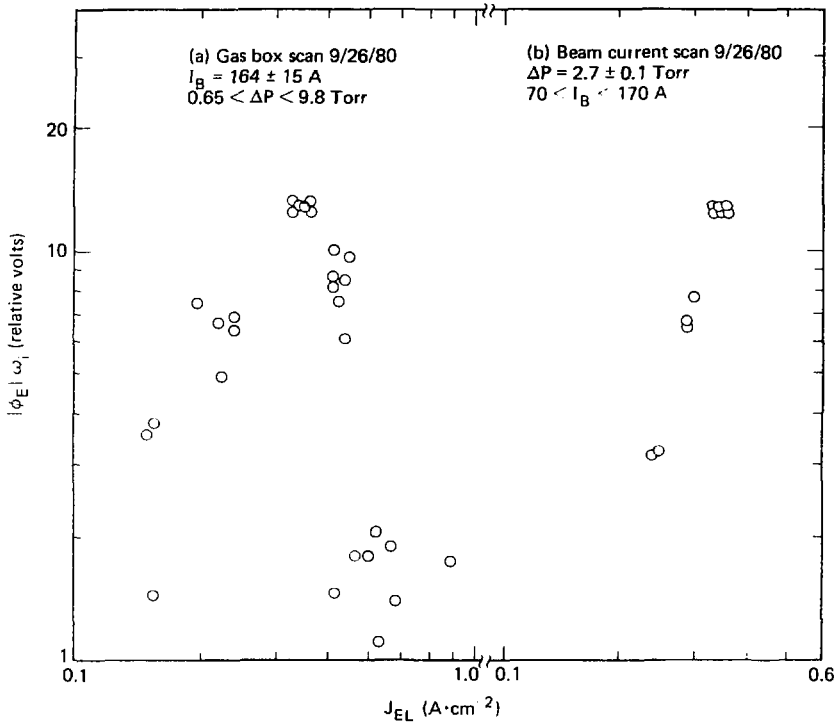

FIG. 6-2. Potential fluctuation vs end-loss current for the gas-box scan and beam-current scan.

functional relation $\beta^n(E_\perp/E_\parallel)$ = constant, (n = constant exponent). Thus, if β increases, the anisotropy must decrease, and vice versa. Bearing in mind that $E_\perp$ is due primarily to the hot injected ions, and $E_\parallel$ is mostly associated with the lower energy mirror confined ions, we can write the anisotropy as

$$\frac{E_\perp}{E_\parallel} \sim \frac{n_H E_\perp}{n_H E_\parallel + n_W T_W}, \quad n_p = n_W + n_H \quad ,$$

where n_H is the hot density, n_W the warm density, and T_W the parallel temperature of the warm ions.

The equation shows the two limits of the behavior of the anisotropy described above. If there is no external supply of warm ions (i.e., no resonant absorption within the mirror points), then $n_W \sim 0$, and the anisotropy $E_\perp/E_\parallel$ changes as a result of rf-induced velocity diffusion which increases $E_\parallel$ at the expense of $E_\perp$. In the limit where sufficient warm ions are resonant with the rf, these absorb the rf power, gain energy, and constitute the n_W population. Thus, $E_\perp/E_\parallel$ of the hot population need not appreciably change. We now have

$$\beta^n \left(\frac{n_H E}{n_H E + n_W T_W} \right) = \text{const} \quad :$$

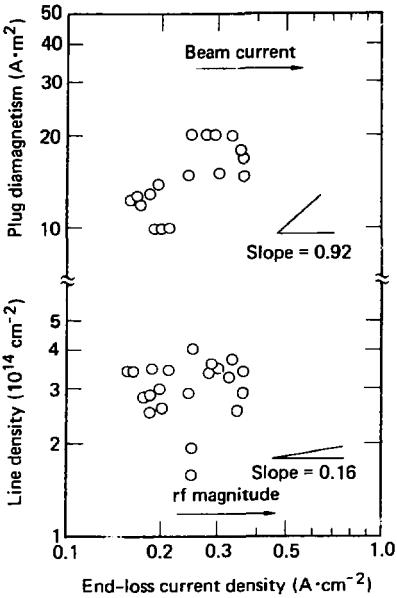

FIG. 6-3. East end-cell diamagnetism and line density vs end-loss current for the beam scan of 9-26-80, $T_e \simeq 60$ eV.

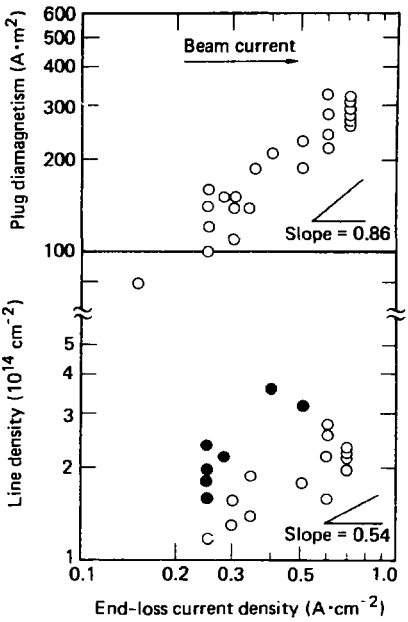

FIG. 6-4. East end-cell diamagnetism and line density vs end-loss current for the beam scan of 9-28-79 with puffer-gas feed, $T_e \simeq 175$ eV.

to get to a relationship that can be observed experimentally, we relate the quantity $\beta^n(n_H E_\perp)$ to the diamagnetism, M, of the plug plasma: $\beta^n(n_H E_\perp) \propto M^a$, where a is some exponent (constant); we have assumed the magnetic field and volume are constant for the data to be analyzed. The quantity $(n_H E_\perp + n_W T_W)$ can be viewed in two limits. In the case where no external resonant ions are available to damp the instability and contribute warm, mirror-confined ions, the rf-induced velocity diffusion causes the hot-ion velocity distribution to spread, increasing $E_\parallel$ or decreasing $E_\perp$. The stream will equal the trapped beam current. The data relevant to this limit (2XIIB and some TMX data) are not discussed here. In the limit most relevant to TMX operation, the warm-ion population is supplied by the interaction of the rf with external warm ions. We view the anisotropy of the hot-ion population as constant. The stream is related directly to the mirror-confined warm population by $j \propto n_W/\tau_W$; here, τ_W is the lifetime of the warm ions. Thus, in the limit where the ion loss from the plug greatly exceeds the trapped beam current, we hypothesize $(n_H E + n_W T_W) \propto j^b$. Combining, we get a relation that can be tested with data $M \propto j^p$, where M is plug diamagnetism, j is end loss current density, and p is a constant (b/a). The effects of volume, magnetic field, injection energy, etc. can be tested after we find whether the M vs j relation describes the data.

To summarize, we have argued that the end-loss current directly reflects the stability requirement and that the AIC instability drives would be reflected in a scaling relation of the form $M \propto j^p$.

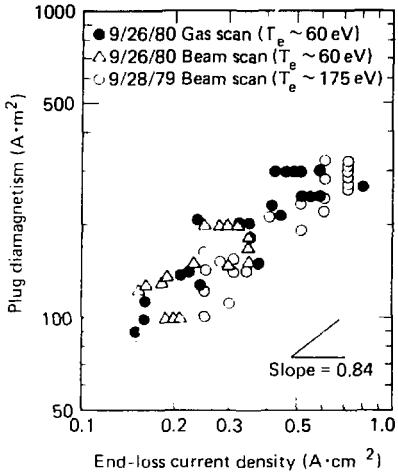

FIG. 6-5. East end-cell diamagnetism vs end-loss current.

6.6 INTERACTION BETWEEN THE END CELLS, THE rf, AND THE CENTRAL CELL PLASMA

The model of the ion flow from the end cell and the interaction of the rf with the central cell ions is demonstrated clearly by measurements of the behavior of the end loss ion current and energy spectrum as the machine was operated with asymmetric end cells. These observations, described below, contradict an earlier model[5] in which the ion end loss was due to central cell heating by an oscillating electric field perpendicular to the magnetic field. As the waves alone cannot cause a potential confined ion to be lost, collisions are also necessary. This model therefore implies that in a tandem mirror with equal end cells, potential waves generated in a single end cell should produce nearly equal end-loss currents and energy spectra out either end. In unbalanced end-cell operation, more end-loss current would be expected out of the end cell with the lower density; the temperature of the ion end loss would be expected to be comparable on either end. Instead our measurements show higher temperature ions flowing from the operating plug.

6.7 EXPERIMENTAL OBSERVATIONS

The early model is contradicted by at least two experimental observations. The first observation is that there exists machine parameters for which the greater end flow is through the end cell having the greatest density.[7] If the density is related to the confining potential $\Delta\phi$ through $\Delta\phi = T_c \ln(n_p/n_i)$, this behavior is not consistent with the classical (i.e., collisional) picture of tandem mirror confinement. An example of this type of unbalanced end-cell operation is shown in the shot summary plot in Fig. 6-6.

The second observation by D. P. Grubb (see Sec. 12) shows that the end-loss energy spectrum on either end varies as the end cell neutral injectors are turned on or off.[7] A central-cell ion temperature of ~50 eV was suggested by several measurements. This temperature can be compared to temperatures up to 1000 eV detected by end-loss analyzers while both end cells have neutral-beam input. After the beams on the west end cell are turned off, the west end-loss temperature is ~100 eV while that of the east end cell remains at ~1000 eV. These observations preclude heating to ~1000 eV in the region between the mirror peaks bounding the central cell.

These observations are the reason that our present model rf end-cell ion flow specifies that the primary interaction between the rf and the central-cell ions occurs in the Yushmanov region, that is, in the region between the inner mirror point and the hot, dense plasma. The rf can cause loss of ions by heating first at the $k_{\parallel}V_{\parallel} = \omega - \omega_{ci}$ resonance; the ion can subsequently, having gained sufficient $V_{\perp}$, become mirror confined in the end cell. Further, interaction with the rf can result in the gain of parallel velocity by $(V_{\perp} \times \tilde{B})_{\parallel}$ forces and a consequent loss of mirror confinement. In this picture, therefore, the end cell can "pump" warm ions from the Yushmanov region of the central cell through the hot plasma. A condition on the change of ion energy during the period of mirror confinement is that the change in energy is small relative to the difference in potential between the inner and outer mirror points of the central cell. If this condition were not satisifed, the high-temperature ions would

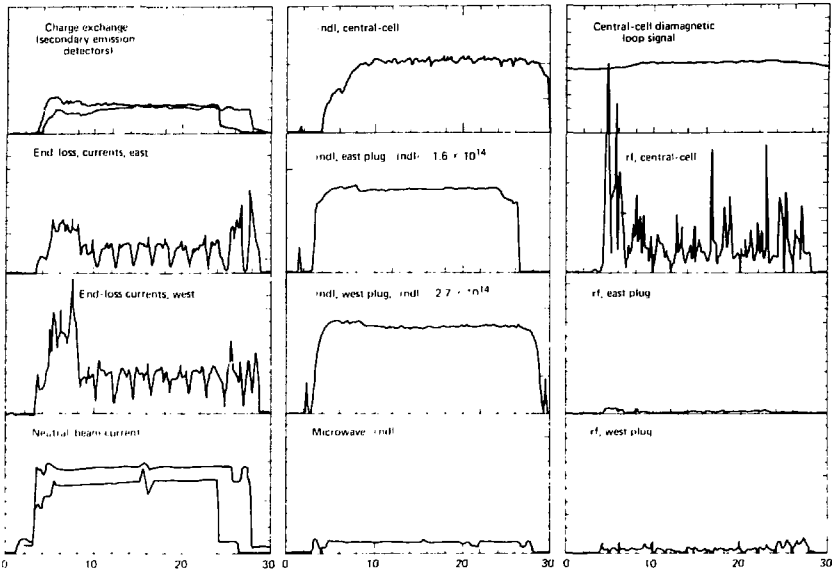

FIG. 6-6. Summary plot for unbalanced end-cell operation. End losses are greatest out the denser end cell.

not preferentially be lost to the outside of the end-cell plasma, as required by consistency with the experimental observations.

To illustrate the effect of ion pumping by the end-cell-generated rf, we show in Fig. 6-7 the behavior of end losses during rf dominated operation. The end losses of the denser plug can decrease greatly immediately after the beams powering that end cell are turned off. We suggest the following reason: Prior to turn-off, the rf generated by the plug pumps ions over the potential barrier to produce the greater part of the end-loss current. Immediately after turn-off, the hot-ion distribution relaxes to reduce the anisotropy and virtually eliminate the rf turbulence. The plug no longer pumps, and the plug density, though decreasing, is still sufficient to maintain a potential barrier. The dip in end losses is interpreted as the flow of thermal central-cell ions over the potential barrier. As the barrier decreases due to the decreasing plug density and electron temperature, the end losses increase to the limit allowed by the magnetic geometry. We note that the large dip in end losses occurs only for high rf plugs. Lower rf plugs show little or no decrease in end losses upon beam turn-off (Fig. 6-8).

6.8 rf-DOMINATED PARTICLE CONFINEMENT

Turning to the data of Figs. 1, 3, and 4, we note the relation between rf level, end loss current, and the central-cell density. The relations are shown schematically in Fig. 6-9. The picture that evolves is that a plug that has a certain diamagnetism must have a corresponding end loss, satisfying the $M \propto j^p$ relation. If the number of ions that can absorb rf through the cyclotron resonance is small, the rf level must be large to supply the required current. If the opposite is true, that is, if the density of power-absorbing ions is large, a low level of rf suffices to supply the required end-loss current. This picture is consistent with (and derived from) the behavior of the rf during beam

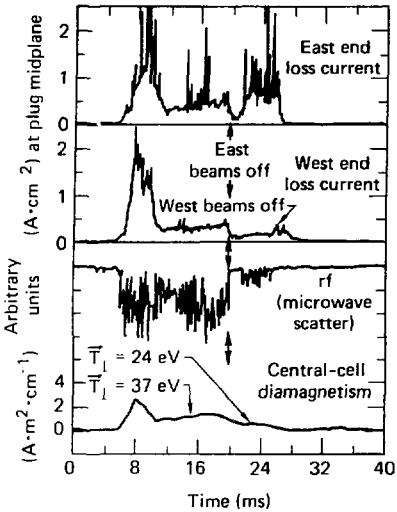

FIG. 6-7. TMX confinement with significant rf; the east end cell is denser, I_E = 210 A, I_W = 105 A.

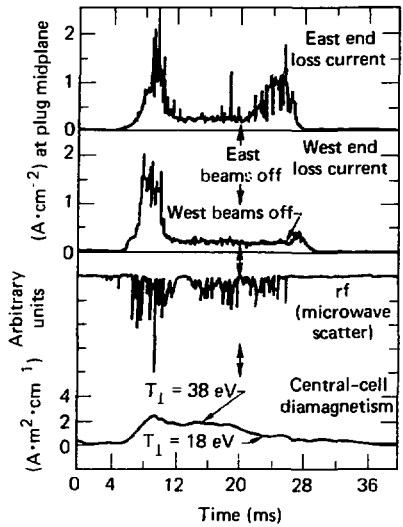

FIG. 6-8. TMX confinement with low rf; $I_E = I_W$ = 110 A.

scans and gas scans. In a beam scan, the central-cell density is nearly constant, and the diamagnetism, and hence the end loss current requirement, increases. The rf level therefore increases with increasing injected current. In a gas scan, on the other hand, the central-cell density increases as fast or faster than the plug diamagnetism. The rf level first increases, with increasing gas, and then decreases. This behavior is consistent with a view of $M = kj^p$ corresponding to a marginal stability limit. As Fig. 6-10 shows, a small movement in parameters normal to the stability curve can cause large increases or decreases in the rf level. The stability curve and the paths followed during a gas scan and a beam scan are illustrated.

These perceptions of the interaction of the rf, the central-cell density and temperature, and the end-loss current can be put together in a model for the central-cell (and hence machine) confinement. Though the model is still evolving, the parts that have been tested appear to fit.

The model is as follows. We first identify the parameters that are important; the first is the plug diamagnetism. Whether we use low density and high ion energy or high density and low ion energy to produce the same diamagnetism, the end loss is related by $M = kj^p$. It is, of course, most "economical" to use high density and low ion energy to produce good confinement parameters since the rf-pumped end loss is smaller. The next parameter that is important is the time required for the rf to drive a resonant central-cell ion over the potential barrier. That time is related to the rf level $\tilde{\phi}$ and confining potential $\Delta\phi_c$ by $1/\tau = G(\tilde{\phi}^2/\Delta\phi_c)$, where G is some monotonic function. The third parameter that is important is the density of central-cell ions between the hot ions and the inside mirror point that is capable of being resonant with the rf. That is, the number of ions in the Yushmanov region that can satisfy the resonance condition $k_\parallel v_\parallel = \omega - \omega_{ci}$, where ω_{ci} is the local ion cyclotron frequency. We define the resonant fraction to be $F(T_{ic})$, and hence the resonant density is $n_c F(T_{ic})$. We can now make a plot that relates the quantities; the plot in a schematic form is shown in Fig. 6-11. We can test the plot in various ways. It

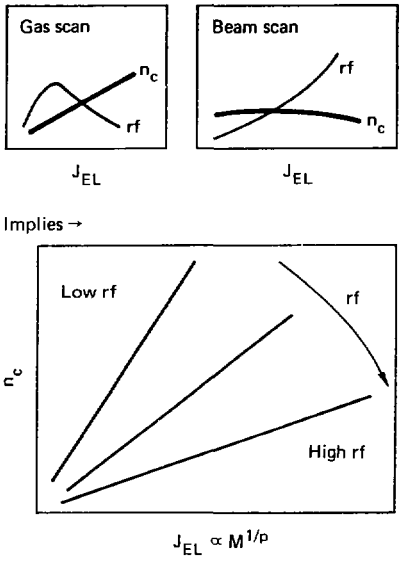

FIG. 6-9. Schematic relationship of rf-dominated central-cell confinement.

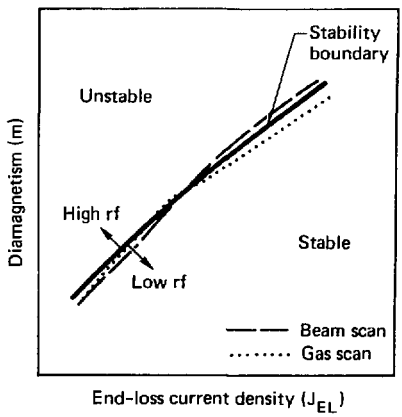

FIG. 6-10. Schematic of the proposed stability boundary and the paths followed during a beam scan and during a gas scan.

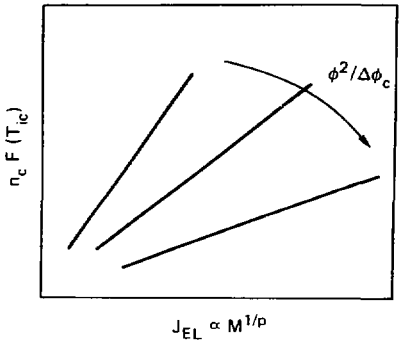

FIG. 6-11. Schematic variation of end-loss current with density of Yushmanov-trapped ions.

says, for example, that for a constant value of $\widetilde{\phi^2}/\Delta\phi_c$, we will have a fixed relation between $n_c F(T_{ic})$ and j. We have plotted the data of 9-20-80 in a similar format in Fig. 6-12. The ranges of rf level are indicated by the symbols. The important point is that although the areas covered by the different symbols abut, they do not overlap. This is an important test, because it allows us to write the central-cell (and thus machine) confinement in the form $j = n_c G(\widetilde{\phi^2}/\Delta\phi_c)$ and, in terms of $(n\tau)_c$,

$$(n\tau)_c \propto \frac{n_c F(T_{ic})}{G(\widetilde{\phi^2}/\Delta\phi_c)}$$

The model is good if the end flow is mostly rf pumped. We need to add the thermal flow component and the trapped-beam current to cover the whole range of TMX operation. We note that the limit of $(n\tau)$ for rf-dominated operation corresponds to magnetic confinement of the plasma in the central cell. For this limit, the ions that flow through the inner magnetic mirror are rapidly pumped by rf interaction from the Yushmanov region through the end cell. The situation is illustrated in the data of Ref. 2, reproduced here as Fig. 6-13.

In this section, we have pointed out a number of the features of plug end losses; we have shown that the plugs can actually pump ions out of the central cell, and indicated inconsistency with the

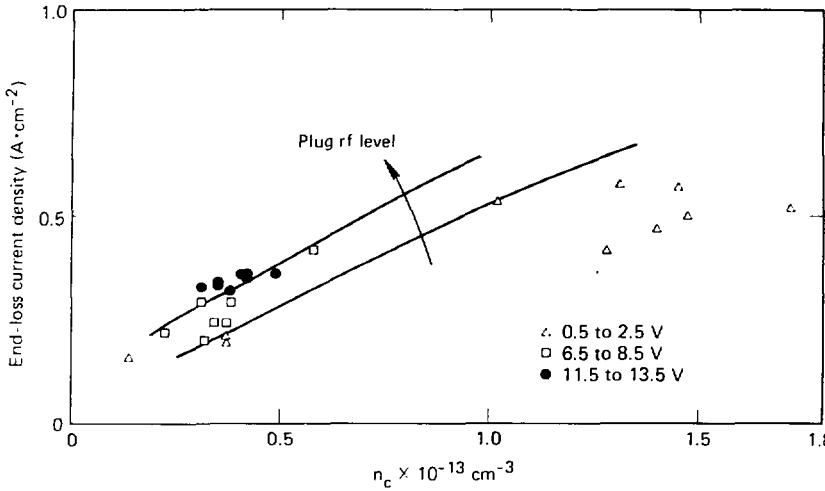

FIG. 6-12. End-loss current vs central-cell density and plug rf level.

Rognlien-Matsuda model. We then suggested an embryonic model for the interaction between the rf, the end losses, and the central-cell ions, and showed how the model, together with the $M = kj^p$ relations, characterize the confinement properties of the central cell of TMX.

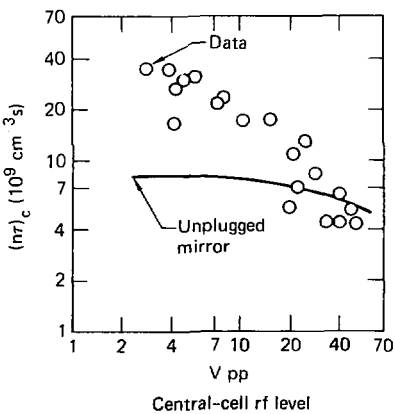

FIG. 6-13. Central-cell confinement vs rf level.

6.9 CONCLUSION

A scaling of the plug end losses associated with a stability requirement has been identified and is $M = kj^p$, where M is the plug diamagnetism, j the end-loss current density, and p is a constant having the value 0.84 ± 0.08. It appears fairly evident that the M vs j scaling of end losses contains at least an element of the truth. It should also be evident that the scaling, though it holds for a large range of operating parameters, may be highly profile and geometry dependent. The scaling is plausible from a theoretical point of view, but the details of the scaling are not as yet theoretically tractable.

The stability requirement is consistent with the instability drives of the Alfvén ion-cyclotron (AIC) mode. Although the DCLC stability criterion is satisfied in these experiments, the observed scaling is not consistent with DCLC scaling. The M vs j scaling together with the observed rf properties described in Sec. 11 show that the dominant instability in TMX is not DCLC; rather, the observed end loss scaling and the measured electromagnetic

wave properties are consistent with the AIC instability.

We have shown that the end-cell plasma can by direct rf interaction and with no ion collisions pump ions from the central cell through the end-cell plasma. This observation, together with the measured ion energy spectra of the end losses for various operating conditions, shows that the significant interaction between the central-cell ions and the rf occurs in the Yushmanov region. The resonant rf heating causes mirror trapping of a warm ion population which in turn stabilizes the end-cell plasma. We then describe a developing model in which the rf level is related to the central-cell and end-cell plasma parameters. The stream is determined from the end-cell diamagnetism through the $M \propto \beta'$ relation. The current of ions from the Yushmanov region that corresponds to this requirement is produced by the ion cyclotron fluctuations interacting with a resonant population of central-cell ions in the Yushmanov region. The model illustrates the behavior of particle confinement in TMX for rf-dominated operation.

REFERENCES

1. F. H. Coensgen et al., "2XIIB Plasma Confinement Experiments," *Proceedings of Sixth International Conference on Plasma Physics and Controlled Nuclear Fusion Research, Berchtesgaden, Fed. Rep. of Germany*, Oct. 6-13, 1976.
2. R. P. Drake et al., "The Effect of End-Cell Stability on the Confinement of the Central-Cell Plasma in TMX," *Nucl. Fusion* **21**, 350 (1981).
3. C. R. Smith and W. M. Nevins, "Warm Ion Stabilization of Alfvén-Ion Cyclotron Instability," *Mirror Theory Monthly*, Feb. 15, 1981.
4. P. Poulsen, "Quiet rf Operation," *Mirror Fusion Quarterly Report*, January through March 1980, UCAR-10060-80-1.
5. T. D. Rognlien and Y. Matsuda, "Tandem Mirror Confinement in the Presence of Ion Cyclotron Fluctuations," *Nucl. Fusion* **21**, 345 (1981).
6. T. D. Rognlien and D. C. Watson, *Phys. Fluids* **22**, 1958 (1979).
7. P. Poulsen and G. R. Smith, Internal Memo, Lawrence Livermore National Laboratory, Livermore, Calif.

SECTION 7
POWER BALANCE AND POWER FLOW IN TMX

(D. P. Grubb)

7. Power Balance and Power Flow in TMX

7.1 INTRODUCTION

This section presents our analysis of the flow of power between the different species of particles in TMX and through the different regions within TMX. We follow the energy from the point where it enters the system either by ionization or charge exchange of a neutral-beam particle until it escapes to the walls of the containment vessel either by axial or radial transport. We find that we can account for 70% to 100% of the power input into TMX by the neutral beams.

In TMX power was injected into the plasma solely by energetic neutral beams which both fueled and heated the end cells. The resulting flow of the neutral beam power through TMX can be explained in terms of a simple classical model which agrees with experimental measurements. In this model interaction between the energetic beam neutrals and the end cell (Tandem) plasma creates hot mirror confined ions. Of these ions (especially those near the plasma periphery) 30% to 40% are subsequently lost by charge exchange with background gas. The remaining plug ions diffuse downward in energy until they scatter into the unconfined region of velocity space and escape to the end walls. The energy which is lost by the ions as they diffuse downward in velocity space transfers to the plug electrons by Coulomb drag. The plug electrons then exchange this energy with the slightly cooler central-cell electrons which circulate through the plugs. The central-cell electrons ionize the cold gas which fuels the central cell. They also heat (by one process or drag) the resulting central cell ions and electrons. Eventually the central cell electrons escape axially to the end walls. As they go, they carry to the end walls thermal energy kT_{e_c} and give up energy $e\phi_c$ to the electrical potential that had confined them in the central cell. In equilibrium a central cell ion is lost for each electron. This ion carries thermal energy $(e\phi_c + kT_{i_c})$ and the potential energy $e\phi_{p_c}$ to the end wall. In this fashion the central-cell ions transport 80% to 90% of the plug-ion electron drag power to the end wall. We have found that this classical picture must be modified in three ways in order to more completely describe the power balance in TMX:

1. Plug-driven ion cyclotron waves heat the central-cell ions[1,2] thereby providing a second (and often dominant) power input into the central cell ions.
2. The plug fluctuations also heat the end-loss ions from the central cell as they escape through the plugs so that they smash into the end wall with thermal energy 10 to 20 times that which they had in the central cell.
3. The electron axial energy transport is as much as a factor of 10 less than the predicted classical value.

Finally, we note that the power loss by secondary electron emission from the end walls of TMX was only 1/3 of the expected value (Section 15). This may have important and favorable consequence for other tandem mirrors such as TMX Upgrade and MFTF-B.

The remainder of this section gives the reader increasingly detailed information about the TMX plasma and the analysis techniques which lead to our conclusions. In the following subsection we present detailed studies of the power balance on four days of TMX operation under different operating conditions. Following this we describe the power flow through TMX on one of those days. Finally, in our last subsection we present a brief summary of our conclusions and indicate areas where investigations into the details of the power balance in tandem mirrors are still progressing.

7.2 OPERATING RANGE OF TMX

Calculation of the power balance in a fusion device can be a useful tool for determining how well the device is running and for improving its operation. We carried out detailed measurements and computed the power balance in TMX for several days running.

The data in this section was selected to present an overview of the power balance in TMX over its operating range for which we had detailed diagnostic measurements. The knowledge gained from this effort has aided in the design of

TABLE 7-1a. Characteristics of TMX operations: power balance days.

Date	Neutral-beam current	Central-cell fueling technique	Plug T_e
9/26/79	High	Gas box	Intermediate
9/28/79	Low	Puffer valve	High
7/18/80	High	Gas box	Low
9/24/80	Intermediate	Puffer valve	Low

TABLE 7-1b. Dominant power loss mechanisms in TMX.

Date	9/26/79	9/28/79	7/18/80	9/24/80
Net input power P_{net},[a] kW	470	280	370	420
Loss mechanism, values in % of net input power				
Axial particle loss	40 ± 10	60 ± 20	30 ± 10	35 ± 10
Plug ions charge exchange on background gas	30 ± 15	40 ± 20	40 ± 20	30 ± 15
Fueling of central cell	10 ± 5	10 ± 5	10 ± 5	15 ± 5
Impurity radiation	5 ± 2	5 ± 2	5 ± 2	7 ± 2
Other central-cell losses[b]	15 ± 5	No measurement	10 ± 5	10 ± 10
Total	100 ± 28	115 ± 35	95 ± 31	97 ± 30

[a] P_{net} = P_B (trapped) - P (beam induced charge exchange).

[b] Based on measured power loss to central cell walls.

diagnostics and computer-aided analysis techniques for the TMX-Upgrade which will be used to obtain feedback from the power balance calculations during operation.

To describe the power balance in TMX we present the data from four days of operation. Between them, these four days characterize the operating modes and regimes of TMX (Table 7-1a). The data from three of these days (9/26/79, 9/28/79, and 7/18/80) has been presented in previous publications. Changes in the details of the power balance for those same dates as presented here reflect changes in our understanding of the power balance in TMX as indicated in Table 7-2.

Specifically, we have found that the profile of the power loss to the end walls of TMX is more peaked than previously assumed so that the total end-loss power is approximately one-half of the previously calculated value. Secondly, the west plug-ion energy appears to be significantly lower than that of the east plug so that the total power input to the west plug is larger than previously calculated. The third change to the power balance picture previously presented results from recent calculations of the power lost by the hot plug ions due to charge exchange with cold background gas atoms in the thin fan regions of the plugs.

These calculations were performed using the radial Fokker-Planck (RFP) code of A. H. Futch (Appendix F) and are supported by measurements of the charge exchange flux. For the data analyzed, this power loss accounted for 30% to 40% of the total, net input power.

A summary of the power balance for the four days analyzed in this section is presented in two forms. In Table 7-1b we show the dominant power loss mechanisms and the percentage of the net power input which each of these terms represents. In this table we have included estimates of the uncertainties of each of the values. The total uncertainty in a given value is our estimate of the cumulative effect of all of the uncertainties associated with calculating the value. In some cases (e.g., the power loss by charge exchange on background gas) the dominant source of the uncertainty comes from the fact that our understanding of this phenomena is still evolving. In other cases, the dominant source of uncertainty comes from the

TABLE 7-2. Progress in TMX power balance studies.

Model	New measurements	Conclusions
Central Chord August 1979	Electrostatic end loss analyzer End-wall and central-cell calorimeters Neutral beam attenuation diagnostic	On axis, most beam power deposited on end wall by ions Plug ion cyclotron fluctuations heat central-cell ions
Global November 1979	Single channel EUV spectrometer Radial arrays of end loss current detectors	Impurity radiation small End loss current profile shape comparable to density profile Dominant power loss to end walls Overall power balance achieved
Radial Profiles September 1980	Movable end-loss analyzer Arrays of end-wall calorimeters Additional calorimeters in central cell End-plug charge exchange from SED Central-cell Thomson scattering End-wall probes Solid-state surface probes Multichannel EUV spectrometers	Plug potential has radial profile End loss power peaked on axis Radial power loss to walls generally small Charge exchange of plug ions not negligible Central-cell T_e cooler than plug T_e End wall density small and cool Wall flux and energy corroborate other measurements Impurities less than 0.5% of central cell plasma Lower ionization states of impurities at edge
Complete Radial Model March 1981	More complete models being implemented in TAMBAR and TOARBUC codes for comparison with TMX data	Work in progress

fact that we were only able to measure the plasma parameters at a finite number of locations.

At the time that TMX ceased operation in Oct.-Nov. 1980 we had developed a significant diagnostic capability (Appendix B). (Some of the diagnostics which played particularly important roles in the power balance are shown in Fig. 7-1.) However, the number of detecting elements was finite and, therefore, we must fit model profiles through the measured data points to determine an analog form for the plasma parameters. To the degree that there is a finite accuracy to each measurement and that our fitted profiles are inexact, we recognize that calculated values in the power balance are uncertain. Within these bounds, it is still clear that certain terms are more important than others in determining the power balance and that we can account for the majority of the power input to TMX as being lost by known mechanisms.

The flow of the power through the regions of TMX for each of the four days studied in this section is shown in a schematic figure (Fig. 7-2). The power (in kW) associated with each of the terms represented in Fig. 7-2 is then presented in Table 7-3. The uncertainties associated with these values are not shown. We refer the reader to Table 7-1b for this information. (Appendix E provides a formulary of the equations used to calculate the values presented in Table 7-3.)

Although there were significant differences between the plasma parameters and the details of the power balance on each of the four days, we can summarize the results of the power balance calculations presented in Fig. 7-2 and Table 7-3.

Axial power loss played a dominant role in the power balance in TMX. Detailed measurements of the ion end-loss current density and energy spectra show that the ions carried almost all of the axial-loss power to the end wall. Our analysis also shows that these were ions which escaped the central cell and then gained energy as they fell down the potential hill created by the electrons. This was in contrast to similar measurements made in 2XIIB which showed that electrons carried more power to the end walls than did the ions[3] (Table 7-4). As described by Drake, et al. in Ref. 4, this improvement in the electron thermal isolation from the end wall was the result of careful design of the TMX

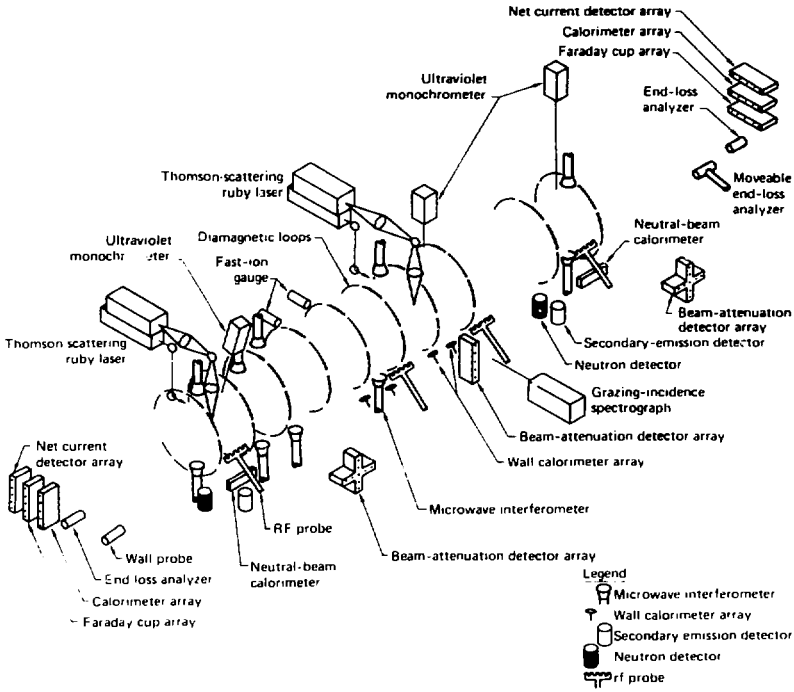

FIG. 7-1. TMX power- and particle-loss diagnostics.

magnet and vacuum systems and is applicable to other tandem mirror devices such as MFTF-B.

Our present understanding of the charge exchange of the plug ions on gas indicates that this process represents a power loss which can be as large as the axial power loss. Improved vacuum design will allow us to significantly reduce the magnitude of this term in the TMX-Upgrade and MFTF-B.

The remaining three terms, power loss associated with the gas fueling of the central cell, impurity radiation, and other measured losses contribute only 10% to 15% each of the total power loss.

We conclude this subsection by noting that on each of the four days studied we can account for nearly 100% of the power trapped in TMX. We are cognizant of the uncertainties in our data and our analysis. However, even within these uncertainties it is clear that the dominant power loss mechanisms in TMX are known—axial particle loss and hot-ion charge exchange—and, therefore, that much of the power balance in TMX can be explained in terms of a simple, classical model which includes these phenomena.

7.3 DETAILED ANALYSIS

We now present a detailed analysis of the power flow through TMX based upon data obtained during experimentation on September 24,

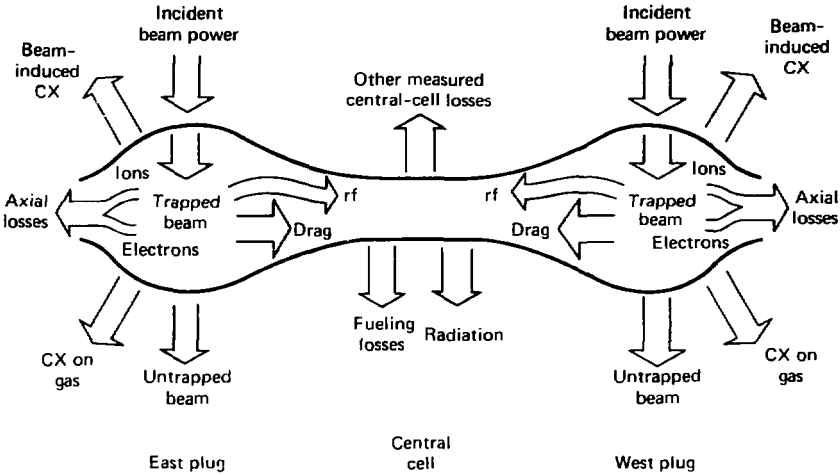

FIG. 7-2. Schematic of power flow in TMX.

1980. The experiment was particularly carefully monitored and controlled on this date so that we could obtain the clearest possible picture of the plasma equilibrium. (This equilibrium is characterized by the plasma parameters presented in Table 7-5.) This data also represents one of our most complete data sets on the TMX plasma. Therefore, we can use the data from this date to provide as complete a test as possible of our theoretical models of the power flow in a tandem mirror.

On this date we balanced the neutral-beam current injected into the plugs of TMX (referred to by their geographical location as east and west). A total of 3.4 MW of neutral beam power was injected into the plugs (1.8 MW east and 1.6 MW west). Of this, a total of 910 kW (390 kW east and 520 kW west) was stopped in the plug(s) by the process of charge exchange and ionization. The details of the flow of that power through TMX are shown schematically in Fig. 7-3 through Fig. 7-8.

We have organized our analysis of the power flow in TMX by region and particle type. Thus, we consider four groups of particles: plug ions, plug electrons, central-cell ions, and central-cell electrons. In addition, we have calculated the energy inputs and losses for each plug (east and west) separately. We do this because the density, total plasma volume, and ion temperature are distinctly different for the two plugs. The reason(s) for these differences are not well understood at this time, but may be related to the relative orientation between the plasma fan entering the central cell and the neutral beams in the two plugs (Appendix E).

In Table 7-5 we present the peak value (on axis) for the plasma parameters typical of the September 24, 1980, running. These values came from time averaging the measured values during the equilibrium phase of the shot and then by averaging over a total of 29 data shots. In Table 7-6, we present analytic fits to the measured profiles of the plasma parameters. These values were used to calculate the power balance presented in this section.

7.3.1 Plug Ions

The neutral beams were the sole source of energy into the equilibrium plasma. On September 24, 1980, the beam currents to the plugs were balanced at I_b = 150 Atom Amperes equivalent per plug. Using a neutral-beam trapping code developed by Turner and Kaiser[5] we determined

TABLE 7-3. Calculated values for power balance. All values in kW.

Term	Region	9/26/79	9/28/79	7/18/80	9/24/80
Incident beam power	EP[a]	2000	1300	2240	1780
	WP[b]	2000	1500	1720	1650
Trapped beam power	EP	450	240	600	390
	WP	720	420	280	520
Untrapped beam power	EP	1550	1060	1640	1390
	WP	1280	1080	1440	1130
Beam-induced charge exchange	EP	380	200	390	310
	WP	320	180	120	180
Charge exchange on gas	EP	80	60	70	80
	WP	80	80	80	60
Axial losses thru plug	EP	100	100	40	75
	WP	110	70	70	70
rf heating of central-cell ions	EP	50	–	–	20
	WP	50	No measurement	No measurement	15
Electron drag on plug ions	EP	70	15	100	110
	WP	140	30	40	130
Fueling-induced losses	Central cell	30	30	30	50
Total impurity radiation losses	Primarily central cell	40	20	20	30
Other measured losses	Central cell	70	No measurement	40	50

[a]East plug.
[b]West plug

the fraction of the neutral beam which was stopped by ionization (both electron and ion impact) and by charge exchange (Table 7-7).

In TMX the principal targets for the neutral beams were the plug ions and electrons. On the average charge exchange between a neutral beam particle and a plug ion resulted in a net energy input equal to (E_b – $\bar{W}$) where E_b was the mean neutral-beam injection energy and $\bar{W}$ was the mean plug-ion energy. Since charge exchange events were roughly 2.5 times more probable than ionization for the TMX plug parameters, this process was very important to the power balance.

TABLE 7-4. Comparison of end-Loss power measurements.

	2XIIB	TMX
Power onto calorimeter (Watts/cm^2)	680	250
Ion-end-loss power from gridded analyzer (Watts/cm^2)	100	230
Ratio of ion-end-loss power to total end loss power	0.15	0.9

As anticipated, the dominant power loss for the plug ions was Coulomb drag with the plug electrons. There are, however, several other important loss mechanisms. These are rf heating of the central-cell ions (see central-cell ion power balance), rf heating of the end-loss ions (Section 11), and charge exchange loss on the cold background gas.

TABLE 7-5. Plasma parameters—peak value on axis.

Parameter	East plug	Location central cell	West plug
Density, 10^{13} cm^{-3}	1.3	0.27	1.7
Electron temperature, eV	87	49	77[a]
Ion energy, keV	13.1	0.06	5.6
Plasma potential, volts	540	325	480
End-loss current, A/cm^2 (at plug midplane)	0.18	–	0.21
End-loss ion energy, keV (at end wall)	1.3	–	0.8

[a]Estimated according to $\phi_{plug}/T_{e,plug}$ = constant.

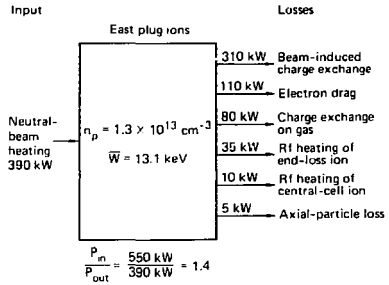

FIG. 7-3. East plug ion power balance.

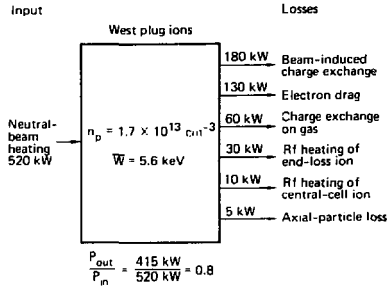

FIG. 7-4. West plug ion power balance.

As noted earlier, we have begun to model the power loss from the plug plasma due to the directed neutral gas flux from the neutral beam neutralizer cells. Poulsen[6] estimates that this gas flux is equivalent to approximately 1 to 2 mA/cm^2 per beam of neutral, diatomic deuterium on the surface of the plug plasma. Without the benefit of a halo of cool plasma to protect the hot plug ions, this flux is sufficient to cause the rapid loss of the plug ions. We are presently using a radial Fokker-Planck code (Appendix A) and a neutral-gas fueling code to learn more about the nature of the cool plasma halo and the equilibrium power loss by the plug ions and electrons. Preliminary results indicate that the plug ion power loss by this mechanism was 60 to 80 kW per plug on this date.

We can estimate the power lost by this process by examining the change in the signal detected by the secondary emission detectors (SED) in the plugs when the neutral beams are turned off. While the neutral beams are on, the SED signal is proportional to the sum of two terms: the loss of plug ions by charge exchange with the energetic beam neutrals (a term we can calculate from the beam trapping code) and the loss of plug ions by charge exchange of the plug ions with background gas. However, soon after the neutral beams are turned off, the remaining SED signal is proportional to only the current from the beam attenuation diagnostic beam and the charge exchange on the background gas. We can, therefore, obtain an estimate of the plug-ion power lost by this mechanism by comparing the SED signals before and after beam turnoff. When we perform this analysis for the 9/24/80 data we obtain P_{cx} (east) = 40 kW and P_{cx} (west) = 30 kW in factor two agreement with the predictions of the Fokker-Planck code.

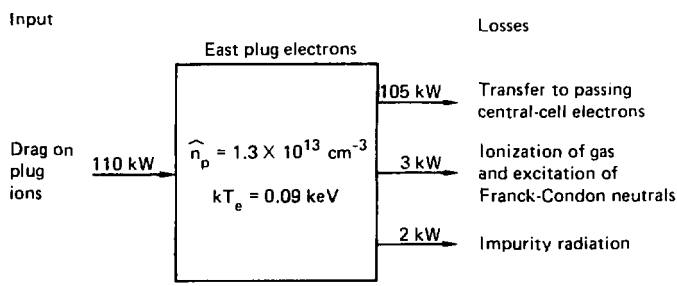

FIG. 7-5. East plug electron power balance.

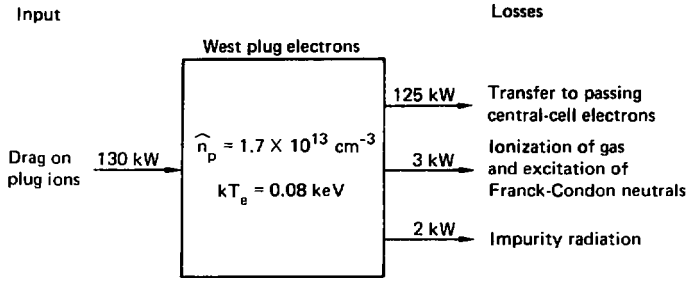

FIG. 7-6. West plug electron power balance.

Based on the analysis as summarized in Fig. 7-3 and Fig. 7-4, we obtained an approximate power balance for the ions in each end cell.

7.3.2 Plug Electrons

The plug electrons gain energy by the process of Coulomb drag on the plug ions. Impurity radiation (Sec. 13) and ionization of cold gas at the plasma boundary are small power losses (Fig. 7-5 and 7-6). Nearly all of the drag power should, therefore, be transferred to the passing electrons from the central cell. Using the formalism of Cohen, et al.,[7] we can calculate the power per unit volume being exchanged between the two classes of electrons at the center of the plug midplane. For the east-plug electrons (T_{ep} = 87 eV) the power transferred to the passing central-cell electrons (T_{ec} = 49 eV) is P_E(ep - ec) = 23 W/cm^3. This is more than twice the power which is being input to the plug electrons at this location: P_D = 10 W/cm^3. A similar calculation for the west plug gives P_W (ep - ec) = 20 W/cm^3 while P_D = 9 W/cm^3. It appears therefore, that the electron axial-energy transport is less than expected.

One possible explanation for this phenomena is a thermal barrier to the electron power flow. We

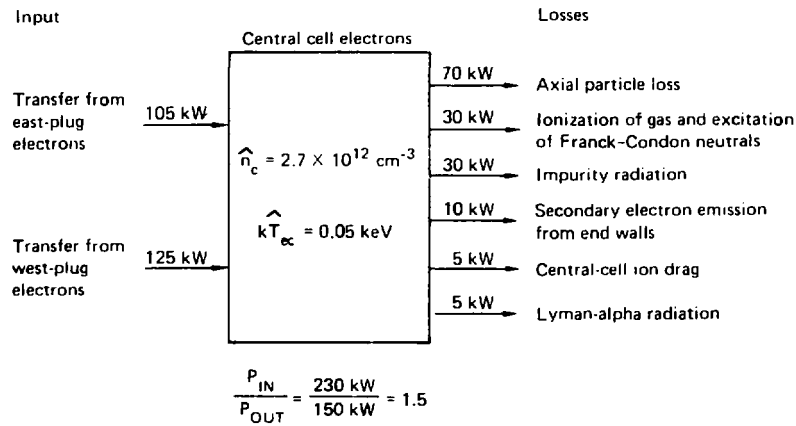

FIG. 7-7. Central-cell electron power balance.

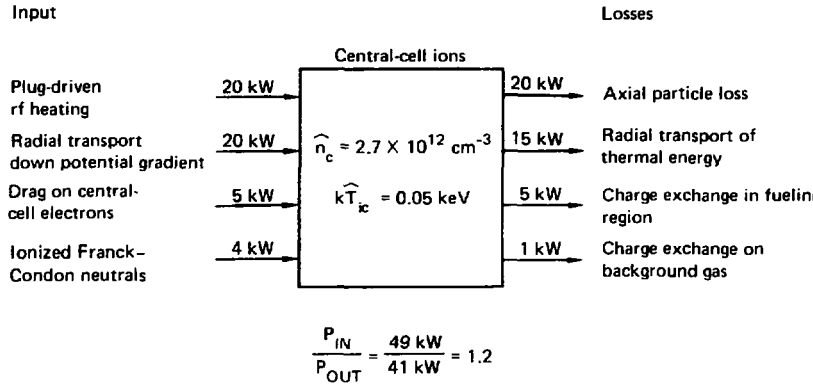

FIG. 7-8. Central-cell ion power balance.

can use Cohen's formalism to determine the plasma density in a thermal barrier region which is consistent with the measured plasma temperatures and densities. Doing so we find that $n_b = 1$ to 2×10^{12} cm^{-3}, i.e., $n_b/n_i = 0.3$ to 0.5 would be required to balance the plug-electron power gain (P_{ID}) and loss [P(ep ec)].

To determine if a thermal barrier existed in TMX, we made several measurements of the axial profile of the plasma density on this date (Sec. 3). Our measurements did not reveal the presence of a depression in the axial density profile, however, a 50% density depression may have been difficult to detect or at a location not measured.

We believe that such an axial density depression could be caused by the heating of the central-cell ions by plug-driven ion cyclotron fluctuations. Rognlien and Matsuda[1] have shown that when the fluctuating electric field in the resonance region exceeds a critical value the central-cell ion velocity space distribution is significantly distorted. This distortion reflects the fact that the ions are being preferentially heated in the perpendicular direction at B(z) = 10 kG. This can cause a density depression of factor 2 to occur at B(z) = 20 kG. For the September 24, 1980 parameters, the critical field is calculated to be 10 V/cm. Our interpretation of probe measurements indicates that the fluctuating electric field was approximately 20 V/cm, twice the critical value. Under these circumstances it is possible that the heating of the central-cell ions by the plug-driven fluctuations resulted in a thermal barrier between the plugs and the central cell.

Analysis of similar data on other dates, e.g., 9/28/79, shows that the reduced thermal conductivity appears to be present even though the rf fluctuation level was low. We believe, therefore, that the plug-driven ion cyclotron fluctuations may have caused the thermal barrier effects seen on

TABLE 7-6. Profiles of plasma parameters.

East plug density

$$n(r,z) = 1.3 \times 10^{13}\left[1 - \left(\frac{r}{12.2}\right)^2\right]^{1/2} \exp - \left(\frac{z}{13}\right)^2$$

West plug density

$$n(r,z) = 1.7 \times 10^{13}\left[1 - \left(\frac{r}{12.2}\right)^2\right]^{1/2} \exp - \left(\frac{z}{16}\right)^2$$

Central-cell density

$$n(r) = 3.5 \times 10^{12}\left[0.77 + 0.91\left(\frac{r}{38.6}\right)^2\right]\left[1 - \left(\frac{r}{38.6}\right)^2\right]^{1.2}$$

East-plug electron temperature

$$T_e(r) = 87\left[1 - \left(\frac{r}{12.2}\right)^2\right]$$

TABLE 7-7. Parameters for plug ion power balance.

Process plug	East	West
Incident beam current, A	150	150
Average accelerating voltage, kV	16.5	15.5
Mean neutral energy, kV	11.7	11.0
Ionization fraction	0.062	0.095
Charge-exchange fraction	0.16	0.22
Power input by ionization, kW	110	160
Total power input by charge exchange, kW	280	360
Net power input by charge exchange, kW	-30	180
Electron drag power, kW	110	130
Power lost by charge exchange on background gas, kW[a]	80	60
rf heating of central-cell ions, kW	10	10
rf heating of end-loss current, kW	35	30
Axial loss of plug ions	5	5

[a]From Fokker-Planck and gas fueling codes

9-24-80. However, there must also be other mechanisms, as yet undetermined, which account for the apparently large differences between the plug and central-cell electron temperatures which were detected on other dates.

7.3.3 Central-Cell Electrons

Even in the presence of reduced thermal conductivity, almost all of the power transferred by Coulomb drag to the plug electrons should subsequently be transferred to the central-cell electrons. In a classical, simple tandem mirror machine some of this energy would be transferred to the central-cell ions by drag. However, for much of the TMX data, T_{e_c} is nearly equal to T_{e_p}. This was true on September 24, 1980. We calculate that very little power ($\lesssim$5 kW) was exchanged between the central cell ions and electrons by the process of drag.

There is a second mechanism by which electron energy can be transferred to the central-cell ions. As the ions drift radially across the magnetic field they fall down the radial gradient of the central-cell plasma potential and, thereby, gain energy. This energy comes (indirectly) from the central-cell electrons which created the potential hill. We estimate the power transferred by this mechanism to be of order 15 kW to 20 kW. (See the following subsection on the central-cell ions.)

Ionization and heating of the neutral gas which fuels the central cell causes 30 kW of electron power loss. The emission of Lyman alpha radiation by excited neutrals due to the gas fueling leads to another 5 kW of power loss. Impurity radiation (Sec. 13) results in the loss of an additional 30 kW of electron power.

In addition to the power losses from the electrons associated with impurities and fueling, the electrons which escape axially along the field lines cause the loss of 70 kW of power. The electron and the ion end losses which bombard the end walls give rise to the emission of secondary electrons from the end walls. These secondary electrons cause an additional power loss from the central cell electrons.[8] For the September 24, 1980, parameters we estimate this power loss to be of order 10 kW.

Within the limits of our present understanding of the central-cell electron physics we can account for approximately 150 kW of electron power losses. Even within the uncertainties in the measurements it appears that 50 kW to 100 kW of the power input to the electrons is not accounted for by these loss mechanisms. We will return to this point when we examine other measured central-cell losses.

7.3.4 Central-Cell Ions

Since the central cell ion and electron temperatures are nearly equal, drag is neither a significant power input nor loss for the central-cell ions. We estimate that the ions gain approximately 5 kW of power by drag on the electrons. Most of this is acquired on the edge of the plasma where we believe that $T_{i_c} < T_{i_p}$.

An important power input to the ions comes from the plug-driven ion cyclotron fluctuations.[1] From measurements of the plasma fluctuations in the plugs on this date we estimate that the fluctuating electric field in the central cell was 20 V/cm. According to Ref. 1 this electric field would result in an rf power input to the central-cell ions of 20 kW.

As noted in the power balance for the central-cell electrons, radial transport of the central-cell ions can also be a power input (Sec. 9). We estimate the ion cross-field energy transport due to non-ambipolar particle transport by analyzing the

measured non-ambipolar particle fluxes. In doing so, we calculate the energy flux associated with the radial transport of an ion from the point where it is born at r_1 with thermal energy kT_1 and potential energy $e\phi_1$ to the point where it is lost at r_2 with thermal energy kT_1 and potential energy $e\phi_2$. In transporting from r_1 to r_2 the ion has fallen down a radial potential hill of $(\phi_1 - \phi_2)/(r_2 - r_1)$. The ion is assumed to move radially with a velocity given by Γ/n where n and Γ are the local values of the plasma density and radial particle flux, respectively. The ion is assumed to drift radially for an axial confinement time given by $\tau = neL/j$ where e is the ion charge, L is the length of the central cell, and j is the local end-loss current density. In this manner we can obtain a rough estimate of the cross-field energy transport. Assuming a Gaussian ion-energy profile with T_{ii} (r = 0) = 60 eV and using the measured plasma parameters (Secs. 3 and 5) we find that the ions gained approximately 10 kW to 20 kW of energy as they fell down the potential hill and lost 10 kW to 15 kW due to cross-field transport of ion thermal energy.

The energy transported across field lines in this manner is eventually lost either by axial loss as the ions escape over the confining potential hill or as charge exchange with neutral gas at the edge of the plasma. At the edge of the plasma the neutral-gas density is high enough that few of the ions reach the plasma limiter with significant energy. It is this last fact that makes the comparison of the measured power deposited on the calorimeters in the gas fueling region of the central cell (between the limiters) to the power loss due to charge exchange of plasma ions and escaping Franck-Condon neutrals (predicted by the neutral-gas fueling code) especially informative. The measured power losses in this region were P_{cal} = 15 kW to 20 kW. The total radial power loss in this region predicted by the fueling code was 9 kW. In addition to this, there were 5 kW of L_α radiation and approximately 8 kW of impurity radiation emitted within the fueling region viewed by the calorimeters. The total anticipated power loss in this region, therefore, was 20 kW to 25 kW. The fact that this value is very nearly equal to the radial power loss detected in the fueling region allows us to conclude that we do not have ambipolar particle losses (and, therefore, energy loss) in the central cell which was significantly greater than the non-ambipolar losses. Rapid ambipolar losses would lead to more charge-exchange power loss at the edge of the plasma which would have been detected by the calorimeters.

7.3.5 Other Measured Central-Cell Losses

In addition to the calorimeters in the fueling region, there were two other calorimeters mounted in the central cell outside of this region. The mean value of the power delivered to each of the four calorimeters, averaged over several shots, is shown in Fig. 7-9. The error bars represent the standard deviation about the mean. Inside the gas fueling region between the ICRH limiters (z = +54 cm to z = −54 cm) the radial power loss appears to be uniform as a function of z and the shot-to-shot variations in the power loss are small. The calorimeter signal in this region is equivalent to a radial power loss of 0.4 W cm^{-2} − 0.6 W/cm^2 at a radius of 53 cm. The total power loss in the fueling region between the ICRH limiters is, therefore, 15 kW to 20 kW. As reported earlier in this section this power loss is consistent with the radial power loss associated with the neutral gas fueling in this region plus the power loss due to radial particle transport and impurity radiations.

Data also came from two central-cell calorimeters outside of the fueling region (C and D). As indicated by the error bars, the shot-to-shot variations in the power detected on these calorimeters were large. Over the eight shots on which data from these calorimeters was recorded, the power received on calorimeter C was 0 W cm^{-2} on 3 shots and ranged between 1.2 W cm^{-2} and 3.6 W cm^{-2} on the other 5 shots. The data from

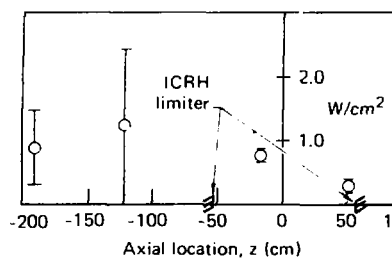

FIG. 7-9. Central-cell calorimeter measurements.

calorimeter D was similar. Since the central-cell density, the radial-density profile, the electron temperature and the total plasma diamagnetism varied very little between those shots during which calorimeters C and D recorded large power losses and those shots during which these calorimeters received zero power loss, we concluded that the signals on calorimeters C and D were due to localized power losses or power losses after the end cells were turned off (MHD activity is possible in this region when the end-cells are not present) and are not representative of a plasma loss over a large fraction of the central cell during steady state operation. The total power loss associated with the signals from these calorimeters is therefore highly uncertain. We estimate that this value could be as small as 1 kW or as large as 100 kW on those shots during which these calorimeters received signals.

In determining the quantity labeled "Other measured central-cell losses" in Fig. 7-2 and Table 7-3, we first calculated the total power loss measured by the calorimeter array. We then subtracted from this value known sources of radial loss. These sources were charge exchange of ions, loss of Franck-Condon neutrals created in the fueling process, Lyman alpha radiation and impurity radiation. The remaining power is representative of ion radial transport and anomalous radial losses. On this date this category of power loss (i.e., other central-cell losses) represents 10 ± 10% of the net power input to TMX by the neutral beams.

7.4 CONCLUSIONS

We have calculated a power balance for TMX based on the measured plasma parameters which accounts for 70% to 100% of the net input power. An understanding of the physics involved in the power balance and power flow in TMX points out the importance of the following conclusions:

- As theoretically predicted, the ions escaping from the central cell carried almost all of the axial loss power to the end walls.
- Power loss associated with the emission of secondary electrons from the end walls was small.
- The ion cyclotron fluctuation heating of the central-cell ions was an important and often dominant power input to the central-cell ions.
- Reduced electron axial energy transport was necessary to explain the measured differences between the plug and central-cell electron temperatures.
- Power loss associated with the charge exchange of plug ions with background gas was an important power loss mechanism. A cool plasma halo was necessary to explain our ability to sustain the end-cell plasmas in the presence of these losses.

7.5 WORK IN PROGRESS

We are continuing to advance our understanding of the power balance in TMX and to extrapolate our results to the TMX Upgrade experiment. Special emphasis is being placed upon the following subjects:

- We are making detailed numerical studies of the interaction between the background gas and the end-cell plasma so that we can more accurately estimate the power lost by this mechanism and so that we can learn more about the source and nature of the plasma "halo" which protected the end-cell plasmas.
- In order to understand the reduced electron axial energy transport in TMX and the low power loss due to secondary electron emission from the end walls, we are continuing to improve our models of the interaction between the electrons in the three regions of a simple tandem mirror: the central cell, the end cell, and the end wall.
- In this section we have assumed that the end-loss ions were heated from energies of tens or hundreds of eV to nearly a keV by rf in the plugs. We are examining other relevant data to determine the validity of this assumption.

8. Plasma Beta Measurements on the Tandem Mirror Experiment (TMX)

8.1 SUMMARY

The Tandem Mirror Experiment (TMX) results have demonstrated the existence of a scalable magnetic field geometry which maintained macroscopic stability at finite beta. In a first set of experiments, the end-plug beta (β_p) was increased and the resulting central-cell beta (β_c) measured. Over the range of the experiment, the central-cell beta continued to increase as plug beta was increased. These experiments always operated with central-cell beta values (maximum 7%) that were theoretically magnetohydrodynamically (MHD) stable. In a second series of experiments the central-cell magnetic field (B_c) was changed from 0.1 to 0.2 T. The ratio of end-plug to central-cell beta was approximately constant and independent of central magnetic field strength. This observation is in contrast to the results of the TAMRAC code which predicts that $\beta_c \sim \beta_p / B_c^{3/2}$. While we can't be certain, we conclude that it is unlikely that this unexpected result can be explained as MHD-stability connected. Rather, we believe it to be an artifact of the plugs' microstability requirements, although we have not modeled this behavior successfully.

Auxiliary heating of the central-cell plasma produced a short high beta plasma. That betas up to 40% were produced is attributed to finite Larmor-orbit stabilizing effects and the localization of the high beta plasma near the central-cell mid plane where the vacuum field curvature is small. We measured an increase in electron temperature

8.2 INTRODUCTION

In a tandem mirror two distinct sources of guiding-center drift motion can drive MHD instabilities.[1] For TMX the more serious of these is negative field-line curvature (bad curvature) which unavoidably occurs in certain localized regions of the machine. The second source not believed to be of comparable importance in TMX is the radial gradient of the ambipolar potential which is responsible for drifts of the E × B variety. The end plugs of TMX are designed to have absolute minimum B in the region occupied by the high pressure plasmas, however the central cell has sufficient bad curvature to force the vacuum average curvature over the entire system to be bad also. A necessary condition for MHD interchange stability is that the high-pressure plugs stabilize the central cell in a pressure-weighted average.

The high-beta [$\beta = 8\pi n (T_\perp + T_\parallel) B^{-2}$] performance of tandem mirrors is believed to be determined by ballooning interchange modes that localize in regions of bad curvature. theory predicts a maximum value of central-cell beta which is insensitive to the plug beta. The exact values of the central-cell limit (and the value of β_p at the low-beta flute interchange limit) are dependent on finite Larmor radius (FLR) effects which are only now being included in the theory.

One of the three main physics objectives of TMX was to demonstrate a scalable magnetic geometry that was MHD stable at high central-cell beta. As described below, part of the experimental program was to explore the MHD stability boundary. The shape of the MHD stability boundary is sketched in Fig. 8-1 for a case where FLR effects have been ignored. The custom of plotting β_p vs β_c rather than vice versa is an artifact of the manner in which the stability boundary is calculated.

The stability boundary can best be explored by increasing the central-cell beta. Three approaches present themselves for accomplishing this:

- Increase plug beta which is observed to increase central-cell beta
- Decrease central-cell magnetic field
- Heat central cell directly

These approaches naturally divide into experiments without and experiments with auxiliary heating of the central cell. In the following sections after a brief discussion of experimental method, we shall examine the results of these two groups of experiments.

8.3 EXPERIMENTAL METHOD

We are interested in comparing the peak values of plasma beta in the central cell with peak

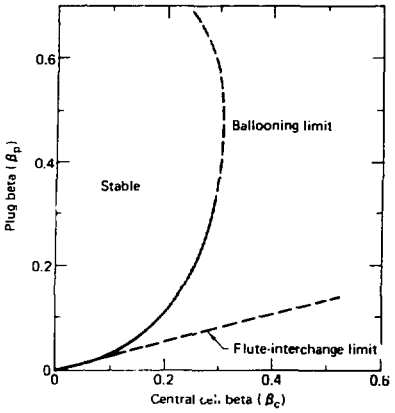

FIG 3-1. A tandem mirror MHD stability diagram for a case in which finite Larmor radius effects have been ignored.

values in the plugs. The mean plasma beta ($\bar{\beta}$) can be obtained by combining a measurement of the plasma perpendicular energy content with its volume (V) according to

$$\bar{\beta} = 8\pi \frac{W_\perp}{VB^2} \quad .$$

The energy content of the plasma can be obtained from a measurement of the plasma *diamagnetism*. An array of *diamagnetic* loops, described in the diagnostic section, measures the magnetic moments of the plugs and the magnetic moment/unit length of the central cell. The plasma energy component perpendicular to the magnetic field is then given by

$$W_\perp = 10^{-8} M_p B_p \text{ (J)}$$

for the plugs and

$$W_\perp = 10^{-8} m_c B_c \text{ (J/cm)}$$

for the central cell. Here M_p is the magnetic moment of the plug in A·cm^2, m_c is the magnetic moment/cm for the central cell in A·cm^2/cm, and B_c is the magnetic field in gauss.

We estimate the peak plasma beta and perpendicular energy/ion pair in the central cell and plug by including the effects of density and temperature profiles.

For the plug plasmas, which are quite similar to those in 2XIIB, we assume that the diamagnetic signal is due to ions only and that the ion energy is independent of radius and axis (z). Then for low beta (<50%) and assuming Gaussian density profiles in radius and z we find that the peak beta value of the plug is given by

$$\beta_p = \frac{0.45\, M_p}{L_p\, B_p\, r_p^2} \quad . \qquad (1)$$

where L_p and r_p are the 1/e half-length and radius of the plug plasma. For the central cell we assume that the ions and electrons both have a Gaussian profile with temperature scale length r_w and density scale length r_c, and then calculate

$$\beta_c = \frac{0.8\left[1 + (r_c/r_w)^2\right] m_c}{B_c\, r_c^2} \quad . \qquad (2)$$

We do not have a measurement of r_w for TMX. Thomson scattering measurements of the radial variation of the plug electron temperature yield a scale length almost identical to the density scale length, and we assume that the central-cell electron temperature has the same radial variation. Much of the central-cell energy is carried by ions, however, and since these ions are heated mainly by fluctuating fields whose radial variation is not known, the radial variation of their temperature is also not known. For the purposes of data reduction we have assumed that $r_w = r_c$, realizing that this introduces a possible error in our determination of β_c.

8.4 EXPERIMENTS WITHOUT AUXILIARY CENTRAL-CELL HEATING

In the absence of direct heating of the central plasma, the only energy sources for the central cell are the neutral-beam heated plugs. Energy transfers

to the central cell through the electrons by classical processes and through ion cyclotron resonance heating of the central ions by rf fields generated by plug instabilities. In a series of experiments, we have studied the variation of the central-cell beta as we have varied the plug beta by varying the neutral-beam current injected into the plugs.

Figures 8-2 and 8-3 summarize the general results obtained for a scan of the plug beam current. These results show that we succeeded in producing plasmas with finite beta (over 6% in the central cell) in the TMX geometry, and that over the range of the experiment there was no sign of saturation.

The TAMRAC computer code was developed to predict the density and temperatures in tandem mirror devices.[2] TAMRAC is a (zero-dimensional) coupled-rate equation code that includes end-loss expressions for electrostatically confined species, with an electron-drag model for confinement of the plug ions. This code also includes, among other things, the effects of sources, charge exchange, temperature equilibration between species, degradation of plug confinement by the drift-cyclotron loss-cone (DCLC) mode, etc. It does not include radial diffusion, nor does it correct for the radial profile of the central-cell gas source and does not include the effects of plug fluctuations on central-cell confinement. The code calculates time-dependent energy and density (and thus β) for an arbitrary number of species, as well as self-consistent electron and ion confining potentials.

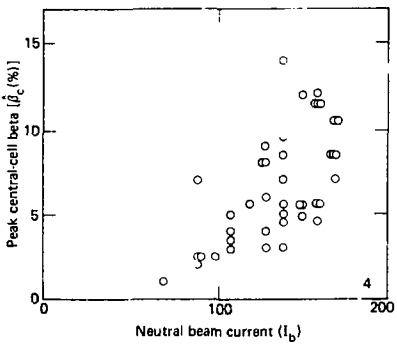

FIG. 8-2. TMX plug beta as a function of injected neutral beam current.

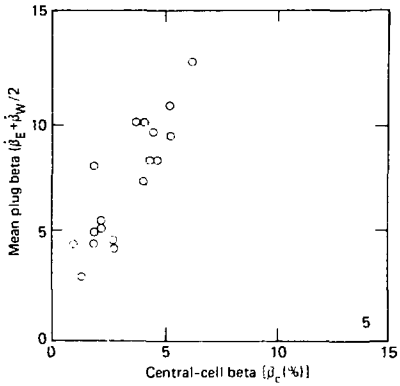

FIG. 8-3. TMX plug beta vs central-cell beta (beam scan of 9/26/79).

For the case of stable TMX plugs TAMRAC predicts for a given plug beta that the central-cell beta should vary roughly as $B_c^{-3/2}$.

If this model holds, for a fixed plug beta we would expect to vary the central-cell beta over a range of values by changing the central-cell magnetic field. As we lower B_c we should eventually encounter the MHD stability boundary; below this value of B_c central-cell beta would be determined by MHD stability.

Figure 8-4 shows the experimental data for a series of shots during which the central-cell magnetic field was varied. Also plotted on the figure is the MHD stability boundary for the 1-kG central-field case (calculated ignoring FLR effects and $\mathbf{E} \times \mathbf{B}$ contributions to the drive). The dashed lines indicate the regions of operation predicted by the TAMRAC code for the three central-field values. There is no indication of the sensitivity to magnetic field predicted by the TAMRAC code.

This lack of sensitivity of central-cell beta to the central-cell magnetic field was unexpected and is unexplained. We pursued two hypotheses:

- The central-cell plasma is MHD limited.
- The behavior is an artifact of plug microstability requirements.

As described below, we conclude that the behavior is not MHD related but rather an artifact of plug microstability.

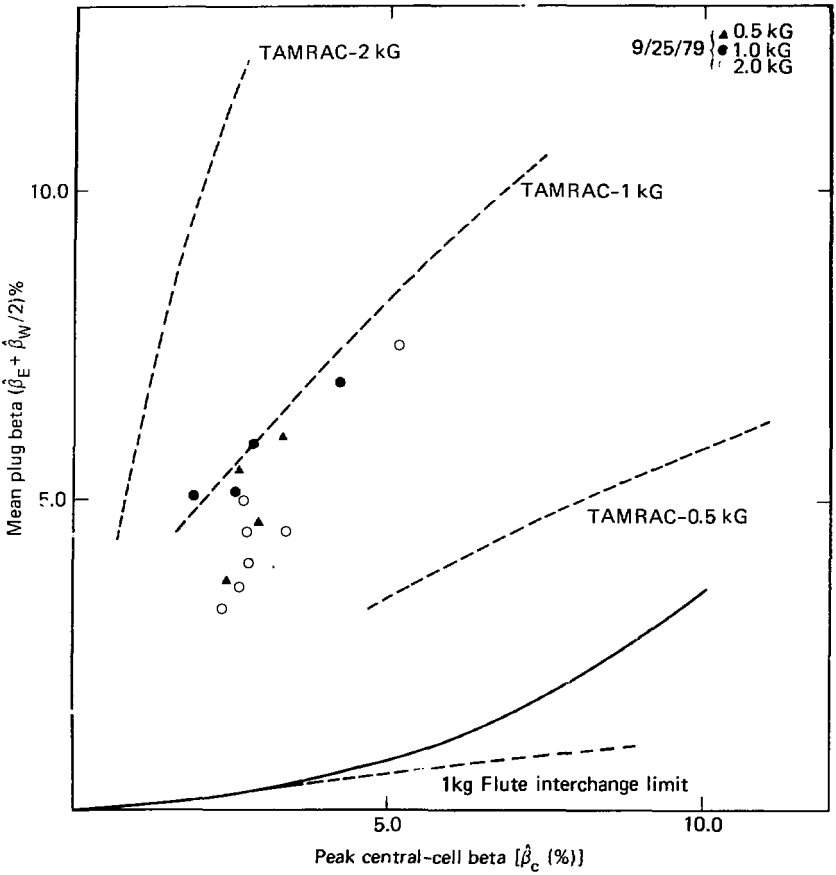

FIG. 8-4. TMX plug beta vs central cell beta for three values of the central-cell field. Also plotted are the 1 kG stability boundary and the TAMRAC predictions for the central-cell fields.

8.4.1 The Central-Cell Plasma is not MHD Limited

The value of β_p/β_c on the MHD stability boundary depends on the relative pressure weighting of good and bad curvature regions in the central cell and transition regions. Because the bad curvature regions are mainly in the high-field transition regions where they are not very sensitive to changes in the field, the stability boundary is not a strong function of central-cell field. Thus the observed lack of sensitivity of the experimental data to the central-cell magnetic field value is consistent with central-cell beta's being MHD limited.

Systematic Errors in Reduction of Data. If we assume that the scatter in the experimental points in Fig. 8-4 is a measure of the random experimental error in reducing the data (certainly a very pessimistic assumption since in actuality the neutral beam current varied somewhat from shot to shot), then we must consider whether there can be systematic errors in the reduction of the data or modifications to the theory that can reconcile the more-than-a-factor-of-ten difference between the observed values of β_p/β_c and the stability boundary values.

If we combine Eqs. (1) and (2) we obtain

$$\frac{\beta_p}{\beta_c} = 0.5\sigma \left(\frac{B_c r_c^2}{B_p r_p^2}\right) \frac{1}{L_p[1 + (r_c/r_w)^2]} \frac{M_p}{m_c} \quad .$$

Generally, we have observed good flux mapping of the plasma density profiles between the central cell and the end plugs, i.e.,

$$B_c r_c^2 \approx B_p r_p^2 \quad ,$$

thus

$$\frac{\beta_p}{\beta_c} = \frac{0.5\sigma}{L_p[1 + (r_c/r_w)^2]} \frac{M_p}{m_c} \quad .$$

We calibrated the loop array by moving a small pulse coil of known magnetic moment along the axis of the machine. We estimate the errors in the calibration to be of the order of ±10%. The main source of systematic error therefore lies in the determinations of the plug plasma length of the plug plasma and the central-cell temperature scale length. The length of the hot-ion plasma may be masked by the presence of cold plasma in the wings; consequently, we probably overestimate the plasma length. Correcting for this effect would, then, increase β_p and move the data points farther away from the stability boundary. The assumption of $r_c = r_w$ which is used to reduce the data is at best an educated guess since we have no direct measurement of the ion and electron temperature gradient. For the data discussed in Sec. 4, the radial variation of the central-cell potential was consistent with $r_p = r_w$ for the electrons, but for the data reported here the electron contribution to the central-cell diamagnetism is probably a small part of the total. We base this statement on the observations after central-cell Thomson scattering was installed that central-cell electron temperature was usually $T_e <$ 60 eV on axis. If we assume this same order of electron temperature value for this data, then the central-cell diamagnetic measurements combined with density profile measurements would yield values for the peak central-cell ion temperature in the range of $2T_e$ to $5T_e$ for $r_w = r_c$. Temperatures in this range show the importance of plasma fluctuations for the heating of central-cell ions. For the data points of Fig. 8-4 to lie on the stability boundary would require that β_c be increased by a factor of 4 or 5, which in turn would require that $r_w \approx 1/3\ r_c$ and that the peak perpendicular ion temperatures on the axis are as high as 1 keV. While we cannot rule this out completely it seems doubtful that the rf fluctuation mode structure could produce such a highly peaked radial distribution. We would expect the stabilizing effect of the addition of FLR effects to need an even higher value of β_c and perpendicular-ion temperature and a smaller value of r_w for the data to lie on the boundary.

We conclude that the errors and uncertainties in the reduction of the experimental data are not large enough alone to bring the data and theory into agreement.

Discrepancies Between Theory Assumptions and TMX Conditions. A number of assumptions and approximations are made in order to obtain the stability limit of Fig. 8-4:

Radial profiles. It is assumed that the plasma has the same radial variation of plasma pressure in the central cell and plug. This assumption, in conjunction with the long thin approximation for the plasma shape leads to a value for the stability boundary which is independent of the plasma radius. In the TMX plugs the pressure profile is dominated by the neutral beam heating while the central-cell profile in most cases is dominated by ion heating by rf fluctuations. Based on measurements on 2XIIB we assume that the radial variation of the plug ion temperature is small; therefore the plug pressure profile resembles the density profile. As discussed earlier, we assume that the central-cell temperature has the same scale length as the density and that therefore the central-cell pressure profile resembles the square of the density profile. This model implies a radial variation of $\beta_p/\beta_c \propto \exp[(r/r_w)^2]$ with the minimum value near

the axis. Thus in comparing the experimental values of β_p/β_c with the stability boundary, we are considering the most pessimistic case. Plasma on field lines at a distance from the axis will have values of $\beta_p/\beta_c > \hat{\beta}_p/\hat{\beta}_c$ and therefore will be more stable.

Mode number. The stability boundary is derived in the large azimuthal mode number limit which is believed to be the most unstable case in the absence of FLR effects. The introduction of FLR corrections tends to stabilize the high m-number modes with the result that the lower-order modes should be the most unstable. The theory at present cannot predict the stability boundary for low m-number modes, but it is assumed that it will not be any worse than the high m-number limit without FLR corrections.

E × B *rotation.* The additional drive due to **E** × **B** rotation is ignored. Estimates of its value in the original TMX proposal[3] indicated that it should be small compared to the curvature drive

Non-Maxwellian central-cell plasma. An important assumption is that the central-cell ions and electrons have a Maxwellian distribution. This means that the pressure is constant along a field line.

Although the data plotted in Fig. 8-4 is for beta perpendicular to the magnetic field, it is the total beta which enters into the stability integral. This difference is of no importance if the central-cell ions are Maxwellian (both the data and the limits being shifted by a factor of 2), however, there is both experimental evidence of, and theoretical reason for, the existence of an energetic non-Maxwellian group of central-cell ions with $T_{i\parallel} > T_{i\perp}$ in the center plane. For such a group the total β_c would be greater than $2\beta_\perp$, and this would result in a decrease in the slope of the experimental β_p vs β_c plot while the slope of the stability boundary may increase because the non-Maxwellian particle pressure may be greater in regions of bad curvature. The net result of this is to move the data points of Fig. 8-4 closer to the stability boundary.

a. *Experimental evidence.* Experimental evidence of the existence of a non-Maxwellian energetic central-cell component comes from the central-cell array of diamagnetic loops. The time-integrated loop signal is related to the plasma parameters by

$$V_K = \int V_K\, dt = \int_{-\infty}^{\infty} f_K(z)\, m(z)\, dz$$

where

$$m(z) = n(z)\left[\frac{T_{i\perp}(z) + T_e(z)}{B}\right] \pi r_c^2(z)$$

is the plasma magnetic moment per unit length, and $f_K(z)$ is the response function of loop K, located at z_K. Normalizing to the center plane value and assuming flux mapping of the plasma density profiles we obtain

$$\frac{m(z)}{m(o)} = \frac{n(z)}{n(o)} \frac{T_{i\perp}(z) + T_e(z)}{T_{i\perp}(o) + T_e(o)} \frac{B^2(o)}{B^2(z)}$$

For a Maxwellian central-cell plasma, density and temperature along a field line are constant, from which follows

$$\frac{m(z)}{m(o)} = \left[\frac{B(o)}{B(z)}\right]^2$$

and

$$V_K = m(o)\, B^2(o) \int_{-\infty}^{\infty} \frac{f(z)}{B(z)^2}\, dz \qquad (3)$$

The loop signals would be expected to maintain a constant ratio to each other determined by the magnetic field and the response functions.

That this conclusion is in disagreement with actual experience is illustrated by Fig. 8-5 where the signals from two shots are arranged side by side. Not only are the loop ratios different from the two shots but the ratio changes during the course of the shot. The fine scale structure appears to be real and may indicate fluctuations of either energetic particle density or angular distribution.

In Fig. 8-6 the experimental loop ratios from Fig. 8-5 are plotted versus the expected ratios for a Maxwellian distribution with time as a parameter. The expected ratios were

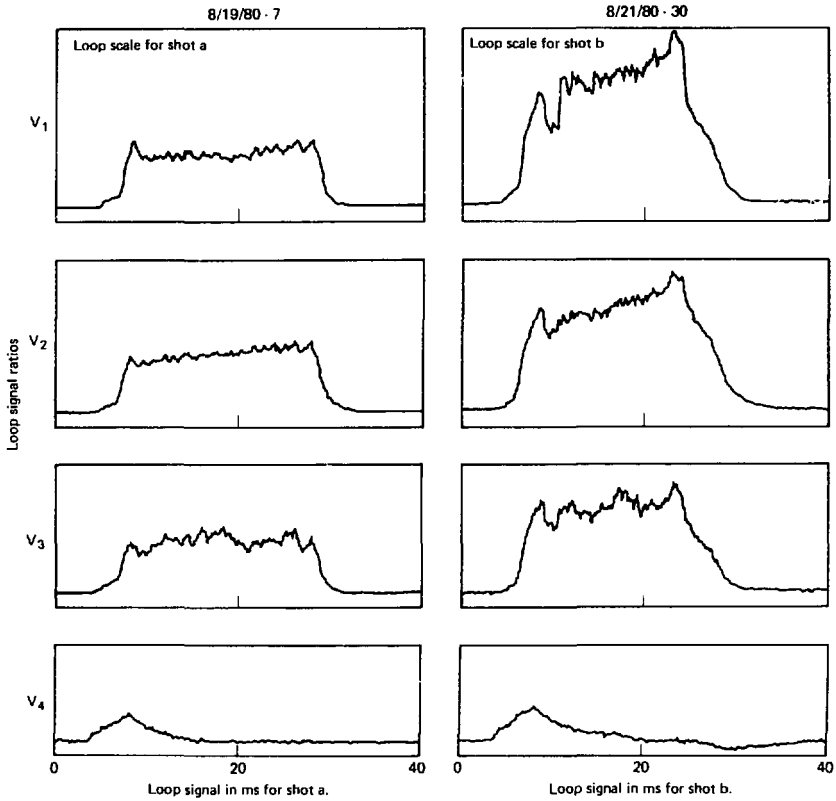

FIG. 8-5. Diamagnetic loop signals for two shots show ratio of loop signals are not constant.

calculated using Eq. (3) and the experimental loop response functions obtained during the loop calibration. The lines connect data points read out at the designated time, the circles indicate the expected experimental value for a Maxwellian distribution, and the loop positions and field values are also indicated on the figure. We conclude that there must be a significant non-Maxwellian component in the central-cell plasma.

b. *Theoretical reason.* The theory of Rognlien and Matsuda[4] which appears to explain TMX central-cell confinement quite well[5] is based on central-cell ion heating in a region where plug-generated ion-cyclotron waves are resonant with the fundamental of

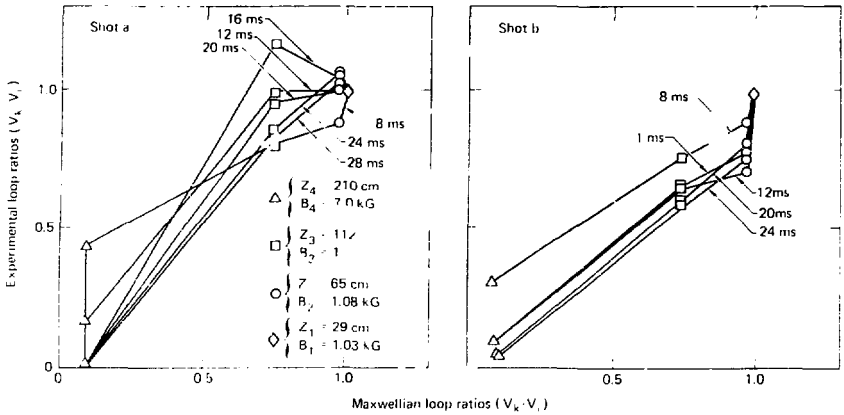

FIG. 8-6. Experimental loop ratio vs predicted values based on a Maxwellian distribution for the data of Fig. 8-5(a,b). Lines link data read out at indicated time, and circles indicate the expected experimental values for a Maxwellian distribution. The loop positions and field values are also indicated.

the local cyclotron frequency. For a value of fluctuating electric field and central-cell density consistent with TMX measurements Rognlein and Matsuda have calculated the axial profile of the central-cell density and the ion temperature perpendicular and parallel to the magnetic field. We calculate the ratio of their total beta to the total beta of a Maxwellian distribution with the same center plane perpendicular beta

$$\frac{\beta_{RM}(z)}{\beta_{Maxwellian}} = \frac{1}{2}\,\frac{n(z)}{n(o)}\,\frac{\left[T_{i\perp}(z) + T_{i\parallel} + 2\,T_e\right]}{\left[T_{i\perp}(o) + T_e\right]}$$

where T_e is the electron temperature (assumed Maxwellian). If we take T_e = 50 eV and use Rognlein and Matsuda's axial profiles, we obtain Fig. 8-7, the axial profile of β_{RM}/β_{Max}. A pressure distribution approximating that of Fig. 8-7 has been used in the interchange stability code to investigate whether the stability boundary would be affected appreciably.[6] The results showed that the interchange boundary value of β_p/β_c was increased a little over a factor of two higher than the Maxwellian value, and we concluded that the effect is not strong enough to explain the data of Fig. 8-4 as being MHD limited.

Based on our present understanding, it seems unlikely that the lack of sensitivity of central-cell beta to the central-cell magnetic field can be connected to MHD stability. There is one reservation

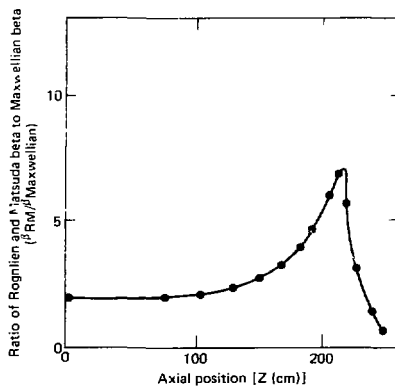

FIG. 8-7. Axial profile of the ratio of beta predicted by the Rognlien-Matsuda model to beta for a Maxwellian central-cell plasma.

to this conclusion: the observation of plasma structure rotating at the **E** × **B** velocity (see Sec. 6) which may be indicative of the effect of the **E** × **B** drive (which was disregarded in the theory) on the plasma stability.

8.4.2 Central-Cell Beta Dependence is an Artifact of Plug Microstability Requirements

An alternative explanation of the scaling of the data of Fig. 8-4 involved the assumption that the power transfer between the plug and central cell did not change appreciably when the central-cell field was changed. At first glance, this assumption seems reasonable since the plug parameters did not appear to be too different for the two cases. From this assumption it would follow that the global energy containment time scales as

$$\tau_E = \frac{W_c}{P_c} \propto W_c \propto m_c B_c \quad .$$

The data of Table 8-1 shows that m scales as $B_c^{0.3}$ and therefore

$$\tau_E \propto B_c^{1.3} \quad .$$

Thus if the central-cell power input remained constant, any dominant central-cell energy loss process that scales as $B_c^{-1.3}$ could explain the observed data.

In Table 8-1 we compare the plasma parameters for the 1 kG and 2 kG data of Fig. 8-4. Although the 0.5 kG beta values confirm the findings of the other field settings, the data for much of the other plasma parameters is either noisy or not available, and the central-cell plasma radius is very large, raising questions about wall interactions; consequently, we have concentrated on the data for the two higher field values.

Some light on the processes that are occurring is shed by examination of several characteristic lifetimes for the plasma. For this purpose we select three easily calculable energy lifetimes. They are the mean global plug energy lifetime defined by

$$\tau_{EP} = \frac{\Sigma W_p}{\Sigma P_b} \quad ,$$

the global machine energy lifetime, defined by

$$\tau_{EG} = \frac{\Sigma(W_p + W_c)}{\Sigma P_b} \quad ,$$

and axial machine energy lifetime, defined by

$$\tau_{EA} = \frac{\Sigma(W_p + W_{cc})}{\pi r_p^2 \cdot \Sigma J(\overline{W}_{EL} + 5\,T_{ec})} \quad ,$$

where $\overline{W}_{EL}$ is the average ion end loss energy, J is end loss current density on axis in the plug center plane, and $5\,T_{ec}$ approximates the energy carried out by electrons. We assume $T_{ec} \approx 60$ eV and use the values of Table 8-1 to obtain Table 8-2. We see from Table 8-2 that the plug energy containment decreased when the central-cell magnetic field was increased. The machine global and axial containment time remained virtually unchanged. Thus it appears that varying the central-cell field does not affect any of the machine energy loss processes but affects only the energy transfer from the plug to the central cell.

Since this energy transfer is mainly through ion heating by rf fluctuations, we conclude that the most probable explanation of the data of Fig. 8-4 is that the coupling between the plugs and central cell improves with increasing central-cell field. Initial attempts to model this behavior using a modification of the TAMBAR code (described in Sec. 3) have not been successful.

8.5 EXPERIMENTS WITH AUXILIARY CENTRAL-CELL HEATING

In an attempt to explore the TMX MHD stability boundary by increasing the central-cell beta, we investigated auxiliary central-cell heating by neutral-beam injection. In these experiments we injected three neutral beams ($\bar{E}_b \approx 11$ keV) at 90° to a 2 kG magnetic field in the central-cell midplane. The beams were aimed below the axis so that trapped ions had gyrocenters near the magnetic axis.

Large increases in the central-cell diamagnetic loop signal occurred when the beams were injected. Most of these experiments were carried out when only one central-cell loop was installed, so there was no direct measurement of the length of the beam-heated plasma; however, we argued from

TABLE 8-1. Comparison of plasma parameters for two values of central-cell magnetic field data of 9/25/79 with west plug density estimated from SED signal.

Parameter	0 kG	1 kG
CENTRAL CELL[a]		
$n\ell$ (10^{14} A·cm^2/cm)	1.55 ± 0.10	1.97 ± 0.08
W_{cc} (J)[b]	73 ± 5	186 ± 8
r_c (cm)	30 ± 1.6	22.6 ± 0.7
$n\ell_c$ (10^{14}/cm^2)[c]	2.55 ± 0.34	3.3 ± 0.14
$\hat{n}_c$ (10^{13}/cm^2)	0.48 ± 0.1	0.82 ± 0.06
$(\hat{T}_c + \hat{T}_e)$ (keV)	0.150 ± 0.014	0.386 ± 0.022
$\hat{\beta}_c$	0.029 ± 0.005	0.033 ± 0.003
rf (V_p to p)	40 ± 2	21 ± 1
$I_{E/W}$ (A/cm^2)	0.94 ± 0.13	1.28 ± 0.077
I_W (A/cm^2)	0.74 ± 0.07	0.84 ± 0.05
PLUGS		
T_{ep} (keV)	0.102 ± 0.011	0.105 ± 0.011
$n\ell$ (E) (10^{14}/cm^2)	3.1	2.6
$n\ell$ (W) (10^{14} cm^2)	3.0[d]	3.7
r_p (cm)[e]	9.5	10.0
$\hat{\beta}$	0.062	0.045
I_b E/W (A)	160/140	132/104
$\hat{W}_p$ (E) (keV)	9.9 ± 1.1	7.2 ± 0.5
W_p (W) (keV)	6.9 ± 0.5	4.5 ± 1.2
M_p E/W (10^6 A·cm^2)	2.5/1.7	1.8/1.6
W_p (E+W) (J)[f]	420	240
P_b (E+W) (kW)[g]	496 ± 69	509 ± 31
$\hat{n}$ (E/W) (10^{13}/cm^3)	1.9/1.8	1.4/2.1
rf (L^2) (V_p to p)	3.1 ± 0.1	1.5 ± 0.2

[a] We assume L_c = 314 cm
L_p = 18 cm.
[b] $W_c = 3/2 \times 10^{-8}$ m $B_c L_c$.
[c] $\hat{n}_{cc} = n\ell/\sqrt{\pi} r_c$.
[d] Inferred from SED signal.
[e] Assume flux conservation $\hat{\beta} = (\hat{\beta}_{East} + \hat{\beta}_{West})/2$.
[f] $W_p = \Sigma 10^{-8} M_p B$.
[g] $P_b = \Sigma[f_i E_b + f_{cx}(E_b - W_p)] I_b$.

energy considerations,[7] that the data was more consistent with the production of a high beta short plasma rather than the bulk heating of the background plasma. We confirmed this conclusion when we took data after additional central-cell loops were installed, and we analyzed the ratio of signals from loops located at different distances from the center plane. If we approximate the axial variation of the magnetic moment of the beam heated component by a Gaussian

$$m(z) \propto \exp[-(z/\ell_z)^2]$$

we may calculate the loop signal ratio from

$$V_2/V_1 = \frac{\int_{-\infty}^{\infty} f_2(z) \exp[-(z/\ell_z)^2]\, dz}{\int_{-\infty}^{\infty} f_1(z) \exp[-(z/\ell_z)^2]\, dz}$$

TABLE 8-2. Characteristic TMX Energy Lifetimes for the data of Table 8-1.

Energy lifetimes	Central-cell magnetic field (ms) 1 kG	2 kG
Global plug energy lifetime (τ_{EP})	0.84	0.67
Global machine energy lifetime (τ_{EG})	0.99	1.03
Axial machine energy lifetime (τ_{EA})	0.74	0.72

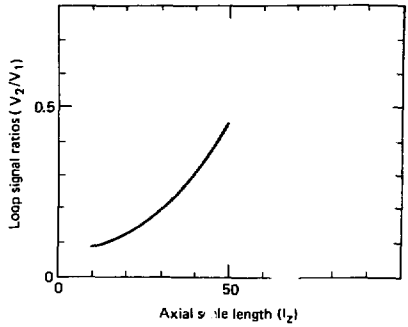

FIG. 8-8. Ratio of z = 65 cm loop to z = 29 cm loop signals as a function of beam-injected plasma Gaussian scale length.

where $f_1(z)$, $f_2(z)$ are the experimentally measured response functions of two loops located at z = 29 cm and z = 65 cm respectively. Figure 8-8 plots the expected signal ratio as a function of the Gaussian scale length ℓ_z.

Analysis of beam-heating experiments for which loop ratios could be obtained yielded a value of 0.21 ± 0.01 for V_2/V_1 corresponding to a Gaussian scale length of 30 cm for the beam component.

Since injection conditions were similar to those of the earlier experiment, although beam current values and loop signals were less, we use this value of scale length for reduction of the earlier data. The central-cell diagnostic beam crosses the machine axis ≈50 cm from the central plane; consequently, it does not measure the radius or density of the hot plasma component. We use the value of the warm plasma radius to reduce the data on the assumption that the hot ions are trapped mainly by interaction with the warm plasma and therefore will have density profiles similar to the warm plasma. Since this is a beam-heated plasma, we assume a flat temperature profile and for ℓ_z = 30 and $r_m = r_i$ obtain the values which are plotted in Fig. 8-9. We see that central-cell beta of about 40% has been obtained. In this experiment we have

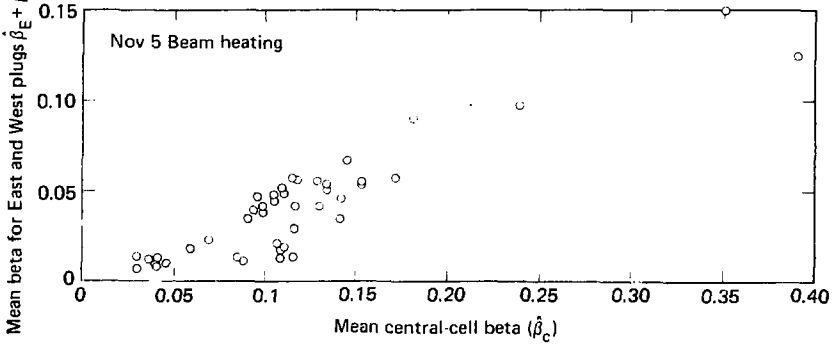

FIG. 8-9. TMX plug beta vs central-cell beta for a beam-heated central-cell plasma. We have assumed a Gaussian scale length of the central-cell hot plasma of 30 cm.

demonstrated the ability of the plugs to stabilize a plasma with quite respectable parameters, even though the plasma is short in length. Such information is of importance for possible field reversal experiments in the central cell of a tandem mirror.

For $\beta \approx 0.4$ and $W_\perp \approx 10$ keV we find a peak hot density $\hat{n} \approx 4 \times 10^{12}$. The total number of hot particles is

$$N = \hat{n}\pi r_c^2 \cdot \sqrt{\pi \ell_z}$$

$$= (4 \times 10^{12})(16)^2(30\ (\pi^{3/2}) = 1.7 \times 10^{17} \quad .$$

For an injected-beam current of 60 amps and a trapping fraction of 0.6 the particle confinement time is

$$\tau_i = \frac{N}{ii_b} = \frac{1.7 \times 10^{17}}{0.6 \times 60} 1.6 \times 10^{-19} = 760\ \mu s \quad .$$

This result agrees remarkably well with the measured decay rate of the diamagnetic signal after beam turnoff of 740 μs! We attribute this lifetime to charge-exchange loss on cold gas. This decay rate would require an average neutral density over the hot-ion orbits

$$\bar{n}_0 = \frac{1}{\sigma v_{ex} \tau_{ex}}$$

$$= \frac{1}{1.1 \times 10^{-7} \times 7.4 \times 10^{-4}} \approx 10^{10}\ cm^{-3}$$

or a neutral pressure of 3×10^{-7} Torr, a not unreasonable value considering that the neutral pressure external to the plasma column is measured to be many times higher. Beam ions which are 50 times more energetic than the electrons transfer their energy primarily to the electrons rather than to the background ions. Energy loss by electron drag, however, is relatively less important than by charge exchange:

$$\tau_{drag} = 4.4 \times 10^7\ T_e^{3/2}(eV)/n_e(cm^{-3})$$

$$= \frac{4.4 \times 10^7\ (200)^{3/2}}{1.6 \times 10^{13}} \approx 7.5\ ms$$

if we assume a beam-heated, central-cell electron temperature of 200 eV and a density of 1.6×10^{13} cm^{-3}. Evidence of the heating of plug electrons by the hot central-cell ions is shown in Fig. 8-10 where we plot the Thomson scattering value of the east plug electron temperature before and after beam turn on for a number of shots.

During the beam-heating experiments we sometimes observed a rapid loss or dump of the hot ions, as evidenced by a rapid change in the plasma diamagnetism. An example of this type of behavior is shown in Fig. 8-11. These dumps were accompanied by decreases in plug density and end loss current but the plug diamagnetism did not change indicating that the main effect on the plug was the interruption of the warm plasma escaping from the central cell. Figure 8-12 shows that the maximum diamagnetic signal obtained during the central-cell heating continues to increase linearly with the central-cell neutral-beam current suggesting that MHD ballooning processes are not limiting the central-cell beta.

The occurrence of dumps is influenced by the plug magnetic field in a manner that is not understood. It was noted that the two highest values of Fig. 8-9 occurred on the only shots which had lower plug baseball-coil currents because of power supply problems and that one of these shots did not have a dump (of this day's run, 90% of the shots had dumps). Following this observation, we took a series of shots for various values of the baseball-coil currents while holding all other fields and injection conditions constant. There was a transition between 70% and 80% of full baseball field below which level no dumps were observed in a six-shot sample. Since the ratio of the central-cell beta to plug beta was actually higher for the 70% case where no dumps were observed, it appears probable that the dumps are not MHD related.

We observe the growth of a 5 kHz, m = 1 central-cell rotation preceding each dump. An example of an expanded time scale is shown in Fig. 8-13. The r = 19, central cell-beam-attenuation

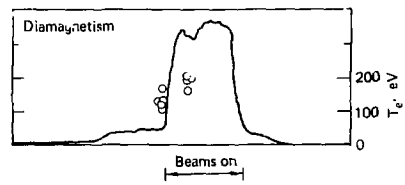

FIG. 8-10. The Thomson scattering value of the east plug electron temperature before and after central-cell beam turn on for a number of shots.

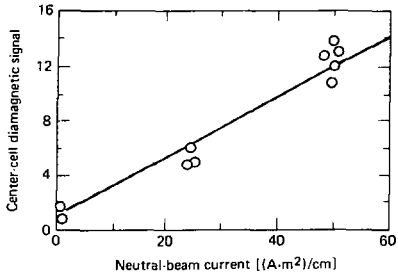

FIG. 8-11. An example of a dump of energetic ions during central-cell neutral beam injection.

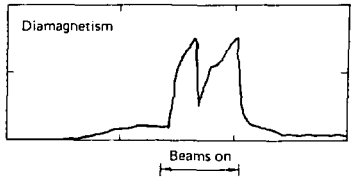

FIG. 8-12. Central-cell diamagnetic signal increases with central-cell neutral-beam current, showing no indication of saturation.

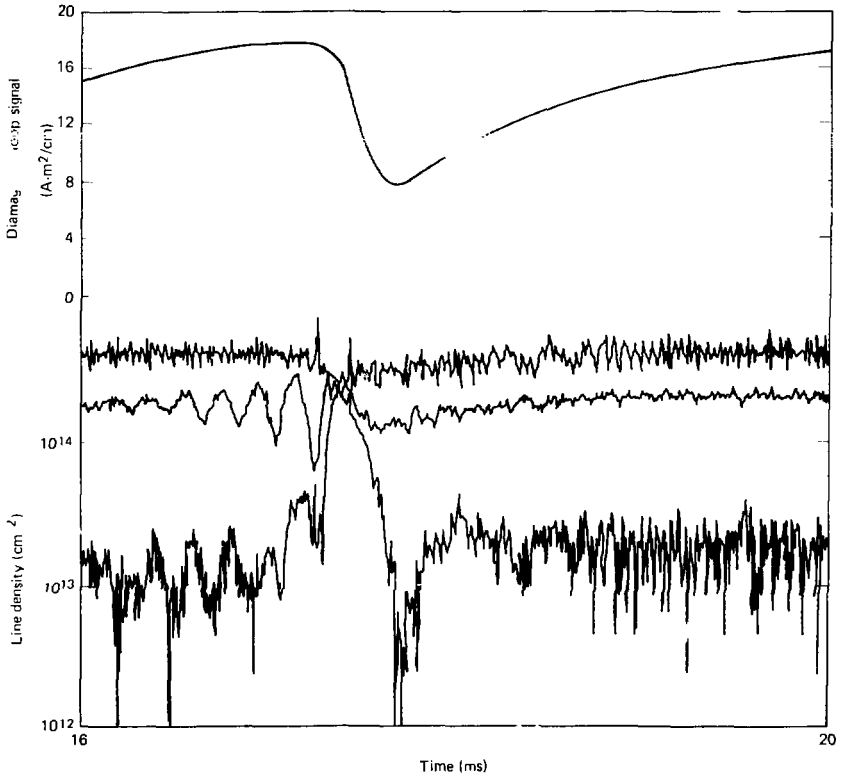

FIG. 8-13. Central-cell plasma diamagnetic signal and beam-attenuation signals at r = 0, 19, and 30 cm are shown on an expanded time scale.

channel shows this most clearly. That little modulation is seen at $r = 0$ indicates that the mode number is odd. By observing the signals from disk probes on the top, north, and bottom of the central cell, we conclude that this mode is probably $m = 1$ and is rotating in the $E \times B$ or ion diamagnetic drift direction. The disk probes show that particles are lost radially to the central-cell wall during the dumps.

This mode may be the rotational instability discussed by Pearlstein and Friedberg.[8] For a plasma radius of 20 cm, a frequency of 5 kHz, and for $m = 1$, the velocity of rotation of the surface is

$$\begin{aligned} v &= \omega r_c \\ &= (2\pi)(20)(5 \times 10^3) \\ &= 6 \times 10^5 \text{ cm/s}. \end{aligned}$$

Setting this velocity equal to the $E \times B$ rotation velocity of a rigid rotor model of the plasma and solving for the central-cell potential, we find

$$\begin{aligned} \Phi &= 10^{-8} v r_c B \\ &= (10^{-8})(6 \times 10^5)(20)(2000) \\ &= 240 \text{ V}. \end{aligned}$$

This is in the range of the central-cell TMX plasma potential measurements.

REFERENCES

1. T. B. Kaiser et al., *Physics of Fluids* (to be submitted).
2. R. H. Cohen, *Nucl. Fusion* **19**, 1295 (1979).
3. F. H. Coensgen, *TMX Major Project Proposal*, LLL-Prop-148 (1977).
4. T. D. Rognlien and Y. Matsuda, *Nucl. Fusion* **21**, 345 (1981).
5. R. P. Drake et al., "The Effect of End-Cell Stability on the Confinement of the Central-Cell Plasma in TMX," *Nucl. Fusion* **21**, 359 (1981).
6. T. B. Kaiser, private communication.
7. UCID-18496, Part 1, *Physics Basis for MFTF-B*.
8. L. D. Pearlstein and J. P. Freidberg, *Phys. Fluids* **21**, 1207 (1978).

9. Radial Transport and Particle Balance

9.1 INTRODUCTION

All magnetic-confinement devices rely on the slow transport of particles and energy across magnetic field lines. This transport limits the performance of any confinement concept as a fusion reactor. A mirror machine may lose plasma either axially or radially. The axial losses have been the primary concern of mirror research for many years, but the tandem-mirror concept[1,2] has made possible microstable mirror machines with very small end losses, thus increasing the importance of radial transport. Radial transport may significantly limit the performance of future tandem mirrors.[3,4] This section reports the results of an experiment to study radial transport in the Tandem Mirror Experiment (TMX).

TMX was constructed at the Lawrence Livermore National Laboratory as a basic test of the tandem mirror concept.[5] It consists of two small neutral-beam-fueled plasmas which plug the two ends of a much larger central-cell plasma. The end-cell (plug) plasmas reduce the central-cell end losses by confining the central-cell ions in an electrostatic potential well, which exists because the end-cell plasmas become more positively charged than the central-cell plasma. A gas feed fuels the central cell. In TMX, the central-cell end losses also provide the warm-plasma stabilization required by the end-cell plasmas. (This will not be the case in future tandem mirrors.[4]) If the central-cell end losses do not provide adequate stabilization, the plasma fluctuations in the end cells may act to increase the central-cell end losses.[6] The end losses in TMX were lower than those from single-cell mirror machines; in addition the plasma was isolated from the end wall by expanding the magnetic flux tube into a large end-fan chamber (see Sec. 15, also Refs. 7 and 8).

We have developed techniques in TMX that will be used to study transport in future tandem mirrors. Some of our radial transport data and several key conclusions are summarized in Sec. 9.2. Section 9.3 reports the analysis of one detailed radial transport experiment, as well as describing the theory of ambipolar and nonambipolar radial transport. Section 9.4 describes modeling of radial transport in the TMX central cell. One key conclusion of the Sec. 9.4 is that the end-cell density profile significantly affects the central-cell potential profile and hence radial transport in the central cell.

9.2 SUMMARY OF TRANSPORT DATA AND ANALYSIS

Figure 9-1 summarizes the information we use to analyze transport. Each row in the figure corresponds to a different plasma fueling condition. The first column shows the plasma density profile, as determined by a polynomial fit to the measured line-density profile in the central cell. As is shown, the density profiles in TMX could be peaked, flat, or inverted, depending on the gas feed and other plasma conditions. The second column shows the end-loss flux of ions escaping the plasma. The magnetic-field-line radius and the end-loss flux (in equivalent A/cm^2) are evaluated in the central cell; although the measurements are made at the end wall. The ion end losses are measured using two arrays of Faraday cups, as well as two gridded end-loss analyzers (ELA's). The central cell dominates the measured fluxes: no more than 20% of the total ion end losses originate in the end-cells, and the ion losses originating in the end-fan chambers are negligible (see Sec. 15). Ion end-loss fluxes from less than ten to several hundred equivalent mA/cm^2 (in central-cell coordinates) have been measured. The third column plots the electron flux to the end wall. (Secondary electrons are not included.) The data is the sum of measurements of the negative electric current that flows to the end wall and of the electron flux that neutralizes the ion end-loss flux measured by the Faraday cups. If there were no electron radial transport, the data plotted in this column would equal the electron source due to the gas feed and the neutral beams. In the absence of ion radial transport, the data in the second and third columns would be identical. Secondary-electron emission was found to be only 30% of the total end losses, (see Sec. 15) so it does not significantly affect the radial-transport conclusions, as is discussed below. Secondaries may affect the plasma potential[9] and the electron power balance.[8]

The fourth column in Fig. 9-1 shows the source of plasma in the central cell due to ionization of gas. It is calculated by the gas-penetration computer code described below, using the measured profiles of the plasma parameters. Because of uncertainties in the data and in wall-reflection coefficients, the ionized source is uncertain by about a factor of two.

The data shown in the top row of Fig. 9-1 are analyzed further in Sec. 9.3. In another experiment, we changed the plasma fueling to obtain information on radial-transport scaling. The results are shown in the lower three rows of Fig. 9-1. The data is now being analyzed, but some conclusions can be drawn directly from the figure. Observe that the ionized source, the electron end loss, and the ion end loss have similar magnitudes. This shows that radial transport does not dominate the central-cell confinement. The radial loss rate is at most comparable to the axial loss rate, except near the edge of the plasma. The observed correlation between radial transport at the plasma edge and low-frequency density fluctuations is discussed in Sec. 11.

In addition, the electron end-loss flux is always larger than the ion end-loss flux. That is, a negative electric current flows to the end wall. A positive ion current is believed to flow to the central-cell limiter. This shows that nonambipolar transport is present in TMX. The magnitude of this transport is evaluated in the following section. Resonant-neoclassical ion transport is nonambipolar and should produce a negative electric current. The observed electric current is consistent with the theoretical predictions, but there is a significant uncertainty in this comparison.

9.3 DETAILED STUDY OF RADIAL TRANSPORT IN THE TMX CENTRAL CELL

In the work reported here, plasma parameters, including the ion and electron end losses, were measured for many shots taken under constant plasma conditions. The fueling of the plasma was calculated on the basis of the results, and was compared to the measured electron end losses to estimate the losses due to ambipolar transport. The radial electron (and ion) loss rate due to ambipolar transport was no larger than the measured axial loss rate, and might have been as small as the rate determined by Coulomb collisions. The nonambipolar radial transport of central-cell ions was measured directly by detecting the negative electric current that flowed to the end wall. It was 80 ± 40% of the axial loss rate. Resonant-neoclassical transport[10-12] should produce a negative electric current at the end wall, as was observed. The measured transport is consistent with the resonant-neoclassical prediction; although there is a large uncertainty. This and other types of transport are discussed in the following section.

9.3.1 *Transport Theory*

Radial transport processes are either ambipolar or nonambipolar. Ambipolar transport produces equal radial fluxes of electrons and ions. It is produced, for example, by electron-ion collisions and low-frequency fluctuations. Several processes produce nonambipolar transport, which moves ions radially without transporting electrons. In a toroidal plasma device, the electrons will stop nonambipolar transport as the plasma acquires a negative charge, but in mirror systems the electrons can flow to the end wall to maintain charge neutrality. The resulting negative electric current is a direct result of nonambipolar transport.

The largest expected nonambipolar radial ion-transport process resulting from collisions is resonant-neoclassical transport. The theory of radial losses from a nonaxisymmetric tandem mirror has been given in a series of papers by Ryutov and Stupakov[10-12] and others,[13,14] who have shown that these losses can be much larger than classical estimates because the magnetic field is not axisymmetric. The enhanced transport is associated with radial drifts that arise from the azimuthal components of the nonaxisymmetric field. There are quadrupole fields in the transition regions between the central cell and the end cell of TMX (see Fig. 9-5), which produce a radial displacement proportional to cos 2ψ, where ψ is the azimuthal angle. Because the quadrupole field at one end of the central cell is rotated by 90° with respect to the field at the other end, successive radial displacements experienced by a particle with negligible azimuthal drift nearly cancel. This cancellation is not complete; a small residual displacement proportional to cos 4ψ remains.

The character of the radial losses is determined by the azimuthal drift, $\Delta\psi$, of an ion in one axial

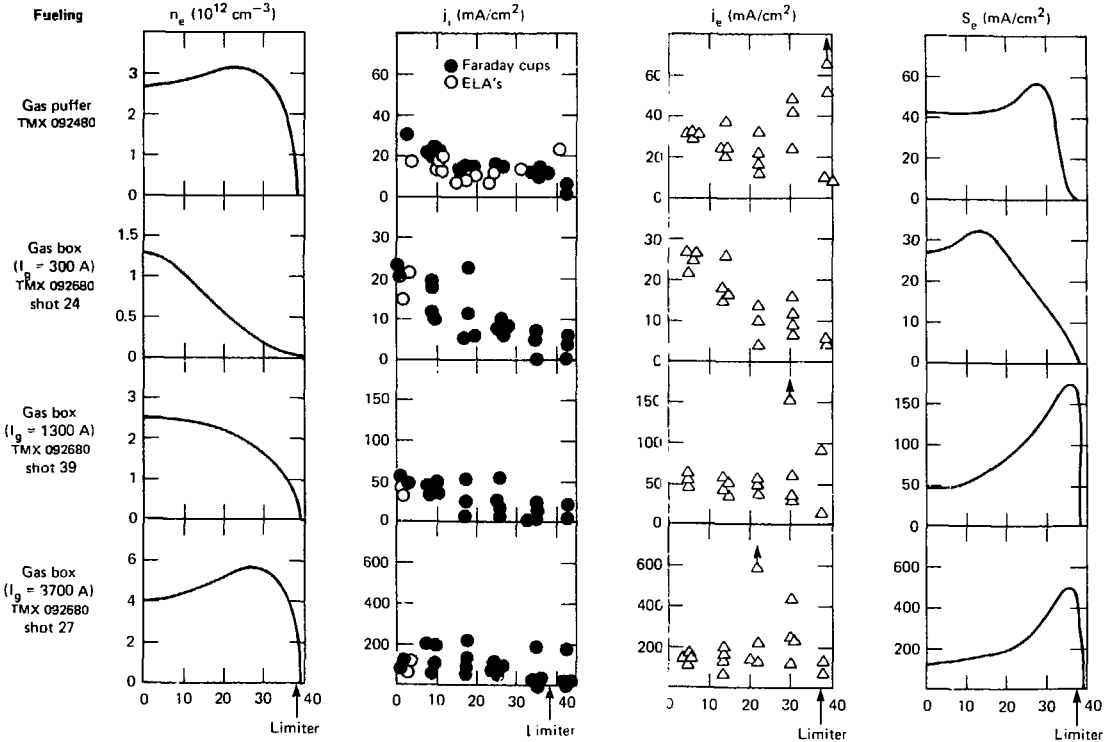

FIG. 9-1. Data used in radial-transport studies. Plasma densities (n_e), ion end losses (j_i), electron end losses (j_e), and electron source by ionization (S_e) are shown for four different gas feed conditions.

transit of the central cell. In TMX, this guiding-center drift is produced by the radial electric field in the plasma. Three modes of diffusion have been identified, depending on the magnitude of:

- Ions for which $\Delta\psi \ll 1$ diffuse radially in the neoclassical diffusion mode
- Ions for which $\Delta\psi \gtrsim 1$ diffuse radially in the resonant-neoclassical diffusion mode
- Ions for which $\Delta\psi \gg 1$ diffuse radially in the stochastic diffusion mode.

All three types of diffusion may be occurring in a given device in different regions of phase space. The amount of diffusion in each mode depends on the collisionality of the ions in the solenoid, on the plasma beta, and on the structure of the magnetic field in the transition regions. In TMX, resonant diffusion is the dominant mode.

Neoclassical diffusion ($\Delta\psi \ll 1$) in tandem mirrors is similar to neoclassical diffusion in tokamaks, and is associated with the residual ($\cos 4\psi$) component of the radial drift. Ion drift orbits viewed at the midplane of the tandem mirror solenoid exhibit the same general features (e.g., banana-shaped orbits) as the ion drift orbits in the poloidal plane of a tokamak. The neoclassical diffusion coefficient is shown as a function of collision frequency and plasma beta in Fig. 9-2(a).

Resonant-neoclassical diffusion ($\Delta\psi \gtrsim 1$) derives its name from ions that drift azimuthally so as to resonate with the quadrupole field. For example, an ion that drifts 90° per transit is a resonant ion. The resonant ions receive additive successive displacements as they bounce back and forth. As a result, resonant-ion drift orbits show comparatively large deviations from circles. The combination of the resonant drift motions and Coulomb collisions produces resonant-neoclassical transport. The resonant-diffusion coefficient is shown as a function of collision frequency in Fig. 9-2(b). Such transport has banana and plateau regimes similar to those found in tokamaks; TMX operates toward the collisional boundary of the plateau regime. Resonant diffusion significantly exceeds neoclassical diffusion in TMX. If the bounce time, $t_{\parallel}$, equals the azimuthal-drift time, t_{dr}, the ratio

$$\frac{a^2}{\alpha^2 r_c^2} = \frac{\rho_c^2 L_b^2 L_{tr}^4}{r_c^8}$$

is approximately 100. In this ratio, a is the maximum radial displacement experienced by an ion in a single bounce, α characterizes the deviation of the neoclassical drift orbits from circles, r_c is the central-cell radius (about 30 cm), ρ_c is the ion gyroradius (about 2 cm), L_b is the distance between bounces (about 450 cm), and L_{tr} is the transition scale length (about 100 cm).

The quantity $[\partial(\Delta\psi)/\partial r]^{-1}$ is the radial distance between resonant points for an ion with specified energy and magnetic moment; when $a \geq [\partial(\Delta\psi)/\partial r]^{-1}$, the resonances overlap, and the diffusion becomes stochastic. In the stochastic mode, the ion diffusion is independent of the presence or absence of collisions. This requires that $\Delta\psi$ be much greater than one, and does not correspond to TMX operation.

These neoclassical diffusion processes produce a measurable effect: a negative electric current flows to the end wall. Because electron transport due to quadrupole fields is not significant in TMX and the electrons can easily flow to the end wall, resonant transport is expected to cause a negative electric current to flow to the end wall from the plasma. Resonant transport also

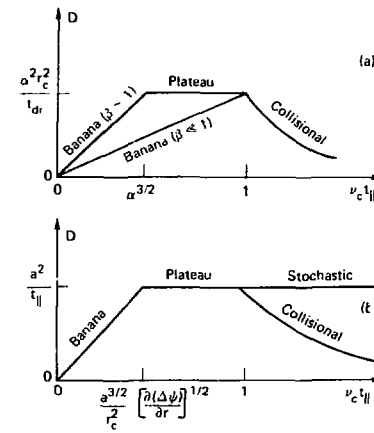

FIG. 9-2. Diffusion of ions in tandem mirrors: (a) neoclassical diffusion and (b) resonant-neoclassical diffusion. α characterizes the deviation of the neoclassical drift orbits from circles, r_c is the central-cell radius, t_{dr} is the time required for an ion to drift around the solenoid once, ν_c is the collision frequency, $t_{\parallel}$ is the longitudinal transit time in the solenoid, and a is the maximum radial displacement experienced by an ion in a single bounce.

transports impurities outward, and this too can produce a negative electric current at the end wall. However, so long as the impurity concentrations are only a few percent, the negative current they produce is small compared to that produced by the deuterons.

The radial ion flux due to resonant-neoclassical transport is[10-12]

$$-\Gamma(\mathrm{cm^{-2}\cdot s^{-1}}) = D_0\left(\frac{\partial n}{\partial r} + \frac{n}{T_i}\frac{\partial \phi}{\partial r}\right) + (D_1 - 1.5\,D_0)\frac{n}{T_i}\frac{\partial T_i}{\partial r} \quad . \qquad (1)$$

The flux, Γ, is driven by the radial gradients of density, n (cm^{-3}), potential, ϕ (kV), and ion temperature, T_i (keV). In TMX, the transport due to the potential gradient is dominant. The diffusion coefficients D_0 and D_1 (cm^2/s) depend on the details of the magnetic field and the value of the electric field.[3,10-12] Figure 9-3 shows the calculated Γ as a function of the potential gradient, $\partial\phi/\partial r$, for several ion temperatures. The local maximum of Γ occurs at the first electric field for which a thermal ion becomes resonant. The further resonances at higher electric fields overlap, producing a continuous increase. The other parameters used to evaluate Γ are appropriate to the experiment described below. If the radial flux at a radius of 30 cm in the TMX central cell were $2 \times 10^{15}\ cm^{-2}\cdot s^{-1}$, the radial ion current would be 19 A. (The effective cylindrical length of the central cell is 314 cm.) Thus, a negative current of order 10 A per end might be observed within this radius at the end wall. Equation (1) gives the azimuthal average of the radial flux; current theory does not predict the azimuthal distribution. This complicates the comparison to measurements that must rely on a limited array of detectors.

Near the metal limiter at the edge of the plasma in TMX, two processes can enhance the nonambipolar transport. First, the ions, which have Larmor radii of about 2 cm, can intercept the limiter and be neutralized, causing an electron close to the limiter to be lost to the end wall. If gas fueling produces large ionization rates near the limiter, this negative electric current can be quite large (see below). Second, the assumptions in Eq. (1) break down in two ways near the limiter: the magnetic drift surfaces change shape at large distances from the magnetic centerline, which may lead to enhanced transport. Also, Eq. (1) describes the net radial flow of ions, including many ions that move outward and then inward along their drift orbits. Near the plasma edge, any particle that moves outward so as to intercept the limiter is lost.

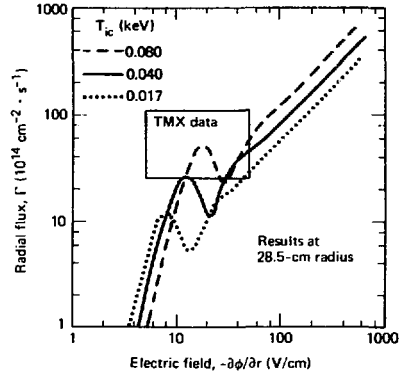

FIG. 9-3. Theoretical radial transport. The outward radial flux (Γ), was evaluated as a function of electric field ($-\partial\phi/\partial r$), at a 28.5 cm radius. The TMX data allows radial fluxes in the box. The plasma parameters were $n = 3 \times 10^{12}\ cm^{-3}$, $-\partial n/\partial r = 3 \times 10^{10}\ cm^{-4}$, $-\partial T_{ic}/\partial r = 1$ eV/cm, and T_{ic} as shown.

Other mechanisms can also cause nonambipolar transport; Table 9-1 summarizes some of them. The fluxes were evaluated for gradients at a radius of 30 cm, near the plasma edge; they would be much smaller in the plasma core. A small nonambipolar radial flux is caused by charge exchange and ion-neutral collisions. Because the neutral atoms fuel the plasma, ionization events are roughly as common as charge exchange and other collision processes. As a result, the diffusive transport due to the small steps resulting from ion-neutral collisions is small compared to other ion loss processes. Magnetic-field errors can enhance several types of transport, including resonant-neoclassical transport. However, the distortions of the drift surfaces due to the measured field errors were calculated to be small, so that they result in only a small additional transport. Finally, various instabilities may produce nonambipolar transport; in particular, end-cell ion-cyclotron-frequency plasma fluctuations may have this effect. However,

TABLE 9-1. Possible radial fluxes from theory.

Process	Radial flux	Approximate magnitude (10^{15} cm$^{-2}\cdot$s^{-1})
Nonambipolar		
Resonant-neoclassical[3]	$-\left[D_0\left(\frac{\partial n}{\partial r}+\frac{n}{T_i}\frac{\partial \phi}{\partial r}\right)+(D_I-1.5\,D_0)\,\frac{n}{T_i}\frac{\partial T_i}{\partial r}\right]$	2
Neoclassical[3]	$-\frac{\alpha^2 r^2}{t_{dr}}\left(\frac{\partial n}{\partial r}+\frac{n}{T_i}\frac{\partial \phi}{\partial r}+\frac{n}{T_i}\frac{\partial T_i}{\partial r}\right)$	0.2
Charge-exchange	$-\rho_i^2\, n_0\, \langle\sigma v\rangle_{cx}\frac{\partial n}{\partial r}$	0.07
Ion-cyclotron fluctuations[15]	$-\frac{r_c^2}{2}\nu_{rd}\frac{\partial n}{\partial r}$	0.16
Ambipolar		
Electron-ion collisions[16]	$-\frac{2\,n\,kT_i c^2}{B^2}\eta_\perp\frac{\partial n}{\partial r}$	0.03
Impurity-ion collisions[16]	$-\frac{n_z\,kT_i c^2}{B^2}\eta_{DZ}\frac{\partial n}{\partial r}$	0.04
Bohm	$-6.25\times10^6\frac{T_i}{B}\frac{\partial n}{\partial r}$	13

Parameters used:

$n = 3\times10^{12}$ cm^{-3}; $\partial n/\partial r = -10^{11}$ cm^{-4}; $T_i = 20$ eV; $B = 10^3$ G; $\partial\phi/\partial r = -30$ V/cm; $\partial T_i/\partial r = -1$ eV/cm; $\rho_i = 1.5$ cm; $n_0 = 3\times10^{10}$ cm^{-3}; $r_c = 35$ cm; $\eta_\perp = 2\times10^{-15}$; $n_z = 1.5\times10^{10}$ cm^{-3}; $\eta_{DZ} = 10^{-12}$; $\nu_{rd} = 2.7$ s^{-1}

theoretical estimates of this process have shown it to be small.[15]

Ambipolar transport is produced by four processes. The most familiar of these is "classical" transport due to electron-ion collisions, which is quite small. The classical transport due to impurity-ion collisions is larger. The outward flux of deuterons due to impurities of the same temperature is[16]

$$\Gamma_{DZ} = \frac{\eta_{DZ}\, c^2\, kT}{B^2}\left(\frac{n}{Z}\frac{\partial n_z}{\partial r} - n_z\frac{\partial n}{\partial r}\right) \quad . \qquad (2)$$

This equation is in cgs units with the magnetic field, B, in gauss, and the temperature, kT, in ergs. Z is the impurity charge, c is the speed of light, and

$$\eta_{DZ} = \frac{8\sqrt{\pi}e^2 Z^2 \log\Lambda}{3\sqrt{2}\,(KT)^{3/2}}\left(\frac{MM_z}{M_z+M}\right)^{1/2} \quad , \qquad (3)$$

in which e is the unit charge, $\log\Lambda$ is the Coulomb logarithm, and M and M_z are the deuteron and impurity masses. This classical transport moves impurities inward and deuterons outward and is explicitly ambipolar. An electron current may flow to

the end wall if the impurities come back out of the plasma by resonant neoclassical transport.

Plasma fluctuations, particularly low-frequency ones, may also produce ambipolar transport.[17] This type of process has often produced transport as large as Bohm diffusion. Table 9-1 shows the flux due to Bohm diffusion, which would correspond to a radial loss of 120 equivalent amperes of electrons (and ions) at a radius of 30 cm. Finally, if gross MHD instabilities are present, the plasma can be lost to the radial walls even more rapidly. However, the TMX plasma was maintained in steady state without such disastrous effects.

9.3.2 Experimental Data

In this experiment, the incident neutral-beam current was held constant at 150 A per end cell, with a mean injection energy of 11 keV. The central-cell gas feed was 150 Torr liters per second. The gas was introduced at the bottom of the central cell near the midplane, between two 38-cm-radius limiters spaced 108 cm apart. We obtained 29 shots with neutral-beam currents within the range 150 ± 20 A in both end-cells. Plasma parameters were reproducible to within ±15% for these shots. The data reported below was averaged over a 4-ms interval during the steady-state phase of each shot and then over the 29 shots. The reported uncertainties are the standard deviation of the 29-shot average.

Figure 9-4 shows the central-cell line-density profile and the density profile resulting from Abel inversion of a least-squares polynomial fit to the line density. The density profile appears slightly inverted, with a steep density gradient near the plasma edge. Table 9-2 shows other plasma parameters for this experiment. The end-cell plasmas were denser and hotter than the central-cell plasma—the end-cell electron temperature was 87 eV, the central-cell temperature was 49 eV. The central-cell plasma potential was 330 V, as measured by a thalium-ion-beam probe (see App. B). The radial profile of the plasma potential is shown in Fig. 9-5. The plasma-potential data places limits on the electric field in the plasma.

The important elements in our study of radial transport are illustrated in Fig. 9-6. The gas feed

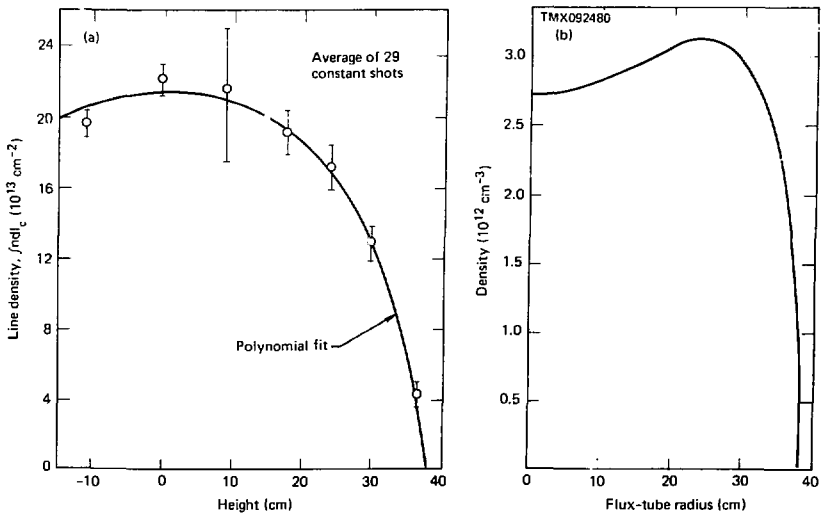

FIG. 9-4. Plasma density profiles. The density profile was obtained by Abel inversion of a least-squares polynomial fit of the line density. The error bars show the standard deviations of the data.

TABLE 9-2. Summary of September 24, 1980 plasma parameters.

Parameter	Value on axis
End-cell density	1.5×10^{13} cm^{-3}
Central-cell density	2.8×10^{12} cm^{-3}
End-cell electron temperature	87 ± 22 eV
Central-cell electron temperature	49 ± 15 eV
Central-cell diamagnetism (global)	$(8.9 \pm 1.4) \times 10^{3}$ A·cm
Central-cell plasma potential	330 V

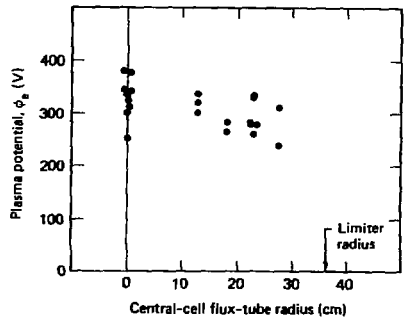

FIG. 9-5. The measured plasma-potential profile.

fuels the central cell and the neutral beams fuel the end cells (see Sec. 9.4). Faraday-cup arrays and gridded end-loss analyzers (ELAs)[18] measure the ion flux reaching the end wall at a number of positions (see App. B for a description of the diagnostics, Sec. 5 and Refs. 5 and 18 for the results). The net electric current flowing to the end wall is measured by passing it through 5-Ω resistors. The voltage drop across the resistor is measured; it was verified that this voltage is so

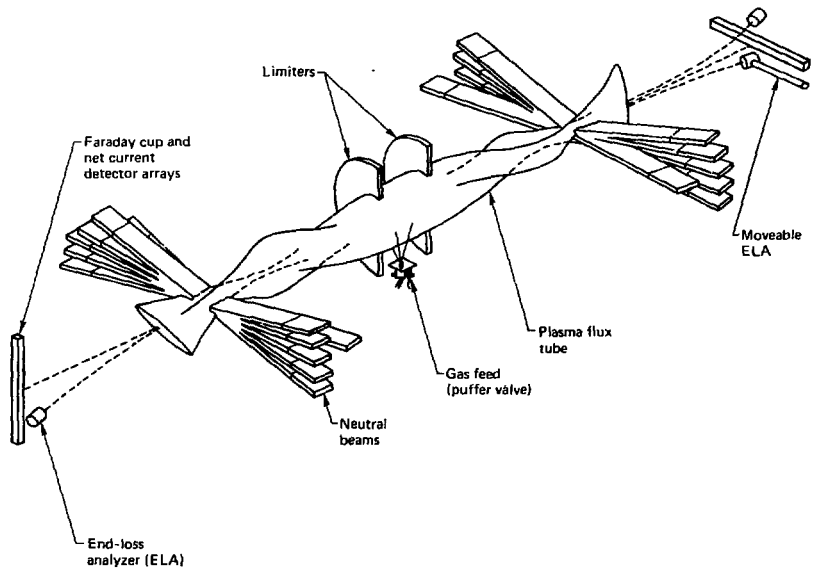

FIG. 9-6. Schematic of the radial transport experiment. Neutral beams fuel the end cells, a puffer valve fuels the central cell. Limiters (shown in cutaway) confine gas near the central-cell midplane. End-wall diagnostics include a Faraday-cup array, a net-current detector array, and end-loss analyzers.

small that it does not affect the measurement. The electric current is negative; it must be neutralized by ions that strike other surfaces in the machine. The limiter in the central cell is the closest surface to the plasma and thus probably collects most of the radial flux; however, we did not measure the fluxes to the limiter. The Faraday cups and net current detectors are mounted in arrays that span the narrow dimension of the magnetic fans at the ends of TMX.

Figure 9-7 shows the measured ion end losses as a function of radial distance. The end-loss profiles are symmetric about points that differ from the geometric axis by about one detector spacing, presumably because of coil misalignments. We used these symmetry points as axes in our analysis. Measurements from both sides of the symmetry point are plotted against a common radius. The radial distance and the loss current per unit area are evaluated in central-cell coordinates. The data from the Faraday-cup arrays (solid dots) and two fixed ELAs (squares) is averaged over 29 shots as described above. In addition, a movable ELA was scanned across the plasma[8] with two shots at each position (open circles). The ion end losses are, in general, largest near the machine axis and decrease at larger radii. For a variety of data, including scaling experiments with large variations in end-loss current, the current indicated by the Faraday cups is about 1.4 times that indicated by the ELAs. The calibration of the Faraday cups is the more reliable, and these results are used below. At a very large radius the movable ELA measured a large current of low-energy ions. The Faraday cups might not detect these losses, either because the cups repel ions with energies less than 100 eV or because a well-localized flux may flow between two detectors. As is seen below, our knowledge of the plasma parameters beyond a 30-cm radius is uncertain for other reasons as well. Within a 30-cm radius, the ion current to the end wall is about 50 A per end.

The net electric current flowing to the end wall, measured as described above, is shown in Fig. 9-8. All the detectors measured negative net current or no net current. In general, the negative current increases with radius, but drops to zero at the radius of the limiter. The negative electric current is of the same magnitude as the equivalent current of ions to the end wall (40 ± 20 A per end). In consequence, the total electron flow to the end wall is roughly twice the total ion flow. Smooth

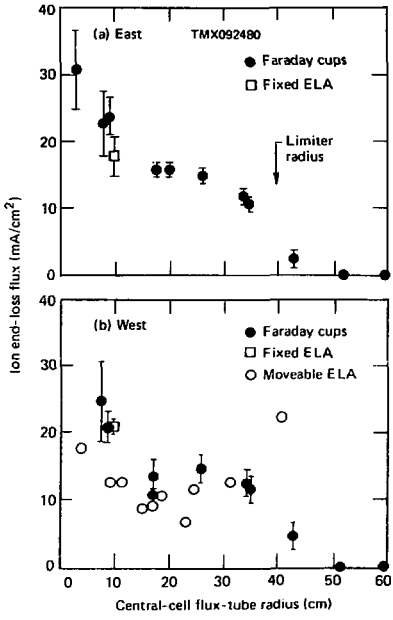

FIG. 9-7. Ion end losses vs radius for (a) the east end, and (b) the west end of TMX. Measurements were made at the end wall but are reported in central-cell coordinates.

curves drawn through the data in Fig. 9-8 were used to estimate the radial ion flux. The net-current detectors do not detect any secondary electrons, which are emitted and reabsorbed by the end wall. If these electrons were transported radially, the negative current detected at the end wall would be reduced. However, this would require transport on the time scale of an electron bounce (10 μs), which is much faster than the time scale of any transport allowed by the data. As a result, secondary electrons are ignored in this paper.

9.3.3 Ambipolar Transport

This section evaluates ambipolar transport during the experiment just described, by comparing the sources of electrons in the plasma to the measured end losses.

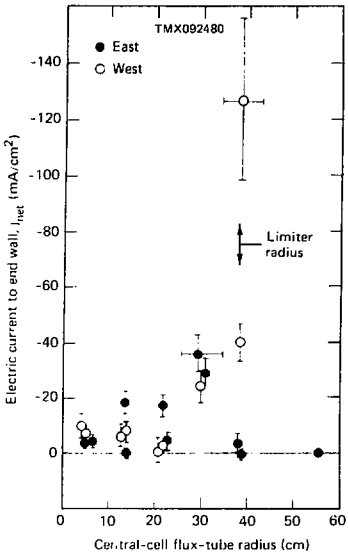

FIG. 9.8. The electric current detected by net current detectors at the end wall. This (negative) electric current is assumed to be neutralized by the radial loss of ions.

Central-Cell Fueling. Central-cell fueling was calculated using a gas-penetration code, and the results were compared to several measurements. The gas-penetration code models molecular D_2 gas incident on a cylindrical plasma, with plasma density and temperature profiles specified on the basis of experimental data. The code then follows the penetration and breakup of the molecules and the resulting ionization and charge-exchange events throughout the plasma. Three-dimensional effects and reflection from the vacuum chamber walls are included.

The sensitivity of predicted central-cell fueling to allowed variations in the plasma parameters was investigated. The results for various electron temperatures are shown in Fig. 9-9. The electron (or ion) source per unit area is determined by multiplying the code result per unit volume by the distance between the limiters. The source per end (half

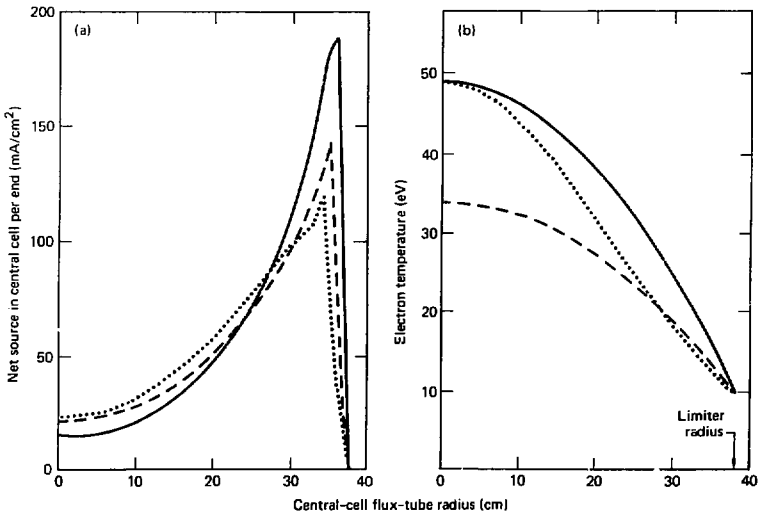

FIG. 9-9. Results of gas penetration studies. As the electron temperature near the limiter was increased, the fueling of the edge increased and that of the plasma core was reduced.

the total) is plotted as a function of radius in the central cell in Fig. 9-9(a). The curves in Fig. 9-9(a) correspond to the electron temperature profiles in Fig. 9-9(b). Between 30 and 38 cm, the results are very sensitive to the electron temperature. As the electron temperature in this region decreases, the Franck-Condon neutral atoms produced by molecular dissociation near the plasma boundary penetrate more easily to the plasma core. As a result, the ionization rate in the core of the plasma increases. (This effect was important in an experiment reported previously.[5] In that experiment, the neutral beams fueling one of the two end cells were turned off. The end-cell plasma decayed and the central-cell electron temperature decreased; as a result, there was more fueling of the central-cell core and the total end losses from the plasma core increased, but the central-cell line density did not change. Most of the end-losses flowed out the unplugged end of the central cell, which was an indication that the other end-cell plasma was an effective end plug.)

The sensitivity of the predicted central-cell fueling to variations of plasma density, ion temperature, and particle reflection from the walls was also investigated. Allowed variations in plasma density and ion temperature produced 10% changes in the ionization rate. Particle reflection from the vacuum chamber walls was more significant (a ±25% effect). This effect could have been larger; it was limited by large holes in the central-cell vacuum tank which reduced the surface area that reflected particles back into the plasma. (The holes led to other vacuum tanks attached to the central cell.)

The results of the code were checked by comparisons with three measurements: the Lyman alpha emissions, the neutral flux to the wall, and the neutral gas pressure.

The spatial Lyman-alpha profile was measured by an extreme ultraviolet spectrometer that measured 22 chords per plasma shot (see Sec. 13). The spectrometer measured the entire Lyman-alpha profile during this experiment. The photon production per unit length was 8×10^{18} photons $cm^{-1} \cdot s^{-1}$. On the basis of the gas-penetration code results, the expected photon emission was 2×10^{19} to 5×10^{19} $cm^{-1} \cdot s^{-1}$. The uncertainty is a factor of 3 or 4. These results show that the actual fueling of the plasma is no larger than the fueling predicted by the code, and might be smaller. The spatial profiles cannot be compared because the code assumes azimuthal symmetry; whereas the gas injection and the observed profile are not symmetric.

The neutral flux to the wall was measured using a surface probe (see Sec. 14). A carbon sample was exposed to the plasma at a radius of 50 cm, where the plasma density was negligible, and nuclear-reaction analysis was used to determine the amount of deuterium retained in the sample. The deuterium flux striking the sample is greater than the amount retained, because some of the incident particles are reflected. The exact reflection coefficient is uncertain because it depends on the distribution function of the neutral flux to the probe. On the basis of the code predictions, this reflection coefficient is about 50%. Assuming 50% reflection, the flux incident on the sample was about 2×10^{16} $cm^{-2} \cdot s^{-1}$. The code predicts a flux of order 3×10^{16} $cm^{-2} \cdot s^{-1}$. The surface-probe measurements thus also suggest that the actual fueling is no larger than the fueling predicted by the code.

The neutral-gas pressure in TMX was measured during the shot using a shielded nude ion gauge with a fast controller. The gas pressure between the limiters was about 10^{-4} Torr, which is consistent with the value expected from the fueling geometry and gas flow rate. Outside of the limiters, the pressure in the central-cell chamber during steady state was 4×10^{-6} Torr, which contributed negligibly to the plasma fueling. Thus, the three independent checks of the gas-penetration code all gave order-of-magnitude verification of its results. It appears that, if anything, the code overestimates the fueling of the plasma.

Fueling and Transport in the End Cells. The end-cell plasmas also produce end losses. Although the total end-cell losses are small (15 A per end compared to 90 A per end from the central cell within a 30-cm radius), they may be important near the plasma centerline. We have computed the ion and electron sources in the end-cell using a radial Fokker-Planck computer code.[20] The end-cell ion source for this experiment (evaluated in central-cell coordinates) is shown in Fig. 9-10(a). The sources of ions and electrons differ slightly because the ions have a large gyroradius, but this effect is not significant here because the data is too coarse to detect the difference. The source is peaked at the machine centerline. Most end-cell ions are transported radially before they are lost, by means of charge exchange with neutral-beam atoms (see

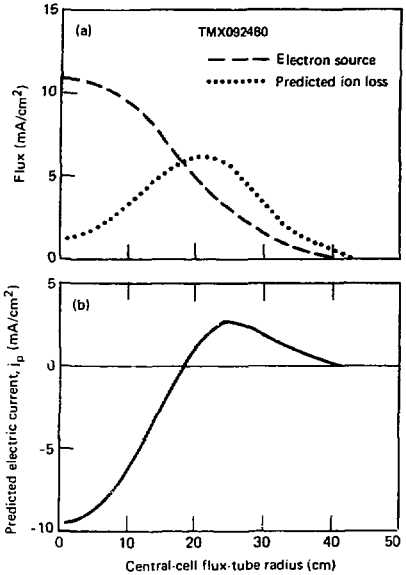

FIG. 9-10. Results of radial Fokker-Planck studies of the end plug: (a) electron source and predicted losses, and (b) resulting electric current to end wall. All quantities are in central-cell coordinates. The uncertainties are about a factor of 2. The measured ion end losses at r = 0 were about 30 mA/cm² and the electric current was about −5 mA/cm².

Sec. 5). The deuteron end losses predicted by the code are also shown in Fig. 9-10(a), and Fig. 9-10(b) gives the net electric current expected to flow from the end cell to the end wall as a function of radius. Two conclusions follow from these results: near the plasma centerline, the end-cell losses may account for all of the net current detected at the end wall (Fig. 9-8), but at large radii a net electric current originates in the central cell (see Sec. 9.3.4).

The end-cell fueling produces one additional complication. The calculations just described correctly determine the azimuthally averaged electric current produced by the end cell, but the electric current in TMX may not have been azimuthally symmetric, because the neutral-beam injection was not azimuthally symmetric. The data was not sufficient to resolve this issue, which therefore adds some uncertainty to its interpretation.

Limits on Ambipolar Transport. The radial losses due to ambipolar transport can be estimated from the measurements and calculations described above. The difference between the source of electrons throughout the plasma and the measured electron end losses is due to ambipolar transport. These are compared in Fig 9-11. The observed electron end losses (the data points) are the current measured by the Faraday cups (Fig. 9-7) added to the magnitude of the negative electric current flowing to the end wall (Fig. 9-8). The location of the data points is uncertain by about ±5 cm because the location of the symmetry point of the end-loss profiles is uncertain. The observed electron end losses are roughly 90 A per end within a 30-cm

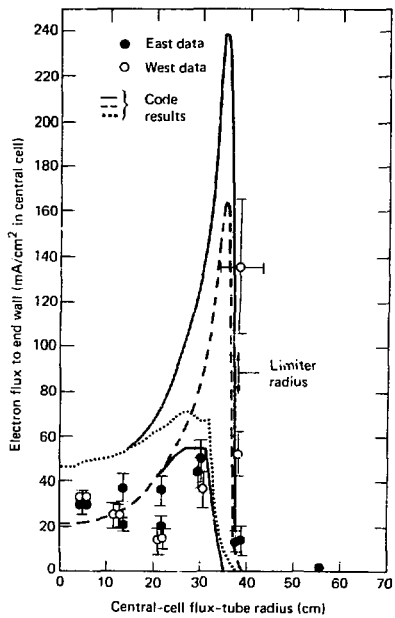

FIG. 9-11. Measured and predicted electron end loss. Data points show measured losses. The solid curves show envelope of gas penetration results, the dashed curve shows a case with low wall reflection, and the dotted curve shows a case with low T_e

radius. As a result, the total axial electron confinement time is about 2.4 ms near the axis and 2.6 ms within 30 cm. These confinement times include electrons in the central cell (94%) and in the end cells (6%). The corresponding axial ion confinement times are 2.8 ms and 4.8 ms.

Figure 9-11 also shows half the total predicted electron source (the amount per end). The total electron source is the sum of the sours in the end cells (Fig. 9-10) and the central cell (Fig. 9-9). The two solid curves show the upper and lower limits of the central-cell fueling that re taieed during the sensitivity studies discussed at the beginning of this section. Two specific cases are also shown. The dashed curve shows a case with zero wall reflection and relatively high T_e, which produced low fueling of the plasma core. The dotted curve shows a case with relatively low T_e (Gaussian profile with 8 eV at 38 cm) and high wall reflection (0.75); the fueling of the plasma core was high.

On the basis of the data shown in Fig. 9-11, the ambipolar radial losses are no larger than the measured axial losses. The "lower limit" fueling rate shows that, throughout the plasma, the ionized source might be as small as the measured axial losses. (The classical ambipolar losses due to Coulomb collisions are negligibly small.) If this were true, no enhanced ambipolar transport would be present. On the basis of the "upper limit" fueling rate, the ambipolar radial losses in the plasma core are clearly smaller than the axial losses; integrated over a 30-cm cylinder, the radial losses could equal the axial losses; and at the edge of the plasma they might significantly exceed the axial losses. Power balance studies using calorimeters at the radial walls show that the radial particle losses within a 30-cm radius do not significantly exceed the axial losses (see Sec. 7). Thus, this data places limits on the radial losses due to ambipolar transport. Unfortunately, the magnitude of the radial transport is not very well determined by this data. The lower limit corresponds to the transport due to Coulomb collisions, and the upper limit corresponds to ambipolar radial transport at the Bohm rate.

9.3.4 Nonambipolar Transport

This section evaluates the nonambipolar transport in the TMX central cell. The net radial ion flux, uncompensated by a radial electron flux, is obtained from the measured electric current, and compared to the flux due to resonant-neoclassical transport.

There was a net radial ion flux in TMX. The negative electric current which flowed to the end wall (Fig. 9.8) implies that some nonambipolar transport mechanism was present. The negative current near the plasma center may have originated in the end cells, as discussed in the previous section, but the negative current at the plasma edge was too large to have originated in the end cells (compare Fig. 9-8 and Fig. 9-10). The total negative current, assuming azimuthal symmetry, was 40 ± 20 A per end within a 30-cm radius. This implies that the nonambipolar radial ion confinement time is about 6 ms. It is dominated by losses near the plasma edge. The data in Figs. 9-7 and 9-8 was obtained along a diameter at each end of the machine and shows that any azimuthal asymmetry corresponds to an even azimuthal mode number.

Resonant-neoclassical transport theory should describe this experiment. An ion drifts 90° in azimuth in about 50 μs. For comparison, the transit time for a central-cell ion is 100 to 200 μs. Thus, the azimuthal drift is large ($\Delta\psi \gtrsim 1$), and resonant transport should dominate in TMX (see Sec. 9.2). TMX operates near the collisional boundary of the plateau regime (Fig. 9-1), because the ion-ion collision time is also 100 to 200 μs.

The net radial ion flux was computed from the negative electric current:

$$\Gamma(r) = \frac{2}{eLr}\int_0^r (-j_{net} + j_p)\, r\, dr \quad . \qquad (4)$$

In this equation, L is the central-cell length (314 cm), j_{net} is the electric current per end (A/cm^2 in the central cell) (Fig. 9-8), and j_p is the predicted electric current from each end-cell (Fig. 9-10). Figure 9-12 shows the radial fluxes determined using Eq. (4); theoretical results are shown for comparison. In the interior of the plasma ($r \lesssim 20$ cm), the net radial ion flux is small and may be inward. The large uncertainty is due to the end-cell losses j_p. Near 30 cm there is a significant outward net flux of ions in the central cell. At 28.5 cm, the flux is between 2.4×10^{15} cm$^{-2}\cdot$s^{-1} and 1.1×10^{16} cm$^{-2}\cdot$s^{-1}.

The bars in Fig. 9-12 show the range of predicted radial fluxes at several radii. The measured profiles were substituted into Eq. (1) to determine the resonant-neoclassical flux. The

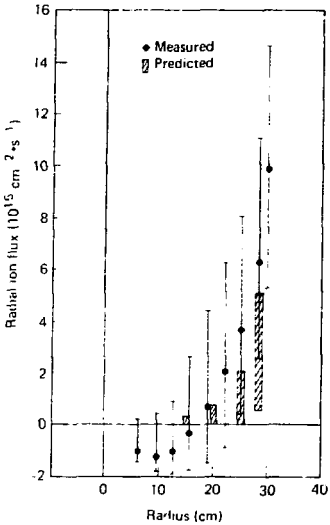

FIG. 9-12. **The radial ion fluxes in the central cell were determined based on Figs. 9-8 and 9-10. The solid data points are the experimental results and the cross-hatched bars are the theoretical limits.**

predicted flux depends on the derivative of the measured plasma-potential profile (Fig. 9-5). This derivative is not accurately determined by the data. As a result, the theoretical predictions are quite uncertain. The predicted fluxes due to other classical processes are less than 10^{14} cm^{-2}·s^{-1} and are too small to be shown on the figure.

The theoretical and experimental results overlap, but the actual flux might be larger than the resonant flux. The data at a 28.5-cm radius (shown also in Fig. 9-3) is significant. Both the measured flux and the predicted flux significantly exceed the fluxes due to other processes. The theoretical result at this radius corresponds to electric fields of 5 to 50 V/cm, on the basis of the plasma-potential data, and to an ion temperature of 10 to 60 eV, on the basis of the plasma diamagnetism and electron temperature. If the actual fluxes exceed the predicted fluxes, several explanations are possible. First, the measured negative electric current flowing to the end wall may not be azimuthally symmetric as assumed. Second, low-frequency fluctuations were detected in the central-cell plasma (see Sec. 11), and such fluctuations are known to cause ambipolar transport.[17] The assumptions of the present theories of these fluctuations imply that they cannot predict nonambipolar transport. If TMX violates these assumptions, such fluctuations might contribute to the nonambipolar transport. Third, parallel electric currents (Stupakov currents) may result from the quadrupole magnetic fields.[19,20] These currents may significantly increase the amount of neoclassical transport, but the increase of resonant transport is expected to be small. These parallel currents cannot affect the measurements, however, because they are zero on the vertical and horizontal magnetic axes where the measurements were made. Finally, other anomalous effects such as end-cell ion-cyclotron-frequency fluctuations or magnetic-field errors may contribute to the transport in ways that have not yet been discovered. TMX Upgrade will be a more sensitive test of resonant-transport theory; resonant transport is predicted to significantly affect its plasma parameters.

The results just discussed do not extend beyond a 30-cm radius because the profiles of electric current and plasma potential are not known. There appears to be a large negative electric current near the limiter (Fig. 9-8); the width of this current spike is uncertain. It might result from the scrape-off effect discussed in Sec. 9.2. The fueling at this radius could supply the observed electric current of 130 mA/cm^2 (Fig. 9-9). Thus, although the data is not sufficient to evaluate the electric current near the limiter in detail, the observed value is plausible.

9.3.5 Conclusions

Table 9-3 summarizes the results of this investigation of radial particle transport in TMX. The axial ion lifetime is implied by the measured densities and end-loss. A negative electric current was measured at the end wall; this has two implications. First, the axial electron lifetime is shorter than the axial ion lifetime, as indicated. Second, there must be a nonambipolar radial flux of ions, to neutralize the negative current that flows to the end wall. The negative electric current is 90 ± 40 A; the radial ion flux necessary to neutralize this current corresponds to a radial ion lifetime between 4 and 12 ms. Finally, gas-penetration studies showed that the fueling of the plasma was between 1 and 2.5 times

TABLE 9-3. **Measured current and time scales. Results are given as total losses from both ends of TMX.**

Process	Centerline results		Results for 30-cm cylinder	
	Current (A/cm^2)	Lifetime[a] (ms)	Current (A)	Lifetime[a] (ms)
Ion axial loss	0.055	2.8	90	4.8
Electron axial loss	0.004	2.4	180	2.0
Nonambipolar ion radial loss	-	-	90	∞
Ambipolar radial loss	-	-	≥0 ≤200	≤∞ ≥1.8

	Central cell	End cells	Total
Number of particles on centerline	8.8×10^{14}	7.5×10^{13}	9.5×10^{14}
Number of particles with a 30-cm radius	2.7×10^{18}	1.8×10^{17}	2.9×10^{18}

[a] Lifetime = eN/current, N = number of particles.

the axial electron losses. Both the Lyman-alpha data and the surface-probe data indicate that the code results may overestimate the fueling. As a result, the ambipolar radial losses are probably smaller than the losses due to other processes.

The nonambipolar radial ion flux implied by the observed negative electric current is consistent with the predicted radial ion flux due to resonant transport. However, the predicted flux is determined largely by the electric field; and the electric field is not accurately determined by the data. Thus, the actual net radial ion flux could be several times the flux due to resonant transport.

The ambipolar radial flux due to classical processes should be quite small compared to the observed end losses. This is possible, based on the gas-penetration code, the Lyman-alpha measurements, and the surface-probe data. However, the uncertainty in these results would allow ambipolar radial fluxes that were many times the classical value. However, the allowed ambipolar radial losses are at most equal to the axial losses; they are not large enough to dominate the power balance in the central cell.

Several possible causes of radial transport will be reduced in the TMX Upgrade. The central cell was designed to significantly reduce the resonant-neoclassical transport,[4] although such transport is still expected to affect the plasma parameters. The end cells are expected to be much less unstable to the modes observed in TMX (see Sec. 5). This should reduce any transport driven by ion-cyclotron-frequency fluctuations. The magnet alignment procedures and power-supply capabilities have been improved to reduce magnetic-field errors. Finally, the central-cell neutral beams and other equipment should allow control of the central-cell profiles.

9.4 RESULTS OF THE TMT RADIAL TRANSPORT CODE

Resonant-neoclassical transport is a complicated nonlinear process. It modifies the plasma characteristics that produce it, which include density, ion temperature, and electric field. It is difficult to predict simple scalings that can be compared with the data. The discussion in Section 9.3 illustrated these difficulties. A computer code can be uniquely useful in radial-transport studies because it can assess the expected role of transport in a self-consistent plasma model, which can then serve as a guide to help perform and interpret radial-transport experiments.

The TMT radial-transport code was developed to self-consistently treat resonant neoclassical transport, power balance, and particle balance. It determines equilibrium central-cell plasma-density profiles, temperature profiles, and

potential profiles. The end-cell plasma parameters are fixed and, for the runs described below, the ionized source of ions and electrons is an input to the code.

In summary, the code results indicate that the potential profile of the central-cell plasma is strongly influenced by the density profile of the plasma in the end cell. Variations in transport, ionized-source profiles, and other factors are much less important. Because the resonant-neoclassical transport is dominated by the electric field in the plasma, the end-cell plasma characteristics may be the largest determinant of central-cell radial transport. A comparison of code results from runs with and without resonant-neoclassical transport shows that this transport can significantly change the ion end losses and affect the ion-temperature profile.

governs axial ion loss from the central cell; and the radial variation of the potentials governs transverse diffusion of ions in the central cell.

The model equations used in the code have been described elsewhere.[3] For the TMX modeling, key input parameters include:

- The density and ion-energy profiles of the end-cell plasmas.

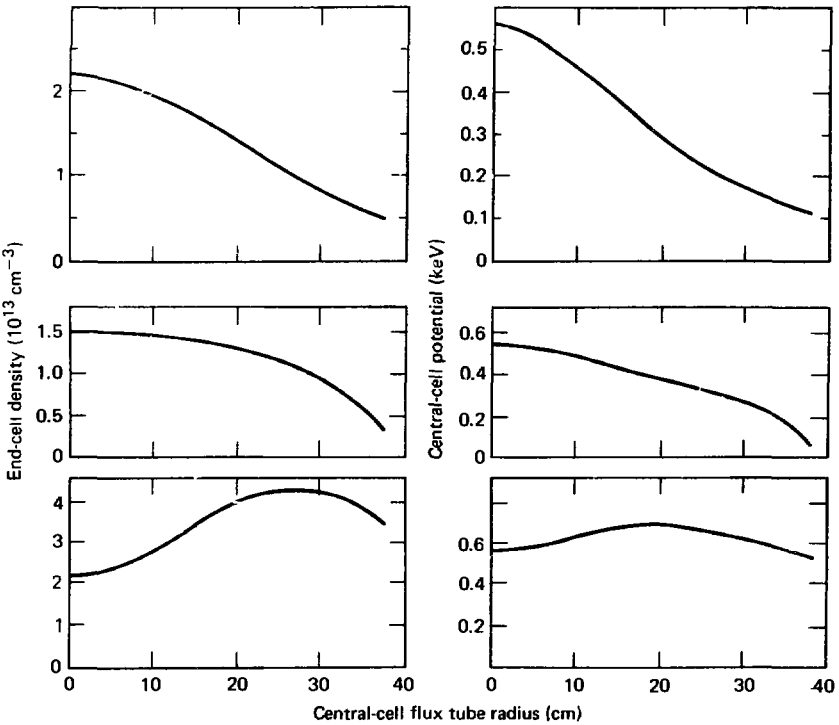

FIG. 9-13. TMT code results show how the shape of the central-cell potential profile follows the shape of the end-cell density profile.

- The ionized source of electrons and ions in the central cell as a function of central-cell radius.
- The fluctuating electric field in the central cell.

This fluctuating electric field is produced by the ion-cyclotron-frequency instabilities in the TMX end cells. It heats the central-cell ions and enhances their axial loss rate. These effects were included in the code on the basis of recent theoretical work (see Sec. 11).

Near the magnetic centerline, the code can easily reproduce the observed plasma parameters, by means of reasonable adjustments of the inputs described above. The radial profiles produced by the code may then be compared to the observed radial profiles.

9.4.1 The TMT Code

We are developing a computational model for tandem mirrors that includes an accurate description of both radial and axial losses. The system is governed by a set of moment equations for the densities and temperatures of the various plasma species. We reduce these to a one-dimensional (radial) form by averaging over a magnetic flux tube both azimuthally and longitudinally, with the flux tube labeled by its radial position, r, at the central-cell midplane. Thus, the independent variables for this model are radius, r, and time, t. The dependent variables are the plug ion density, n_p, and temperature at the end-cell midplane, T_p, the central-cell ion densities, n_c, and temperatures, T_c, and the electron temperature, T_e, which is assumed to be uniform over the entire length of a flux tube, including both end cells and the central cell.

The electron density is set equal to the local ion charge density in each flux tube. End-cell and central-cell ions are coupled by their energy exchange with the electrons that move freely between the end cell and central cell as well as by the plasma fluctuations. This electron model is currently being modified to incorporate the thermal-barrier concept. In addition to the densities and temperatures of the plasma species, we also compute self-consistent ambipolar potentials in both the end-cell (ϕ_p) and central-cell (ϕ_c). This is a very important feature of the model, because the potential difference between the end cell and central cell

9.4.2 Plasma Potential Profile

We found that the radial plasma-potential profile in the central-cell is most strongly influenced by the plasma-density profile in the end cell. Although other factors, such as the amount of radial transport or the fueling rate, affect the detailed radial dependence of the central-cell potential, they are less important. This result probably is due to the effect of the end-cell plasma on central-cell confinement. A larger end-cell density confines the central-cell ions better, and a larger plasma potential is needed to hold in the electrons.

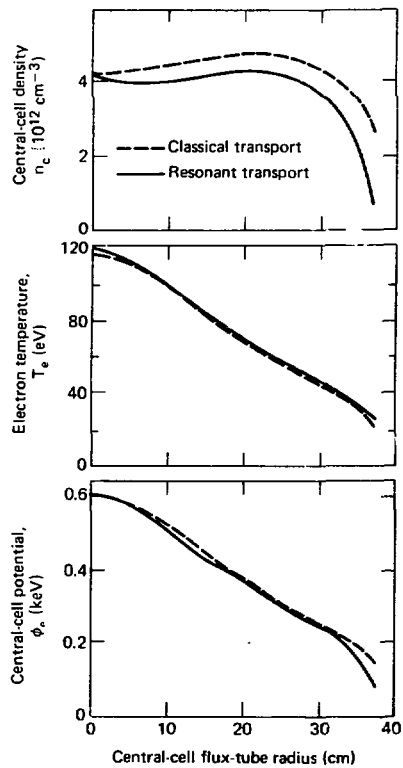

FIG. 9-14. TMT results for central-cell plasma density, electron temperature, and potential.

This result is illustrated in Fig. 9-13, which shows three end-cell plasma-density profiles and the corresponding central-cell potential profiles. Peaked (Gaussian), flat, and inverted profiles are shown. The shape of the central-cell potential profile is quite similar to that of the end-cell density profile. We changed the other input parameters, and the amount of radial transport, without changing this relation.

9.4.3 Effect of Transport

Some effects of radial transport are shown in Figs. 9-14, 9-15, and 9-16. These code results are similar to the data described in Section 9.3. Various plasma parameters are plotted as a function of radius in these figures. The dashed curves in these figures show results of a code run without transport; the solid curves show the results of a run with resonant-neoclassical transport. Except for the amount of transport, the inputs to these two runs were identical.

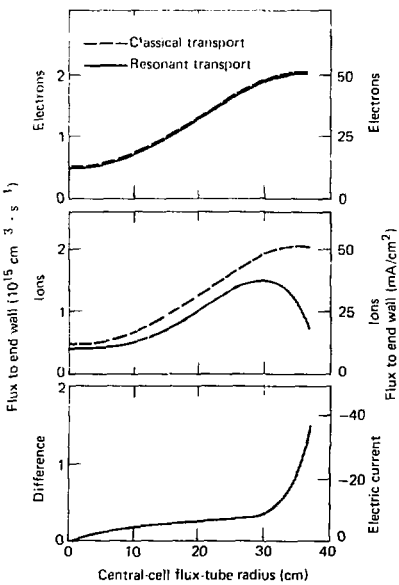

FIG. 9-15. TMT results for end losses. Radial transport produces a significant electric current.

Figure 9-14 shows central-cell density, electron temperature, and plasma potential as a function of radius. When resonant-neoclassical transport was included, these profiles became smoother. The plasma density near the plasma edge was reduced by the radial ion losses.

The negative electric current produced by resonant-neoclassical transport is shown in Fig. 9-15, which plots the central-cell axial electron losses, the central-cell axial ion losses, and the difference. The code assumes classical radial electron transport, so the axial electron losses are almost equal to the ionized plasma source. Without resonant-neoclassical transport, the axial ion losses equal the axial electron losses. With transport, the ions move radially and the net electric current is of the same general magnitude as the experimental result.

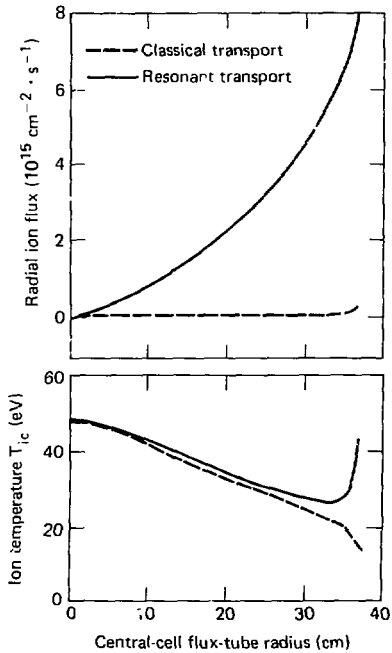

FIG. 9-16. TMT results for radial flux and ion temperature. Resonant-neoclassical transport can heat the ions at the edge.

The radial flux of ions and the central-cell ion-temperature profile are shown in Fig. 9-16. Resonant-neoclassical transport produces a significant radial ion flux, which, in turn, transports significant energy into the plasma at large radii. As the ions are transported down the radial potential hill, they are heated by the energy they acquire. The transport thus modifies the ion-temperature profile of the plasma.

REFERENCES

1. T. K. Fowler and B. G. Logan, "The Tandem Mirror Reactor," *Comments Plasma Phys. Cont. Fusion* **2**, 167 (1977).
2. G. I. Dimov, V. V. Zakaidakov, and M. E. Kishinevsley, "Thermonuclear Confinement System with Twin Mirror-Systems," *Fiz. Plazmy* **2**, 597 (1976).
3. M. E. Rensink, R. H. Cohen, and A. A. Mirin, "Radial Transport" in *Physics Basis of MFTF-B*, Lawrence Livermore National Laboratory, Livermore, CA, UCID-18496 (1980), p. IV-45.
4. F. H. Coensgen, T. C. Simonen, A. K. Chargin, and B. G. Logan, *TMX Upgrade Major Project Proposal*, Lawrence Livermore National Laboratory, Livermore, CA, LLL-PROP-172 (1980).
5. F. H. Coensgen, C. A. Anderson, T. A. Casper, J. F. Clauser, W. C. Condit, D. L. Correll, W. F. Cummins, J. C. Davis, R. P. Drake, J. H. Foote, A. H. Futch, R. K. Goodman, D. P. Grubb, G. A. Hallock, R. S. Hornady, A. L. Hunt, B. G. Logan, R. H. Munger, W. E. Nexsen, T. C. Simonen, D. R. Slaughter, B. W. Stallard, and O. T. Strand, "Electrostatic Plasma-Confinement Experiments in a Tandem Mirror System," *Phys. Rev. Lett.* **44**, 1132 (1980).
6. R. P. Drake, T. A. Casper, J. F. Clauser, F. H. Coensgen, D. L. Correll, W. F. Cummins, J. C. Davis, J. H. Foote, A. H. Futch, R. K. Goodman, D. P. Grubb, R. S. Hornady, W. E. Nexsen, T. C. Simonen, and B. W. Stallard, "The Effect of End-Cell Stability on the Confinement of the Central-Cell Plasma in TMX," *Nucl. Fusion* **21**, 359 (1981).
7. R. P. Drake, G. Deis, M. Richardson, and T. C. Simonen, "Gas Control and Wall Conditioning in TMX," *J. Nucl. Mat.* **93** and **94**, 291 (1980).
8. R. P. Drake, "Control of Plasma-Wall Interactions in Tandem Mirrors," in preparation.
9. A. H. Futch, "Radial Fokker Planck Code Studies of TMX," in preparation.
10. D. D. Ryutov and G. V. Stupakov, "Transverse Particle Losses in an Ambipolar Plasma Trap," *JETP Lett* **26**, 174 (1977).
11. D. D. Ryutov and G. V. Stupakov, "Neoclassical Transport in Ambipolar Confinement System," *Fiz Plazmy* **4**, 501 (1978) [*Sov. J. Plasma Phys.* **4**, 278 (1978)].
12. D. D. Ryutov and G. V. Stupakov, "Diffusion of Resonance Particles in Ambipolar Plasma Traps," *Dokl. Akad. Nauk SSSR* **240**, 1086 (1978) [*Sov. Phys. Dokl.* **23**, 412 (1978)].
13. R. H. Cohen, "Analytic Approximation to Resonant Plateau Transport Coefficients for Tandem Mirrors," *Nucl. Fusion* **19**, 1579 (1979).
14. R. H. Cohen, "Orbital Resonances in Non-axisymmetric Mirror Machines," *Comments Plas. Phys. Cont. Fusion* **4**, 157 (1979).
15. T. D. Rognlien and Y. Matsuda, "Tandem Mirror Confinement in the Presence of Ion Cyclotron Fluctuations," *Nucl. Fusion* **21**, 345 (1981).
16. J. B. Taylor, "Diffusion of Plasma Ions Across a Magnetic Field," *Phys. Fluids* **4**, 1141 (1961).
17. W. Horton, "Drift Mode Stability Analysis for the Tandem Mirror," *Nucl. Fusion* **20**, 321 (1980).
18. A. W. Molvik, "Large-Acceptance-Angle Retarding-Potential Analyzers," *Rev. Sci. Instrum.* **52**, 5 (1981).
19. G. V. Stupakov, "MHD Equilibrium in a Tandem Mirror System," *Fiz. Plazmy* **5**, 871 (1979); [*Sov. J. Plasma Phys.* **5**, 486 (1979)].
20. L. D. Pearlstein, T. B. Kaiser, and W. A. Newcomb, "Analytic Equilibria with Quadrupole Symmetry in the Paraxial Limit," submitted to *Phys. Fluids*; Lawrence Livermore National Laboratory, Livermore, CA, UCRL-85039 (1980).

SECTION 10
END PLUG OPTIMIZATION EXPERIMENTS

(D. L. Correll, R. P. Drake, D. P. Grubb, W. E. Nexsen, and P. Poulsen)

10. End Plug Optimization Experiments

10.1 INTRODUCTION

This section describes three experiments directed at optimization of TMX end plugs by reducing the level of ion cyclotron fluctuations. The scaling of TMX confinement was described in Sections 4 and 5. We were able to approach Coulomb confinement in the end plugs with conditions of high density and low electron temperature, but under other conditions, end-plug ion cyclotron fluctuations degraded confinement.

In an attempt to extend the region of classical confinement, we carried out separate end-plug optimization experiments by:

In an attempt to extend the region of classical confinement, we carried out separate end-plug optimization experiments by:

- Increasing the end-plug ion energy with higher-voltage neutral beams.
- Injecting electron beams along the axis of TMX.
- Feeding gas at the outside mirrors using a gas box.

In the neutral-beam experiments, increasing the beam energy of one end-plug reduced the central-cell plasma losses through that plug, in agreement with our expectations based on drift-cyclotron loss-cone (DCLC) quasi-linear stabilization requirements. In the electron-beam experiments, the injected beam did not substantially affect the fluctuation level or plasma parameters. We concluded that absorption of energy from the electron beam is inhibited in TMX by the peaked axial density distribution. In the outside-gas-box experiments, we found that we could obtain independent control of end-plug densities relative to central-cell densities. The outside gas box did not suppress the fluctuation levels.

While these stabilization experiments were being performed, a new method for achieving end-plug microstability emerged, involving the use of sloshing ions. Neutral beams injected off normal (e.g., 45°) will generate a longitudinal density profile with a peak off of the midplane. The midplane density depression will accumulate low-energy ions which provide DCLC stability. Because these ions would not simply flow through the end-plugs, much less power would be lost than is the case in TMX. The TMX magnet geometry did not allow neutral beam access for such experiments; therefore this new concept will be tested in the TMX Upgrade thermal barrier experiment.

10.2 VARIABLE NEUTRAL-BEAM VOLTAGE EXPERIMENT

According to DCLC theory, end-plug stability is expected to improve as the end-plug ion energy is increased. This theoretical scaling arises because a higher ion energy relative to a fixed ambipolar hole in velocity space reduces the drive for the DCLC microinstability, and thus also reduces the current required for stabilization. As a result, the central cell does not need to supply as much plasma to the end plug for stability, and central-cell confinement improves. If the ambipolar potential increases, confinement improves further. The neutral-beam energy-variation experiments reported here show that central-cell confinement improvements do occur.

The experimental arrangement was as follows: B_c = 1 kG, B_p = 8.5 kG (83% of full current in the baseball coils (3715 A) and 100% everywhere else), deuterium gas box at 400 T, and deuterium plug beams (no central-cell beams were used). The gas-box feed varied from 680 to 920 A of D° (note that at 400 Torr the gas box normally supplied 1360 A). The west plug was sustained with a constant 85 A of injected-beam current with a beam voltage of 16 kV; we were unable to further increase the beam voltage of the west plug. The east plug was run in three modes with injected beams of: (1) 70 A at 11 kV, (2) 70 A at 16 kV, and (3) 50 A at 32 kV and 20 A at 16 kV (the beam-attenuation-detector beam), which gives an average beam voltage of 27.5 kV.

In order to test whether the central-cell confinement improves with higher end-plug ion energies, we determined experimentally the ratio of the particle-containment parameter, $n\tau$, to that expected for collision-dominated flow, $n\tau_{flow}$. If the end losses are determined simply by collision-dominated flow over a potential hill,

$$\phi = T_{ep} \ln (n_p/n_c) \quad , \qquad (1)$$

then we expect

$$\frac{\langle n\tau \rangle}{2\langle n\tau_{flow} \rangle} = \left(\frac{n_p}{n_c}\right) T_{ep}/T_{ic} \quad , \qquad (2)$$

where n_p is plug density, n_c is central-cell density, T_{ep} is plug electron temperature, T_{ic} is central-cell ion temperature, and R is the mirror ratio between the central cell and the center of the plug. We had direct measurements of all of these parameters except T_{ic}. To determine T_{ic} on the centerline, we assumed that the central-cell electron and ion temperatures were equal and that both had a radial scale length equal to the radial density scale length. With this model we found

$$\hat{T}_{ic} = \hat{T}_{ec} = (\bar{T}_{ic} + \bar{T}_{ec}) \frac{3.55 \times 10^{10} \, m \, B_z}{(nl)_c \, r_c} \quad ,$$

where $\wedge$ denotes a peak value, – denotes an average value, and where we have assumed that

$$\frac{\bar{T}_{ic} + \bar{T}_{ec}}{\bar{T}_{ic}} = 1 \quad .$$

Here m is the central-cell magnetic moment obtained from diamagnetic loops. Using this model, we have plotted in Fig. 10-1 the experimental values of both sides of Eq. (2). Here each point is the mean of several shots with beam accel voltage as designated. While the left and right sides of Eq. (2) are not exactly equal, the trend is in the right direction. The lack of better agreement is probably due to our model for T_{ic}; in fact, considering the sensitivity of Eq. (.) to T_{ic}, the agreement that we do have is perhaps surprising.

The quasi-linear warm plasma end-loss current j_{ql} necessary for stabilizing the DCLC scales as

$$j_{ql} \propto \frac{n_p T_{ep}^{3/2}}{E_p} \quad , \qquad (3)$$

where E_p is the average plug ion energy, obtainable from reduction of the plug diamagnetic signal. In

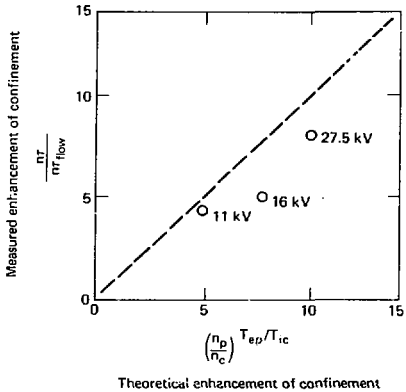

FIG. 10-1. Comparison of measured and theoretical tandem confinements for three neutral-beam accel voltages.

Eq. (3), ϕ_p is assumed to be proportional to T_{ep}. In Fig. 10-2, we plot the experimental values of the east end-loss current versus the values of Eq. (3), having normalized both to the 11-kV injection values. These end-loss currents exceed the trapped neutral-beam current by about an order of magnitude, indicating that the end-loss current is from the central cell. We see that the end losses appear to obey the scaling of Eq. (3) quite well.

For comparison of the magnitude of the experimental end-loss current with the value predicted by the quasi-linear theory, we use two equations for the quasi-linear stabilization current,

$$j_{ql} = \frac{6.3 \times 10^{-13} \, (e\phi/T_{ep})^{3/2} n_p T_{ep}^{3/2}}{(R - 1) A^{1/2} E_p} \quad , \qquad (4)$$

and

$$j_{ql} = \frac{1.9 \times 10^{-12} \, (e\phi/T_{ep})^{3/2} n_p T_{ep}^{3/2}}{(R - 1) A^{1/2} E_p} \times (r_p/a_i)^{-4/3} \quad , \qquad (5)$$

where Eq. (5) includes the effects of (r_p/a_i) scaling on the quasi-linear requirements. Here T_{ep}, E_p are in keV, n_p in cm^{-3}, R is the effective plug mirror

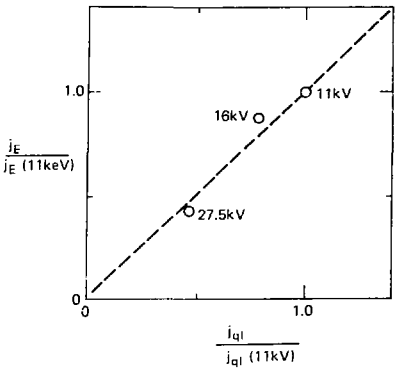

FIG. 10-2. Comparison of measured and theoretical end-loss currents normalized to their respective values at 11 kV beam voltage. j_E is the mean end-loss current measured for 11-, 16-, and 27.5-kV injected neutral beams, j_{ql} is the quasi-linear end-loss current calculated from Eq. (3). Both j_E and j_{ql} are normalized to the 11-kV injection values.

ratio, r_p is the plasma radius, a_i is the ion gyroradius, A is the ion mass in amu, and $(e\phi/T_{ep})$ is constant at approximately 3.5. Although steady state equilibrium was only approximately achieved for the low beam currents at which these experiments were carried out, the basic conclusions are not altered. The values tabulated in Table 10-1 were obtained using (R - 1) = 1 and A = 2. Equation (4) appears to give a more nearly constant value for the ratio of the measured to the quasi-linear end loss, j_e/j_{ql}, than does Eq. (5). Equations (4) and (5) assume equal flow of stabilizing current out both ends of the plug. If the flow is mainly from the central cell through the plugs, then the quasi-linear requirement is a factor of 2 higher. Thus, we expect the agreement between experimental values and twice the calculated values from Eq. (4) that is shown in Table 10-1 ($j_e/2j_{ql}$ = 1).

The minimum quasi-linear current of Eq. (4) occurs when the temperature of the stabilizing ions, $T_{w'}$ is equal to the hole temperature, or $T_w \approx 3\text{-}6\ T_{ep} \approx 300\text{–}600$ eV; experimental values of the central-cell ion temperatures are of the order of 50

TABLE 10-1. Effects of increasing east end-plug neutral-beam energy on TMX east plug and central-cell parameters.

	Increasing beam voltage (V_{inj})		
	11 kV	16 kV	27.5 kV
Beam current, I_{inj} (A)	70A	70	50A @ 32 k 20A @ 16 kV
Plug mean ion energy, E (keV)	5.7	9.2	14.6
Plug electron temperature, T_{ep} (eV)	96 ± 21	121 ± 35	133 ± 20
Plug density, n_p (10^{13} cm^{-3})	1.1	1	0.84
Plug beta, β_p (%)	3.5	5.1	6.8
Central-cell density, n_c (10^{12} cm^{-3})	3.9	4.8	3.7
Central-cell ion temperature, T_{ic} (eV)	62	44	48
Central-cell beta, β_c (%)	1.9	1.7	1.4
Theoretical enhancement of confinement, $(n_p/n_c)T_{ep}/T_{ic}$	4.9	7.7	10.0
Measured enhancement of confinement, $n\tau_c/2n\tau_{flow}$	4.3	5	8.2
Measured end loss current density, J_E (A/cm^2)	0.32	0.28	0.14
Required theoretical end loss current density			
j_{ql} (A/cm^2), Eq. (4)	0.168	0.134	0.082
j_{ql} (A/cm^2), Eq. (5)	0.062	0.061	0.052
Ratio of measured to theoretical end loss current density			
$j_E/2j_{ql}$, Eq. (4)	0.9[c]	1.35	0.85
$j_E/2j_{ql}$, Eq. (5)	2.	2.3	1.35

eV. With such a low-temperature stream, the plasma is predicted to be unstable to "double-humped" modes. The quasi-linear model shows that the nonlinear effect of these double-humped modes is to heat the lower energy component. This may explain why the temperature of the end-loss current appears to be quite a bit higher than the values of T_{ic} inferred from the diamagnetic-loop measurements. Baldwin has pointed out that, if this process is important, we would not expect to have $(r_p/a_i)^{-4/3}$ scaling; i.e., that Eq. (4), which best fits the data, is the proper relation to use.

In conclusion, we found experimentally that the measured central-cell end-loss current required for plug microstability decreased with end-plug ion energy, in accordance with DCLC requirements. As a consequence, the central-cell electrostatic confinement improved, as shown in Fig. 10-1.

10.3 ELECTRON-BEAM STABILIZATION EXPERIMENTS

Experiments carried out on Constance I demonstrated that DCLC fluctuations could be stabilized by injecting an electron beam into the plasma. The Constance I experiments were motivated by earlier PR6 and PR7 experiments that used microwave electron-cyclotron resonance heating (ECRH) for stabilization. Although certain aspects of these ECRH experiments are unexplained, the basic explanation is that a potential well is generated that confines low-energy ions for stability. On the basis of this empirical knowledge and some preliminary experience on 2XIIB, we initiated electron-beam (e-beam) experiments on TMX. In order that the effects of the electron beam could be competitive to other processes we selected a megawatt e-beam (30 keV, 30 A).

Electron beams were injected into the TMX plasma from positions in the end fan and along the centerline magnetic field line. Figure 10-3 shows the approximate position of the electron-guns. The electron-guns were first mounted at "a" on the east-end flange of TMX. In succeeding experiments, electron-guns were placed on the centerline of the machine, first at "b", 30 cm outside the outer mirror points and then at "c", 5 cm outside the outer mirror points.

The "a" experiments, discussed in detail by Poulsen and Grubb,[1] showed that injection of the e-beams did not in general affect the fluctuation level or the plasma parameters. At high plasma densities in the end plug (greater than 10^{13} cm^{-3}), neither the rf level nor any of the plasma

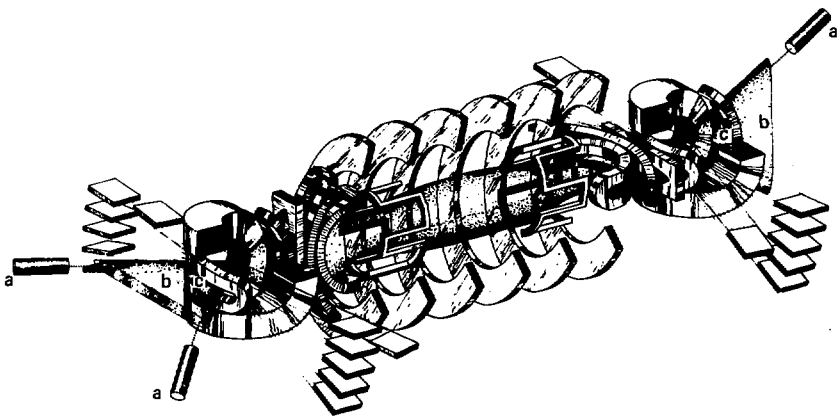

FIG. 10-3. Schematic of TMX indicating electron-gun positions. Points marked are (a) positions of guns for end-fan experiments, (b) positions of guns for the first axial-injection experiment, and (c) positions of guns for the second axial-injection experiment.

parameters were affected by injection of the e-beam. Instances of reduced ion-cyclotron fluctuations and of bulk heating of electrons were found at low end-plug plasma densities (less than about 10^{13} cm^{-3}), i.e., with the plasma frequency less than the electron-cyclotron frequency at B_{min} and low fluctuation levels. Ion-cyclotron fluctuations at low plasma densities are observed to be weak and sensitive to plasma parameters and boundary conditions. The e-beams did not consistently reduce the fluctuations, and the effects noted could be ascribed to perturbations of the plasma and its boundaries due to the injection of the e-beams. Electron heating occurred in a set of experiments in which only the east plug was operated. The electron temperature increased from approximately 90 to 140 eV. The plug was started with streaming guns and the e-beams were injected 0.5 ms after the guns were turned off. The e-beams had no significant effect on the ion-cyclotron fluctuations under these conditions.

Injection of the e-beams into the normal TMX configuration did not produce hard (> 50-keV) x-rays because of the presence of mirror-confined electrons, and did not increase the bulk electron temperature. These results are at variance with the results obtained in previous experiments in which e-beams were injected into plasmas of similar density and magnetic field.[2] This difference in results points to a difference in the mechanism of either the beam-plasma interaction or a difference in the wave absorption.

Analysis of the interaction of electron beams with a mirror-confined plasma shows that the mechanism for wave absorption depends upon the axial profiles of density and magnetic field. The waves are generated at a frequency between that of the upper hybrid [$\omega_H = (\omega_c^2 + \omega_p^2)^{1/2}$], and the greater of the plasma frequency, ω_p, or the electron-cyclotron frequency, ω_c (see Ref. 3). At low density (less than 10^{13} cm^{-3}), the propagating waves in a TMX plug will encounter an electron-cyclotron resonance, as indicated in Fig. 10-4. However, we hypothesize that the absorption is not efficient because of the relatively low density in the resonance region. At densities greater than 2×10^{13} cm^{-3} (illustrated in Fig. 10-5), the waves can reflect from the envelope of the upper hybrid cut-off and be absorbed at a plasma resonance. Bulk electron heating has not been observed in either the 2XIIB[4] or the TMX experiments under these conditions. Absorption at the plasma resonance tends to add energy to the electrons in a direction parallel to the magnetic field lines.[5] It is possible, therefore, that the electrons that gain energy from the waves will leave the plasma if allowed to do so by the ambipolar potential and the collisionality of the plasma. Since the wave potentials can exceed the ambipolar potential and the collisionality of the electrons is small, these conditions can be satisfied in TMX.

We find, therefore, that absorption at the cyclotron resonances in TMX is inhibited by the peaked axial density distribution, and that hot, mirror-confined electrons are not produced. Under conditions where it is plausible that the axial density profile is less peaked, i.e., after stream gun turnoff, an increase in bulk electron temperature with beam injection was measured. The ion-cyclotron fluctuations were not significantly affected by injection of the electron beam for the range of plasma parameters investigated.

10.4 OUTSIDE GAS-BOX EXPERIMENTS

The outside-gas-box experiments were an attempt to obtain an extended electrostatic scaling of the axial confinement of central-cell ions. The scaling of axial central-cell confinement in TMX is limited by end-plug stability (see Sections 4, 5, and 6). The central-cell losses cannot be reduced below the amount required to stabilize the end plugs. The outside gas boxes were intended to improve the stability of the end plugs in order to decrease the losses needed from the central cell. In particular, the outside gas boxes were expected to reduce the instability drive in the end plugs by increasing the plasma density at the outer mirror, which would decrease the difference between the plasma potentials of the end-plug midplane and the outer mirror. This plasma-potential difference (corresponding to ambipolar hole in velocity space) is one of the causes of the DCLC instability. Thus, the outside gas boxes might improve end-plug stability and allow us to observe a scaling of axial central-cell confinement determined by electrostatic effects.

The outside gas boxes on each end of TMX extended 10 cm along the magnetic field; the outer

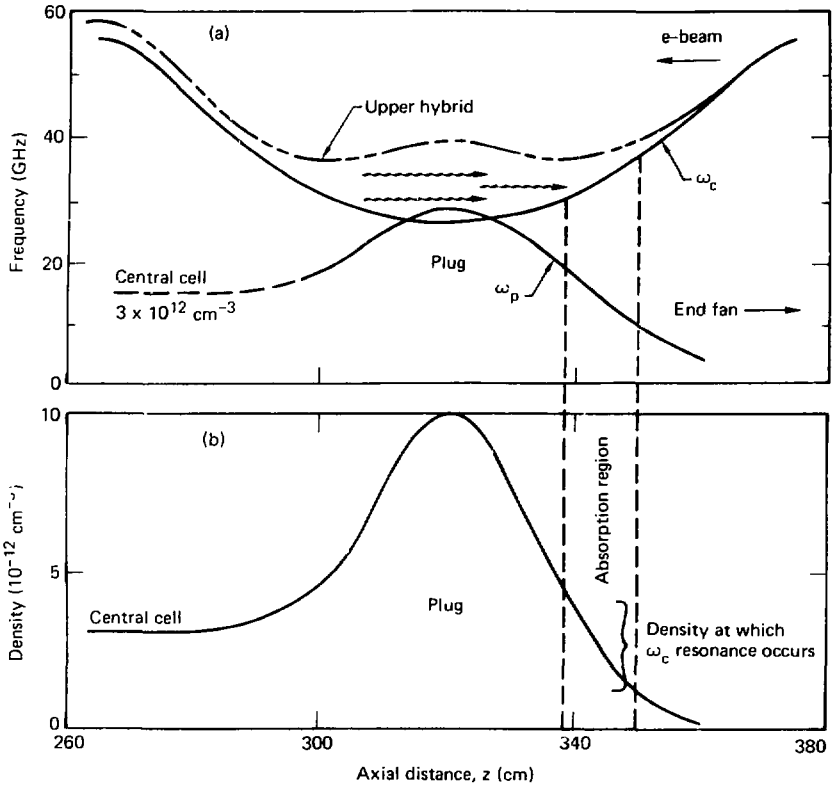

FIG. 10-4. Axial frequency and density profiles for a TMX plug. The frequency plot (a) indicates the axial position of the fundamental electron-cyclotron resonance. The corresponding density of the absorption region is indicated in (b).

jaw of each one was positioned at the outer magnetic mirror of the end cell. The opening in the gas-box jaws was shaped to conform to the flux surface defined by a circle of 15-cm radius at the end-cell midplane. Each outside gas box was equipped with four piezoelectric valves that were controlled and operated by the same techniques used to run the inside gas boxes (see Appendix A).

The type and amount of gas fueling affected the plasma parameters. Some of these effects are illustrated in Fig. 10-6. The left column shows the effects of fueling with roughly 550 A of current from the outside gas boxes only. When both gas boxes were used (1170 A total), the central-cell density increased, the end-plug density increased slightly, and n_p/n_c decreased by a factor of 2, as the central column shows. Then, when only the inside gas boxes were used, the central-cell density again increased and n_p/n_c decreased to the characteristic value of 3 to 4 (shown in the right column). Use of the outside gas boxes did not substantially reduce the plasma fluctuations.

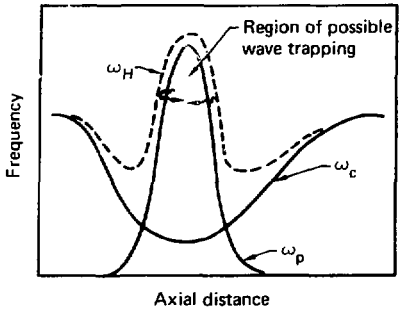

FIG. 10-5. Frequency of a plasma with a highly peaked axial density distribution. The waves that are generated may be trapped within the upper hybrid cutoff and absorbed by the plasma resonance.

These results were unexpected. We had thought that the outside gas box would stabilize the end plug and allow the central-cell density to increase; on the contrary, use of the outside gas box led to a decrease in central-cell density.

Evidence regarding radial transport is provided by the end-loss current and the radial profile of ion-saturation current. As Fig. 10-6 shows, the end-losses on centerline are independent of the gas-fueling technique. However, the radial profile of end losses varies substantially with method of fueling, as Fig. 10-7 shows. The end-loss profiles at the east end wall were measured with ion-saturation-current detectors biased at -1000 V. The signal on these probes is an indication of the density of the end-loss ions. The calibration is not known, but large qualitative changes are significant. Inverted end-loss profiles were observed when the outside gas box was used alone. These are expected because most of the gas is ionized near the edge of the plasma. In contrast, the inside gas box produced a peaked end-loss profile. The end losses on centerline were the same in the two cases, but the shots with the inside gas box produced lower total end losses. When both gas boxes were used, a flat profile of end losses was observed. The significant difference in the end-loss-current profiles may reflect both fueling and radial transport in the plasma. A peaked end-loss profile similar to that obtained with the inside gas box only is described

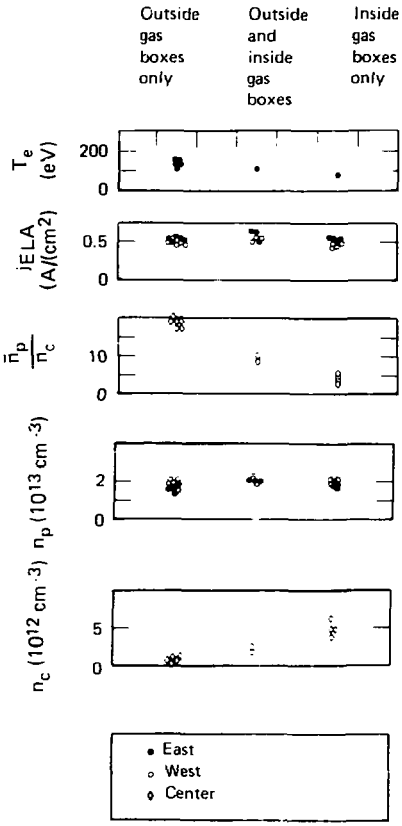

FIG. 10-6. The effects of the type and amount of gas fueling on plasma parameters including electron temperature (T_e), end-loss current (j_{ELA}), end-cell to central-cell density ratio (n_p/n_c), end-cell density (n_p), and central-cell density (n_c).

and evaluated in the radial-transport section (Sec. 9).

The use of the outside gas boxes did not substantially affect the stability of the end plugs. Two explanations are suggested here. First, perhaps the plug-to-mirror potential drop was not affected by

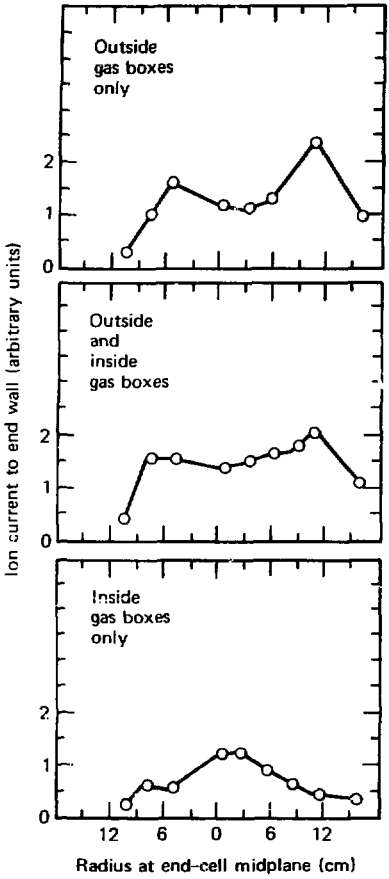

FIG. 10-7 End-loss profiles, measured by ion-saturation current detectors, for various gas-fueling techniques

the fueling at the outside mirror point. The end-loss current density at the machine centerline did not change, which suggests that the plasma density at the outer mirror was not changed. (At large radii, the density at the outer mirror was increased). Second, perhaps the dominant instability is not driven by the plasma potential. That is, the instability may not be the DCLC mode. These possibilities are being investigated. Since the outside gas box did not produce substantial improvements in central-cell plasma confinement, we did not pursue the experiment further.

REFERENCES

1. P. Poulsen and D. P. Grubb, *Results and Analysis of the TMX Electron-Beam Injection Experiments*, Lawrence Livermore National Laboratory, Livermore, CA, UCID-18725 (1980).
2. R. E. Klinkowstein and L. D. Smullin, "Suppression of ω_{ci} Instability in a Mirror-Confined Plasma by Injection of an Electron Beam," *Phys. Rev. Lett.* **40**, 771 (1978).
3. M. Seidl, "Temperature Effects on High-Frequency Beam Plasma Interaction," *Phys. Fluids* **13**, 966 (1970).
4. D. P. Grubb, B. G. Logan, J. F. Clauser, F. H. Coensgen, D. L. Correll, W. F. Cummins, R. P. Drake, J. H. Foote, A. H. Futch, R. K. Goodman, W. E. Nexsen, M. Siedel, T. C. Simonen, and W. C. Turner, "Electron Beam Stabilization Experiments," in *Magnetic Fusion Energy Quarterly Report—July through September, 1978*, M. A. Harrison and J. R. Strack, eds., Lawrence Livermore National Laboratory, Livermore, CA, UCRL-50051-78-3 (1978).
5. M. Seidl, *A Review of Electron Beam Heating of Magnetic Mirror Confined Plasmas, with Applications to the Tandem Mirror Experiment*, Lawrence Livermore National Laboratory, Livermore, CA, UCRL-52759 (1979).

11. Fluctuation Measurements

11.1 INTRODUCTION AND SUMMARY

Several analyses are presently on-going to determine the nature of fluctuations observed and their effects on confinement. Our present understanding leads to a description of the high-frequency plug-generated fluctuations which is most often consistent with an Alfvén ion cyclotron (AIC) instability. Three observations are consistent with the AIC-like wave:

1. The measured small values for azimuthal mode number, m = 2 to 7, in the end cells.
2. Propagation often occurs in the electron rather than ion diamagnetic direction.
3. The polarization of magnetic fluctuations.

These measurements show that in TMX we succeeded in suppressing the DCLC mode and that our measurements were the first observation of the theoretically predicted AIC mode.

Additional evidence lending support to the AIC interpretation of the data is the lack of consistency in the amount of stream stabilization current measured relative to that predicted by drift cyclotron loss cone (DCLC) theory. This agreed well with the 2XIIB data with variations interpreted as being due to a non-optimum value of stream temperature. In TMX, end-loss measurements often exhibit transmitted stream energies to 1 keV indicating the experimentally measured[2] high end-loss densities relative to the DCLC stability limit are not due to a lack of stream quality. In addition, end-cell performance empirically scales with the AIC instability drives as discussed in Section 6. Finally, the relatively low value of the oscillation frequency, $f/f_{ci} \sim 0.85$–0.9, which cannot be totally accounted for by the β-depressed magnetic field, is more easily explained by AIC rather than DCLC.

The AIC mode is driven by beta and anisotropy[3,4] and tends to be more stable as finite length corrections are included.[4] The TMX end-cell plasmas, while being lower β than 2XIIB, are more anisotropic and thus more susceptible to the AIC mode. The 2XIIB plasma had smaller radial scale lengths than TMX and thus was more susceptible to a DCLC mode. These comparisons are summarized in Table 11-1 where small R_p/a_i is DCLC unstable and large $\beta < W_\perp/W_{||} >^2$ is AIC unstable. This provides an explanation of why the AIC mode should play a greater role in TMX. It is also noted that depending on the mode of operation, data consistent with DCLC-like fluctuations have been observed on TMX. Some evidence exists for the simultaneous presence of both instabilities. Those parameter variations leading to the existence of either or both modes are presently under consideration.

Independent of the exact nature of the instability present, the performance of the TMX end cells is limited in peak density by the marginal stability requirements for the dominant mode. Here, marginal stability refers to steady-state operation where competing processes remain in balance and determine a macroscopic operating condition at a finite level of fluctuations. Evidence exists for propagation of end-cell generated modes into the central cell where they degrade central-cell confinement[5] as evidenced by decreasing $(n\tau)_c$ with increasing fluctuation levels. The fluctuations heat central-cell ions (present model of fluctuations is that only a flute-like, perpendicular electric field is important[6]) and result in an increased ion end-loss current at average energies exceeding the central-cell ion temperature.

It is believed that the rather high end-loss energies experimentally measured along with the large values of end-loss current are a response of the system to optimize the quality (temperature as well as density) of the stabilizing plasma. This ought to provide adequate stream to stabilize the DCLC mode and explain why it is usually not observed in TMX. Whether or not the enhancement of the end-loss current over that predicted for

TABLE 11-1. Stability parameters.

	R_p/a_i	β	$\left\langle \frac{W_\perp}{W_{\|\|}} \right\rangle \beta$	$\left\langle \frac{W_\perp}{W_{\|\|}} \right\rangle^2 \beta$
2XIIB	3 typical	0.4	4.8	6.9
TMX	6-8	0.07	13.8	13.3

DCLC stability[7] is an attempt to satisfy the AIC stability condition is as yet uncertain. The stabilizing effect of stream on AIC is presently[8] under study. In any event, the sloshing-ion distribution employed in the TMX-Upgrade design should reduce the AIC drive by spreading the anisotropy of the end-cell ion velocity distribution because the hot-ion beta is low. Likewise, the sloshing-ion distribution will confine low-energy ions to provide DCLC stability.

11.2 SUMMARY OF MICROSTABILITY THEORY FOR TMX

The TMX end-cell magnet design was based on 2XIIB experience, and for this reason the anticipated performance was expected to be similar. The central cell was designed to supply plasma to stabilize the DCLC mode, namely, by partial filling of the loss cone of the ion velocity distribution with warm plasma lost from the central-cell region. TMX experiments showed that the end-plug densities were similar to that achieved in 2XIIB for comparable neutral-beam currents. The TMX electron temperatures were higher. Analysis of the TMX fluctuation characteristics (reported in this section) as well as scaling (reported in Section 6) showed marked differences with 2XIIB. The DCLC and AIC modes are theoretically unstable in both TMX and 2XIIB. The 2XIIB experiment was found to agree fairly well with a quasilinear stability theory based on the DCLC mode in terms of the density evolution, mode characteristics, and magnitude of stabilizing stream measured from ion end losses. In TMX we appear to have succeeded in suppressing the DCLC mode. Instead the fluctuations and scaling were those related to the AIC mode.

The DCLC characteristics as determined from an electromagnetic dispersion relation that allows for variation along the magnetic field have been discussed in several reports[9-12] along with various other loss-cone modes. The salient features[10] are reviewed here. The flute-like mode taps energy from the loss-cone feature (inverted energy population) of the perpendicular velocity distribution. It is driven unstable in the presence of radial density gradients by coupling to an ion drift wave. These features predict both a dependence on the radial density scale lengths measured in units of ion gyroradii, R_p/a_i, with large values being stable and moderate values of azimuthal mode number m, $k_\# \simeq m/R_p$, indicating considerable spatial structure perpendicular to the magnetic field in order to tap the unstable region of the ion velocity distribution. Given a plasma size determined from the designed magnet and neutral-beam injection geometry, the required stabilization stream current to provide warm plasma to fill the loss cone to marginal stability can be determined.[10,12,13] Typical results for 2XIIB and, by design, reasonably applicable to TMX end cells are shown in Fig. 11-1.

A second mode predicted to be unstable[14] in 2XIIB but not experimentally identified is the Alfvén Ion Cyclotron[15] (AIC) mode driven unstable by plasma beta, β, and the anisotropy of the hot-ion velocity distribution, $\langle W_\perp/W_{||}\rangle$. This is an electromagnetic instability which has been studied in the limit $k_\perp = 0$ for infinite plasmas[3] and more recently using finite geometries[4] including a model for nonzero perpendicular wave numbers. Given the limit $k_\perp = 0$ or $k_\perp \sim 1/R_p$, a signature of this mode would include the appearance of small

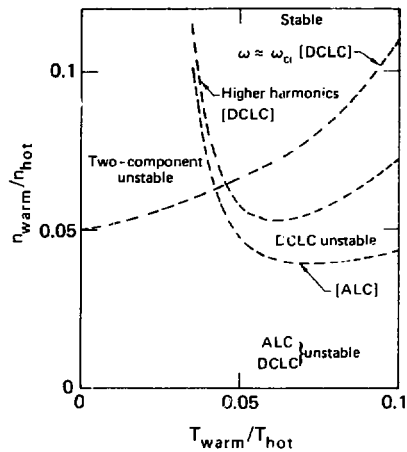

FIG. 11-1. Fraction of warm plasma versus temperature ratio required for stability for a 2XIIB parameter range; $T_{hot}/T_{hole} = 10$, $E_i = 13$ keV, $R_{vac} = 2$, $\beta \simeq 0.5$.

azimuthal mode numbers. Theory does not predict a preferred direction of perpendicular propagation. Similarly, depending upon the beta and anisotropy, the mode may appear at frequencies substantially below the ion cyclotron frequency with parallel wavelengths in the range $\lambda_{\parallel} \approx 2\pi c/\omega_{p_i}$. The infinite medium stability boundary is shown in Fig. 11-2 where it is noted that finite dimensions[4] tend to reduce the region of absolute instability at higher betas. The quasilinear stabilization mechanism results in a spreading of the anisotropy of the hot-ion velocity distribution. At the present time, theoretical studies are being conducted[8] concerning stabilizing effects of the central-cell plasma either by the streaming of unconfined central-cell ions through the end cells or by the density overlap of confined particles between the two regions. Stability is achieved[3] by cyclotron damping of the wave on a warm plasma component.

Other loss-cone modes which have been analyzed are the axial loss cone (ALC) mode, the negative energy wave (NEW), and the two-component instability. Due to the fanning of field lines in the minimum-B geometry of the end cells, a spatial variation of the perpendicular wave number is introduced. This effect eliminates a necessary condition[16] (unique value for the Bessel function argument in the dispersion relation) for the Dory-Guest-Harris instability which is therefore not expected to occur. The relatively short axial scale length $L_m \approx a_p$ of the TMX end-cell magnetic geometry limits the growth rate for the ALC instability[17] which is expected to be stable. The resulting stream stabilization requirements for the ALC are less restrictive than for the DCLC mode as evidenced in Fig. 11-1 and thus the ALC should not limit the performance. As indicated in Fig. 11-1, the two-component mode[15] is also more stable than the DCLC mode provided the stream source is warm enough i.e. $T_{warm}/T_{hot} > 0.04$. The two-component mode may be a problem if only cold stream is available such as during buildup. It is expected that the two-component mode would heat the stream and force the system to evolve to a steady-state condition at the minimum of the stability boundary where this mode does not constitute a problem. At large radial scale lengths the DCLC mode evolves into a negative energy wave[18] for $\omega \approx \omega_{c_i}$. At short axial scale lengths the NEW is stable and not considered important for the TMX geometry.

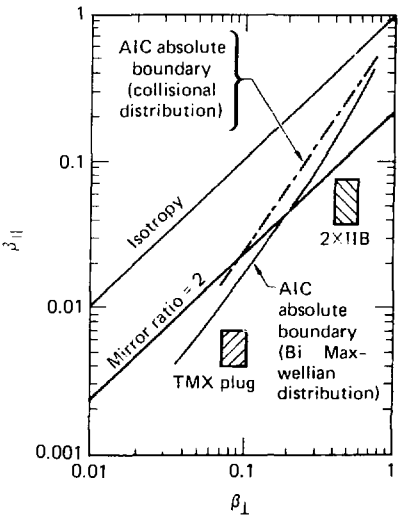

FIG. 11-2. Stability boundary to absolute Alfvén ion cyclotron (AIC) mode. Stable region lies above the AIC absolute boundary curves. This curve indicates that the TMX plug is expected to be unstable to the AIC mode.

Turning now to stability of the central-cell plasma, a drift mode analysis[20] for the tandem mirror shows two potentially unstable waves. The first is an electron drift wave having an odd axial eigenfunction with $k_z \sim 2\pi/L_c$, frequencies in the range $C_s < \omega_r/k_{\parallel} < V_A$, C_s = ion sound speed and V_A = Alfvén speed and rotating in the electron diamagnetic direction. The second mode, an ion drift wave, is flute-like and has an even axial eigenfunction. It extends from low frequencies to the ion cyclotron frequency (of the central cell) and rotates in the ion diamagnetic direction. The most dangerous mode with respect to transport considerations is the electron drift mode. It is unstable for $k_{\theta} < 1$ and localized in regions of maximum $\omega_{*_e}(r)$,

$$\omega_{*_e}(r) = \frac{ck_{\theta}}{e n_e B} \frac{d}{dr} (nT_e) \quad .$$

The drift cyclotron[21] instability (DCI = Maxwellian ion limit of DCLC) arises due to coupling of stable ion cyclotron modes with drift waves propagating in the ion diamagnetic direction. Instability occurs at multiples of the central-cell ion cyclotron frequency, $\omega \simeq N\Omega_{ci}$, with azimuthal wave numbers $k_\theta \rho_i \simeq 2Nr_n/\rho_c$ where r_n = radial density scale length, $\rho_i = v_{Ti}/\Omega_{ci}$ and $v_{Ti} = (2kT_i/M_i)^{1/2}$. The radial density scale length for stability[21] is

$$\frac{r_n}{\rho_i} \geq \frac{1}{2^{5/2}}\left(\frac{m_e}{m_i} + \frac{\Omega_{ci}^2}{\omega_{pi}^2}\right)^{-1/2} \simeq 15 \text{ for TMX} \quad .$$

Continuation of the drift-cyclotron branch of the dispersion relation to high frequencies where ions are unmagnetized yields the lower-hybrid-drift instability. Stability of this mode requires density scale lengths of the same order as required for DCI stability above. The maximum growth rate occurs for $k_\perp \rho_i \sim 1$.

During neutral-beam injection experiments in the central cell additional instabilities such as a two component mode of the bump-in-tail type or the velocity ring instability[22] are possible. Similarly, if an anisotropic distribution is supported by the neutral-beam injection, it is possible to drive an AIC instability. These instabilities would occur near the central-cell ion-cyclotron frequency or its harmonics.

Finally, it is possible that modes generated in the end cell can propagate out and be observed in the central cell. A cold-plasma description for the central-cell plasma predicts[23] that fluctuations can propagate to the central-cell midplane only in the form of low $k_\perp$ waves. The values of k may be determined by the high-field region between the end cells and central cell where the plasma shape is highly elliptical. Analysis of the cold-plasma dispersion relation indicates a shear Alfvén wave (slow wave) and a magnetosonic wave (compressional Alfvén or fast wave) have characteristics suited to propagation out of the end-cell region. Some mechanism for transferring energy between different spatial scale lengths (i.e., mode coupling) may be necessary to explain any observation of modes in the central cell at frequencies representative of high-$k_\perp$ end-cell instabilities such as the DCLC. This is certainly plausible in regions of high-flux surface ellipticity. The AIC mode is a shear Alfvén wave (with some coupling to a magnetosonic wave) driven unstable by anisotropy and possessing little cross-field structure. It is capable of propagating out of the end cells and producing fluctuations in the central cell.

In summary, depending upon the efficiency of the central cell as a source of stabilizing plasma, a finite level of fluctuations exhibiting characteristics of either the DCLC or AIC instabilities can be expected in the end cells and central cell of TMX. Additional low-frequency fluctuations of the drift wave variety are also possible in the central cell. Experimental data exhibiting these characteristics are discussed in the following section.

11.3 FLUCTUATION MEASUREMENTS

Several rf probe arrays located at the plasma edge have been used to study fluctuations in TMX. Their axial locations are shown in Fig. 2-5 with their nominal radial location between 2 and 3 plasma radii (e^{-1} point of density profiles). The high impedance probes (10 kΩ) respond to electrostatic (floating potential) perturbations while the loop probes provide information concerning fluctuating magnetic fields. Since the probes may not be inserted into the hot plasma region, we rely on either the radial eigenfunction extent or propagation of the disturbance to provide information at the probe location concerning the internal mode structure. The spatially separated electrostatic probe tips (across an array at a given axial location) provide a measurement of the local fluctuation wavelength.

Generally speaking, the frequency content of fluctuations observed by the probes agrees with that measured by forward scattering of microwaves. For this reason, we believe the probe signals provide a reasonable measurement of the internal characteristics of the instabilities except for the absolute fluctuation levels at the point of instability. There is, however, some concern that highly localized modes will not be observed by the edge probes. Similarly, only limited radial spatial resolution is possible and modes generated at different radii may appear simultaneously at the probe locations where they interfere with each other. These probes respond to frequencies in excess of 50 MHz though some low pass filtering due to

parasitic capacitance does occur; 3 dB cut off at about 26 MHz. From these arrays we can determine $k_\perp$, $k_{||}$, $|\tilde{\phi}|$, $|\tilde{B}|$ and polarization of $\tilde{B}$ in the end cells and central cell of TMX.

In addition to the rf probe arrays, low-frequency oscillations can be observed on other diagnostics. In particular, density fluctuations have been observed on the beam attenuation detectors. The response bandwidth as determined by amplifiers required to provide line density measurements is limited to a few hundred kilohertz making them useful only for very low frequency modes. Potential and density fluctuations have been observed in the central cell using a heavy-ion beam probe which has a maximum frequency response of 1 MHz. Finally, end-loss analyzers exhibit bursts of end-loss current which seem to be correlated with rf activity.

The data analysis technique used to determine high frequency instability characteristics, k and ω, is the digital estimation[24] of cross power spectral densities. Fluctuating time series signals, $\tilde{\phi}$ and B, are recorded with fast transient recorders at sampling rates to 50 MHz and stored in the data analysis computer. Using a fast Fourier transform routine, discrete Fourier transforms of the time series data, $F_\ell(\omega)$, are taken and the cross power spectrum is calculated,

$$S_{12}(\omega) = F_1^*(\omega)\, F_2(\omega)$$

where the subscripts indicate two spatially separated probe tips. For a time series signal of the form

$$f(t) = \int_{-\infty}^{\infty} F_\ell(\omega) \exp\left[-i(\omega t - \vec{k}\cdot\vec{r}_\ell)\right] d\omega/2\pi$$

the cross power spectrum is

$$S_{12}(\omega) = |F(\omega)|^2 \exp\left(i\vec{k}\cdot\Delta\vec{r}\right)$$

$$= P(\omega) \exp\left[i\theta_{12}(\omega)\right]$$

for probe separation $\Delta\vec{r}_{12} = \vec{r}_2 - \vec{r}_1$. The actual estimates used must be smoothed[24] to reduce statistical variance. Using these average spectra, a measure of the instability frequency is given by (coherent) peaks of the magnitude spectrum, $P(\omega)$ and estimates for the wave number determined from the phase spectrum $\theta_{12}(\omega) = k(\omega)\,\Delta r_{12}$. This in turn provides the mode number from $k = m/r$ for an azimuthally propagating disturbance. Note also that a measure of the correlation time of the fluctuation is determined as the inverse bandwidth, $\Delta\omega^{-1}$, of the measured spectra. From these measurements the electrostatic mode characteristics are inferred. Similarly, a circularly polarized electromagnetic wave will have fluctuating magnetic field components, $\tilde{B}_x$, $\tilde{B}_y$, at the same axial location which are 90° out of phase. Using the cross spectra between $\tilde{B}_x$ and $\tilde{B}_y$ at the same location the phase spectrum is interpreted as the measured polarization of the magnetic fluctuations.

11.3.1 End-Cell Fluctuation Measurements

The 5-tip electrostatic probes located at the end-cell midplane have been used to measure the spectral[25] characteristics of potential fluctuations. Typical cross power density spectra are shown in Fig. 11-3 for (a) the east end cell and (b) the west end cell. It is obvious that a coherent oscillation exists at a frequency near the vacuum cyclotron frequency indicated plus harmonics to n = 3 are observed (maximum frequency observable is 25 MHz). The oscillation frequency in the east is f_E = 5.6 MHz which is substantially less than the vacuum cyclotron frequency f_{co} = 6.6 MHz for the 87% (of 10 kG) field setting used. This is also substantially less than would be estimated by a β-depressed magnetic field.

As is often the case in TMX, a splitting of the mode frequency is observed as indicated by the presence of two peaks in Fig. 11-3b, the spectra calculated for the west end cell. This is a result of either the simultaneous presence of two unstable frequencies, i.e., different instabilities or perhaps the same instability with two modes generated at spatially different locations, or the appearance of a mode generated in the opposite end cell which has propagated the length of TMX. The simultaneous presence of these modes results in the corruption of the measurement of either due to phase mixing at the probe tips. The net result is to introduce a greater uncertainty in the measurement of the wave number from the phase and, to a lesser extent, of the oscillation frequency of the mode. It is, however, possible to obtain reasonably good data for several shots and to determine the dominant

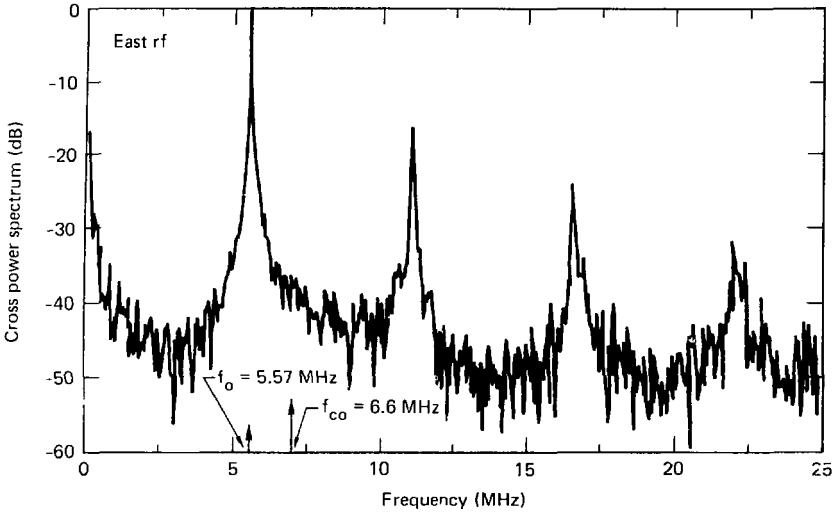

FIG. 11-3a. Cross-power spectrum of potential fluctuations for east TMX end cell.

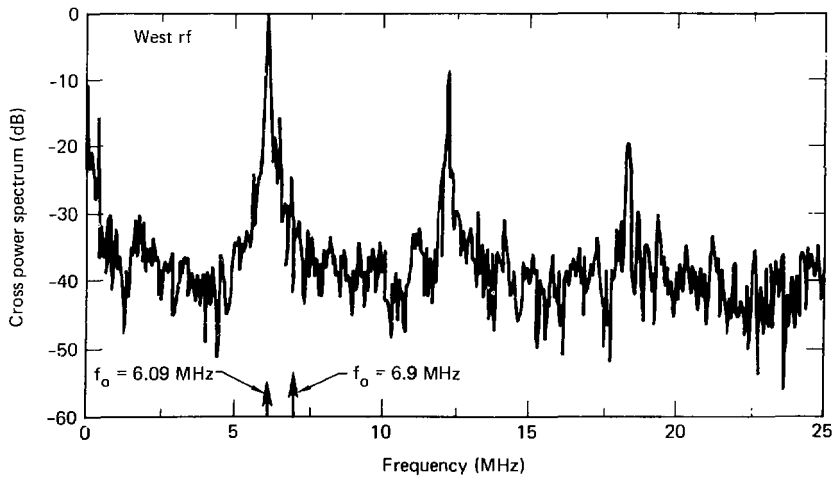

FIG. 11-3b. Cross-power spectrum of potential fluctuations for west TMX end cell.

wave number and an indication of those wave numbers present when interfering modes exist.

Typical measured phase spectra for three values of probe separation Δr are shown in Fig. 11-4 for the east end cell and Fig. 11-5 for the west end cell for the same shots as shown in Fig. 11-3. The three sets of data were taken simultaneously by recording signals from different tips of the arrays with the orientation sensitive to the azimuthal direction. The phase spectra are well-defined only over regions of significant modal power, i.e., near peaks of the cross power spectra. Away from these regions, noise results in phase spectra uniformly distributed in angle as exhibited by the rapid phase variations. Figure 11-6 shows the variation of measured phase which is a linear function of the probe separation as expected from $\theta_{12}(\omega) = k(\omega)\,\Delta r_{12}$. The data are consistent with azimuthal mode numbers $m_E = 3$ and $m_w = 6$ for the east and west end cells. Both propagate in the electron diamagnetic direction. Plasma rotation due to $\vec{E} \times \vec{B}$ drift is negligible in its effect on the interpretation of these results. It must also be recognized that a $2\pi n$ ambiguity in the data is possible. Taking this into account, the data are also consistent with mode numbers $m_E = 92$ and $m_w = 88$ with propagation in the ion diamagnetic direction. To see that these results are inconsistent with the hypothesis that the observed fluctuations are due to the DCLC instability, we note the following. The perpendicular wave number $k_\perp = m/r = 2\pi/\lambda_\perp$ implies $\lambda_\perp = 0.6$ cm $\sim \rho_i/4$. Since $\lambda_\perp < \rho_i$, the ion gyroradius, it is difficult to justify the measured phase shift as being due to a nigh azimuthal mode number fluctuation. Similarly, if m = 3 then $k_\perp \rho_i = 0.6$ or if m = 92 then $k_\perp \rho_i = 18.4$, both of which are outside the range for unstable DCLC fluctuations. These results do not agree with the mode structure theoretically predicted for unstable DCLC fluctuations.

A leading candidate is the AIC instability which has been analyzed in the limit $k_\perp = 0$. Since this mode is electromagnetic in character with left circular polarization, loop probes were installed on

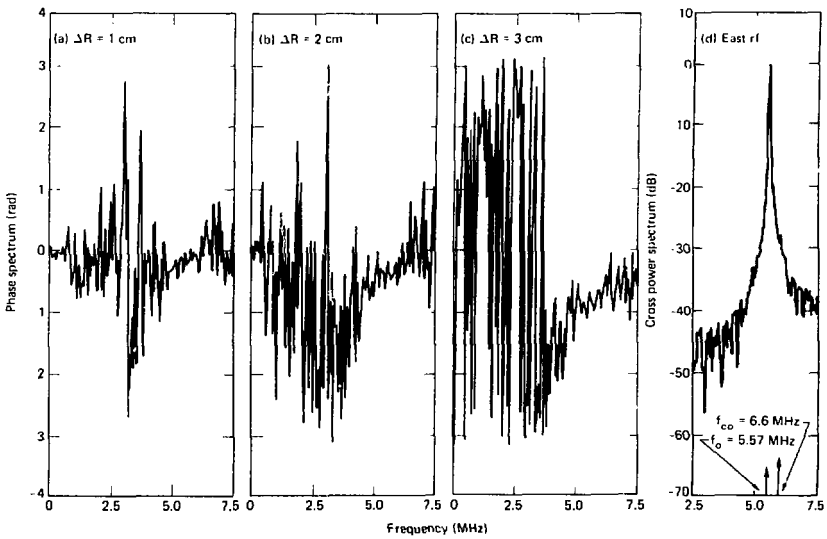

FIG. 11-4. Phase spectra for fluctuations measured in the east end cell for probe separations (a) Δr = 1 cm, (b) Δr = 2 cm, (c) Δr = 3 cm with (d) the cross power spectrum near the fundamental.

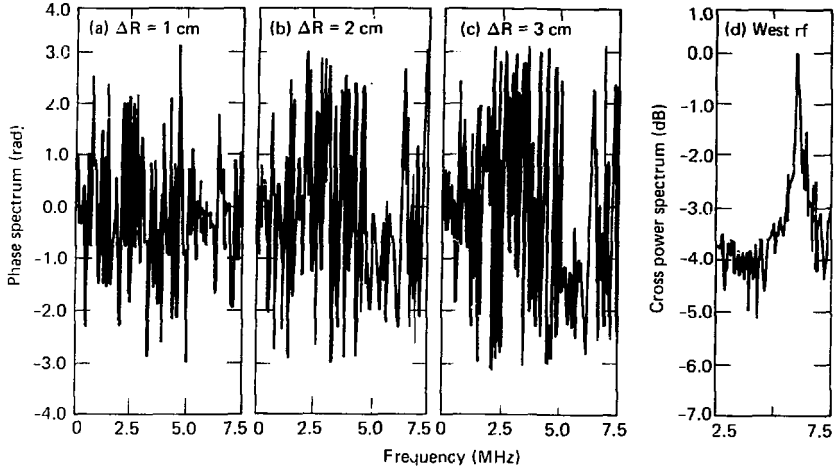

FIG. 11-5. Phase spectra for fluctuations measured in the west end cell for probe separations (a) Δr = 1 cm, (b) Δr = 2 cm, (c) Δr = 3 cm with (d) the cross-power spectrum near the fundamental.

TMX for identification. A typical cross-power spectrum between $\tilde{B}_R$ and $\tilde{B}_\theta$ in the east end cell of TMX is shown in Fig. 11-7a. This data was taken during full field operation which yields a vacuum cyclotron frequency value of f_{co} = 7.63 MHz. Note that the mode frequency f_E = 6.88 MHz is again substantially less than the β depressed value for $\beta \simeq 10\%$. The phase spectrum shown in Fig. 11-7b indicates a phase angle of $\theta_{12} \simeq -1.28$ (73°) between $\tilde{B}_R$ and $\tilde{B}_\theta$ where the sign is consistent with left circular polarization. Thus, the loop measurements are consistent with the left circularly polarized AIC mode. Additional loop data is being analyzed to compare the measured fluctuation levels with AIC theory and the electrostatic probes. The tentative conclusion at this time is that the AIC instability is present in the TMX end cells.

Under certain conditions, modes which appear more DCLC-like in nature have been observed. Since the drives for these two instabilities (loss cone for DCLC and anisotropy for AIC) are so different, it would not be surprising to have conditions where they occur simultaneously. The data presented in Fig. 11-5 clearly exhibits the simultaneous existence of two interfering modes. The resulting phase interference precludes accurate measurement of either wave number with existing computational routines. They do, however, exhibit a phase structure consistent with the simultaneous presence of both AIC and DCLC-like character. This is observed in Fig. 11-5 as a rapid phase variation with frequency between the interfering modes. At the lower frequency, f_ℓ = 6.1 MHz, the measured phase difference is $\theta_{12} \simeq -0.3$ (m = 6 propagating electron diamagnetic and presumed to be AIC) which rapidly changes to $\theta \simeq 1.2$ (m = 18 propagating ion diamagnetic and presumed to be DCLC) near the second peak at f_u = 6.56 MHz. These values should only be considered indicative of the structure present and not as precisely determined values. Additional data analyses are required to separate these effects and determine if they are real and under what conditions they are present. Note that the same structure does exist for phase spectra determined from data simultaneously recorded at probe tips with greater separation as is shown in Fig. 11-5.

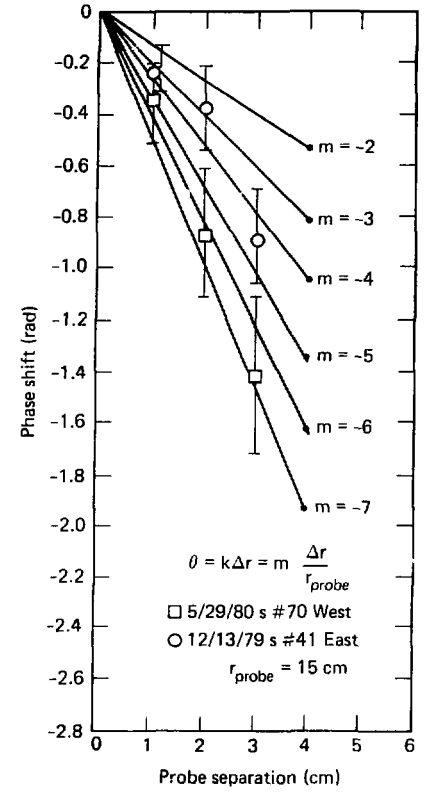

FIG. 11-6. Phase variation at dominant oscillation frequency versus probe separation.

11.3.2 Central-Cell Fluctuation Measurements

A variety of fluctuations have been observed in the central cell of TMX. Figure 11-8a is typical of the high frequency fluctuation spectra observed in the central cell. A comparison of Figs. 11-8b and 11-8c showing the spectra recorded in the east and west end cells respectively with the central-cell spectra indicate that modes generated in the east and west end cells have propagated to the central cell. Note also that the lower peak in Fig. 11-8c aligns with a mode generated in the east end cell thus indicating the capacity for high-frequency, end-cell generated modes to propagate the entire length of TMX. A comparison of the relative power levels measured in each mode is given in Table 11-2. The mode at f ≈ 6.5 MHz is generated in the east end cell and propagates the length of TMX where it appears at a much reduced power level in the west. Similarly a mode at f = 7.1 MHz is generated in the west end cell but very little of its power appears in the east.

The end-cell rf probes are located on equivalent field lines (not the same field line) at r = 15 cm and are presumed to have similar coupling to the plasma. It is unclear at this time which end generates the mode at f = 6.9 MHz though it appears to be able to propagate unattenuated through the system. The increase in power observed at the central-cell probe is fictitious and due to the following effects: a) The central-cell probe dimensions are much larger than those of the end-cell probes and may lead to an increase in sensitivity and b) the probe is located at r = 30 cm in the central cell which maps to r ≈ 10 cm in the plug. Since the potential fluctuations increase rather rapidly as probes are moved closer to the hot plasma, the end-cell generated fluctuations which have propagated to this central-cell probe ought to be larger in amplitude (even though attenuated as they propagate) due to this field line mapping. The presence of these modes in the central cell does, however, confirm their ability to propagate through TMX. Note that the relative magnitudes observed on the central-cell probes agrees with the inferred capability of mode propagation from east to west but less so from west to east for this data. Note also the existence of a low frequency spectrum in Fig 11-8a. A portion of this low frequency noiselike spectra calculated with data recorded simultaneously at a slower rate (and therefore with greater frequency resolution) is shown in Fig. 11-8d. This is presently under study and is believed to be associated with turbulent drift-wave phenomena though positive identification has not yet been determined.

At very low frequencies (~15 kHz) oscillations have been observed on many TMX diagnostics,[26,27] notably the beam attenuation detectors (BAD's), end loss analyzers, and the ω_{ci}-band envelope of rf fluctuations in the end cells. Two

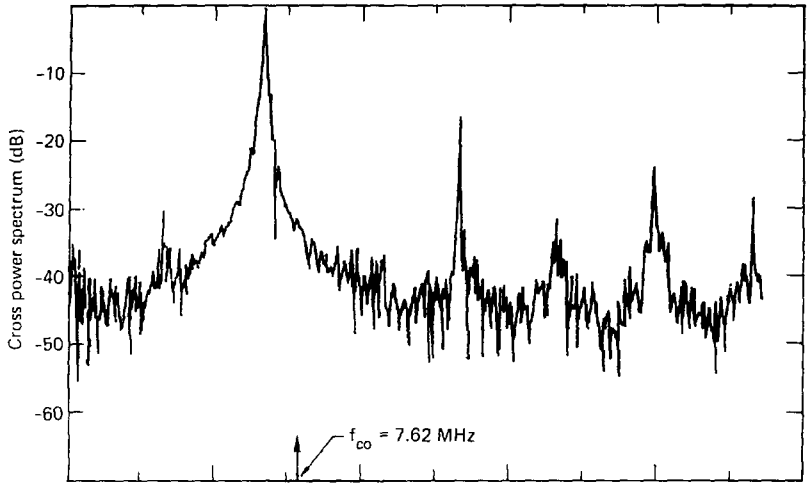

FIG. 11-7a. Cross power spectrum for magnetic fluctuations $B_{\parallel}$ vs B_{n}.

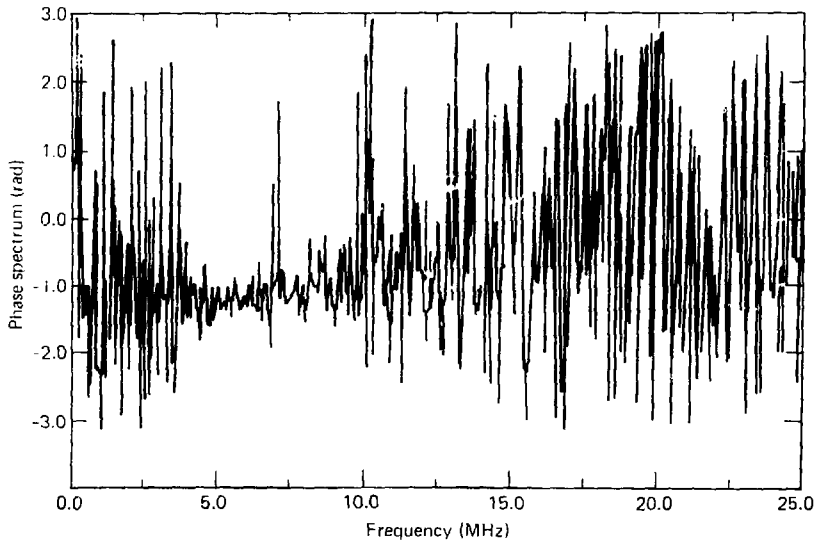

FIG. 11-7b. Cross Phase spectrum for magnetic fluctuations B_{t} vs $B_{\parallel}$.

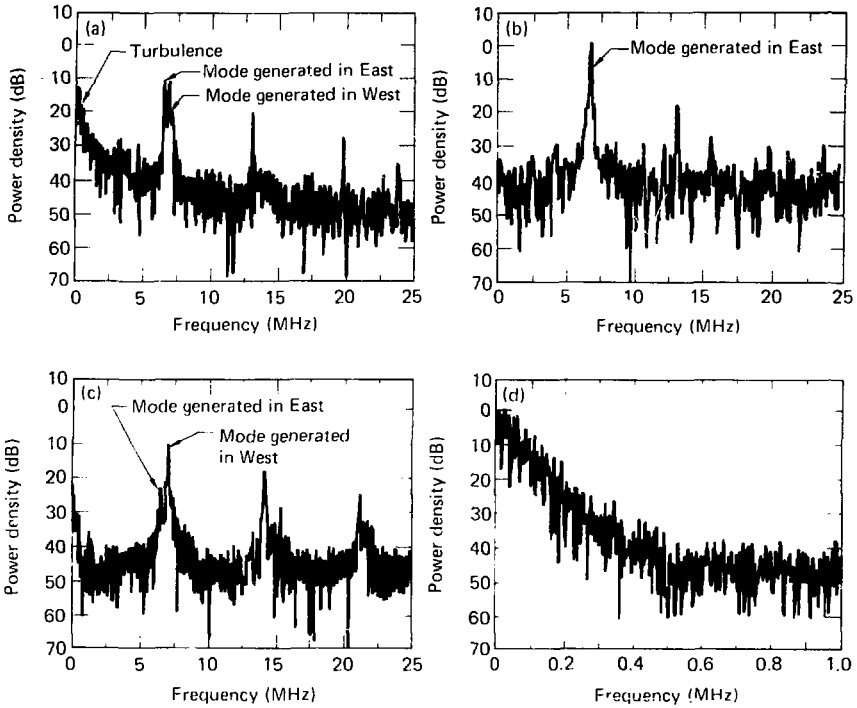

FIG. 11-8. Cross spectra of potential fluctuations in TMX (a) central cell, (b) east end cell, (c) west end cell and (d) central cell showing low-frequency turbulence.

modes have been identified, an m = 0 (azimuthal mode number) mode which couples the center cell and end cells and an m = 1 mode in the central cell. The oscillations can be very intense. The density fluctuation signal, Fig. 11-9a, detected on the central cell BAD channel at the edge (y = 24 cm) exhibits a peak-to-peak amplitude $\tilde{n}/n_0 \simeq 50\%$ for n_0 = average density. Closer to the plasma edge this amplitude can approach 100% with oscillations particularly strong for gas-box operation when the gas feed yields flat topped or slightly hollow radial density profiles. During puffer operation, the oscillations are present but generally at a reduced level, $\tilde{n}/n_0 < 10\%$.

TABLE 11-2. Relative power in one frequency resolution bin at peaks of spectra.

	Power-relative μW		
f-MHz	End cell (E)	Central cell	End cell (W)
6.54	62.46	109.3	2.596
6.88	1.254	105.4	4.460
7.08	0.003	38.16	663.7

The data has been processed using auto- and cross-correlation techniques,[28] the time series equivalent of the spectral calculations, with averaging over an 8 ms period during steady-state operation (12 ms to 20 ms during shot). A typical autocorrelation function is shown in Fig. 11-9b for

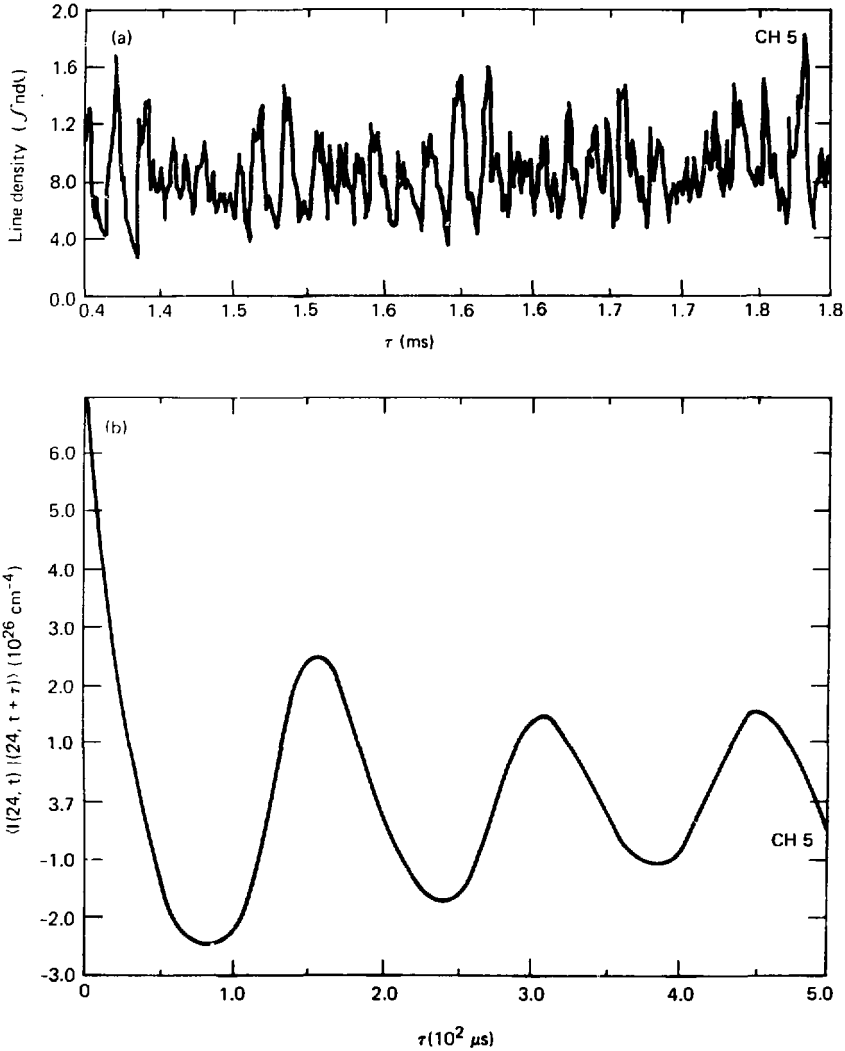

FIG. 11-9. Line density oscillations (a) along the central-cell chord at y = 24 cm and (b) autocorrelation function for the same oscillations, averaged from 12 to 20 ms.

the data shown in Fig. 11-9a where $I(y_0, t) = \int n(t)dl$ along chord at $y = y_0$. The low frequency content is observed to be quite coherent and extrapolates to a root-mean-square (RMS) amplitude of $\tilde{n}/n_0 \sim 25\%$. Correlation techniques have been used to distinguish between the m = 0 mode at f ~ 12 kHz and the m = 1 mode at f ~ 7 kHz in the central cell. The BAD channel through the axis (r = 0) discriminates against odd modes and is used to probe the m = 0 mode whereas the BAD channel at y = 24 cm is dominated by the m = 1 mode.

The characteristics of the m = 0 mode will now be discussed. The azimuthal mode number is identified by three observations:

1. The phase observed on the BAD array does not change across the axis, indicating m even.
2. During low gas feed operation this mode dominates. The signals on the rotation probes located at z = 50 cm, θ = 0° and ±90° are in phase implying m = 0, 4, 8.
3. The mode amplitude measured by the HIBP and the end-loss detectors is a maximum at r = 0 indicating m = 0.

The axial variation in amplitude and phase was determined from cross correlations between the central-cell BAD, the end-cell BAD and interferometer at the inner 10 kG field with results shown in Fig. 11-10. The west end cell is in phase with the central cell but the east end cell experiences a 180° phase shift in the vicinity of the inner mirror point and east gas-box location. End

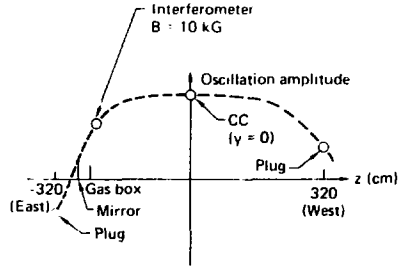

FIG. 11-10. Axial dependence of the line density along chords through the machine axis, (m = 0 mode). Found by cross correlation with the line density oscillations at z = 0.

losses are in phase with the low-frequency oscillations of the corresponding plug. As shown in Fig. 11-11 the envelope of ω_{ci} fluctuations in the plug is in phase with the low frequency oscillations. There exists a high correlation between the central-cell density fluctuation and the rf envelopes. Extrapolating the autocorrelation function envelopes to zero to remove high frequency effects yields

$$\left[\left\langle\left(\int \tilde{n}\,dl\right)^2_{y=0}\right\rangle\left\langle|\omega_{ci}|^2\right\rangle\right]^{1/2} = 4.6 \times 10^{11}\ \text{cm}^{-2}\text{V}$$

which is in agreement with the peak amplitude of the cross-correlation function. This indicates a coupling of the m = 0 mode to the envelope of the end-cell fluctuations and thus a coherency of interaction between the end cells. This correlation suggests that the m = 0 mode may be a consequence of end-plug fluctuations and would possibly be absent in microstable sloshing-ion end plugs such as in TMX Upgrade.

Turning now to the m = 1 mode identification arises from three observations.

Turning now to the m = 1 mode identification arises from three observations:

1. The 7-kHz component of fluctuations observed by the central-cell BAD changes phase across the machine axis.
2. The three rotation probes exhibit a 90° phase difference corresponding to m = 1.
3. The oscillating part of the line density has the same sign for all chords on the same side of the axis, consistent only with m = 1.

The mode amplitude is observed to be large at the plasma edge, r ≥ 25 cm. The HIBP measurements indicate $E_\perp \sim 9$-10 v/cm in this region. The

TABLE 11-3. Rotating mode and gas feed.

Gas feed	Density profile	Observation
Low	Gaussian	m = 1 mode absent
		m = 0 mode present
Medium	Flat topped to slightly hollow	m = 1 mode present and coherent
		m = 0 mode present
High	Strongly hollow	m = 1 mode[a] (turbulent)
		m = 0 mode present

[a]Mode identification uncertain because of turbulence.

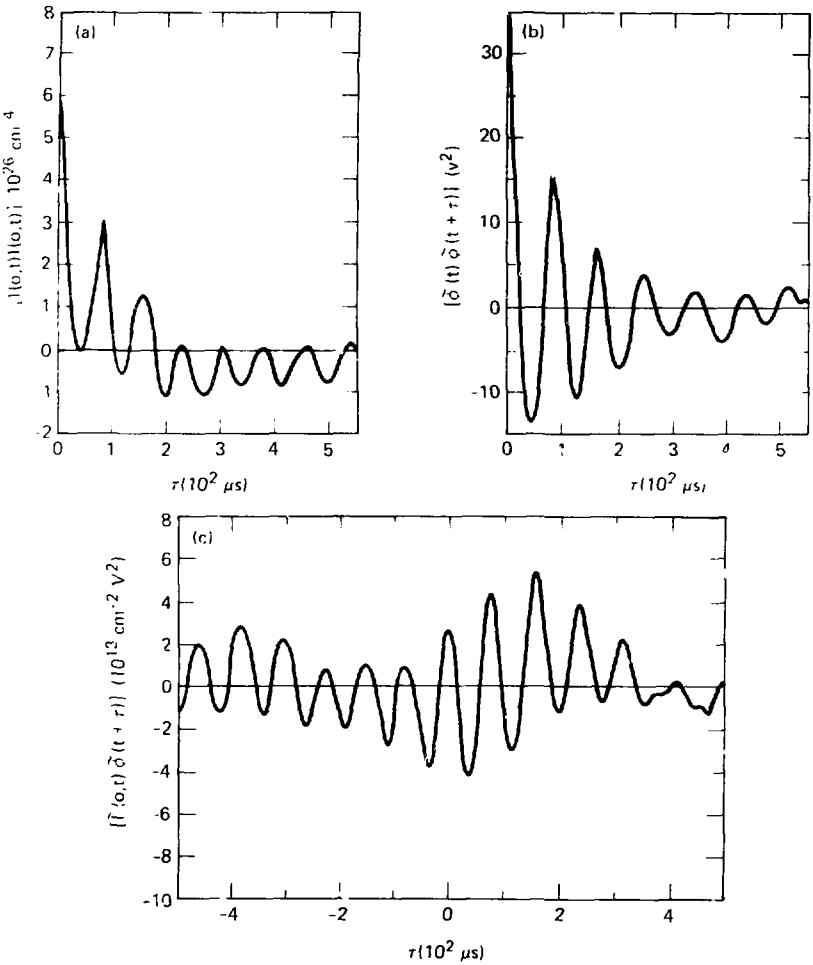

FIG. 11-11. (a) Autocorrelation for the cc line density, chord through the axis. (b) Autocorrelation of the envelope of the west plug rf oscillations at ω_{ci}. (c) Cross correlation of the line density and rf.

azimuthal phase velocity in the laboratory frame is in the ion diamagnetic direction at roughly the $\vec{E} \times \vec{B}$ velocity. The mode amplitude and phases were measured in the end cells using the BAD's. The results, Fig. 11-12, indicate the density oscillations in the end cells are in phase with those in the central cell but reduced in amplitude by a factor of about 20. HIBP measurements confirm the large amplitude central-cell oscillations as indicated in the radial potential sweep in Fig. 11-13. The oscillations at r = 25 cm are dominated by the m = 1 mode. The extremely large potential amplitude modulation (100%) is in agreement with the large density fluctuations observed on the BAD's near the plasma edge.

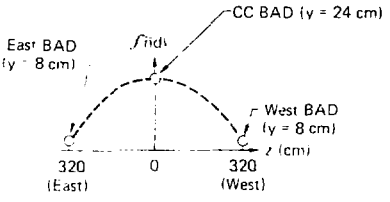

FIG. 11-12. Axial dependence of the line density for the m = 1 mode.

The m = 1 mode is not present for all operating conditions. Table 11-3 summarizes observations for three shots at differing operating conditions. For the medium gas input case, the calculated particle deposition and the measured ion end losses are compared in Fig. 11-14, together with the average and oscillating densities obtained by inverting the line density measurements. We see that at large radii there is a large discrepancy between deposited ions and the measured end losses, implying a significant radial transport. The amplitude of the m = 1 mode is large at these radii and it seems likely that the mode is a significant contributor to this transport. This is in contrast to lower gas input without such a discrepancy.

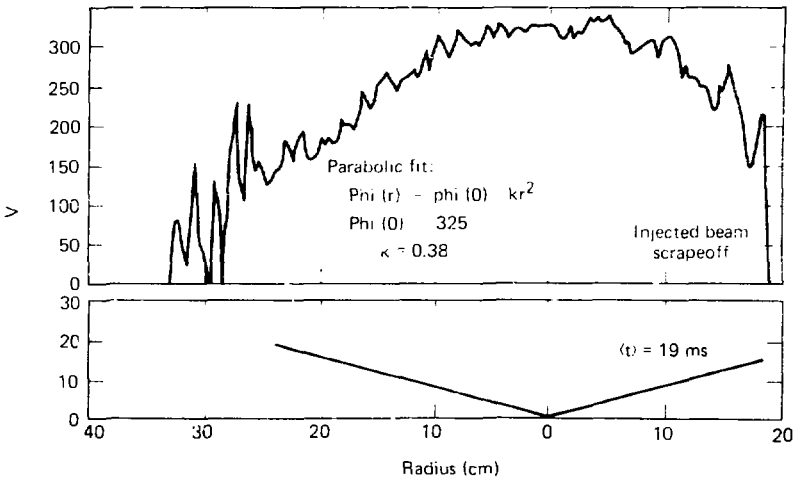

FIG. 11-13. Measurement of the space potential by a radial sweep of the HIBP.

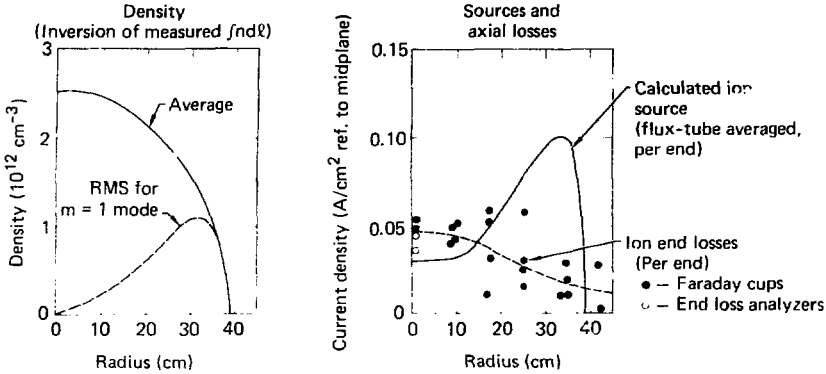

FIG. 11-14. Central-cell low-frequency instability and ion particle balance. Gas box operation at medium gas input.

REFERENCES

1. W. C. Turner, E. J. Powers and T. C. Simonen, *Phys. Rev. Lett.* 39, 1087 (1977).
2. D. B. Grubb T. A. Casper, J. F. Clauser, D. L. Correll R. P. Drake, R. K. Goodman, Y. Matsuda, D. L. Pearlstein, and T. D. Rognlien, *APS, San Diego, November 1980.*
3. R. C. Davidson and J. M Ogden, *Phys. Flu.* 18, 1045 (1975).
4. D. C. Watson, *Phys. Flu.* 23, 2485 (1980).
5. T. C. Simonen, C. A. Anderson, T. A. Casper, J. F. Clauser, F. H. Coensgen, W. C. Condit, D. L. Correll,, W. F. Cummins, J. C. Davis, R. P. Drake, J. H. Foote, R. J. Fortner, A. H. Futch, R. K. Goodman, D. P. Grubb, E. B. Hooper, R. S. Hornady, A. L. Hunt, C. V. Karmency, B. G. Logan, R. H. Munger, W. E. Nexsen, W. L. Pickles, P. Poulsen, D. R. Slaughter, B. W. Stallard, G. A. Hallock, and O. T. Strand, *IAEA-CN-38, Brussels, July 1980.*
6. T. D. Rognlien and Y. Matsuda, *Nucl. Fusion* 21, 1981.
7. This report, see Section 5.
8. G. R. Smith and W. M. Nevins, *Mirror Theory Monthly*, February 15, 1981.
9. *Physics Basis for MFTF-B*, Lawrence Livermore National Laboratory, Livermore, CA, UCID-18496, Pt. 2 (1980)
10. D. E. Baldwin, *Rev. of Mod. Phys.* 49 317 (1977).
11. *Status of Mirror Fusion Research*, Lawrence Livermore National Laboratory, Livermore CA, UCAR-10049-80 Rev. 1 (1980).
12. *TMX Major Project Proposal*, Lawrence Livermore National Laboratory, Livermore, CA, LLL-PROP-148 (1977)
13. D. L. Correll, Lawrence Livermore National Laboratory private memo on quasilinear stream current.
14. H. L. Berk, et al., IAEA-CN-35IC2.
15. J. G. Cordey and R. J. Hastie, *Phys. Flu.* 15, 2291 (1972).
16. D. E. Baldwin, *Phys. Flu.* 17, 1346 (1974).
17. H. L. Berk, L. D. Pearlstein, and J. G. Cordey, *Phys. Flu.* 15, 891 (1972).
18. L. D. Pearlstein, M. N. Rosenbluth, and D. B. Cheng, *Phys. Flu.* 9, 953 (1966).
19. D. E. Baldwin, C. O. Beasley, Jr., H. L. Berk, W. M. Farr, R. C. Harding, J. E. McCune L. D. Pearlstein, and A. Sen, IAEA-CN-28/G-13 (Madison, 1971) Vol. 2, p. 735.
20. W. Horton, University of Texas Report FRCR #182, August 1979.
21. A. B. Mikhailovskii and A. V. Timofeev, *Zh. Eksp. Theor. Fix.* 44, 919 (1963) *Sov. Phys. JETP* 17, 626 (1963).

22. J. K. Lee and C. K. Birdsall, *Phys. Flu.* **22**, 1306 (1976).
23. G. R. Smith and M. J. Gerver, *Mirror Theory Monthly*. July 15, 1980.
24. D. Smith and E. J. Powers, IEEE Trans. *Plasma Sci.* **2**, 261 (1974).
25. T. A. Casper, D. P. Grubb, G. R. Smith, and B. W. Stallard, APS. San Diego, November 1980.
26. G. A. Hallock, R. H. Hickock, W. C. Jennings, E. B. Hooper, Jr., E. J. Powers, Y. C. Kim and J. Y. Hong, submitted to 1981 IEEE Conf. on Plasma Sci.
27. E. B. Hooper, submitted to 1981 IEEE Intern. Conf. on Plasma Sci.
28. E. B. Hooper, Jr., *Plasma Physics* 13, 1 (1971).

SECTION 12
RELATION OF FLUCTUATIONS TO ION END-LOSS ENERGY

(D. P. Grubb, T. A. Casper, and W. M. Nevins)

12. Relation of Fluctuations to Ion End-Loss Energy

12.1 INTRODUCTION

In this section we first examine the energy spectra of the central ions which escaped along the field lines (end loss) to the end walls of TMX. Our analysis shows that the energy spectra of the ions was influenced by the plug-ion cyclotron fluctuations and the resulting energy spectra provide important clues about the nature of the fluctuations in the plug. We then compare the measured energy and density of the end-loss ions to the stream requirements of the possible loss-cone modes in TMX. We find that the density of the end-loss ions was less than the theoretical stream requirements.

12.2 END-LOSS ION ENERGY SPECTRA—MODIFICATIONS BY PLUG rf

The TMX central cell was the principal source of end-loss ions. The energy distribution of these ions, therefore, contains information about the loss processes of the central-cell ions as well as a measure of the plug potential. In Fig. 12-1 we present typical end-loss ion energy spectra. Figure 12-1a shows the energy distribution of end-loss ions which passed through the west end cell when both the east and west end cells were being fueled by neutral beams (full tandem operation). The end-loss energy distribution for the ions escaping through the east end cell was similar. Both show a plug potential of approximately 500 volts with a mean end-loss ion energy, W_{EL}, of roughly 1000 eV.

Since—for tandem operation—ϕ_c must be less than ϕ_p, the value of $W_{EL} = 2\phi_p$ would imply very poor confinement of the central-cell ions if W_{EL} were actually a measure of the central-cell ion energy. However, data from this same date (9/24/80) which is presented in Section 3 shows that the energy content of the central-cell ions was consistent with a central-cell ion energy, $3/2\ kT_{ic}$, of 75-100 eV, a factor of ten less than W_{EL}.

This point is reinforced when we observe the change in the W_{EL} of the west plug end-loss ions when the west-plug neutral beams were turned off. After turnoff, the energy spectra rapidly evolved to that shown in Fig. 12-1b, showing that the west plug potential dropped and the end-loss current through the west end cell increased. At the same time, W_{EL} dropped to about 100 eV, which is equal to the central-cell ion energy determined from diamagnetic loop (total energy) and Thomson scattering (electron energy) measurements. The energy distribution of the east-end losses, however, was nearly unchanged when the west end cell was turned off. These measurements show that at the same time that the end losses through the west end cell had a mean energy of 100 eV, those passing through the east plug had an energy of 1000 eV, ten times greater. Based on these observations we conclude that the majority of the heating of the end-loss ions occurred in the beam heated end cells.

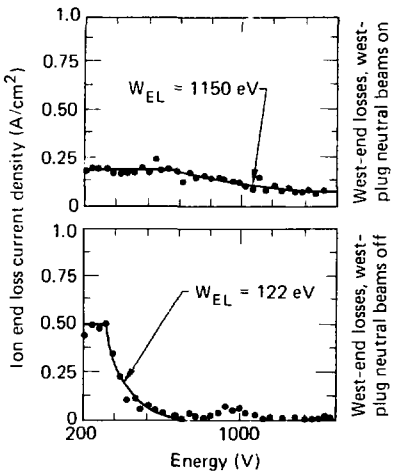

FIG. 12-1. Measured end loss energy spectra. a) Ions passing through plugged (beam heated) mirror, and b) Ions passing through unplugged (without beams) mirror.

Based upon these measurements we now believe that the plug rf heats the central-cell ions in two locations. Previous measurements have shown that $T_{ic} \simeq T_{ec}$ in the central cell; therefore there must be an auxiliary power input to the central-cell ions since classical energy exchange (drag) between the central-cell electrons and ions would result in $T_{ic} < T_{ec}$. This auxiliary heating is related to a reduction of the confinement of central ions as discussed in Sections 4, 5, and 7. As explained in these sections, the plug rf interacts with the central-cell ions to produce the observed scaling of central-cell confinement. After leaving the center cell, ions experience an additional, more intense heating mechanism (to about 1 keV observed at the end wall) which does not directly contribute to the degradation of central-cell confinement.

We also believe that the end-loss measurements combine with the measurements of the plug plasma length and beta to provide important clues about the nature of the plug instability. Here is a summary of our observations and their implications:

1. The length and beta of the plug plasmas indicate that the plug ions have an anisotropic velocity distribution with $W_{\parallel} \sim 0.05$ to 0.07 $W_{\perp}$ (i.e., $W_{\parallel}$ = 500 eV to 1 keV). For the neutral beam and magnetic geometry in TMX this is approximately the ratio of $W_{\parallel}$ to $W_{\perp}$ that is expected for the measured values of beta and T_{ep} (plug electron temperature). The instability apparently does not, therefore, significantly reduce the anisotropy of the plug ions.

2. The plug instability must be capable of heating the end-loss ions (nominal thermal energy = 100 eV) to a thermal energy of 1 keV. If it does so in a single pass of the end-loss ions through the plugs, it must heat the ions parallel to the field line as well as perpendicular to it such that $E_{\parallel} \geq E_{\perp}$. This is a necessary condition because an ion with $E_{\perp} > e\phi_{p\text{-}m}$ (~500 eV) at the plug midplane is trapped in the plugs. This violates our assumption that the end-loss ions simply pass through the plugs. ($\phi_{p\text{-}m}$ is the difference in the plasma potential between the midplane of the plug and the outer mirror point.) In conjunction with this restriction it is necessary to require that the parallel heating of the end-loss ions occur without violating the previous (number 1 above) restrictions.

3. If the instability heating of the end-loss ions occurs while the ions make several passes through resonance with the wave because the end-loss ions become temporarily trapped in the end cells, there are also restrictions on the nature of the instability. The wave must again heat the particles in both the perpendicular and parallel directions. It must heat in the perpendicular direction to increase the end-loss ion energy to greater than $e\phi_{p\text{-}m}$ so that the ion is confined in the end cell and it must must heat in the parallel direction or the ion could subsequently be lost only with energy $\simeq e\phi_{p\text{-}m}$. Since $e\phi_{p\text{-}m}$ is approximately one half of the measured end-loss energy, parallel heating is required to explain the observed energy. The proposed instability must be able to accomplish this heating without violating the first observation and without causing a significant number of the end-loss ions heated in the end cell to be lost so that they pass through the central cell to the far end wall. (Recall that our measurements indicate that 1-keV ions were being lost only to the end wall adjacent to the neutral-beam-fueled plug and that 100-eV ions are escaping from the central cell to the far end wall through the unfueled plug.)

We are presently studying the characteristics of possible instabilities to see if one or more of these modes satisfy these restrictions.

12.3 STREAM REQUIREMENTS OF LOSS-CONE MODES IN TMX

We now examine the question of fulfilling the quasilinear stream requirements of the plugs. The spectral measurements indicate that the DCLC (Drift Cyclotron Loss Cone) mode is often stable in TMX. Comparing the characteristics of the measured end-loss ions to the theoretical DCLC stream requirement, we find that the central-cell ions escaping through the plugs of a classical tandem mirror could provide enough warm plasma density at the plug midplane, but the temperature is too cold (~0.1 keV) for stabilization. The end losses measured in TMX had a higher temperature than classically predicted (~0.5 to 1.0 keV) which is suitable for stabiliaztion. However, at the high temperature, a simple model of the flow predicts that the density within the end plug would be too low for stabilization. Finally, we consider additional stabilizing effects which are presently under study.

Figure 12-2 presents the marginal stability boundaries for the DCLC and ALC (Axial Loss

Cone) modes calculated for typical TMX parameters.[1] The fundamental of the DCLC mode is labeled $\omega \sim \omega_{ci}$ ($n_z = 0$), the higher harmonics of the DCLC mode ($\omega > \omega_c$) are labeled harmonics ($n_z = 0$), and the AI C mode is labeled ALC ($n_z = 1$). A mode is stable for values of n_w/n_h, T_w/T_h which lie above the marginal stability line for that mode. (n_w/n_h) is the ratio of the warm, streaming plasma density (n_w) to the hot-ion density (n_h). T_w/T_h is the ratio of the temperature of the streaming plasma (T_w) to the hot-ion temperature (T_h). We see from Fig. 12-2 that the DCLC mode (of the three modes shown) typically requires the greatest value of n_w/n_h, T_w/T_h and, therefore, the largest amount of stream current to be stable.

Because the total ion end-loss current is much greater than the neutral-beam current which is trapped in the plugs by ionization, we know that the majority of the end-loss ions originated in the central cell. In passing through the plug(s) these escaping ions provide a source of warm-plasma stream for the end plug(s). We now address the question of whether the density and temperature of this stream of ions are correct for the stabilization of the DCLC mode.

Earlier in this section we presented experimental evidence which showed that the ion energy in the central cell was much less than that of the end-loss ions. At this time we have not determined precisely where the extra heating of the end-loss

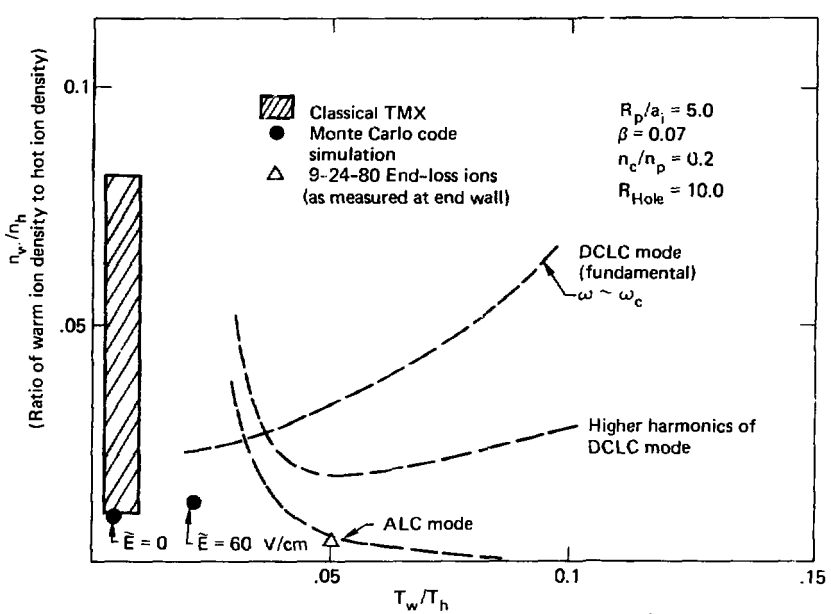

FIG. 12-2. Loss-cone mode(s) stability boundary(s). The radial profile of the plasma density is described by $n_p(r) = n_o e^{-(r/R_p)^2}$. β is the ratio of the plasma pressure to the magnetic field pressure. n_c and n_p are the central-cell and plug densities respectively. n_w/n_h and T_w/T_h are the ratios of the warm-ion density and temperature (w) to those of the hot ions (h). $\tilde{E}$ is the strength of the fluctuating electric field due to the plug driven ion cyclotron fluctuations. R_{Hole} is defined by the velocity space distribution function of the hot ions:

$$f(V_\perp^2) = \alpha\left(e^{-\alpha V_\perp^2} - e^{-\alpha V_\perp^2 + R_{Hole}}\right)\frac{R_{Hole}}{R_{Hole}^{-1}}, \text{ where } a_i^2 = \frac{1}{2\alpha\omega_{ci}^2}.$$

ions occurs. We must, therefore, assume models for the energy of the end-loss ions as they pass through the plug midplane.

For low rf fluctuation levels, we might assume that the classical model of tandem mirror confinement applies. In this model the central-cell ions are heated by collisions with the central-cell electrons. In equilibrium $T_{ic} \simeq 1/3\text{-}1/2\ T_{ec}$ (Ref. 2). These ions provide a warm plasma density at the plug midplane $n = n_c e^{-e\phi_c/T_{ic}}$ with perpendicular energy kT_{ic}. In Fig. 12-2 we show a region labeled "Classical TMX." Values of $(n_w/n_h, T_w/T_h)$ which lie in this region are typical of point model calculations of equilibrium TMX parameters based upon the classical model. We note that there is a sufficient density of warm ions, but that their temperature is too low to provide stability. In principle the low temperature of the stream ions should cause the plugs to be unstable to the two component mode. This mode is certainly a candidate for the observed instability in TMX. However present theoretical predictions for the characteristics of this mode are inconsistent with the measured fluctuations. Most notably, the two-component mode is predicted to occur with $\omega > \omega_{ci}$ in contradiction to the spectral measurements.

At high rf fluctuation levels we model the warm plasma stream according to the Rognlien-Matsuda Theory of heating of the central-cell ions by the plug-driven fluctuations.[3] The heating of the central-cell ions allows them to escape the central cell more easily. This also changes the characteristics of the end-loss current (n_w, T_w). In Fig. 12-2 we have traced out the locus of points $(n_w/n_h, T_w/T_h)$ which the code predicts as the value of the fluctuating rf electric field in the code varied between 0 to 60 V/cm. Within the factor of two uncertainties in the calculations of the stability boundary and the Monte-Carlo results, it is possible that the rf heating of the central-cell ions could provide an effective source of stabilizing stream for the end plugs.

In both of the previous models (Classical and Rognlien-Matsuda) we made the implicit assumption that the heating of the end-loss ions to energies of 1 keV occurs after they pass through the end-plug midplane on their way to the end wall. In our third model we relax this assumption so that the ions are heated to their final (measured) energies as they pass out of the central cell and through the plugs. The result of applying this model to TMX data acquired during experimentation on 9-24-80 is shown in Fig. 12-2. The temperature of the end-loss ions is sufficiently high, but the density of these ions is too low to provide stability.

We have also examined a model which assumes that the end-loss ions are trapped and heated in the plug mirrors for several bounce times before they are eventually lost to the end walls. In terms of the stability of the loss-cone modes, the results of this model are not significantly different from those we just discussed (ions heated before they pass through the plug midplane.) As long as the warm ions are trapped in the plug mirrors, they can only fill a small portion of the hole in the velocity space of the plug ions. (Low-energy ions will be expelled by the plasma potential.) When they finally escape the plug, the high-energy and low-current density of the end losses leads us to calculate a low density of these ions in the rest of the hole in velocity space. Under these circumstances we do not expect stability.

To summarize, we note that we have examined several models for the characteristics of the warm-plasma stream at the plug midplane. All of these models could be made consistent with the measured end losses by appropriately localizing the additional rf heating of end losses. Only one of these models, Rognlien-Matsuda, comes within a factor of two of predicting DCLC stability. We conclude, therefore, that additional analysis and modeling are necessary if we are to understand the apparent stability of the DCLC mode in TMX.

We are presently evaluating the DCLC mode stability boundaries for a wider range of plasma parameters. In particular, we are evaluating the effect(s) of increasing the ratio of R_p/a_i. Detailed analysis of the radial profiles of the plug-ion density shows that the density profile can be very flat or even slightly inverted (Sec. 3). The flat density profiles imply values of R_p/a_i greater than the value of 5 used in Fig. 12-2. Previous reported studies on 2XIIB have shown that the stream requirements of the DCLC mode decrease approximately as $(R_p/a_i)^{4/3}$ (see Ref. 2). It is possible, therefore, that we will find better agreement between one or more of our models of the warm plasma in the plug and the stability requirements of the DCLC mode when

we evaluate the stability boundaries for parameters which more precisely represent experimentally measured values for a particular experiment.

In addition, we are developing new models of the spatially-dependent velocity distribution of the stream ions used in the marginal stability code. And finally, we are examining ways in which coupling between an instability with the experimentally observed characteristics and a DCLC mode could result in the stability of the DCLC mode.

REFERENCES

1. D. L. Pearlstein, Lawrence Livermore National Laboratory, Livermore, Calif., private communication.
2. F. H. Coensgen, *TMX Major Project Proposal*, Lawrence Livermore National Laboratory, Livermore, Calif., LLL-Prop-148 (1977).
3. T. D. Rognlien and Y. Matsuda, "Tandem Mirror Confinement in the Presence of Ion Cyclotron Fluctuations," *Nuclear Fusion* **21** (1981).

SECTION 13
TMX IMPURITY STUDIES USING ULTRAVIOLET SPECTROSCOPY

(S. L. Allen, O. T. Strand, H. W. Moos,* R. J. Fortner, T. J. Nash, and D. D. Dietrich)*

*Johns Hopkins University, Baltimore, MD.

13. TMX Impurity Studies Using Ultraviolet Spectroscopy

13.1 INTRODUCTION

Impurities can significantly influence a plasma in several ways. As shown in Table 13-1, the power loss by line radiation from impurities can be an appreciable fraction of the input power in a fusion device. In some extreme cases, hollow electron temperature profiles have been caused by radiation from impurities.[1] In addition, impurities can drive or enhance instabilities in the plasma.

13.1.1 Impurity Studies in Linear Devices

There have been many impurity studies of tokamaks;[1-7] as a result, impurity behavior is fairly well understood in these devices. In contrast, there have been very few impurity measurements on linear devices. Simple mirror machines are expected to expel impurities[8] because of the positive ambipolar potential present in the center of the mirror. In addition, low-energy impurity ions are expected to rapidly scatter ($\tau \sim \sqrt{M_i}\, E_i^{3/2}\, Z^{-4}$) into a region of phase space where they are not confined by the magnetic mirrors.[8] The first detailed impurity study[9] of a beam-fueled linear machine was performed on 2XIIB.[10] The major results were[9,11]: (a) oxygen was the major light impurity (2 to 3%), while carbon, nitrogen, and titanium emissions were also identified, (b) oxygen was injected by the neutral beams, with the OII brightness scaling with the beam current as $I_b^{1.0}$, (c) a small fraction (<5%) of the deposited power was lost through impurity radiation, and (d) low-energy injected impurities were found to be poorly confined by the mirrors. (Reference 12 presents more detail.)

We present here the results of a major impurity study on the Tandem Mirror Experiment (TMX)[13]; it represents the second study on a beam-fueled linear device and the first investigation of a tandem mirror. The tandem mirror concept uses two plugs similar to 2XIIB (minimum-B mirrors, beam-fueled) to confine a plasma in a central cell. From the standpoint of impurities, this configuration provides a mixture of possible impurity sources: high-energy beam-injected impurities in the plugs and desorbed impurities from the surfaces of the vacuum vessel, particularly in the central cell. The presence of electrostatic confinement[14] in TMX should also influence the impurities. A positive impurity ion existing in the central cell should be confined axially by this positive electrostatic potential, ϕ_c. An impurity ion existing in the central region of the plug, on the other hand, may flow into the central cell or out of the machine depending on its energy and position, with the majority expected to flow out. The purpose of this impurity study was to experimentally measure the impurity characteristics in a tandem mirror device, with emphasis on the central-cell plasma.

TABLE 13-1. Power loss by impurity radiation.

Device	Input power lost, %	Date, yr.	Ref.
C-stellarator	30–50	1962	1
ST tokamak	30–40	1974	2
ATC tokamak	≥20	1975	3
TFR tokamak	40–60	1975	4
PLT tokamak	15–25	1976	5
Alcator tokamak	≥20	1978	6
2XIIB	5–10	1979	12

13.1.2 Summary of Impurity Study on TMX

Two survey spectrographs and three time-resolving monochromators were used to measure the impurity emissions from TMX. The instruments are described in Appendix B.

The major impurities were found to be oxygen, nitrogen, carbon, and titanium. The results obtained in the TMX plug were similar to those found on the 2XIIB device; in particular they were consistent with beam-injected oxygen. The time histories and radial profiles of the impurity emissions in the central cell were also measured. These radial brightness profiles were used to obtain the impurity density (0.4% for oxygen and lesser amounts for carbon and nitrogen) and the total radiated power (20 to 30 kW).

Observations made of impurity behavior during vacuum chamber preparation, gettering, and the use of cold liners are discussed. This data shows that the density of light impurities in the central cell is influenced by the wall conditions. Impurity behavior during central-cell neutral-beam heating experiments and the results of an experiment in which a pulsed-gas valve was used to introduce oxygen and neon into the plasma are presented. There is a summary of computer models and overall conclusions.

13.2 EXPERIMENTAL RESULTS

13.2.1 Spectrograph Surveys

A normal-incidence and grazing-incidence spectrograph (Appendix B) was used to record emissions from the central-cell plasma. Typically, a large number of plasma discharges (40 to 50) were recorded on a photographic plate, this was to insure that even the weakest impurity emissions were recorded. The spectra obtained on the photographic plates were then digitized with a recording densitometer. A sample portion of the spectrum between 275 and 310 Å obtained with the grazing incidence spectrograph is shown in Fig. 13-1 (the total scan was from 150 to 1300 Å). Note that several titanium lines have been identified. In addition, emissions from ionization states of oxygen and nitrogen were present in this spectral region.

Figure 13-2 shows a segment of a spectrum obtained from the normal incidence spectrograph. The total spectral range from 1700 to 2000 Å was covered on this scan (first order wavelength), the spectral region shown is from 1875 to 1940 Å. Carbon emissions are identified in this region.

In summary, the primary impurity constituents identified by the survey were carbon, nitrogen, oxygen, and titanium; these are the same impurity species that were identified on 2XIIB. Ionization states up to lithium-like (CIV, NV, and OVI) were observed. The absence of He-like emissions from these light impurities is caused by the expected low density of the ^3S state at the electron temperatures found in the central cell.

While the survey study was extremely useful to identify the most prominent impurity species, it was difficult to determine impurity densities and radiated power from these measurements as the instruments were uncalibrated in sensitivity. In addition, plasma parameters often varied from shot to shot. Furthermore, observed intensity ratios were valid over only a short wavelength region. Therefore, the absolutely calibrated monochromators were used to measure the emissions identified in the survey study.

13.2.2 Impurity Line Study—General

As discussed in Appendix B, the absolutely-calibrated instruments used in this study were sensitive from 300 to 1500 Å. For the light impurities (carbon, nitrogen, and oxygen) there are $\Delta n = 0$ ground state resonance transitions in this wavelength region (Δn is the principal quantum number). In most cases, the metastable transitions (from Be-like and B-like ionization states, for example) are also in this region. In addition, there are some ionization states of Ti which can be observed in this wavelength range.

Each transition was carefully scanned and identified. Some of these emissions were observed under various plasma conditions to ascertain "typical" time histories, radial profiles, and absolute brightnesses.

13.2.3 General Characteristics of Impurity Emission in the TMX Plug

Each plug of the TMX experiment is similar to 2XIIB, so it is important to compare the two. One characteristic of the emissions from 2XIIB and the TMX plug is that the spectral lines are quite broad. Shot-to-shot spectral scans of OV-630 Å and L_{α}-1216 Å are shown in Fig. 13-3. The instrumental resolution in this case was approximately 1 Å as determined by the entrance and exit slits, the spectral line is broadened substantially. As discussed in Ref. 9, this is consistent with the model that high-energy neutral oxygen is introduced by the neutral-beam injectors.

The typical time history of the light impurity emission in the TMX plug is presented in Fig. 13-4. (The sum of the radial chords for OIV-554 Å is shown for the east plug.) The timing sequence is shown for reference. The large increase in the signal at the beginning of the sequence (roughly 5 ms) is caused by the stream-gun plasma; the decrease after approximately 5 ms is due to the turnoff of these stream guns. The emissions reach a steady state soon after the stream guns turn off, and the signal remains roughly constant until the end of the shot.

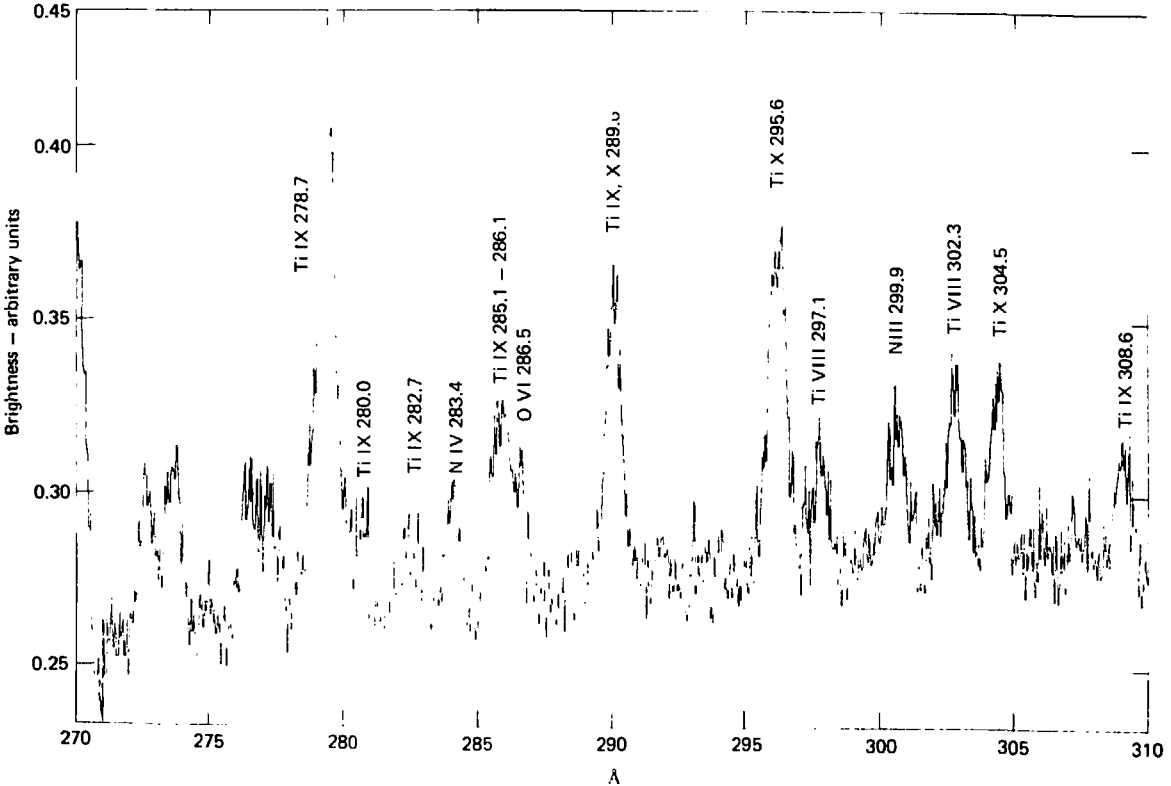

FIG. 13-1. Spectrum between 275 and 310 Å from the grazing incidence spectrograph showing titanium, nitrogen, and oxygen emissions.

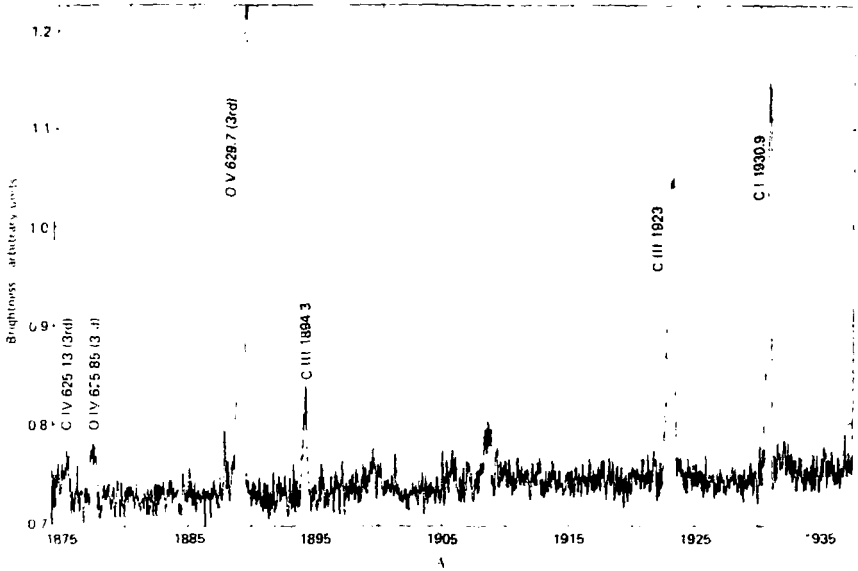

FIG. 13-2. **Spectrum between 1875 and 1940 Å from the normal incidence spectrograph showing carbon emissions.**

The radial profile of the brightness of OVI-1032 Å as a function of time is shown in Fig. 13-5. There is some influence from the stream guns in the first 5 ms of the shot, after this the profile is approximately a Gaussian shape. As was found in 2XIIB the width of the brightness profile is somewhat narrower than the electron density profile for the high ionization states. The behavior of the streaming plasma is even more evident in the emissions from deuterium at 1216 Å. Figure 13-6(a) shows the chord brightness of L_α at 9 ms in the discharge; note the large peaks which correspond to the position of the stream gun plasma. At 10 ms the stream guns are turned off, and the profile at 16 ms [Fig. 13-6(b)] is quite smooth. The time history of the radial brightness profile is summarized in Fig. 13-7, here the influence of the emission at the edge due to the stream guns is seen.

In both 2XIIB and TMX the most abundant impurity in most circumstances was oxygen. For this reason it is important to compare the oxygen density in the TMX plug with 2XIIB. Table 13-2 shows the absolute brightness of the oxygen ionization states from June 14, 1978 on 2XIIB and from September 26, 1980 on TMX. The electron temperature was about 60 eV in each case, and the stream guns were on for both measurements. Note the brightness of each ionization state in the TMX case has been multiplied by about a factor of 2; this was necessary because the instrumental resolution of the monochromator was less than the width of the Doppler-broadened emission lines.

The comparison shows that under these plasma conditions the OII densities are similar in the two machines, while the total density is somewhat less in the TMX plug. The oxygen concentrations differ by about a factor of 2. Note that the densities have been computed using *only* the resonance lines—no metastable contributions have been added—so that the actual densities and concentrations are about a factor of 2 higher. Because the neutral oxygen ionizes almost immediately, OII

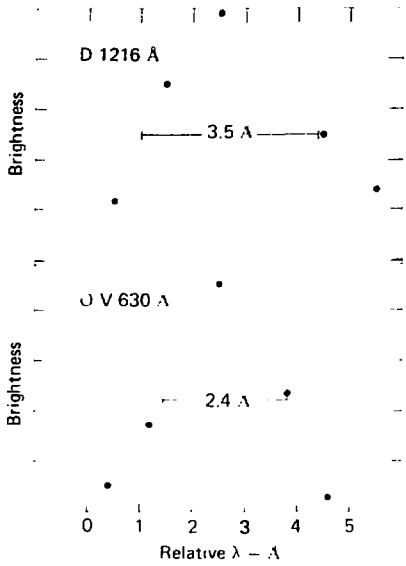

FIG. 13-3. Shot-by-shot spectrum scan of OV-630 Å ∇ and L_{α}-1215 Å ∇ showing Doppler broadening.

(singly ionized) is indicative of the source of oxygen (note it is a small fraction of the total), while the total density is influenced by the confinement of the higher ionization states. These data should also be compared from the standpoint of beam-injected oxygen, as results on 2XIIB[12] indicated that the oxygen current was a constant fraction (~2%) of the total neutral beam current. A model similar to that developed for 2XIIB can be used which accounts for the sources and sinks of beam-injected oxygen

$$f_o I_b (1 - T) = \int \frac{n_2}{\tau} dV = \int n_e n_2 S_2 dV$$

where

f_o = oxygen fraction of the neutral beam
I_b = neutral beam current
T = oxygen transmission through the plasma

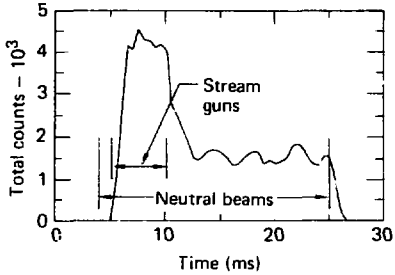

FIG. 13-4. Time history of OIV-554 Å in the east plug of TMX. The timing sequence is also shown for reference.

n_2 = density of OII
τ = ionization lifetime of OII
$1/\tau = n_e S_2$ = (electron density) (ionization rate)

If a constant fraction f_o is assumed for 2XIIB and TMX and the above calculation is performed for the plasma conditions of Table 13-2

$$\frac{\bar{n}_2 (2XIIB)}{\bar{n}_2 (TMX)} \cong 1.7$$

where the bar denotes the volume average. This calculation is accurate to about a factor of 2 due to the uncertainties in the experimental values used. The experimental ratio (factor of 2) was 0.8, so within a factor of 2 the results are consistent with a beam-injected oxygen source which is a constant fraction of the beam current. As mentioned above, the differences in the total density may be due to differences in the confinement of the higher ionization states.

13.2.4 General Characteristics—TMX Central Cell

The main focus of the impurity study in TMX was to determine the general characteristics of the impurity emission in the central cell. As discussed above, some preliminary measurements were obtained with a single chord calibrated monochromator, but the majority of the measurements were obtained with the 22-channel SIDS instrument.

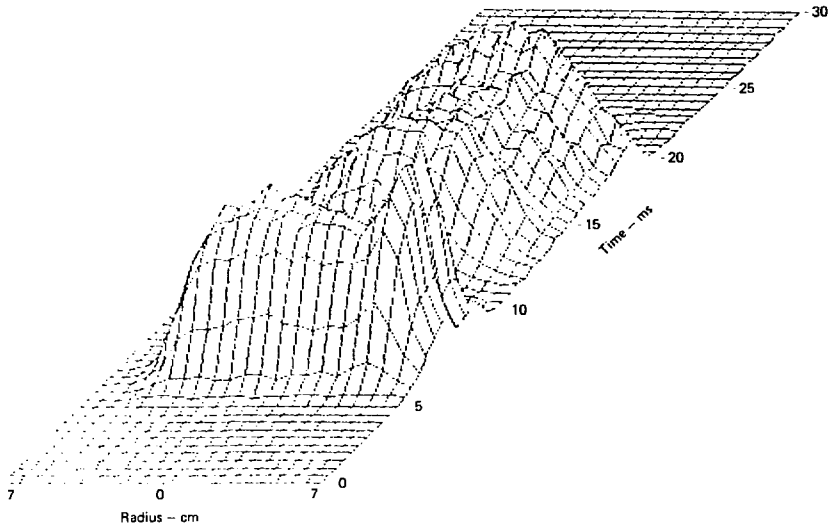

FIG. 13-5. **Radial brightness profile of OVI-1032 Å in the east plug.**

Typical Time Histories. Figure 13-8 shows the typical time histories of OII-539 Å, OIII-703 Å, OIV-554 Å, OV-630 Å, and OVI-1032 Å for both the central-cell plasma and the east plug. For the central-cell, data signals near the central chord of the plasma are shown; the time histories of the other chords are similar. The east-plug data is indicative of the center of the plasma; it does not show the initial feature (5 to 10 ms) (as was present in Fig. 13-4) as the chords, which include the stream guns, were not included in the sum.

The most obvious difference in the time histories is the initial rise. While the plug signals rise quickly because of the interaction of the plasma injected by the stream guns with the neutral beams, the central-cell signals show a delay which is indicative of the onset of plasma buildup in the central cell. In both cases, the signal is quite constant after the initial rise, showing that the impurity emission is free from large fluctuations during the steady-state plasma.

Radial Profiles. The radial profiles of four ionization states of oxygen—OII-539 Å, OIV-554 Å, OV-630 Å, and OVI-1032 Å at 10 ms are shown in Fig. 13-9. This data was obtained during typical running when the plasma was fueled with the gas box. The most obvious trend in the data is that the spatial profiles become more peaked with increasing ionization state. These profiles are quite constant in time; that is, in cases where the total emission increases, the profile shape is fairly constant.

The fact that the brightness profiles are quite broad is either a signature of the source of the oxygen, or an indication of transport effects on the impurities. Computer modeling is being used to investigate possible mechanisms.

Spatial profiles were also measured when the gas puffer was used to fuel the central cell. Figure 13-10 compares the radial brightness profile of OII-539 Å during puffer (top) and gas box (bottom) operation. Note that the brightness profile

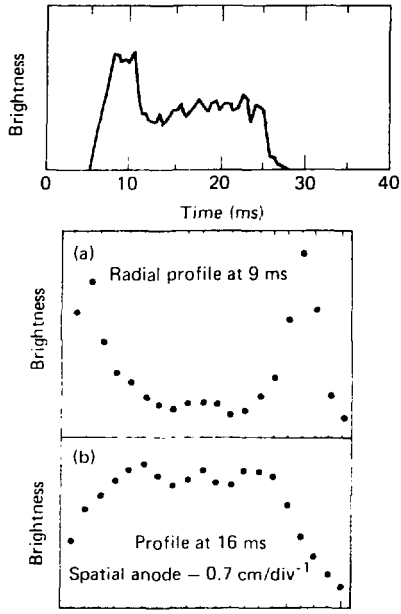

FIG. 13-6. (a) Radial brightness profile of L_α–1216 Å at 9 ms. Note the large peaks corresponding to the stream gun plasma. (b) Radial brightness profile at 16 ms.

during puffer operation is quite broad, the volume emission rate computed from a matrix inversion is a radial shell at the edge. The inverted brightness profile in the gas box case is peaked on axis (the inversion process is discussed more fully in the next section). The difference in these profiles indicated that the impurity source or source-plasma interaction are not identical in the two cases.

Radial Profiles—Inversions. The radial profiles of impurity ions are important for impurity density, power loss, and transport calculations. To more fully understand the usefulness of this data, a short digression on photometric measurements is necessary. The actual quantity measured by the spectroscopic instrument is a chord-integrated brightness. The brightness is the flux received per unit solid angle per unit projected area, with units of photons cm^{-2} sec^{-1} sr^{-1}. In the simplest case, the conversion of instrumental counting rate to absolute brightness B(y) is given by:

$$B(y) = \frac{(CR)\, D_p^2}{(QT)\, A_s A_p}$$

where

(CR) is the observed counting rate

(QT) is the efficiency of the instrument

A_s is the area of the entrance slit,

A_p is the area of the plasma that is viewed, and

D_p is the distance from the plasma to the entrance slit.

Without modeling of the spatial distribution of the emission source, the brightness profiles are useful only for qualitative comparisons. The quantity required for impurity density and radiated power calculations is the spatial distribution of each ionization state. In the cylindrically symmetric case, the data can be inverted to yield the volume emission rate. Mathematically

$$B(y) = \frac{1}{4\pi}\int_{-\infty}^{\infty} E(r)\,dl = \frac{1}{2\pi}\int_{y}^{r_w} \frac{E(r)\,r\,dr}{(r^2 - y^2)^{1/2}}$$

where E(r) is integrated along the line of sight, y is the chord height, and r_w is the plasma radius. Assuming cylindrical symmetry, the common technique used to obtain E(r) is the Abel transform.[15] We have used a matrix technique which is equivalent to the Abel inversion but is much faster. As shown in Fig. 13-11, the plasma is divided into shells, each data point is centered on a shell. The outer-most shell has no contribution from other shells, so $E_4 = 4\pi B_4 L_{44}$. The next chord sees contributions from two shells, by subtracting the contribution from the outer shell E_3 can be obtained. This subtractive technique can be formulated in matrix terms: $\underline{B} = \underline{L}\,\underline{E}$, where $\underline{L}$ is the "length" matrix containing the length of the various chords. Then $\underline{L}^{-1}\underline{B} = \underline{E}$. Because $(\underline{L}^{-1})$ is constant as long as the radial chord positions are constant, the inversion process is a simple matrix multiplication. This is especially useful when several inversions (e.g., brightness profiles versus time) all having a common geometry are required.

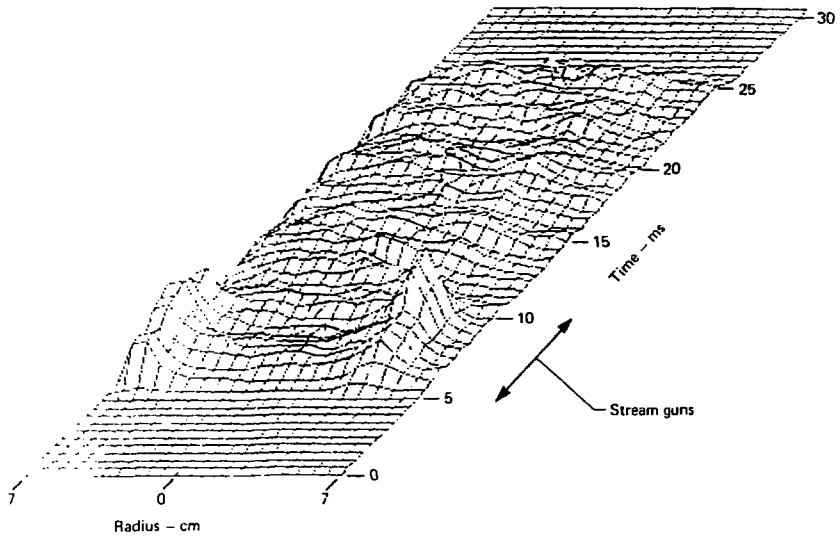

FIG. 13-7. **Three dimensional graph of L_{α}–1216 $\AA$ versus radius and time. Note the influence of the stream guns.**

13.2.5 Impurity Density Determination

The impurity ion density can be calculated from the volume emission rate profiles. In the TMX plasma it is appropriate to use the coronal model to describe the excitation and subsequent emission process. This model assumes that collisional excitation is the dominant mechanism; photo-excitation is negligible (the plasma is optically thin). Second, the spontaneous emission rates are much faster than collisional de-excitation rates. Finally, ionization and recombination times are much longer than the characteristic emission times. Hence, the volume emission rate E for a given transition is given by

$$E = n_e\, n_i\, \sigma v_{ex} \quad ,$$

where

n_e = electron density,
n_i = ion density, and
σv_{ex} = rate coefficient for excitation.

In the central-cell plasma, electron impact excitation is the most prominent mechanism. σv_{ex} is the cross section averaged over a Maxwellian electron energy distribution. A convenient expression is given by Davis[16] for optically allowed transitions:

$$\sigma v_{ex} = \frac{1.0 \times 10^{-5}\, f_{ik}\, \bar{g}}{\Delta E\, (KT)^{1/2}}\, e^{-\Delta E/KT} \quad ,$$

where

f_{ik} = absorption oscillator strength,
ΔE = transition energy (eV),
KT = electron temperature (eV), and
$\bar{g}$ = average Gaunt factor.

The Gaunt factor is a semi-empirically determined quantity which is close to one for resonance transitions. For most resonance transitions, the rate coefficient is fairly insensitive to temperature in the region of interest.

TABLE 13-2. Comparison of the oxygen emissions in 2XIIB and TMX.

Species	σv_{ex}	2XIIB (6-14-78) Brightness (full line) ($\times 10^{16}$)	2XIIB (6-14-78) Density (cm^{-3})	TMX (9-26-80) Brightness (1 Å) ($\times 10^{14}$)	TMX (9-26-80) Brightness Full line ($\times 10^{14}$)	TMX (9-26-80) Density (cm^{-3})
OII	4.7×10^{-9}	0.2	6.3×10^{9}	4.0	7.6	6.8×10^{9}
OIII	9.7×10^{-9}	1.6	2.4×10^{10}	8.0	19.2	8.3×10^{9}
OIV	1.4×10^{-8}	19	2.0×10^{11}	40.0	80.0	2.4×10^{10}
OV	2.7×10^{-8}	56	3.4×10^{11}	40.0	88.0	1.5×10^{10}
OVI	1.7×10^{-8}	43	3.7×10^{11}	100.0	340.0	8.4×10^{10}
Total			9.4×10^{11}			1.4×10^{11}

	Plasma conditions 2XIIB (6-14-78)	Plasma conditions TMX (9-26-80)
Te (eV)	60	60–70
I_b (Amps)	405	115
$\int n_e dl$ (cm^{-2})	8.5×10^{14}	3×10^{14}
$\bar{n}_e$ (cm^{-3}) (R_p = 10 cm)	$\sim 3 \times 10^{13}$	$\sim 1 \times 10^{13}$

Note: Densities are *only* from measured emissions and do not include metastable states.

Emission Model. It is useful to characterize the impurity emission and therefore its density with a model. This facilitates comparison with other data, and in many cases greatly simplifies calculations. In particular, these simple models for the ion density were tried:

1. *Constant Density Model:* $n_i(r)$ is constant. Since

$$B = \frac{1}{4\pi} \int n_e(r) n_i \ \sigma v_{ex} \ dl \quad ,$$

the brightness profile is proportional to $\int n_e dl$ as long as the T_e profile is sufficiently broad so that σv_{ex} = constant.

2. *Constant Concentration Model:* $n_i(r)/n_e(r)$ is a constant, so the shape of $n_i(r)$ is the same as that of $n_e(r)$. Hence, the brightness profile is proportional to the density squared; for a Gaussian profile, the width of the brightness profile is less by a factor of $\sqrt{2}$.

3. *Shell Model:* When the ionization states exist in narrow shells, the brightness is given by:

$$B = \frac{1}{4\pi} \ n_e \ n_i \ 2\Delta W \quad ,$$

where ΔW is the width of the emission shell and n_e and n_i are assumed roughly constant over the width of the shell.

Figure 13-12 shows the radial brightness profile of OV-630 Å and the volume emission profile obtained from it by matrix inversion. In addition, the chord average ($\int n_e dl$) profile obtained by neutral beam attenuation is included. The $\int n_e dl$ profile is well characterized by a Gaussian profile, so the n_e profile will have a similar shape (as the inversion of a Gaussian profile yields a Gaussian). The fact that the brightness and volume emission rate profiles are so similar suggests that this data is also well characterized by a Gaussian profile, furthermore $B(r) \propto E(r) \propto n_e(r)$ which implies that a constant density model is the appropriate choice for this data. A similar result was obtained for OIV; these two ionization states were examined most carefully as they contain the major fraction of the oxygen density in the TMX central cell.

Impurity Density Results. Using the constant density model; the ion density is simply

$$n_i = \frac{4\pi B}{\int n_e dl \ \sigma v_{ex}} \quad ,$$

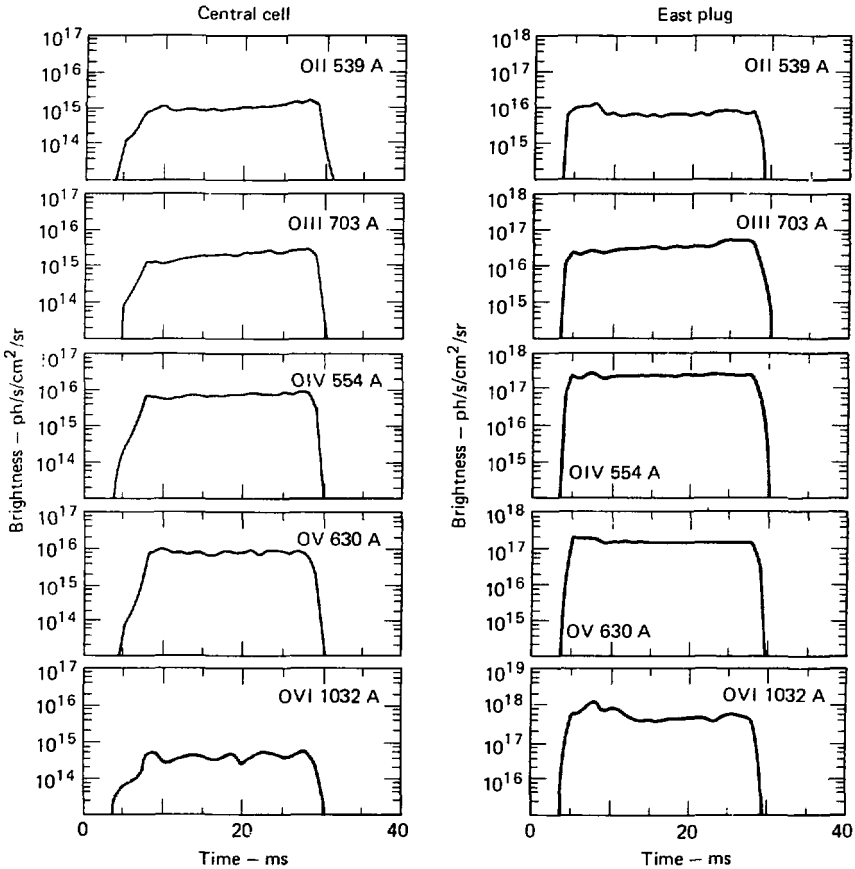

FIG. 13-8. A comparison of the time histories of oxygen emissions in the central cell and the east plug.

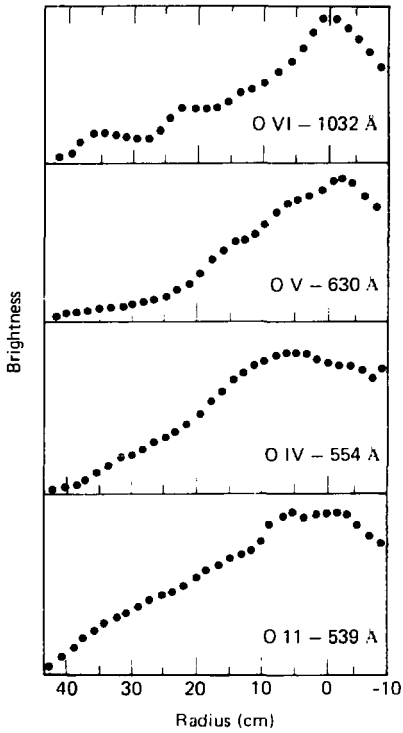

FIG. 13-9. Spatial profiles of OII, OIV, OV, and OVI at 16 ms.

where B is the central chord brightness. Table 13-3 presents the concentrations of the oxygen states obtained during a single run on November 1, 1979, during gas box operation. The OV metastable to ground state density ratio was measured to be 0.7 in these conditions, the other metastable ratios were assumed to be similar to the 2XIIB case. Note that most of the oxygen density is in OIV and OV, with a smaller amount in OVI.

Similar calculations were carried out for carbon and nitrogen, and the results are summarized as follows (factor of 2 uncertainty):

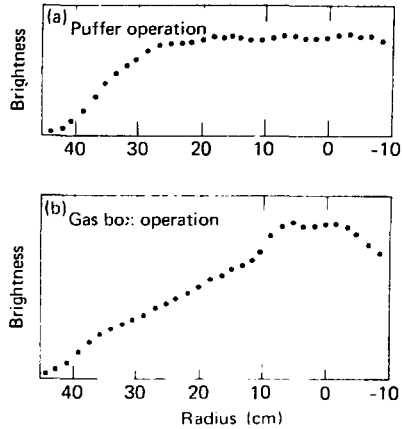

FIG. 13-10. (a) OII radial brightness profile at 16 ms—puffer operation. (b) OII radial brightness profile at 16 ms—gas box operations.

Oxygen	0.4%
Carbon	0.08%
Nitrogen	0.2%

The concentration is defined to be n_i / n_e where

$$n_i = \int_0^{r_p} n_i \, r dr \left(\int_0^{r_p} r dr \right)^{-1}$$

For a Gaussian profile $n_i = 0.632\ n_i$ (n_e = peak density). It should be noted that this emphasizes the section $r < r_p$; this was chosen because the impurity and electron density behavior are less well known outside of this region. However, if one defines the concentration to be n_i (total) n_e (total), the result is only 40% greater. Comparisons with data from other runs indicate that these results, to within a factor of 2, are typical densities of the light impurities. In some cases, the relative populations of the ionization states changed (which would be expected if the electron temperature changed), but the overall density remained fairly constant.

13.2.6 Radiated Power

Radiated Power from Light Impurities and Deuterium. As discussed above, it is also important

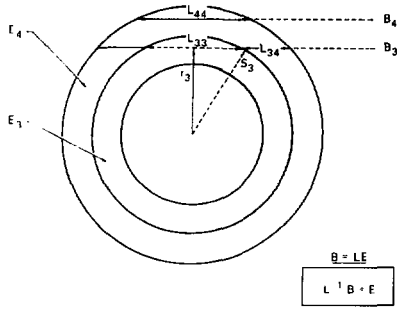

FIG. 13-11. The matrix inversion technique.

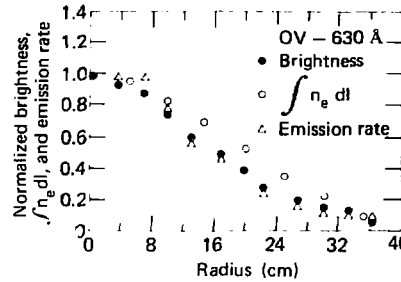

FIG. 13-12. Spatial profile of brightness and volume emission rate for OV-630 Å. The best fit of $\int n_e dl$ is also known.

to determine the amount of radiated power caused by line radiation from the impurities present in the plasma. One approach would be to measure every spectral emission feature and its radial profile; the sum of these measurements would be the total radiated power. This is impractical with a monochromator; as shot-by-shot spectral scans would be required over a large spectral range. However, certain simplifying assumptions can be made so that measurement of the radial profiles of only the resonance and metastable transitions is sufficient. These assumptions are justifiable from a knowledge of the atomic physics of the ionization states. Namely:

1. The principal excitation mechanism is electron impact excitation.

2. Only ground and low-level metastable levels are populated significantly.

3. $\Delta n = 0$ (n = principal quantum number) are the most significant transitions, followed by $\Delta n = 1$.

4. For $\Delta n = 0$ transitions, the effective Gaunt factor g in the excitation rate coefficient is nearly 1; for $\Delta n = 1$ transitions it is less. We will assume $g \cong 1$ for $\Delta n = 0$ and $g = 0.5$ for $\Delta n = 1$. This is based on results by Davis.[16]

With these assumptions, by measuring the resonance transition and the metastable transition of a certain ionization state, the radiated power from all of the transitions can be calculated. Specifically, the volume emission rate is proportional to σv_{ex}, so the radiated power is given by

$$P_o = \frac{A \ \sigma v_{ex\ o}}{\lambda_o} ,$$

where o denotes the measured resonance or metastable transition and A is the proportionality constant; then for another transition

$$P_j = \frac{A \ \sigma v_{ex\ j}}{\lambda_o} .$$

And finally, expressing the power in the j^{th} transition in terms of o equals

$$P_j = \left(\frac{P_j}{P_o}\right) P_o$$

$$= \frac{\lambda_o \ \sigma v_{ex\ j}}{\lambda_j \ \sigma v_{ex\ o}} .$$

To compute the total radiated power P_j must be summed over all of the relevant resonance and metastable transitions. In turn, to compute the total power from one species, all of the power in each ionization state must be added up.

The results of the impurity-radiated power calculation are summarized in Table 13-4, the impurity concentrations are also included. In the case of oxygen, the majority of the power comes from OIV and OV; recall these ionization states also contain most of the density. The power loss from deuterium radiation was estimated in a similar fashion.

TABLE 13-3. Central-cell oxygen concentrations.[a]

Shot	Species	%
37	OII	0.06
26	OIII	0.06
20	OIV	0.20
13	OV	0.11
40	OVI	0.01
Total		0.4

[a]November 1, 1979.

Radiated Power—Titanium. The estimation of radiated power from titanium radiation is more difficult, as the atomic physics coefficents are not well known. A crude estimate was performed by cross-calibrating the survey instrument with the calibrated single-channel instrument in the central cell. Specifically, a photographic spectrum was obtained which included the major oxygen emissions and several titanium lines on the same plate. During the discharges, the absolutely-calibrated monochromator measured the oxygen emissions. By adding up all of the titanium emissions (nearly 300), an estimate of the radiated power from titanium relative to oxygen was obtained. The results are also included in Table 13-4.

It should be noted that this was only a crude estimate (factor of 3 to 4 uncertainty); the measurement assumes that most of the important emissions were measured, and that the radial profiles are not substantially different when compared to other impurity species. Transfer of the absolute calibration from the monochromator to the film and shot-to shot variations in the emissions are probably the largest sources of error.

13.3 EXPERIMENTAL TRENDS—WALL CONDITIONS

It is well known that wall conditions in a plasma device can significantly influence the plasma conditions. Normally, a low temperature plasma (discharge cleaning[17]) and/or titanium gettering is used for wall preparation. In addition, it has been shown by the Alcator group[18] that the wall temperature can influence the light impurity

TABLE 13-4. - Impurities in TMX central cell.

Species	Concentration, % (factor of 2)	Radiated power,[a] kW (factor of 2)
O	0.4	6.0
N	0.1	1.5
C	0.08	1.5
Ti	0.1[b]	10.0[b]
D–La	—	5

Plug oxygen concentration, %			
TMX	TMX scaled[c]	2XIIB	
0.25	1.5	3	

[a]Typical trapped beam power = 450 kW.
[b]Estimated.
[c]Linear scaling was assumed.

density both during discharge cleaning and the plasma discharge. This section discusses the results of two experiments on TMX which examined the effect of wall conditions on the plasma.

13.3.1 Gettering

The first experiment was to measure the effect of titanium gettering on the oxygen density in the central-cell plasma. On September 25, 1980, a specific set of wall conditions existed in the central cell because of previous experiments: the whole machine had been gettered except for a section between the limiters in the central cell (to protect the ICRH antenna). On shots 4 to 15, the machine was run in the same configuration and emissions from oxygen and carbon were monitored. The machine (except for the section noted) was gettered on every shot. On shots 16 to 25, the entire gettering system was used (including the ICRH section of the central cell) and these emissions were again monitored. The results are shown in Table 13-5; the brightness is used for comparison. The discharges shown were similar; the electron density decreased approximately 30% after the new panel was gettered. The results show that gettering does affect the central-cell impurity density.

A second overall trend was noted during the initial phases of several runs. To prolong the lifetime of the gettering system, it is sometimes

TABLE 13-5. Impurity brightness before and after localized central-cell gettering.

Shot	Species	Wavelength, Å	Brightness photons/cm^2-sr	Getter		Decrease[a]
				Before	After	
4	OII	539	3.3×10^{13}	x		
8			2.7×10^{13}	x		
9			2.5×10^{13}	x		
11			2.5×10^{13}	x		
12			3×10^{13}			
10	OII	539	1×10^{13}		x	0.60
5	OIII	703	1×10^{13}	x		
17			4×10^{12}		x	0.60
6	CII	904	1×10^{13}	x		
19			8×10^{12}		x	0.2
7	CIII	977	3.2×10^{14}	x		
20			8×10^{13}		x	0.75

[a] $\frac{\text{Brightness}_{\text{getter}} - \text{Brightness}_{\text{nongetter}}}{\text{Brightness}_{\text{getter}}}$.

used only on alternate shots. During this time, OII-539 Å emission was monitored and changes in the brightness were observed to correlate with the gettering. That is, B $_{in}$dl was approximately 40% greater on nongettered shots than on those with gettering. This sequence usually persisted until shot 15 to 20 of the run (often, a switch to gettering before each shot was made when this mode was detected), after this time, the emission dropped to a plateau and was quite constant even if gettering was performed on alternate shots. This result suggests that the central-cell wall conditions influence the impurity density in this region.

13.3.2 Liner Experiments

As discussed in Ref. 19, liners filled with liquid nitrogen are used in TMX for additional vacuum pumping. These liners are used in the ends of the central cell (outside of the plasma radius) and in both plugs. Emissions from light impurities were monitored before and after the liners were filled to determine their effect on the impurity density. Decreases in the measured brightness in the central cell were observed after the liners were filled in some cases; however in other cases, no change was seen. (In all cases the ambient pressure was decreased at least a factor of 3.) However, the brightness measured in the plug was normally unchanged by liner operation. This result is consistent with a wall source of impurities in the central cell and primarily beam-introduced oxygen in the plugs.

13.4 SUMMARY OF OTHER IMPURITY EXPERIMENTS

13.4.1 Central-Cell Heating Experiment

For a short period, TMX was operated with three neutral-beam injectors mounted on the central cell at approximately Z = 0. The single-channel monochromator was also mounted on the central cell, but at approximately Z = 40 cm, hence it did not view the beams directly. The central-cell injectors were turned on at 14 ms and off at 20 ms for the data presented here.

The central-cell brightness versus $\sin^2\theta$ for OIV-554 Å, OV-630 Å, and OVI-1032 Å are shown

in Fig. 13-13. The beam current injected into the central cell was 60 $\bar{A}$, while the east and west beam currents were 55 $\bar{A}$ and 35 $\bar{A}$, respectively. Note the dramatic increase in OIV, which is accompanied by a rapid increase in OV and a slower increase in OVI. After 2 to 3 ms, the OIV signal decreases, while the OV decreases slightly and the OVI continues to increase.

One interpretation of these results is that the electron temperature in the central cell increases when the central-cell beams are turned on. In addition, the oxygen density may increase, as the OIII and OIV brightness are approximately the same before and after the beams are on. That is, if the only the electron temperature were increasing, a shift to the higher ionization states with a corresponding decrease in the lowest states would be expected. Because the spectrometer is well separated from the injectors, the increase may be an indication of the bulk electron behavior, as opposed to a local effect present only near the beam. It should also be noted that this dramatic behavior was observed only when the plug and central-cell beam currents were of the same order. For example,

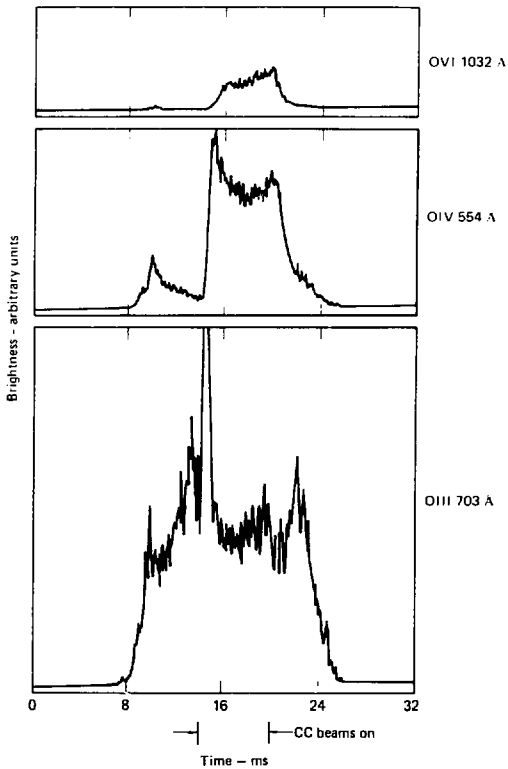

FIG. 13-13. Impurity behavior during the central-cell beam-heating experiment.

with l_p = 100 Å per plug and l_c = 60 Å, the dramatic increases were not seen.

13.4.2 Impurity Injection Experiments

A series of impurity injection experiments was performed on TMX to study three main issues: (a) impurity confinement, (b) impurity sources and penetration, and (c) radial transport in the central cell. These experiments involved puffing an impurity gas into the central cell and measuring the emissions from this impurity as a function of time.

Experimental Procedure. Deuterium, oxygen, and neon were introduced into the central cell by means of a fast-pulsed valve which was located at Z = 0. Two different valve-timing sequences were used. In the first case, the valve was opened for 5 ms starting 4 ms before the shot sequence (i.e. −4 to +1 ms). In this way, the impurity was distributed before the plasma was initiated, minimizing gas penetration effects in the initial phases of the plasma. In the second case, the valve was turned on at 12 ms and off at 17 ms, which introduces the impurity during steady-state plasma conditions. This should allow a determination of the impurity penetration rates and a measure of radial transport in the central cell.

Neon was initially chosen for injection because it is not an intrinsic impurity in TMX. Oxygen was used because it is much more readily pumped by the cold liner surfaces and gettered walls than neon; this provides a different source and presumably different edge plasma conditions. Finally, deuterium was injected because it is the plasma working gas. (In passing, it should be noted that neutral oxygen and deuterium are also similar in that their ionization potentials are equal.) When oxygen and deuterium were injected, the contribution due to the intrinsic levels of these species was subtracted.

The 22-channel monochromator with a spatial imaging detector system (SIDS) mounted on the central cell was the main diagnostic used during the impurity injection experiments. Time-resolved radial profiles of several ionization states of neon, oxygen, and deuterium were monitored. In addition, the monochromators on the plugs were also used to measure the amount of the impurity which penetrated into the plugs from the central cell.

Experimental Results and Discussion. When oxygen was puffed into the central cell before the shot, the emission from the ionization states decreased throughout the entire discharge. Oxygen injection increased the brightness by a factor of approximately 3 over the intrinsic level. Because recycling most certainly influences these results, it is difficult to ascertain estimates of impurity confinement times until a more detailed analysis is completed.

The radial profiles of singly-ionized neon and oxygen at 25 ms are shown in Fig. 13-14. Note that the OII density is less than that of Ne II by a factor of 5 while the amount of oxygen injected was greater by a factor of 2; this suggests that the oxygen recycling was smaller due to the titanium gettering. Figure 13-15 shows the radial profile of the total puffed oxygen density vs time, and the profiles for neon are similar. The large density at the edge suggests that the oxygen does not penetrate efficiently into the core of the discharge.

Another general observation was that the emission in the plug was influenced very little by the injected species. This supports the theory that the central-cell ions are confined axially by the electrostatic potential between the plugs and the central cell and that the ions do not penetrate into the plug.

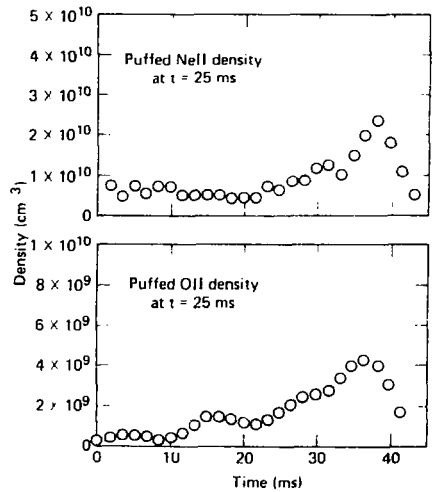

FIG. 13-14. The radial profiles of Ne II and OII at 25 ms.

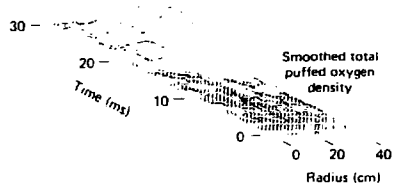

FIG. 13-15. Radial profiles versus time for the injected oxygen density.

Finally, these results are currently undergoing comparisons with a simple computer model. Further analysis should yield information on the confinement times and recycling rates of impurities in TMX.

13.5 COMPUTER MODELING OF RESULTS

Several computer models have been developed to predict the radial impurity brightness profiles using the observed electron density and temperature profiles. Impurity transport has been included (albeit in a somewhat crude sense) by a. including a radially dependent confinement time for each ionization state, and b. assuming a constant impurity velocity in the diffusion equation. While both models are quite simple and are steady state, they do allow qualitative observations to be made.

13.5.1 Steady-State Confinement Time Model

The sources and losses of a particular ionization state are expressed in this model as:

$$0 = \frac{dn_i}{dt} = n_e\, n_{i-1}\, S_{i-1} + n_e\, n_{i+1}\, \alpha_i - n_e\, n_i\, S_i - n_e\, n_i\, \alpha_{i-1} - \frac{n_i}{\tau_i}$$

where

n_e = electron density (a function of radius)
n_i = density of the i^{th} ionization state of a particular element (a function of radius)
S_i = ionization rate out of the i^{th} state (a function of electron temperature)
α_i = recombination rate to the i^{th} state (a function of electron temperature)
τ_i = confinement time of the i^{th} state (a function of radius)

In addition, when i = 1, there is an additional source term of neutrals which is also a function of radius. (Note that S_i and α_i are also functions of radius as T_e is a function of radius.) The coefficients for ionization (S) use the generalized form due to Lotz[20] and the recombination coefficients are a generalized form which includes both radiative and dielectronic terms; the values have been matched to those of Ref. 21. The electron density and temperature profiles used were a Gaussian shape; the width and maximum value were consistent with the experimentally measured values.

An example of the radial ion density profiles from the code for oxygen are shown in Fig. 13-16. In the code they are multiplied by the (radially dependent) electron density and the excitation rate (discussed earlier) to obtain the synthetic volume emission rate profile. Finally, the chord lengths of the cylindrical source are taken into account—essentially the inverse of the Abel transform—to obtain the radial brightness profile which is actually measured in the experiment (Fig. 13-17).

There is fairly good *qualitative* agreement between the synthetic profiles and the experimental profiles. Variations in the code—such as different neutral oxygen-density profiles—are being investigated to understand their affects on these

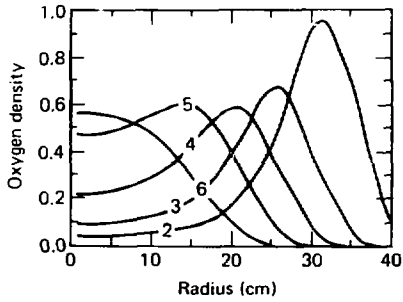

FIG. 13-16. Oxygen density as a function of radius from the steady-state code.

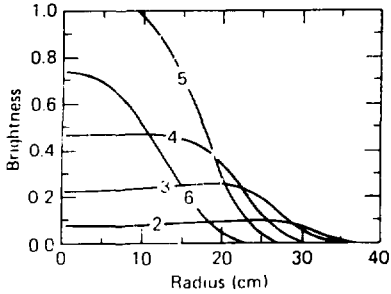

FIG. 13-17. The volume emission is "reinverted" to obtain the brightness profile, which is the actual quantity that is measured in the experiment.

profiles. In addition, code runs have been performed to determine the sensitivity of these profiles to variations in electron temperature and density, atomic physics rates, and confinement times.

13.5.2 Constant Velocity Steady-State Model

This model is also an evaluation of the sources and losses with a one-dimensional constant velocity approximation to the impurity transport. This model is similar to a model used to characterize impurity radiation on the TFR tokamak (Ref. 22). The source and losses can in this case be written

$$\frac{dI}{dt} = \frac{dI}{dt}(\text{in}) - n_e n S_{ion} - n_e n \alpha_{rec}$$

$$+ S_{ion} n_e n_0 + \alpha_{rec} n_e n_{+1} - \frac{n}{\tau}$$

The τ term is again a general confinement time (loss term) and α and S have the same definitions as above. A flux of neutral impurities is incident at the edge of the plasma, so this system of equations is subject to the boundary conditions

$$\Gamma_0 2\pi a = 2\pi a\, n_0(a) v_{n_0}$$

and

$$n_i(a) = 0$$

where

Γ_0 = neutral impurity flux
n_0 = neutral impurity density
a = plasma radius

The system of equations is solved numerically on a computer. A set of radial points is established and then the impurity density of each ionization state is calculated by starting at the boundary and working inward. That is, the boundary value is specified and the equations enable a calculation of the derivative. By knowing the slope, the value at the next (inner) radial point can be determined. This procedure is continued until the radial profiles are computed.

Initial results from this code have shown that, in a qualitative sense, the results are similar to those discussed for Sec. 13.5.1. Variation of input parameters, such as the velocity, is being investigated to try to attain closer agreement with the experimental radial profiles in the gas box case.

13.6 DISCUSSION OF CONCLUSIONS

The results presented here are the first comprehensive impurity study of a tandem mirror machine. The impurity measurements in the TMX plug show that the emission from the ions is significantly Doppler broadened with an effective energy on the order of 10-15 keV; this indicates that oxygen is injected by the neutral beams. Furthermore, the source of oxygen (factor of 2) is similar on 2XIIB and TMX.

The major focus of this study was impurity behavior in the central-cell plasma. Time resolved radial emission profiles were used to calculate the density of light impurities (factor of 2 uncertainty): 0.4% oxygen, 0.1% nitrogen, and 0.08% carbon. The total radiated power from the impurities was estimated to be 20 to 30 kW, which is approximately 10% of the input power. In general, the central-cell impurity concentration was found to be influenced significantly by vacuum vessel conditions such as gettering and, in some cases, use of cold liners.

Finally, oxygen and neon gases were introduced into the plasma to study the details of impurity behavior. While the analyses of these results are incomplete, the spatial profiles of the density as a function of time show that impurity does not penetrate into the core of the plasma.

REFERENCES

1 E Hinnov Princeton Plasr. Physics Laboratory Report MATT-194 rinceton N J (1962)

2 N Bretz D L Dimock L Hinnov and E B Meservey "Energy Balance in a Low-Z High-Density Helium Plasma in the S Tokamak" *Nucl Fusion* **15** 313 (1975)

3 K Bol J J Cecchi C C Daughney F DeMarco R A Ellis Jr H P Eubank H P Furth H Hsuan F Mazzucato and R R Smith in "Experiments on the Adiabatic Toroidal Compressor" *Proc Intl Conf Plasma Phys and Controlled FusioRes 5th, Tokyo* **1** 83 (1975)

4 TFR Group "Space- and Time-Resolved Study of Impurities in TFR Tokamak Plasmas" *Phys Rev Lett* **36** 1306 (1976)

5 D Grove V Arunasalam K Bol D Boyd N Bretz M Brusati S Cohen D Dimock F Dylla D James E Eubank B Fraenkel J Girard R Hawryluk E Hinnov R Horton F Hosea H Hsuan D Ignat F Jobes D Johnson F F Mazzucato E Meservey N Sauthoff J Schivell G Schmidt R Smith F Stauffer W Stodiek J Strachan S Suckewer S von Goeler and K Young "Experimental Results of the PLT Tokamak" in *Proc Intl Conf Plasma Phys and Controlled Fusion Res 6th, Berchtesgaden,* **1** 21 1977

6 J L Terry K J Chen H W Moos and E S Marmar "UV Impurity Study of the Alcator Tokamak" *Nucl Fusion* **18** 485 (1978)

7 E Hinnov K Bol D Dimock R J Hawryluk D Johnson M Mattioli E Meservey and S von Goeler *Bull Am Phys Soc* **22** 2F3 (1977)

8 T C Simonen E H Coensgen W F Cummins and W E Nexsen *Nucl Fusion* **15** 813 (1975)

9 J P Drake and H W Moos *Nucl Fusion* **19** 407 (1979)

10 E H Coensgen W F Cummins B. G. Logan, A W Molvik W E Nexsen T C Simonen, B W Stallard, and W C Turner, "Stabilization of a Neutral-Beam Sustained, Mirror-Confined Plasma," *Phys Rev Lett* **35**, 1501 (1975)

11 R. P. Drake and H. W. Moos, *Nucl Fusion* **20**, 599 (1980)

12 R P Drake *Extreme Ultraviolet Diagnosis of a Neutral-Beam-Heated Mirror Machine* Lawrence Livermore National Laboratory, Livermore CA UCRL-52751 (1980)

13 E H Coensgen *TMX Major Project Proposal* Lawrence Livermore National Laboratory, Livermore CA LLNL-Prop-148.

14 E H Coensgen C A Anderson T A Casper J F Clauser W C Condit D E Correll W F Cummins J C Davis R P Drake, J H Foote A H Futch R K Goodman D P Grubb G A Hallock R S Hornady A L Hunt B G Logan R H Munger W E Nexsen T C Simonen D R Slaughter B W Stallard and O T Strand "Electrostatic Plasma-Confinement Experiments in a Tandem Mirror System" *Phys Rev Lett* **44** 1132 (1980)

15 H R Griem *Plasma Spectroscopy* (McGraw-Hill New York 1964) p 176

16 J Davis J *Quan S, ctrosc Radiat Transfer* **14** 549 (1974)

17 R J Taylor *J Nucl Mat* **76 & 77** 41 (1978)

18 E S Marmar D Overskei H Helava K J Chen J L Terry and H W Moos "The Effects of Wall Temperature on Light Impurities in Alcator" *Nucl Fusion* **19** 485 (1979)

19 J Jolly J Parkinson and D Swan *Installation and Operation of Cryoliners in the TMX Vacuum System* Lawrence Livermore National Laboratory Livermore CA UCRL-82886 (1979).

20 W Lotz *Astrophys J Suppl Ser* **14** 207 (1967)

21 M Matholi *Revue Bibliographique des Coefficients D'Ionisation de Recombinaison et D Excitation des Impurities Presentes dans un Plasma,* EUR-CEA-FC-761 1975

22 C Breton C DeMichelis and M Matholi *Nucl Fus* **16** 891 (1976)

SECTION 14
PASSIVE SOLID-STATE PROBE MEASUREMENTS IN TMX*

*(A. E. Pontau,** R. Bastasz,** K. L. Wilson,** W. Bauer,**
W. R. Wampler,† and R. P. Drake)*

*This work was supported by the U.S. Department of Energy.
**Sandia National Laboratories, Livermore, CA 94550.
†Sandia National Laboratories, Albuquerque, NM 87185.

14. Passive Solid-State Probe Measurements in TMX

14.1 INTRODUCTION

Passive solid-state probes have been utilized on several tokamaks[1-4] to measure plasma parameters in the edge region. The basis of the technique is that energetic atoms and ions incident on a probe inserted into a plasma are trapped and later analyzed to obtain information about the plasma. We describe here the first such work on a tandem mirror machine and present data on energies and fluxes of deuterium and impurity ions as functions of probe positions and orientations.

The measured energy of the central-cell deuterium (D) incident on a grounded probe at r = 30 cm varied markedly with probe orientation. Deuterium incident on samples facing radially inward had an energy of 50 ± 15 eV into the surface while the analogous energy for D incident on a sample facing the east end was ~150 eV. We also observed variations of fluxes with orientation. The measured flux to an inward facing sample in the central cell decreased with increasing radial position so that the flux at r = 30 cm was ~4 × 10^{17} D·cm^{-2}·s^{-1} and at r = 40 cm it was ~1.5 × 10^{17} D·cm^{-2}·s^{-1}.

Impurities were observed with a probe in the central cell at r = 30 cm. O, Ti, Fe, and sometimes Cu impurities were present on samples, but no N was seen.

Other measurements showed that under certain conditions east end-cell losses were ~25% of total east axial losses, and a significant portion of the trapped east neutral beam current was lost axially rather than radially.

The remainder of this introductory section is concerned with the trapping characteristics of suitable probe materials and appropriate analytical techniques. Following this Introduction there is a more specific discussion of the experimental procedures used for TMX. A detailed compilation of results with discussion concludes this part of the report.

The experience gained in this initial effort has aided planning for future experiments on TMX-Upgrade. The adaptation of surface probe techniques to the different geometry of a tandem mirror device has opened several new areas for further exploration.

14.1.1 Trapping Characteristics of Carbon and Silicon

Carbon and silicon are similar in their deuterium trapping characteristics. For a given energy and angular incidence, the non-reflected portion of the D flux is retained in the material up to a saturation trapping level. At that point no increase in the retained D level is observed, i.e., for each new incident D retained, one is released. The saturation level increases as the incident energy increases (see Fig. 14-1). For a spread of incident energies and angles, the approach toward saturation is more gradual (Fig. 14-2).

Phenomenological models[5,6] have been developed to characterize this behavior, providing accurate predictions of D retention under a variety of conditions. The models are generally based on the concept of a saturation D concentration. Once the saturation level is reached within the material, the total retention begins leveling off (see Fig. 14-3).[6] The greater the range of the incident D, the higher the total retention.

The saturation curves of Figs. 14-1 and 14-2 can be used to determine the energy of D incident on carbon. This is done by exposing separate samples to specified numbers of identical plasma shots and measuring the D retention for each sample. The flux and energy are then determined by fitting the measured data to the D retention behavior curves. Once the D energy and angular incidence have been established, the D retention measurement is all that is necessary to derive the incident flux, i.e., it is not necessary to reproduce the whole curve for each flux determination.

Another way to establish incident D energy is to measure the depth distribution of retained D. This distribution may then be compared to measured and/or calculated profiles for known incident D energies and angles.

Incident impurities may also be retained on the material surface and later be analyzed.

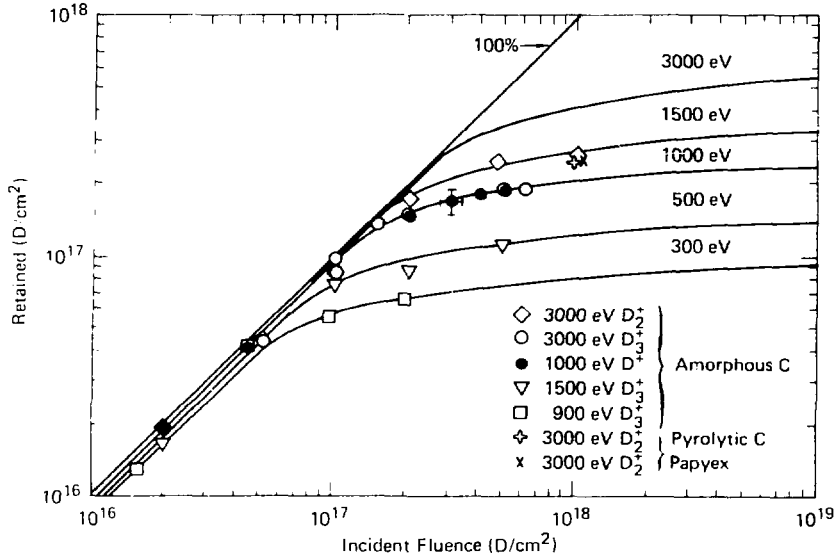

FIG. 14-1. Retention for monoenergetic D at normal incidence on carbon, calculations (curves) and data (symbols). Typical error bars are indicated.[5]

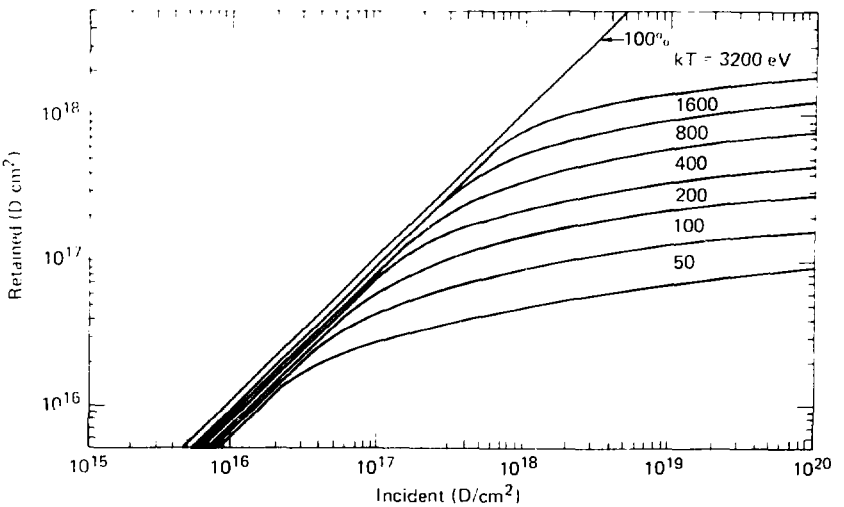

FIG. 14-2. Retention curves for D with a Maxwellian velocity distribution and cosine angular incidence on C, calculated using TRIM profiles and a saturation level of 0.42 D/C.[5]

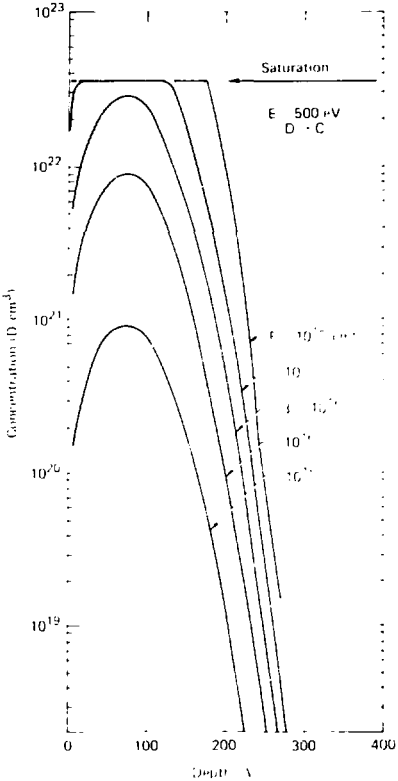

FIG. 14-3. Representation of D saturation in carbon for 500 eV incident D.[6]

14.1.2 Analysis Techniques

Nuclear Reaction Analysis (NRA) and Elastic Recoil Detection (ERD) measure the absolute amount of D trapped in carbon samples. For NRA a 750-keV ^{3}He beam normally incident on the carbon sample produces protons and alphas via the $d(^3He, \alpha)p$ nuclear reaction.[7] At a scattering angle of 165°, the alphas and/or protons are counted with a silicon surface barrier detector and associated electronics. The yield of alphas and/or protons can be calibrated for a given amount of D present in the sample. By counting the number of alphas and/or protons produced per incident ^{3}He ion the total amount of D near the carbon surface may be measured.

ERD works by scattering hydrogen isotopes from a sample using a ^{4}He analyzing beam.[8] The ^{4}He beam strikes the sample surface at a grazing angle dislodging H and D from the sample. The H and D are collected and energy analyzed for mass separation. The yields are established using calibration standards. The low incident and exit angles to the surface require a smooth sample for accurate measurements.

The same ^{4}He beam works for Rutherford Backscattering Spectrometry (RBS).[9] The normally incident ^{4}He ions scatter off of impurities on the sample surface are collected at a scattering angle of 165° and energy analyzed. The mass of the impurity can be determined from the energy of the scattered ^{4}He; the amount of the impurity is determined from the yield at that energy.

Secondary Ion Mass Spectrometry (SIMS) provides a measurement of the depth profile of D implanted in silicon.[10] The shape of this profile may in turn be related to the incident D energy through comparison with calculations or samples implanted at a known energy. For SIMS the samples is sputtered using a 1 keV Ar^+ beam. Sputtered ions are mass analyzed and the D signal is monitored as a function of depth into the surface. This depth is calibrated as a function of the sputtering beam fluence by measuring sputter depths on standards. SIMS relies on a constant sputtering rate so a smooth, uniform sample is necessary.

14.2 EXPERIMENTAL PROCEDURE

14.2.1 Samples

Three different types of samples were used in the TMX passive probe measurements. One-half-mm thick, polished, high purity silicon discs[11] were cut into 6-mm-square samples to be used for SIMS analysis. These Si samples were annealed at 650°C for several hours in vacuum ($< 5 \times 10^{-8}$ torr) prior to their exposure in TMX. Papyex, a flexible, compressed flaked carbon tape[12] was cut into 1-cm diameter samples and used for all NRA and RBS measurements. Seventy-five- $\mu g/cm^2$ carbon films, vapor deposited on glass slides,[13] were used for ERD analysis. The glass slides were broken into ~1-cm squares for exposure. These films were used

(rather than the Papyex) since surface roughness could adversely affect ERD measurements.

14.2.2 Probes

A probe was designed to sequentially expose mixed pairs of C (Papyex) and Si samples to the TMX central-cell plasma and to then protect the samples while Ti was deposited on the TMX interior for gettering. The probe was a demountable sample holder connected to the end of a support tube. A Wilson vacuum seal allowed the probe to be positioned at different depths (TMX radial positions) or withdrawn completely to reload samples. A rotatable shutter served the dual purpose of selecting which samples were exposed and covering the samples during gettering cycles. The shutter allowed sequential exposure of one, two, or three pairs of samples simultaneously. An alternate shutter exposed one pair at a time. The shutter rotated by means of a shaft concentric to the support tube which passed through a second Wilson seal and was connected to a Geneva mechanism which drove the shutter in 60° increments. Four microswitch cam assemblies sensed the four shutter positions of interest, and a fifth assembly sensed when the gear motor-driven input of the Geneva mechanism completed a cycle. A shutter control system was in the TMX control room.

Another version (probe 2) included the capability of mounting the additional pairs of samples at 90° intervals around the outside edge of the probe. Thus sample pairs facing five different directions could be exposed to the plasma simultaneously.

Each of these two probes could be mounted on TMX port #W11o near the center of the machine (#W120 on the top of TMX prior to 8/80). The probe entered the vacuum vessel at 45° from vertical on the north side of the machine. If inserted all the way, the center of the probe would coincide with the centerline of TMX. However, the probe face was not parallel to the centerline, but tilted 5° so that samples mounted on the probe face faced slightly toward the east end of TMX. When rf antennas and a limiter at r = 38 cm were installed in TMX, the probes fit through the ~21-cm space between them. Using probe 2, the five sample orientations were labeled: radial (facing the TMX centerline), east, west, up (the sample actually faced 45° above horizontal toward the south), and down (45° below horizontal, toward the north).

A third sample mounting system was located at the TMX east-end wall. Two sets of two C films were mounted directly to blank flanges on ports. Their positions mapped along magnetic field lines to r = 0 and r = 10 cm.

Preliminary measurements (Dec. 1979) were made using a simple stainless steel block for direct mounting of samples facing the radial direction. There was no shutter, so the probe had to be removed and reinserted for gettering cycles and sample selection.

14.2.3 Energy Measurements

The energy of impinging D was determined using both NRA of the saturation trapping behavior of C (Papyex) samples and SIMS measurements of D profiles in Si exposed in TMX. For the saturation measurements, 3 carbon samples were exposed at r = 30 cm in the central cell to a series of identical TMX shots. We chose the number of shots for each sample so that, following NRA, the data would be fit to established saturation curves (as described in Section 14.1.1) to determine the incident D energy. Simultaneously with the C, Si samples were exposed to the plasma. SIMS was used to measure the D depth distribution in Si to determine incident D energy from calculated and previously measured stopping powers and trapping behavior. The SIMS energy measurement was also conducted as a function of orientation (using probe 2).

14.2.4 Flux Measurements

During the course of this work, D flux measurements were made as a function of position, orientation, and fueling conditions. The bases for these measurements were the established D trapping behavior characteristics of C and Si. The retained D was measured using NRA or ERD on C samples. Prior to saturation, the amount of D retained in a sample is directly proportional to the incident fluence. However, information about the incident D energy and angular distribution is necessary to unambiguously establish fluxes. In most cases this information was inferred from SIMS measurements and observed saturation behavior; also, estimates derived from other sources were used to determine the necessary reflection coefficients.

14.2.5 End Loss Analysis

One use for these flux measurements was analyzing losses to the east-end wall. We conducted a three-part series of TMX shots with varying fueling modes. The first set was five shots with normal D gas box and neutral beam fueling. The second set consisted of five shots, using new samples, with H from the gas box and D neutral beams. Thus, in this set, the central cell was primarily fueled with H while the end cells were D fueled. By measuring the D retained in C and Si samples located on the east-end wall at positions that mapped to r = 0 and r = 10 cm in the end cell, and by comparing these two five-shot sets, we get information as to the origin of end losses (i.e., central cell or end cell). A third set of samples exposed to five shots with no gas box fueling was used to establish a background level for these measurements.

14.2.6 Impurity Analysis

RBS determined the quantity of heavy (Z > 6) impurities deposited on carbon samples exposed in TMX. This analysis showed which impurities were present in the plasma and verified that the samples had not been exposed to gettering cycles.

14.3 RESULTS AND DISCUSSION

14.3.1 Data Compilation

A chronological summary of all passive solid state probe D measurements in TMX is in Table 14-1. The first three columns provide information about the particular shots, plasma conditions, and probe position for each measurement. Column 4 gives the amount of D retained in Papyex carbon samples measured using NRA or ERD.

The retained D fluence per shot can be measured directly but the reflection coefficient and therefore the required incident fluence depends on the incident D energy distribution. In many cases the incident D energy could be estimated. In general, for radial-facing samples in the central cell, the data have been consistent with ~50-eV Maxwell–Boltzmann plasma energy distributions incident on the probes with a cosine angular dependence. These conditions were assumed in cases where actual measurements were not available for confirmation.

14.3.2 Radial Energy Measurements

Measurements, in the central cell, of the energy of D incident on radial-facing samples at r = 30 cm using the C saturation technique were conducted on 7/11, 7/18, and 8/23/80. As may be seen in Fig. 14-4, the NRA data are consistent with a Maxwell–Boltzmann energy distribution of kT = 30 eV incident on the probes with a cosine angular dependence. The data tend to exhibit the more gradual saturation behavior of polyenergetic D incidence. However, at these low energies, it is hard to distinguish these conditions from the case of 100-eV-monoenergetic, normally incident D, as shown in Fig. 14-5. Thus, the actual distribution of incident, energetic D could be made up of components of both. For example, a plasma sheath surrounding the grounded probe could add to the plasma's thermal energy to produce the observed data.

Si samples exposed simultaneously with the C saturation samples yield similar results when analyzed using SIMS. These data correlate well with a 25-eV to 50-eV Maxwellian energy with a cosine angular distribution as seen in Fig. 14-6. In this figure the SIMS data are compared with TRIM calculations for both Maxwellian and monoenergetic distributions. The shape of the D profile appears to be Maxwellian rather than monoenergetic. The TRIM calculation[14] is the product of a Monte Carlo computer code which takes into account nuclear and electronic stopping powers to determine the initial depth distribution of atoms implanted into solids. The NRA and SIMS results could also be accounted for by postulating somewhat higher energy D incident at a larger angle to the normal. Diamagnetic loop studies imply ion temperatures comparable to those indicated by these measurements.

14.3.3 Radial Flux Measurements

Each C sample exposed to the TMX plasma was analyzed using NRA to determine the total amount of D retained. Assuming a kT = 50-eV Maxwellian energy distribution with a cosine angular incidence, the flux to the sample may be reported. In particular, for radial facing samples, the data, including flux vs radius scans on 9/24/80 and 10/4/80, are summarized in Fig. 14-7. Since TMX operating conditions were varied depending

TABLE 14-1. Summary of deuterium measurements with a passive solid state probe.

Date shot numbers	Plasma conditions	Radius (cm)[a]	D-retention via nuclear reaction analysis (NRA) D·cm^{-2} (# shots)	Incident flux[b] D·cm^{-2}·s^{-1}	Incident energy (eV) NRA	 SIMS
12-4-79[c]	1-kG puffer	50			–	–
21			1.8×10^{14} (1)			
26, 28			8.2×10^{14} (3)			
[illegible]			1.8×10^{15} (9)			
			Average:			
			2.1×10^{14} shot	1.5×10^{16}		
12-13-79[c]	2-kG gas box	34	3.9×10^{15} (1)		50	100
			7.5×10^{15} (3)			
			2.0×10^{16} (8)			
			Average:			
			2.6×10^{15} shot	1.8×10^{17}		
2-17-80	1-kG gas box	30			50	25-50
5-7						
32 40-42			1.02×10^{16} (3)	2.4×10^{17}		
32 40-49			2.22×10^{16} (10)			
32 40-72			3.07×10^{16} (26)			
2-18-80	1-kG gas box	30			40	25-50
5-7			9.5×10^{15} (3)	2.2×10^{17}		
5-17			2.01×10^{16} (10)			
5-66			2.87×10^{16} (41)			
5-22-80[c]	1-kG gas box	40			–	–
21-26			7.2×10^{14} (3)			
21-34			2.13×10^{15} (10)			
21-65			5.0×10^{15} (33)			
			Average:			
			1.7×10^{14} shot	1.2×10^{16}		
8-23-80	1-kG gas box	30			60	–
13-15			1.83×10^{16} (3)	4.2×10^{17}		
13-25			3.35×10^{16} (10)			
13-61			4.62×10^{16} (37)			
8-29-80	1-kG gas box	34			–	–
12-16	Low ICRH		1.10×10^{16} (5)	1.5×10^{17}		
37-39	High ICRH		1.16×10^{16} (4)	2.0×10^{17}		
9-24-80	1-kG gas puffer					
53-55		38	1.34×10^{15} (3)	3.1×10^{16}		
47-50		40	1.17×10^{15} (3)	2.7×10^{16}		
38-45		50	1.34×10^{15} (6)	1.6×10^{16}		

TABLE 14-1. (Continued).

Date shot numbers	Plasma conditions	Radius (cm)[a]	D-retention via *nuclear reaction* analysis (NRA) $D \cdot cm^{-2}$ (# shots)	Incident flux[b] $D \cdot cm^{-2} \cdot s^{-1}$	Incident energy (eV) NRA	Incident energy (eV) SIMS
9-25-80	1-kG gas box	30				
36,37		Radial	1.7×10^{16} (2)	5.9×10^{17}		
		East	2.0×10^{16} (2)			~150
		West	2.1×10^{16} (2)			~150
		Up	0.6×10^{16} (2)			
		Down	2.6×10^{16} (2)			
10-4-80	1-kG gas box					
84-86		38	1.4×10^{14} (3)	1.5×10^{14}		
79-83		40	0.9×10^{14} (3)	2.9×10^{15}		
73-78		50	1.3×10^{14} (6)	4.6×10^{15}		
10-4-80[d]	1-kG gas box	East-end wall				
74-78	D central cell	r = 0	6.0×10^{14}(5)			
91-95	H central cell	r = 0	2.9×10^{14}(5)			
100-104	Streamguns and neutral beams only	r = 0	1.4×10^{14}(5)			
74-78	D central cell	r = 10	6.8×10^{13}(5)			
91-95	H central cell	r = 10	4.0×10^{13}(5)			
100-104	Streamguns and neutral beams only	r = 10	2.3×10^{13}(5)			

[a]All samples faced radially inward in the central cell unless otherwise noted.

[b]Assumes a 50-eV Maxwellian energy distribution with a cosine angular distribution. All shots were 0.024 s long except for shots 79-86 on 10/4/80 which were 0.017 s.

[c]No saturation in NRA or peak in SIMS (Secondary Ion Mass Spectrometry).

[d]r = 0 and r = 10 cm map to the end plug which was fueled with D for all of these shots.

on circumstances, not all data are directly comparable: a limiter at r = 38 cm was installed at the end of 7/80, the central-cell plasma was fueled by either the gas box or by a gas puffer near the probe, the plasma density was altered on 10/4/80. However, the general trend of decreasing flux with increasing radius is evident, with a flux ~4 × 10^{17} $D \cdot cm^{-2} \cdot s^{-1}$ at 30-cm radius and ~1.5 × 10^{17} $D \cdot cm^{-2} \cdot s^{-1}$ at 40-cm radius. These values are consistent with other central-cell fueling studies.

14.3.4 Orientation Experiment

On 9/25/80, probe 2 was used at r = 30 cm in the central cell to simultaneously expose five pairs of Papyex C and Si samples to two TMX plasma shots. The D retention for the five carbon samples, as measured using NRA, is listed in Table 14-1. A definite orientation dependence of the retained D flux is observed. The SIMS data (shown in Fig. 14-8) indicate that a high energy D component (~150 eV) was incident on samples which were

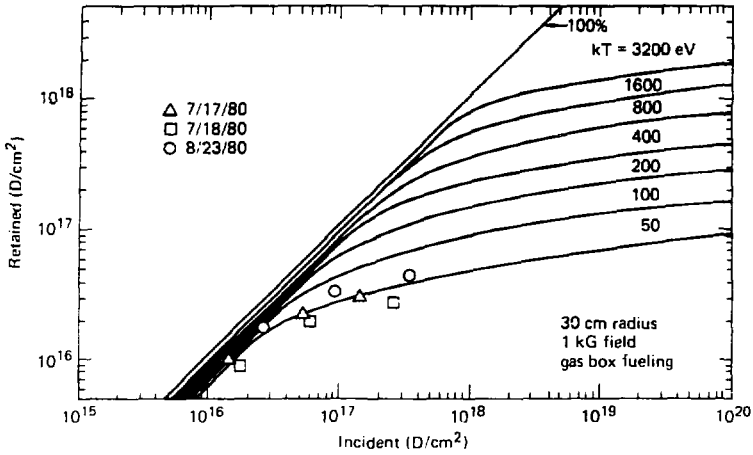

FIG. 14-4. TMX data plotted on the saturation curves for D incident on C with a Maxwellian velocity distribution and cosine angular dependence. The data are consistent with a 40-eV to 60-eV incident energy.

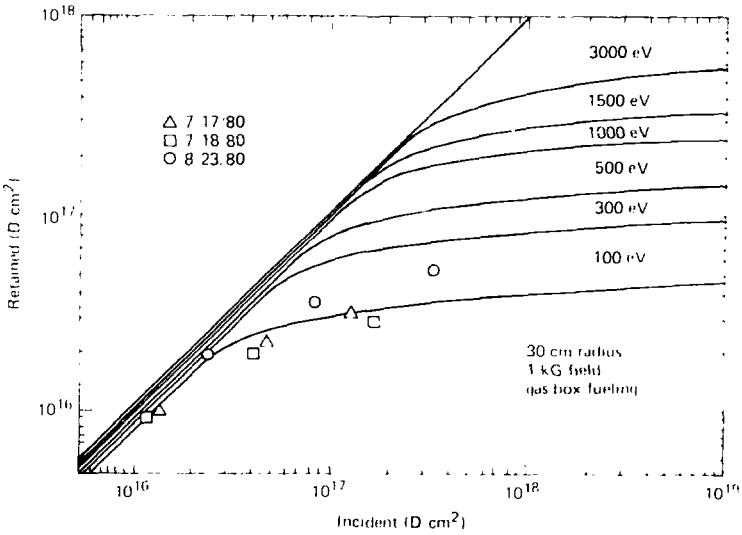

FIG. 14-5. TMX data plotted on the saturation curves for monoenergetic D normally incident on C. Note that the calculated curves tend to bend over more sharply than any of the three data sets.

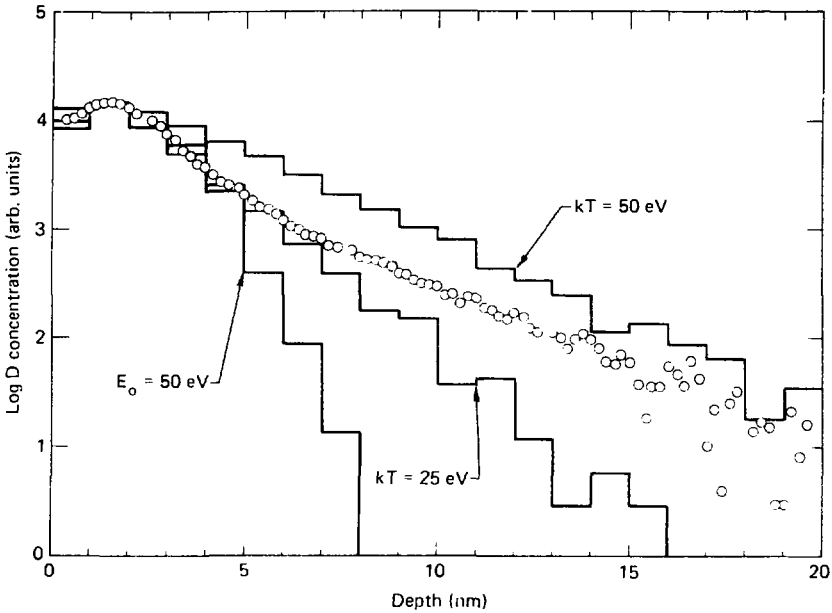

FIG. 14-6. **Comparison of SIMS data with TRIM calculations. The SIMS data show the D profile from a Si probe exposed to 26 discharges at 30-cm radius. TRIM calculations are shown for D distributions in Si resulting from (a) monoenergetic 50-eV D at normal incidence, (b) Maxwellian 25-eV D with a cosine angular distribution, and (c) Maxwellian 50-eV D with a cosine angular distribution. The data correlate well with a 25-eV to 50-eV Maxwellian D flux having a cosine angular distribution.**

oriented toward the east-end plug and 45° below horizontal (down) Evidence of this component was absent in the radially oriented sample and was not clearly seen in the other two samples (west and up)

The interpretation of these data is complex Any complete description of the plasma parameters responsible for these results must account for the combination of the plasma potential, probe sheath potential $\mathbf{E} \times \mathbf{B}$ drift, ion cyclotron motion, radial plasma density variation, 'shadowing' effects, and local plasma perturbation by the probe with the possibility of sloshing ions and plasma waves. Most of these factors have not been measured, and thus must be treated from a theoretical viewpoint. These studies will be pursued further in TMX-Upgrade

14.3.5 End Loss Experiment

Table 14-2 shows the data obtained in the end loss experiment on 10 4 80 described in Section 14 2 e. Because of the low magnetic field at the end wall, the incident D was primarily normally incident, with an energy of at least several hundred eV (Section 3) Under these circumstances the reflection coefficient is about 10%. Thus, the incident fluence is about 1 1 times the absolute D retention, as measured using ERD

In the first series of shots, we used D fueling throughout TMX (normal operating condition) In the second series, we used D beams, but the central cell was fueled with hydrogen. The third series was a set of background shots, with no central-cell gas box fueling. Thus, with 10% reflection, the average

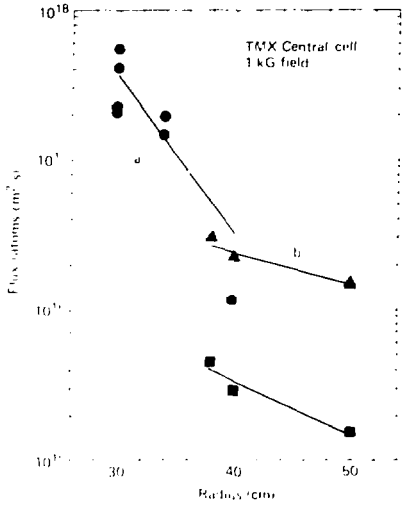

FIG. 14-7. D flux to C probes exposed to TMX facing radially inward. All data are analyzed assuming a 50-eV Maxwellian energy flux with a cosine angular incident distribution. a: Gas box fueling, normal plasma density, various dates. b: Gas puffer fueling, 9/24/80 and 12/4/79. c: Gas box fueling, low plasma density, 10/4/80. The lines are linear regression fits to the three data sets.

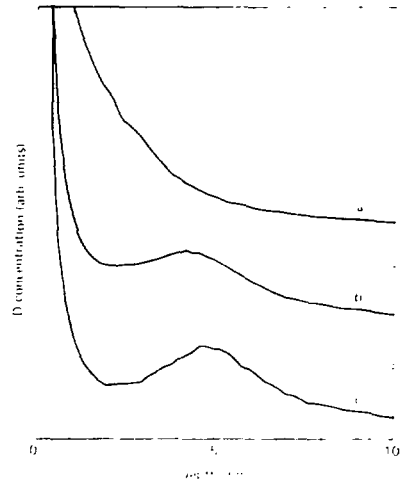

FIG. 14-8. SIMS depth profiles of D retained in three Si probes exposed to the same two discharges at different orientations in the central cell. (a) Probe aligned in a radial direction. (b) Probe facing east-end plug. (c) Probe facing down. In profiles (b) and (c) a peak is observed at 4–5 nm depth, which corresponds to a D energy, for normally incident and monoenergetic particles, of about 150 eV.

TABLE 14-2. End loss experiment.[a]

		Data (D cm^{-2})		Background subtracted	
		$t = 0$	$t = 10$	$t = 0$	10
1	D end plug and D central cell	9.0×10^{14}	9.8×10^{13}	4.6×10^{14}	4.5×10^{13}
2	D end plug and H central cell	2.9×10^{14}	4.0×10^{13}	1.5×10^{14}	$1.^{} \times 10^{13}$
3	Neutral beams and plasma guns	1.4×10^{14}	$2.^{} \times 10^{13}$		

[a]Five shots per sample. NRA and elastic recoil analysis on C

flux to the end wall after the stream guns were shut off (i.e. during the final 17 ms of each shot) is given by flux = (f − bg) × 1.1 (5 shots × 17 ms/shot). The retained fluence, f, the background, bg, and the background-subtracted value (f − bg) are given in Table 14-2 for each series. At r = 0 the flux is then 6×10^{15} D·cm^{-2}·s^{-1} for series 1 and 2×10^{15} D·cm^{-2}·s^{-1} for series 2.

The Faraday cups and the end-loss analyzer measure the ion current to the end wall. The currents measured by the end-loss analyzer and the carbon probe for series 1 are about 70% of the current measured by the Faraday cup at the appropriate radial position. There are three possible explanations for this:

1. Errors in averaging. The averaging intervals for the three diagnostics are different.
2. Calibration errors. The Faraday cups should be accurate to within 10%. The surface probes were analyzed in two independent facilities and absolute calibrations were performed simultaneously.
3. D current ≠ ion current. If either hydrogen or impurities or both account for 30% to 50% of the Faraday cup signal, these measurements are consistent. Hydrogen might be present by isotope exchange as observed in DIVERTOR and PLT. TMX was toward the end of cleanup during these shots and vacuum conditions were poor.

In the analysis of series 2, the surface probe result will be assumed to be correct, but the implications of a 50% larger D current will also be assessed. Before series 2, some test shots were taken, but there was no long series of shots to clean the walls of D. The D current measured by the probe decreased by a factor of 3; the ion end-loss current roughly doubled. Thus, with hydrogen fueling the central cell, the D current was about 10% of the total end losses at r = 0 (15% if the probe value is 50% low). One purpose of the second series was to directly measure the end-plug losses and compare them to calculations. For these five shots, the east plug had beam current I_b = 120 ± 15 A and line density $\int n d\ell_1 = 3.2 \pm 0.3 \times 10^{14}$ cm^{-2}. If the probe measurement is compared to results from the radial Fokker-Planck code by Archer Futch, the D end-loss current measured by the probe is about twice the end-loss current from the plug predicted by the code. The discrepancy may be due to isotope-exchange or other experimental and modeling factors.

The results of series 2 can also be applied to series 1. The sources and losses in the end-plug scale approximately as beam current times line density. In series 1, I_b = 122 A and $\int n d\ell = 2 \times 10^{14}$ cm^{-2}. Thus, using the measured end losses to calculate that the 10 kG flux was 0.044 A·cm^{-2} in series 2, the losses from the end plug in series 1 should be

$$0.044 \times \frac{I_{b1}}{I_{b2}} \times \frac{\int n d\ell_1}{\int n d\ell_2} = 0.036 \text{ A} \cdot \text{cm}^{-2}$$

This is 15% of the loss current indicated by the Faraday cups and 25% of the loss current indicated by the probe (0.13 A·cm^{-2} at 10 kG). We conclude that in ordinary TMX operation (D$^+$ beams, D$_2$ gas box), the end-plug losses are less than the central cell loss, but may not always be negligible.

14.3.6 Impurity Analysis

The results of impurity studies on two sets of samples are reported in Table 14-3. RBS measurements indicated that O, Ti, Fe, and sometimes Cu were present on the carbon samples following exposure to TMX plasmas. The presence of Ti and Fe was not surprising since TMX was Ti gettered and the probes were made of stainless steel. Copper wires were present in the getter structure and other parts of TMX. Oxygen was observed in the plasma by extreme ultraviolet (EUV) spectroscopy. N would also be expected on that basis, but none ($< 0.2 \times 10^{15}$ N·cm^{-2}) was observed on the carbon. Relating impurity retention to plasma impurity levels is difficult; most useful may be comparative analyses and the basic observation that O, Ti, Fe, and sometimes Cu seem to be present.

14.3.7 Acknowledgments

We are grateful to L. G. Haggmark for many useful discussions and to R. A. Burchard, D. M. Morse, S. L. Schneider, and A. A. Ver Berkmoes for their able technical assistance. We also appreciate the useful interactions with many of the TMX staff.

TABLE 14-3. Impurity analysis.

Date shot numbers	Plasma conditions	Radius (cm) orientation (* shots)	Impurities ($\times 10^{15} \cdot cm^{-2}$) O	Ti	Fe	Cu	N
7-17-80[a]	1-kG gas box	r = 30					
32,40-42		(3)	–	0.7	–	–	–
32,40-43		(10)	7.5	2.25	0.27	0.26	–
32,40-72		(26)	15.4	6.0	0.29	0.97	0
9-25-80	1-kG gas box	r = 30					
36,37		Radial (2)	5.5	0.52	0.07	–	–
		Bottom (2)	12.3	1.72	0.63	–	–
		West (2)	7.0	1.19	0.24	–	–
		East (2)	24	5.7	0.56	–	–
Estimated lower limit of detection			0.2	0.02	0.02	0.02	0.2

[a]SIMS measurements indicate that the O extends into the silicon samples studied.

15. End-Wall Plasma Characteristics of TMX

15.1 INTRODUCTION

An array of emitting and collecting probes (described in Appendix B) measured the characteristics of the plasma at the end wall of TMX. This was the first experimental measurement of the local plasma potential and the local distribution of electrons, both cold (from cold-gas ionization) and hot (energetic plug electrons). It was also the first experimental observation of secondary electron production; although, secondary electrons have been of primary interest in several theoretical studies concerning scaling to fusion reactors.[1-3]

The emitting probes indicated a plasma potential with a characteristic value of approximately 8 V measured at 2 and 10 cm from the wall. The wall was at zero volts and the potential in the plug varied from 300 to 1000 V. The emitting probes could serve as a general indicator of the main TMX plasma characteristics, as the sheath potential changed when stream guns, neutral beams, or other parameters changed.

The collecting probes indicated that there were two cold-electron species: one due in part to ionization of gas and in part to a truncated species of electrons able to escape from the mirror, and the other due to emission from the end wall of secondary electrons with a density of about 5×10^8 cm^{-3} and a temperature of about 7 eV. The cold-electron species in the sheath was between 1 and 10 times as dense as the hot ion species, but it was still 4 orders of magnitude less dense than the electrons in the plug. The temperature of the cold electron species was decoupled from the temperature of the electrons in the plug.

A sheath was established at the wall to balance the current densities of the electrons and ions. The ion current was dominated by the hot ions escaping the confinement volume. A cold-ion species is postulated to balance the total density and thus maintain charge neutrality outside the plasma-wall sheath. Comparison with a theoretical model[1] indicates that a consistent model may be achieved if the species of cold ions was indeed cold, with an energy of about 0.2 times the cold-electron temperature at the onset of the sheath.

Plasma escaping from the two end plugs was lost to a large surface area at the end wall, which was approximately 400 cm from the center of the mirror. The magnetic field at the wall was 70 G, down from 10 kG at the center of the mirror and 20 kG at the mirror point. The density of escaping ions at the wall was 6×10^8 cm^{-3}, down from 2×10^{13} cm^{-3} in the plugs. The ambipolar potential through which ions fall from the plug to the wall (i.e., the minimum energy of such ions) was as high as 1 kV. The spread in energy for ions escaping to the wall was found to be of the order of 1 keV (see Sec. 12).

Consider first the simple model in which there is no cold-gas recycling off of the end wall and, hence, no creation of a cold plasma away from the wall. The end-wall sheath characteristics are then determined by the hot electrons and hot ions that leave the machine. At the wall the net current is zero (if there is only ambipolar radial diffusion), and outside the plasma-wall sheath the densities of the two species are equal. If the electrons in the sheath have a Maxwellian velocity distribution, one would expect the electron temperature to be of the order of one-tenth the ion energy. Hence, the electron thermal velocity is approximately 10 to 20 times greater than the directed velocity of the ions. The density of electrons must be reduced by the sheath at the wall by about $e^{2.3}$, and a sheath potential of 2.3 times the local electron temperature, or about 400 V, would be expected.

Data presented in this paper indicates that the potential of the plasma measured 2 and 10 cm from the wall was only of the order of 10 V and that there was a local distribution of cold electrons with a density of about 5×10^9 cm^{-3} and a temperature of about 10 eV. The cold electron density measured here was consistent with previous measurements.[4] In addition, the initial measurements also indicated a species of secondary electrons, which were produced by plasma wall interactions, with a density of about 5×10^8 cm^{-3} and an energy spread of no more than 7 eV.

In a computational study of large mirror experiments and fusion reactors,[1] Porter has proposed that the additional power drain due to mechanisms such as secondary electron production and cold gas recycling increases by as much as 50% but not the factors of 2 or more that have been reported previously.[3] The experimental data is

compared with the computational model for end losses in Sec. 15.3. The comparison shows that there exists a self-consistent (though not unique) solution to the measurements.

15.2 RESULTS

The emitting probes located at 2 cm and 10 cm from the wall were used to monitor the plasma potential during each shot, using the floating-potential method. Figure 15-1 shows traces obtained during a typical shot. Note that the potential increase from 0 V (the potential of the wall and the sheath) to 4 V at 3 ms, the time at which the stream guns were turned on. At 8 ms, another increase in potential, from 4 to 8 V, occurred. The potential difference between the two probes was approximately 1 V during the shot, with the 10-cm probe the more positive. (Note that the traces in Fig. 15-1 have been arbitrarily displaced for clarity.) This small potential difference strongly suggests that the plasma-wall sheath, where the potential changed from 8 to 0 V, and where charge neutrality was violated, occurred within 2 cm of the wall. The region between 2 and 10 cm can then tentatively be identified as being part of a presheath. The east neutral beams were turned off at 24 ms, and the sheath potential increased from 8 to 12 V. Finally, the west neutral beams were turned off at 28 ms, and the whole plasma, as well as the potential, decayed. It appears that the potential at the 2-cm probe decayed more slowly than the potential at the 10-cm probe; in fact the potential measured at 10 cm became more negative than that at 2 cm during the decay. Such a local minimum, if it is not an instrumental error, could be associated with locally trapped cold ions and cold electrons. Figure 15-1 clearly demonstrates that the potential near the wall, really the plasma-wall sheath potential, was quite sensitive to the entire machine operation. Because of this sensitivity, the emissive probes can indicate when the stream guns and neutral beams are actuated or other parameters change.

It is also apparent that the potential fluctuated during a shot. The absolute potential was about +8 V, with about a 3 V fluctuation about that potential. Figure 15-2 gives an expanded view of a shot from 15 to 17 ms. The noise has a frequency of about a 10 kHz and appears to be associated with plasma bursts coming out of the plug. Related

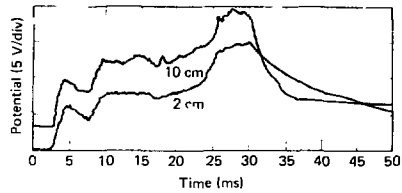

FIG. 15-1. Potentials measured by the 2- and 10-cm probes with getter shields grounded. The two traces have been displaced vertically by an arbitrary amount for clarity.

oscillations are observed in the ion current measured by the end-loss analyzers and are also observed on the collecting probes.

Since the potential was uniform in the region between 2 and 10 cm, collecting probes can give information about the local electron distribution. Sample collecting-probe traces made with cylindrical probes, button probes, and coated disk probes are presented in Figs. 15-3, 15-4, and 15-5 respectively. For the trace in Fig. 15-3, the voltage applied to the cylindrical probe at 10 cm went from -15 to +15 V during a time sweep from 15 to 20 ms. We can determine two "knees" on this trace: one associated with the local plasma potential at +6 V and one at 0 V, characteristic of secondary electrons (or a beam of electrons with a directed energy of 6 eV). If the electron distribution is Maxwellian, then the electron density is about 2.9×10^9 cm^{-3} and the cold electron temperature is about 7 eV. The species of secondaries for this trace has a density of about 2.7×10^8 cm^{-3} and an energy spread of about 5 eV. Evidence of the cold electron

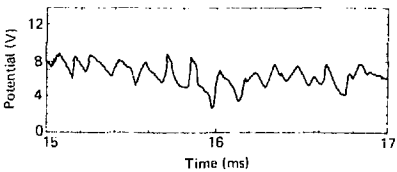

FIG. 15-2. An expanded view of the potential measured by the 10-cm emitting probe between 15 and 17 ms, showing the oscillations that appear to be associated with plasma bursts.

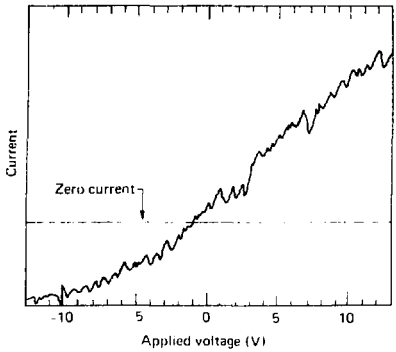

FIG. 15-3. Current-voltage characteristics measured by a cylindrical probe located at 10 cm.

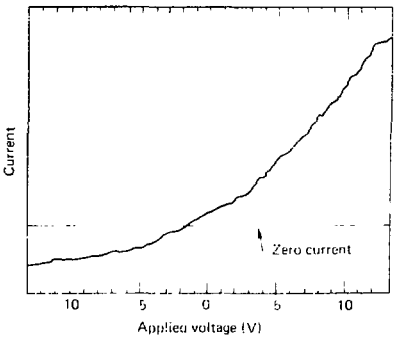

FIG. 15-4. Current-voltage characteristics measured by a button probe located at the wall.

species was first noted when the emitting-probe filament was Debye-shielded from its getter shield during plasma shots in which a voltage bias had been placed on the getter shield.

The electron saturation current density, $j_{e'}$ multiplied by the Boltzmann factor, $\exp(-e\phi_s/T_e)$ where ϕ_s is the potential of the sheath (0 V), e is the electron charge, and T_e is the temperature of the cold electrons, agrees with the ion current density measured by the probe, j_i. This measured current density, which included both hot and cold ions, is

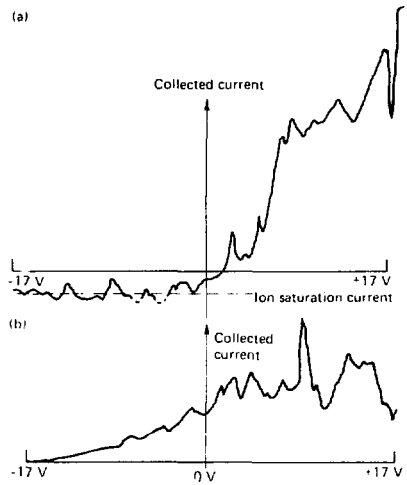

FIG. 15-5. Current-voltage characteristics measured by a 0.95-cm-diam disk probe located at 2 cm (a) and 10 cm (b). The vertical scale for (b) is $2^1/_2$ times the vertical scale for (a).

also within a factor of 2 of the ion current density measured by the end-loss analyzers situated at the wall at zero radius. For Fig. 15-3, $j_i = 10^{-2}$ A/cm^2 and $j_e \exp(-e\phi_s/T_e) = 8.6 \times 10^{-3}$ A/cm^2. Note that the floating potential measured by the probe is always within 2 V of ground. These results suggest that the sheath at the wall, with a potential of about 6 V, was established to balance the ion-beam flux and the cold-electron flux to the wall; i.e., the plasma floated so that the wall drew only a small net current. Other diagnostic measurements indicate a small excess electron current near the magnetic axis (see Sec. 9).

The lower knee in Fig. 15-3 is situated at 0 V. Unlike the upper knee (or plasma potential), which changes by as much as 10 V from shot to shot, the lower knee remains at 0 V. This trait, as well as the energy spread of less than 7 eV, indicates the presence of secondary electrons.[5] Large density fluctuations are apparent at about 8 kHz. The large noise fluctuation and the small size of the cylindrical collecting probe led to the use of the button and disk probes to provide better details, such as

sharper breaks of the collected current at the plasma potential and a separate identification of electrons that may be emitted at the wall.

Figure 15-4 is a typical current-voltage trace generated with a copper button probe located in the plane of the wall. This probe monitored characteristics of plasma far from the plasma-wall sheath. Secondary electrons produced by ion-wall bombardment are not readily apparent on the signal from the button probe. However, there was a 0.3 cm wide space around the button probe, with a surface recessed 0.6 cm deeper than the wall, that might have been responsible for supplying some secondary electrons. The knee at the plasma potential is more readily apparent on data from the button probes than on data from the cylindrical probes, and the energy spread of the electrons is easier to ascertain. For the trace shown in Fig. 15-4, the cold electron temperature is about 6 eV.

Even better current voltage characteristics were achieved by inserting coated disk probes at 2 and 10 cm. These probes were coated on one side with an insulator, allowing us to preferentially observe plasma emitted from the wall or the plug. A typical current voltage curve is shown in Fig. 15-5. The upper trace is a 1 ms 34-V sweep of the 2-cm probe, which is coated to look at particles emerging from the plug. A sharp knee is apparent at +6 V. Note again the large density fluctuations. There is no second knee at 0 V on this trace or on any trace generated by the 2-cm disk probe.

The lower trace in Fig. 15-5, from the probe at 10 cm, which looks toward the wall, shows a knee at 0 V. This trace was recorded at the same time as the upper trace. However, when the data was taken, the bias on the 2-cm probe was swept from +17 to −17 V while the bias on the 10-cm probe was swept from −17 V to +17 V. We have reversed the horizontal axis of the 2-cm-probe data to improve clarity for the comparisons made here. Note that there is no visible ion current on the signal from the 10-cm probe. Furthermore, for small negative-bias voltages, the electron current, which is the difference between the current collected by the probe and the ion-saturation current, is larger on the signal from the 10-cm probe than on the signal from the 2-cm probe. This indicates that the electrons collected by the probe at 10 cm are not coming from the plug. This is expected because the 10-cm probe is coated to collect electrons coming from the wall.

Because the cylindrical and disk probes occupied the same position and used the same support structure, the two kinds of probes were not used simultaneously. The cylindrical probes were used to measure the fraction of secondaries as compared to primaries (incident plasma electrons); the disk probes were used to measure in better detail the distribution of electrons from the plug and to distinguish the separate species of electrons coming from the wall.

The plasma density in the shadow of the disk probe at 10 cm should be less than in the surrounding region since only hot ions can pass freely into this region. Electrons, other than the secondaries emanating from the wall in the shadow region, must diffuse into the region occulted by the probe. The radius of the disk probe is 0.47 cm, whereas the hot-ion gyroradius is 1.7 cm and the cold-electron gyroradius is 0.09 cm, thus only hot ions and secondary electrons can pass freely into the shadow region. A density gradient occurs at the interface of the plasma-shadow region, and hence the actual sheath structure around the probe (which determines the collecting area of the probe) may be altered. The energy spread of the electrons collected by the probe at 10 cm should be accurate, but the absolute density may be off. Secondary electron density obtained from 10-cm-probe data, is plotted against hot-ion density in Fig. 15-6. The density of the secondary electrons appears to be proportional to the density of the ions, with the

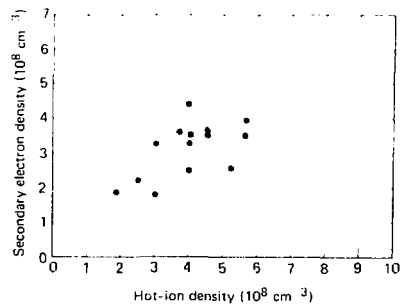

FIG. 15-6. The density of secondary electrons as a function of the hot-ion density. A strong correlation between the secondaries and the incident ions is apparent.

electron density somewhat less than the ion density.

In general, secondary electrons can be produced by both ions and electrons. Although wall bombardment by electrons with temperatures like those in the TMX plug could certainly produce secondary electrons, no relation between secondary yields and the measured primary-electron distribution near the wall was expected or found, because the local electron temperature is too low. There does seem to be a correlation between secondary yields and incident hot-ion energy, as is shown in Fig. 15-7, a plot of γ versus weighted ion energy, where γ is the ratio of secondary electron current to incident-ion current. (The weighted ion energy is used because the ions enter with a minimum energy corresponding to the potential in the plug and a large energy spread equal to or greater than the minimum directed energy.) The curve on Fig. 15-7, for γ versus ion energy of monoenergetic ions incident on a clean surface, is from Hall.[2] The end wall of TMX is gettered with titanium before the shot and hence is clean.

For all the data recorded with the probe array, the values for secondary electron density, n_s, plasma electron density, n_p, plasma electron temperature, T_e, and the sheath plasma potential, ϕ_s, (measured at 10 cm) are in the following ranges:

- $5 \times 10^7 < n_s < 2 \times 10^9\ cm^{-3}$
- $1 \times 10^9 < n_p < 4 \times 10^{10}\ cm^{-3}$
- $1 < T_e < 15$ eV
- $2 < \phi_s < 15$ V

Figure 15-8 shows the electron temperature at the wall versus the temperature in the plug for various shots. The temperature of electrons in the plug was determined by Thomson scattering, as described in Appendix B. Note that although the plug electron temperature varied between 25 and 250 eV, the electron temperature at the wall remained close to 5 eV. Attempts were made to find hot electrons at the wall by sweeping the collecting probes from −40 to −5 V. Because most of the cold electrons were already repelled, the observed change in current to the probe can be assumed to be caused either by the change in sheath size (increasing ion sheath with increasing negative voltage) or perhaps by part of a hot electron species being repelled. The hot electron density, n_{ehot}, can be overestimated if the increased current due to sheath effects is neglected. This density can be determined from the local plasma potential and the change in the measured current:

$$n_{ehot} = \frac{5.2 \times 10^8}{T_{ehot}} \times \frac{\Delta I}{\exp[-e(\phi_p + 5)/T_e] - \exp[-e(\phi_p + 40)/T_e]}$$

where n_{ehot} is the hot electron density (in cm^{-3}), T_{ehot} is the hot electron temperature (in eV), ΔI is the net change in collected current between −40 and

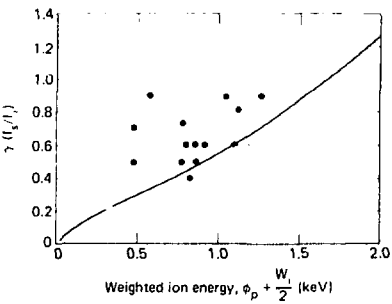

FIG. 15-7. Plot of γ versus weighted ion energy, where γ is the ratio of the secondary electron current to the incident-ion current. W_i is the energy spread of the ions. The data points are experimental data, the curve is for monoenergetic ions (from Ref. 3).

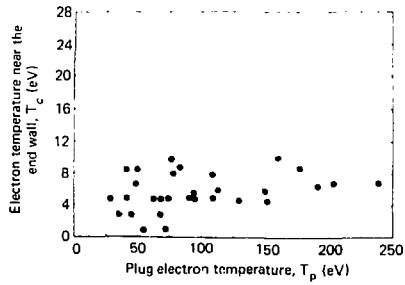

FIG. 15-8. The cold-electron temperature near the wall (determined from the collecting probe current-voltage trace, assuming a Maxwellian distribution) versus the electron temperature in the plug as determined with Thomson scattering.

−5 V (in mA), ϕ_p is the plasma potential (in V), and T_e is the electron temperature (in eV). For shots 42, 44, 45, 48, and 50 on September 26, 1980, an upper limit to the hot-electron density was found to be 2×10^7 cm^{-3}.

A qualitative picture of the electron distribution functions, obtained by combining all the information gathered with the end-probe array, is presented in Figs. 15-9 and 15-10, which show $f(v_\parallel)$ versus E and $f(v_\parallel)$ versus $v_\parallel$ at 10 cm from the wall. The distribution of secondary electrons shown in Fig. 15-9 is inferred from the small bump or knee in the Langmuir trace (see Figs. 15-3 and 15-4). Note that the secondaries have accelerated through the plasma-wall sheath. The distributions presented in Fig. 15-10 are not measured directly with the probes, since the probes measure total energy and not velocity or direction, hence the cutoff of the curve for the distribution of hot electrons is assumed. However, the fact that the total distribution goes to zero just below $v_\parallel = 2(T_e/m_e)^{1/2}$ is measured, and can readily be seen in Figs. 15-3 and 15-4, and particularly in the upper trace in Fig. 15-5.

15.3 COMPARISON WITH A COMPUTATIONAL MODEL

The emitting and collecting probes provide an accurate measure of the plasma potential and the electron dynamics near the end wall, however, they provide little information about the ion distribution. A net ion current is measured, and, as previously mentioned, the ion-saturation current measured by the collecting probes agrees to within a factor of 2 with the ion-saturation current measured by the end-loss analyzer. A cold species must also be present if we are to believe the probe data, which indicate a flat potential structure and a cold-electron species denser than the hot-ion species. No current of cold ions is evident on the end-loss analyzers. The existence of oscillations in the analyzer signals introduces uncertainty in that measurement, so that we infer an upper limit of the current density of the cold ion species to be $j_c \lesssim 0.2\, j_h$, where j_c and j_h are the current densities of the cold and hot ion species, respectively. The end-loss analyzers do provide a measure of the hot-ion flux, energy, and energy spread.

The information on the ion and electron dynamics provided by the probe array can be used as input parameters for the model of gas recycling off of the end wall of mirror machines described in Ref. 1. This model integrates Poisson's equation in the presence of four particle species: (1) a beam of monoenergetic ions from the plug, (2) cold ions, produced predominantly by cold-gas ionization, (3) cold electrons, comprised of plug electrons that have enough energy to reach the wall and electrons

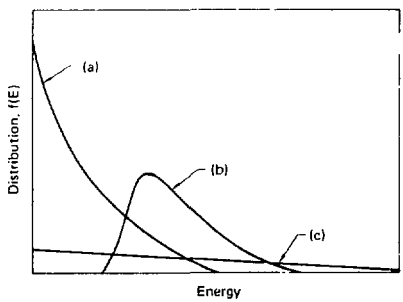

FIG. 15-9. Qualitative graph of the electron distribution function f(E) versus E for electrons found 10 cm from the wall: (a) measured distribution function for cold electrons, (b) measured distribution function for secondary electrons, and (c) upper limit for the distribution function for hot electrons.

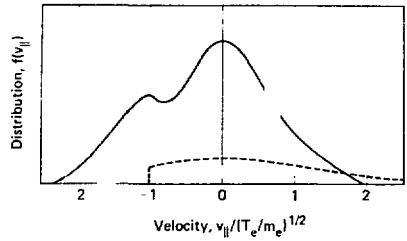

FIG. 15-10. Qualitative graph of the electron distribution function $f(v_\parallel)$ versus $v_\parallel$ for electrons measured 10 cm from the wall. An electron with a positive velocity is moving toward the wall, one with a negative velocity is moving toward the plug. The bump in the curve for negative velocities is caused by secondary electrons. The dotted line is the upper limit for the hot electron distribution. Note that there exist few electrons with a velocity greater than $2(T_e/m_e)^{1/2}$.

produced by cold-gas ionization (one Maxwellian distribution is assumed for both electron components), and (4) a species of secondary electrons emitted from the wall. Poisson's equation is solved to generate a series of self-consistent solutions for the case where the plasma charge is neutral outside the plasma-wall sheath and the net current to the wall is zero.

Using experimental data from shot 36 on September 26, 1980, a set of solutions was generated which indicated that, with a cold gas reflux of 15 to 20% of the incident hot ions, the cold-ion current predicted should be less than 20% of the hot-ion current.[1] As indicated above, such a low cold-ion current cannot be measured with the end-loss analyzers. Values of f_h between 15 and 20% (where f_h is the ratio of the cold-gas current emerging from the wall to the hot-ion current incident) seem plausible for a freshly gettered Ti surface. A summary of the data and the corresponding agreement with the model follows.

Figure 15-11 shows the experimental dependence of the sheath potential (normalized to the cold-electron temperature near the wall) on the secondary electron current (normalized to the cold-electron current). The data are separated on the basis of the ratio of the cold-ion density to the hot-ion density. This ratio is inferred experimentally by measuring the total plasma density and the hot-ion density. The hot ions are those escaping the confinement volume, and the cold ions are those created by gas ionization in the fan. These data are compared with a family of curves calculated using the model of Ref. 1. Several points can be inferred from this figure. First, the data appears to be consistent with the model. The measured secondary electron currents do not appear to be limited by space-charge effects. This can be seen in Fig. 15-11, where all data points lie to the left of the space-charge limit, labeled $\lambda = \lambda_{scl}$. Finally, to achieve the agreement between the model and the experiment, it is necessary to assume that the mean energy of the cold ions entering the sheath is only about 20% of the local electron temperature and that the mean energy of the hot ions is about 100 times the electron temperature. The implied hot-ion energy is consistent with energies measured by the end-loss analyzers (see Sec. 12). Since cold ions arrive at the sheath with an energy equal to the potential differential between the point of origin and the sheath, a low cold-ion energy implies that the potential difference between the mirror peak and the onset of the end-wall sheath is small.

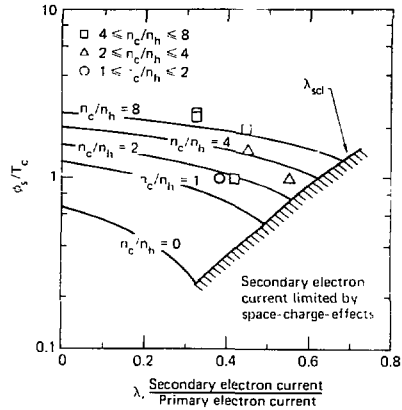

FIG. 15-11. The normalized sheath potential (ϕ_s/T_e) versus the normalized secondary electron current (λ). The data shown were obtained on Sept. 26, 1980. The curves for the calculated results were obtained assuming that the cold-ion energy is 20% of the electron temperature and the hot ion energy is 100 times the electron temperature. The limitation to the secondary electron current by space-charge effects is indicated by the space-charge-limit curve, λ_{scl}. The parameter n_c/n_h is the ratio of the cold-ion density to the hot-ion density.

REFERENCES

1. G. D. Porter, *Effect of Gas Recycling and Secondary Electron Emission in the Axial Flow in an Open-Ended Device*, UCRL-85847 (1981), submitted to *Nucl. Fusion*.
2. L. S. Hall, "Electron Dynamics and the Enhancement of Q in Mirror-Magnetic Wells," *Nucl. Fusion* **17**, 681 (1977).
3. R. F. Post, "Plasma–Surface Interactions in Q-Enhanced Mirror Fusion Systems," *J. Nucl. Mater.* **76-77**, 112 (1978).
4. R. P. Drake, G. Deis, M. Richardson, and T. C. Simonen, "Gas Control and Wall Conditioning in TMX," *J. Nucl. Mater.* **93-94**, p. 291 (1980).

5 M. Kaminsky, *Atomic and Ionic Impact Phenomena on Metal Surfaces* (Academic Press, New York, N.Y. 1965).

6. W. Weber, R. Armstrong, and J. Trulsen, "Ion-Beam Diagnostics by Means of an Electron-Saturated Plane Langmuir Probe," *Appl. Phys.* **50**, 4545 (1979).

Appendix A. Description of the TMX Facility

A1. INTRODUCTION

The goal of the Tandem Mirror Experiment (TMX) was to provide an early test of the tandem mirror confinement concept with a device of significant size. To meet this goal, maximum use had to be made of the existing facilities, technology, and hardware of the LLNL mirror program.[1,2] Construction of TMX, a major device fabrication, began on April 1, 1977, and was completed on schedule October 1, 1978. A checkout period followed. The first significant results were obtained in July 1979, when the principles of the tandem mirror were successfully demonstrated. TMX experiments continued until October 1980, when the facility was shut down for modification into TMX upgrade. Figure A-1 shows the major components of the TMX device.

This appendix describes the various TMX subsystems: the physical facility, the magnet system, the neutral beam and plasma startup system, and the vacuum system. It also summarizes the methods used to evaluate magnet-system alignment and vacuum-system performance. While no correlation between magnet alignment and plasma parameters has been identified, we did find better static and dynamic vacuum conditions are correlated with higher end-plug electron temperatures.

A2. PHYSICAL FACILITY

(J. C. Davis)

The TMX facility is described in Ref. 3. The vacuum vessel of the TMX experiment was located in a two-level pit, 10 m × 17 m, as shown in Fig. A-2. Vacuum-system components, utility and diagnostic trunk lines, and some diagnostic devices occupied the lower level of the pit beneath the

FIG. A-1. Artist's drawing of TMX showing beam sources on the sides of the vessel. The plug magnets are visible in the cutaway portion of the vessel.

FIG. A-2. Photograph of TMX, looking west.

vessel. The magnet system was at ground level and had neutral-beam injectors clustered on the sides of the vessel. Diagnostic systems were mounted above and alongside. Neutron shielding was provided by a 60-cm-thick concrete shield that surrounded the experimental area. The control room and main diagnostics room were at the east end of the experiment. A second diagnostics room, containing the data acquisition computers, was located on the second floor to the southeast.

Power supplies, modulators, and energy storage were in several different locations. Magnet power supplies and capacitor banks for neutral-beam accel power were in adjacent buildings, while all the high-voltage modulators for the beams were on two levels above the control room. Battery banks for neutral-beam arc and filament power were installed in two tiers on either side of the TMX machine. Neutral-beam sources and power supplies were interlocked in groups of six to allow convenient access for maintenance.

A3. MAGNET SYSTEM

(J. C. Davis)

The TMX magnet system is described in Refs. 4-7. A major criterion in the design of the TMX magnet set was to ensure that end-plug performance would correspond closely to that of the successful 2XIIB experiment. This constraint, together with considerations of overall experiment size, power available, neutral-beam footprint at the plasma, and MHD stability, led to construction of water- cooled copper magnets in the configuration shown in Fig. A-3.

Magnet parameters are listed in Table A-1. The size of the plug magnets was determined by the access required for the twelve neutral beams to be installed on each plug. Elevation and plan views of this access are shown in Fig. A-4. The plug central field was 1.0 T.

Although the minimum-B end plugs had strongly MHD-stable field shapes, and the central-cell region had neutral stability, the transition region between plug and central-cell had a field-curvature that was inherently unstable. A -magnet transition set was designed to increase the stability of the transition region. That the resulting magnetic configuration was indeed MHD-stable was demonstrated in TMX experiments.

The variation of the magnetic field on axis is shown in Fig. A-5 for a 0.1 T central-cell field. A field-line plot is shown in Fig. A-6.

The magnet system was controlled by a microprocessor system[5] that set all coil currents

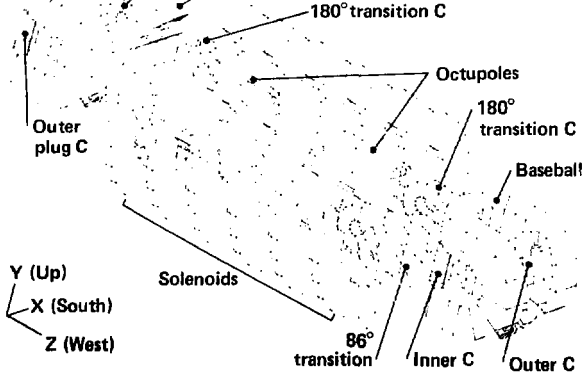

FIG. A-3. Computer-generated drawing of the TMX magnets.

TABLE A-1. TMX magnet parameters.

Magnet type	
- Plug	Baseball plus C-coil pair
- Transition	2 C-coils plus octupole
- Central Cell	Solenoids
Distance between inner mirrors	5.3 m
Distance between plug mirrors	1.1 m
Plug central field	1.0 T
Central-cell field	0.05 to 0.2 T
Maximum plasma radius	
- In plug	0.15 m
- In central cell	0.37 m

and magnet on-and-off times and monitored coil currents and voltages, ground currents, and cooling-water temperatures. Magnet power supplies were regulated by silicon-controlled rectifiers (SCR's), and were arranged in series where necessary to provide adequate power. The supplies were sequenced on and off at different times to minimize line transients at the start and finish of the 3-s magnet pulse. The 25-ms, neutral-beam pulse was fired near the end of the magnet pulse when coil currents had come to equilibrium. When the solenoid field was 0.1 T, power to the coils was about 13 MW.

The TMX magnet set, which comprised 18 coils in 12 individually movable units, was well enough aligned that there were no evident deleterious effects on the plasma traceable to magnet geometry. During the initial assembly of TMX, cross hairs were used for alignment. This initial magnet alignment was judged to be accurate within 0.45 cm of translation and 1.5° of rotation. After several intermediate alignments, the magnetic axes of the east and west plug magnets were determined by means of an electron beam from a 500-V electron gun enclosed in an evacuated glass tube. At low energies the electrons followed field lines well. The beam trajectory was visible, because the electrons caused the residual gas in the tube to fluoresce.

TMX magnetic fields were calculated by using the coil locations measured with the electron beam. The coil displacements and angular rotations from alignment are summarized in Ref. 8. The most dramatic effect occurs from the rotation of the east plug about the z-axis by 1°. The calculated effects are small and appear unlikely to affect plasma confinement seriously.

A4. NEUTRAL-BEAM AND STARTUP SYSTEMS

(J. C. Davis)

High-temperature in plasma in the end plugs of TMX was produced by trapping neutrals (from a neutral beam) in a target plasma produced by plasma guns. The neutral-beam system [9-11] had sixteen 20-kV beams and eight 40-kV beams rated at nominal accel power supply drains of 75 A for 25-ms pulse lengths. The neutral beams were located as shown in Figs. A-1 and A-4. The ion sources and accelerator-grid structures were upgraded versions of the 20-kV sources used on

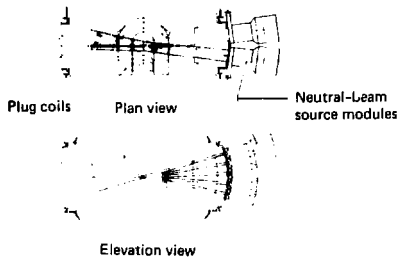

FIG. A-4. Neutral-beam access in plug magnets.

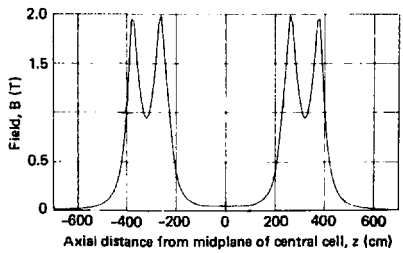

FIG. A-5. Magnetic field strength along the axis of TMX for a 0.10-T central-cell field at z = 0.

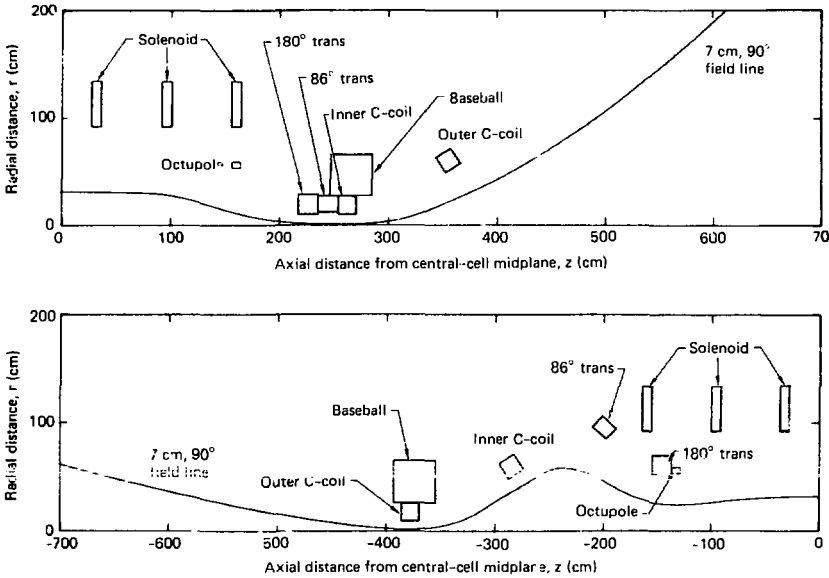

FIG. A-6. Y-projection of end-plug 7-cm field line for the 0.05-T central-cell configuration.

2XIIB. Improvements[12] incorporated in the redesign of these beams included changes in the arc chamber to ease both fabrication and maintenance, and spherical grid curvature on the accelerator sections to provide improved focusing. Each neutral-beam source was mounted on an isolation valve to allow removal and replacement of the source while TMX remained under vacuum. Neutral beams were aimed and optimized by means of calorimeters that were raised to the center of each plug.

Filament and arc power[13] were supplied by banks of 12-V lead-acid batteries. Accel and decel voltages came from electrolytic capacitor banks and were regulated by hard-tube modulators[14-17]. Details of the power supplies are described in Refs. 13-17.

The TMX startup plasma-gun system consisted of four titanium-washer stack guns loaded with deuterium. There were two on each end, located at 0.3 T field strength. The guns produced plasma for 5 ms. The resulting plasma stream flowed along the magnetic field into the plug region.

The guns were composed of a 0.5-cm stack of titanium washers with 1.27-cm-diam holes and a stack of insulating rings alternating with copper rings. A trigger electrode provided the initial breakdown in the stack.

Each gun was powered by a pulse-forming network with a time constant of 5.0 ms. The 6375-μF capacitance of the line was typically charged to 600 V. A small capacitor was discharged by an ignitor through a seven-to-one step-up transformer to supply the trigger pulse. In typical operation all four guns were fired; however, it was possible to build up a plasma with only one gun.

The guns were located on the edge of the plasma and mapped into a location of 7-cm radius in the end plug, as shown in Fig. A-7. The reason for the location on the edge was to avoid cooling the plasma core. Figure A-7 shows that the guns provided an adequate target plasma for the east end

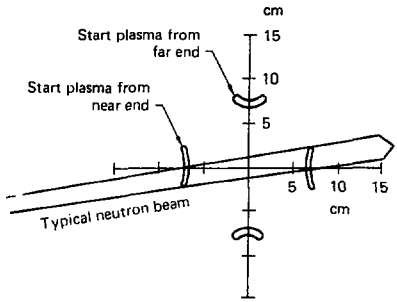

FIG. A-7. Map of the TMX startup plasma on the midplane of the end plugs, showing intersection with a neutral beam.

plug. For the west end, the beams were also horizontal, but the target-plasma-gun footprints were rotated by 90°. We were able to start the west end in spite of the non-optimal target. Once the plasma was started and sustained by end-plug neutral beams and central-cell gas feed, details of the startup guns were unimportant.

A5. GAS FEED SYSTEM

(A. L. Hunt)

A5.1 Gas Box

The gas boxes had limited gas conductance (see Fig. A-8), thus providing for the supply of relatively high-pressure neutral gas near selected mirrors while preserving vacuum conditions in the plasma regions. The gas was admitted to each gas box through four piezoelectric-crystal-controlled valves connected to a gas-supply manifold. The quantity of gas introduced was the product of the change in manifold pressure, ΔP, and the manifold volume, V. The change in manifold pressure was measured as the difference between recorded manifold pressure before and after the shot. The crystal-controlled valves were opened for a time less than the total shot time by a high-voltage pulse. The derived rate of gas introduction was assumed constant over the time interval Δt in which the valves were open, so the rate of gas introduction was $\Delta P \cdot V/\Delta t$. Each valve was calibrated with respect to opening time, because we have found that the time required to fully open the piezoelectric valve depends on the mechanical

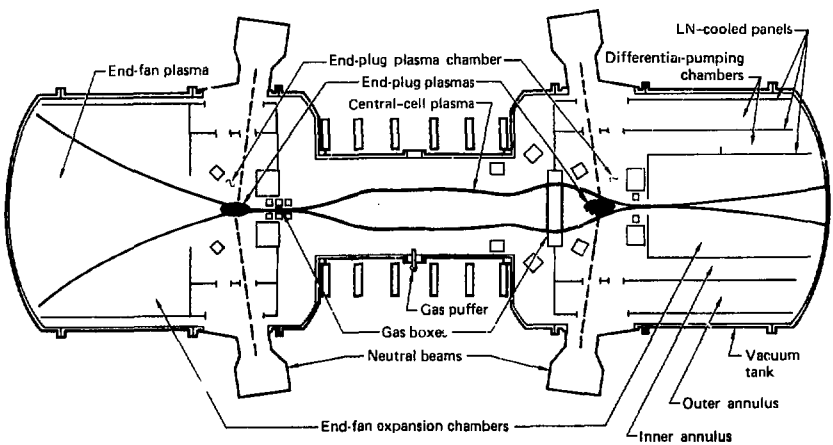

FIG. A-8. Schematic drawing of TMX, showing the plasmas, gas sources, and differential-pumping system.

spring constant as well as on the magnitude of the potential difference across the piezoelectric crystal. The initial opening time was determined by plotting the change in manifold pressure as a function of the duration of the high-voltage pulse for a fixed manifold pressure and pulse magnitude. The result was generally a straight line intercepting $\Delta P = 0$ at an abscissa of $\Delta t = t_s$, where t_s was the pulse duration required to just open the valve. Each valve trigger was then initiated so that the desired gas-input rates for all valves in a given gas box were attained simultaneously. During later operation it was found that such adjustments were not necessary for opening pulses of 200 V if the valves were thermostatically controlled to room temperature.

It has become common to refer to the rate of gas introduction in terms of "amperes" at the gas box or at any valve such as the "puffer" valve on the boundary of the TMX central cell. The average number of atoms introduced per unit time interval in seconds multiplied by the electronic charge in coulombs, 1.60×10^{-19} C, gives the "ampere equivalent."

A5.2 Puffer Valves

The puffer valves were magnetic-solenoid-operated gas valves directed radially inward in the central plane of the central-cell. Although there were two such valves, one on the north side and one on the top of the central cell, the usual experiment required only one. These valves were calibrated by measuring the pressure increase in the TMX volume (after saturation of the getters) for pulse periods of 10 ms to 40 ms.

A6. TMX VACUUM SYSTEM

A6.1 Vacuum System Description

(J. C. Davis)

The TMX vacuum system [18-20] consisted of two large tanks, each containing a plug magnet and transition magnet set, and a smaller central-cell tank with the solenoid magnets outside the vacuum system. These tanks can be seen in Fig. A-8. Beam particles as well as residual gas were gettered by high-surface-area titanium films that were vapor-deposited on all interior tank surfaces and on the liquid-nitrogen (LN)-cooled liners. The plug tanks were divided into mobile and fixed sections; the mobile sections could be rolled back 70 cm, without moving any of the magnets, to provide access to the plug regions for getter replacement, component repair, or diagnostics installation. The plug tanks were divided into three regions by LN-cooled liners to provide differential pumping, which was required to isolate plug plasma from neutral-beam gas loads and to separate the central-cell region from the plugs. The central cell itself was gettered

TABLE A-2. Characteristics of TMX pumping regions.[a]

Region	Volume, ℓ	LN-cooled gettered area, cm^2	Warm gettered area, cm^2
Between outer liner and vacuum tank	3.0×10^3	0	0
Outer annulus	18.2×10^3	6.07×10^5	1.53×10^5
Inner annulus	12.1×10^3	3.47×10^5	1.95×10^5
Plasma chamber, inside the baseball coil, including the holes through magnet	0.92×10^3	0	4.21×10^4
End-fan chamber	16×10^3	2.6×10^5	6.6×10^4
Gas box	13	0	0
Fixed dome between the water-cooled liner and the central-cell tank	8.5×10^3	0	3.1×10^5
Central-cell tank	6.5×10^3	0	1.6×10^5

[a]See Fig. A-8 for configuration of these regions.

but contained no LN liners. The volumes and surface areas of these regions are given in Table A-2. A schematic diagram of the vacuum system is shown in Fig. A-8. The performance of the TMX vacuum system is described below and in Refs. 21 and 22.

Rough pumping for the TMX vacuum system was provided by pairs of mercury-vapor diffusion pumps backed by blowers and mechanical forepumps. Base pressure of the uncooled, ungettered system was about 1×10^{-6} Torr. After gettering on cooled liners, the base pressure dropped to 1×10^{-8} Torr. The TMX vacuum system had many similarities to the 2XIIB system.[23]

The volume of each TMX end-fan chamber was 16,000 liters. The LN-cooled surface area in each TMX end-fan chamber was 26 m^2, and all the walls were coated with titanium by vapor deposition. The end-wall field in TMX was 70 G. The TMX chambers were designed to reduce the plasma density at the end wall, the buildup of gas and cold plasma in the end-fan chamber, and the transport of energy to the end wall by the electrons.[24] These objectives have been met as described in the following section.

The D_2 gas introduced into the TMX end tanks had to be prevented from reaching the end-plug plasma. To satisfy this requirement, the D_2 pressure in the plasma chamber could not exceed a few times 10^{-5} Torr. Somewhat more gas can strike the plasma if a "plasma shield" is present.[25] We used baffles, gettering, and LN-cooled surfaces to maintain a low D_2 pressure in the end plug.[19]

The pumping surfaces in the end tank were covered with a few monolayers of titanium before every one to three plasma shots. The titanium was deposited by sublimation from 0.32-cm-diam titanium-alloy wire (85 wt.% Ti, 15 wt.% Ta). There were 88 such wires distributed throughout TMX.

A6:2 Vacuum System Performance

(R. P. Drake, G. Deis, and M. J. Richardson)

The results of computer modeling of the gas flow are shown in Fig. A-9. Gas was injected into the TMX vacuum chamber through a neutral-beam module. Before gettering, the D_2 pressure rose highest in the outer annulus and slowly reached an equilibrium as the gas flowed into other parts of the machine. The code reproduces the qualitative behavior of the data. The quantitative differences shown in the figure are believed to have resulted from uncertainties in the conductances and volumes used in the code. The effect of gettering is illustrated in Fig. A-9. After a pumpdown and before gettering, the upper trace was observed in the end-fan chamber. After gettering, the pressure remained lower and reached equilibrium faster than it did before gettering. The computer code reproduces these results as shown, using a sticking coefficient of 0.03.

When the panels were cooled by LN, the pumping speed of the system increased. The decrease in maximum pressure and increased response time for the same gas input are shown in Fig. A-10. With the use of LN cooling, the gas introduced by the neutral-beam system was pumped and the gas impinging on the plasma from this source became acceptably small.

Gas can also be desorbed from the surfaces bombarded by the neutral beams, by charge-exchange products from the plasmas, and by UV

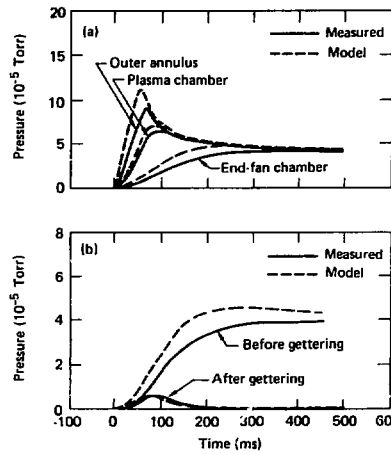

FIG. A-9. Measured and computer-modeled gas flows in TMX. The solid lines show the measured pressure change during and after a 55-ms injection of D_2 gas through a pulsed valve in one neutral-beam module. After pumpdown but before gettering, the effect of the baffles is shown in (a). Gettering significantly changes the system response, as illustrated by data obtained in the end-fan chamber (b). Dashed lines show the results of computer modeling.

radiation. When TMX had been vented to air for maintenance, substantial gettering and neutral-beam operation was needed to obtain plasmas that did not decay prematurely. Figure A-11 shows a characteristic progression from a plasma duration of 5 ms to one of 20 ms. The plasma duration was quite sensitive to the energetic neutral-beam current during this run; in shots with lower beam currents, the plasmas decayed more quickly. Gas desorption is believed to be responsible for these observations and for similar trends observed in 2XIIB. Once full-duration plasmas had been attained, the operating characteristics of the end-plug plasmas did not change significantly until TMX was again vented to air. Gettering alone did not enable us to produce full-duration plasmas, but in one case, after gettering and continual neutral-beam operation, the end-plug plasma did not require the conditioning shots described above.

The central-cell vacuum chamber was separated from the end-plug chambers by disk-shaped baffles to prevent the flow of gas between the two regions. The central-cell walls were at room temperature and were covered with titanium sublimed from getter wires in order to provide a reproducible surface that did not evolve gas. When the central-cell plasma was fueled by the gas boxes

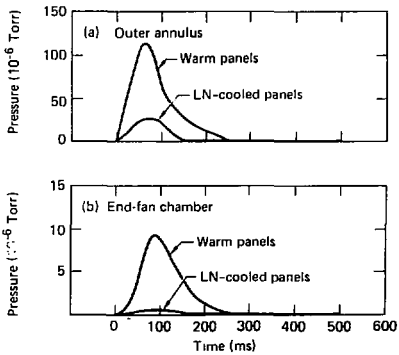

FIG. A-10. The effect of the LN-cooled panels on pumping in TMX. The upper traces show the measured pressure change during and after a 60-ms pulse of gas from eight neutral-beam modules with gettered, room-temperature walls. After the panels are cooled by LN, the pressure rise is less and the gas is pumped more quickly.

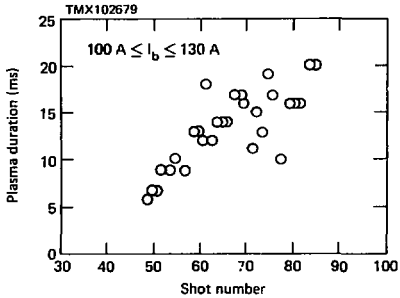

FIG. A-11. The duration of the TMX plasma is shown as a function of the number of plasma shots after a vent.

(see below), the pressure remained below 5.0 × 10^{-6} Torr. At this pressure the flux of D_2 gas impinging on the plasma was negligible by comparison with the gas feed.

The central cell may be fueled either by gas boxes or by a pulsed valve (gas puffer). The two gas boxes were located where the plasma cross-section was very elliptical. Each box was essentially two plasma limiters with gas valves between them. Gas introduced into the gas boxes was very likely to be ionized before it could escape from the gas box. The gas puffer injected gas near the midplane of the central-cell vacuum chamber. Most of the gas was pumped by the plasma, as illustrated in Fig. A-12. The pressure declined slowly while the plasma was present and increased once the plasma had decayed. If no plasma had been produced, the pressure would have risen monotonically.

A6.3 Effect of Vacuum Conditions on Electron Temperature

(D. L. Correll, R. K. Goodman, and W. L. Pickles)

It was observed that poor vacuum conditions reduced the electron temperature. The highest plug electron temperature in TMX (measured by Thomson-scattering techniques) was 260 eV, and it was higher than 200 eV on several occasions during both 1979 and 1980. However, the daily average was lower in 1980 than it was in 1979.[26] Better static and dynamic vacuum conditions have been shown to correlate with the higher plug electron

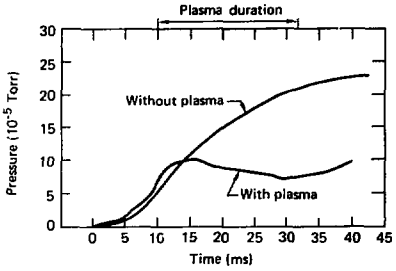

FIG. A-12. The effect of a plasma on the D_2 pressure in the central-cell chamber as a function of time. The gas flow into the chamber was 270 Torr liters per second, and the gas puffer was fired at -5 ms.

temperature. During the last three months of TMX operation, July–September 1980, we were able to show effects on electron temperature from excursions in the machine pressure preceding an experimental shot (static vacuum) and from increases in neutral-gas densities during the experimental shot (dynamic vacuum).

We recorded the plug electron temperature and static vacuum conditions versus experimental shot number for several weeks. If two conditions were met, the subsequent experimental run would begin with lower-than-average electron temperatures and would require more than the usual number of clean-up shots to return to average electron confinement. The two conditions were: (1) the magnet cases of the baseball coils, which are the "first wall", had become the coolest surface in the experiment, and (2) the static vacuum had been seriously degraded since the previous day's running. Condition (1) was easily met because the coil case temperature was determined by radiation losses and therefore had a long thermal constant. Condition (2) occurred because of vacuum system failures.

To help quantify this effect between the electron temperature and vacuum conditions, we used the signal from the secondary-electron-emission detectors to monitor the dynamic gas conditions during the shot. Secondary-emission detectors (SED), which were located at the midplane of each end plug, were used to estimate neutral density sur-

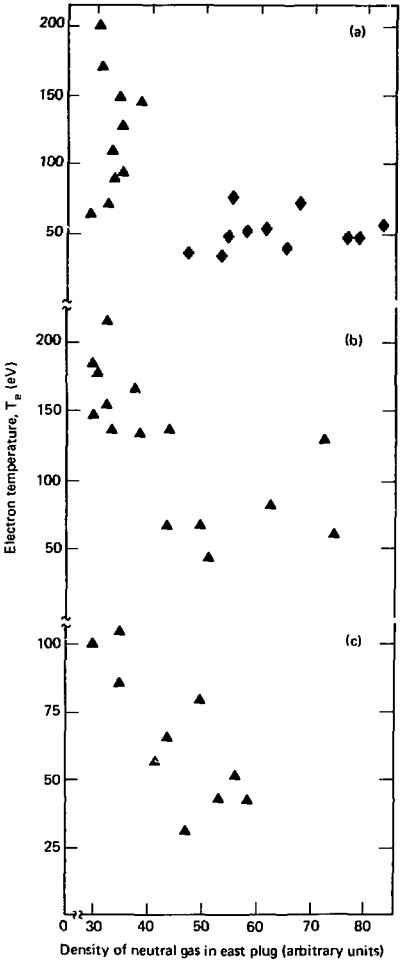

FIG. A-13. Plug electron temperature vs neutral-gas densities: (a) changes in vacuum conditions after the experiment of August 19, 1980, with decreased T_e for run of August 21, 1980; (b) a gas feed change from 600 to 6000 A equivelent of D^o reduces T_e; (c) vacuum system damages of September 29, 1980, reduced T_e.

rounding the plasma. Charge-exchange atoms, which strike the detector cone, release secondary electrons. Ultraviolet light also releases secondary electrons, but tests on 2XIIB indicated that the charge-exchange component dominated. The charge-exchange current incident on the detector was proportional to the product of neutral-atom density, ion density, and angular distribution function in the direction of the detector. These detectors viewed 90° to the magnetic axis and had a large acceptance angle. During neutral-beam injection the neutral density was primarily due to the energetic neutral-beam atoms. In this case the SED signal was proportional to the product of neutral-beam current and ion density. When the neutral beams were turned off, the neutral density was due to background gas impinging on the plasma surface. In this case the signal was proportional to the background gas density. We determined the amount of charge exchange current due to background gas by normalizing the SED signal to the value during beam injection.

We have analyzed measurements of plug electron temperature T_e versus n_{gas} under three different vacuum conditions. Figure A-13a shows data from August 19 and 21, 1980, where conditions (1) and (2), which can drastically alter T_e, occurred after the experimental run of the 19th. Figure A-13b shows data from September 17, 1979, where the gas feed to the central cell was varied from 600 to 6000 A equivalent of neutral atomic deuterium. Finally, Fig. A-13c shows data for September 29, 1980, when relatively good electron temperatures were observed at the beginning of the day, but during the run a vacuum feedthrough was damaged, then repaired, and later the coil case of the west inner C-magnet developed a leak. What is common to all three examples is that the value of T_e declines as n_{gas} increases. In fact, the general dependency of T_e on n_{gas} seems to be independent of whether the source of gas is from known leaks (Fig. A-13c), variations in central cell (Fig. A-13b), or poor "first wall" preparation and conditioning (Fig. A-13a). Figure A-13a shows the plug electron temperature ranging from over 200 eV down to 50 eV as the indirect measurement of the neutral gas impinging on the plasma n_{gas} increases by a relative factor of 2. These data span almost the full operational period of TMX. Its consistency gives strong credence to the hypothesis that the main variation in plug electron confinement was due to background pressure effects.

The specific mechanism by which the background gas lowers the electron temperature is under study. We are presently modeling charge-exchange losses in the fan regions of the plasma, where neutrals can more readily be deposited within the plasma core, as a possible way T_e can be affected by n_{gas}. Secondary emission coefficients of cold electrons at the machine walls are also sensitive to neutral pressure levels through the production of cold plasma at the end walls. Recent measurements of the electron temperature in the central cell indicate the possibility of a thermal barrier between the plugs and the central cell, which in turn could also be sensitive to neutral-gas-generated cold plasma.

REFERENCES

1. F. H. Coensgen, Project Leader; *TMX Major Project Proposal*, Lawrence Livermore National Laboratory, Livermore, CA, LLL-Prop-148 (1977).
2. A. K. Chargin, M. O. Calderon, L. J. Mooney, and G. E. Vogtlin, "System Design for the new TMX Machine," in *Proc. 7th Symposium on Engineering Problems of Fusion Research, Knoxville, Tennessee, October 25–28, 1977* (Institute of Electrical and Electronics Engineers, New York, IEEE Pub. No. 77CH 1267-4 NPS, 1977); also Lawrence Livermore National Laboratory, Livermore, CA, UCRL-79749 (1977).
3. S. R. Thomas, Jr., "TMX, A New Facility," *ibid. 7th Symposium*; also Lawrence Livermore National Laboratory, Livermore, CA, UCRL-79754 (1977).
4. F. K. Chen, A. K. Chargin, B. S. Denhoy, and A. F. Waugh, "Design for the Magnetic Field Requirements of the Tandem Mirror Experiment," *ibid. 7th Symposium*; also Lawrence Livermore National Laboratory, Livermore, CA, UCRL-79743 (1977).
5. R. L. Wong, L. R. Pedrotti, G. A. Leavitt, A. F. Waugh, A. K. Chargin, M. O. Calderon, "The TMX Magnet System, Present and Future," in *Proc. 8th Symposium on Engineering Problems of Fusion Research, San Francisco, California, November 13–16, 1979* (Institute of Electrical and Electronic Engineers, New York, IEEE Pub. No. 79CH 1441-5 NPS, 1979); also Lawrence Livermore

National Laboratory, Livermore, CA, UCRL-92971 (1979).

6. R. E. Henkle, A. R. Harvey, M. O. Calderon, A. K. Chargin, F. F. K. Chen, B. S. Denhoy, J. A. Horvath, J. R. Reed, and A. F. Waugh, "TMX Magnets: Mechanical Design," *ibid. 7th Symposium*; also Lawrence Livermore National Laboratory, Livermore, CA, UCRL-79752 (1977).
7. D. A. Goerz and G. G. Pollock, "TMX Magnet Control System," *ibid. 8th Symposium*; also Lawrence Livermore National Laboratory, Livermore, CA, UCRL-82873 (1979).
8. D. L. Correll and R. P. Drake, Editors, *Results of TMX Operations: January–July 1980*, Lawrence Livermore National Laboratory, Livermore, CA, UCID-18803 (1980).
9. M. O. Calderon, F. F. K. Chen, and B. S. Denhoy, "Mechanical Design for TMX Injector System," *ibid. 7th Symposium*; also Lawrence Livermore National Laboratory, Livermore, CA, UCRL-79753 (1977).
10. D. D. Lang, M. O. Calderon, and K. Gillespie, "Mechanical Design and Installation of the Injector System," *ibid. 8th Symposium*; also Lawrence Livermore National Laboratory, Livermore, CA, UCRL-82916 (1979).
11. T. F. Wieskamp and L. J. Mooney, "Startup of the TMX Neutral Beam System," *ibid. 8th Symposium*; also Lawrence Livermore National Laboratory, Livermore, CA, UCRL-82939 (1979).
12. A. W. Molvik, R. H. Munger, J. J. Duffy, and D. L. Correll, *Geometrically Focused Neutral Beam Accelerators for TMX*, Lawrence Livermore National Laboratory, Livermore, CA, UCRL-84614 (1980).
13. G. T. Santamaria, "A New Generation of Arc and Arc Filament Power Supplies for Pulsed Neutral Beams," *ibid. 7th Symposium*; also Lawrence Livermore National Laboratory, Livermore, CA, UCRL-79683 (1977).
14. G. A. Leavitt, "A 40-kV, 25-ms Neutral Beam Power Supply for TMX," *ibid. 7th Symposium*; also Lawrence Livermore National Laboratory, Livermore, CA, UCRL-79687 (1977).
15. G. A. Leavitt, "Tradeoffs in Capacitor Bank Design," *ibid. 7th Symposium*; also Lawrence Livermore National Laboratory, Livermore, CA, UCRL-79686 (1977).
16. R. I. Ross, "Neutral Beam Control Systems for the Tandem Mirror Experiments," *ibid. 8th Symposium*; also Lawrence Livermore National Laboratory, Livermore, CA, UCRL-82925 (1979).
17. G. G. Pollock, "Fiber Optics in Neutral Beam Control on the TMX Experiment at LLL," *ibid. 8th Symposium*; also Lawrence Livermore National Laboratory, Livermore, CA, UCRL-82874 (1979).
18. D. P. Atkinson, M. O. Calderon, and R. T. Nagel, "Vacuum System for the Tandem Mirror Experiment," *ibid. 7th Symposium*; also Lawrence Livermore National Laboratory, Livermore, CA, UCRL-79750 (1977).
19. M. J. Richardson, D. P. Atkinson, and M. O. Calderon, "Vacuum System for the Tandem Mirror Experiment," *ibid. 8th Symposium*; also Lawrence Livermore National Laboratory, Livermore, CA, UCRL-82918 (1979).
20. J. J. Jolly, J. L. Parkinson, and D. Swan, "The TMX Vacuum System Cryoliners," *ibid. 8th Symposium*; also Lawrence Livermore National Laboratory, Livermore, CA, UCRL-82886 (1979).
21. R. P. Drake, G. Deis, M. J. Richardson, and T. C. Simonen, "Gas Control and Wall Conditioning in TMX," in *Proc. Fourth Int. Conf. on Plasma Surface Interactions, Garmish-Partenkirchen, Federal Republic of Germany, April 21–25, 1980, J. Nucl. Mater. 93-94, 291* (1980); also Lawrence Livermore National Laboratory, Livermore, CA, UCRL-83607 (1980).
22. T. C. Simonen and R. P. Drake, *Hydrogen Recycling in Tandem Mirror Machines*, Lawrence Livermore National Laboratory, Livermore, CA, UCID-18322 (1979).
23. T. C. Simonen, R. H. Bulmer, F. H. Coensgen, W. F. Cummins, C. Gormezano, B. G. Logan, A. W. Molvik, W. E. Nexsen, W. C. Turner, B. W. Stallard, G. E. Vogtlin, and R. R. Vandervoort, "Control of First Wall Surface Conditions in 2XIIB Magnetic Mirror Plasma Confinement Experiment," *J. Nucl. Mater. 63, 59* (1976).

24. G. D. Porter, *Effect of Gas Recycling and Secondary Electron Emission*, in *Physics Basis for MFTF-B*, Lawrence Livermore National Laboratory, Livermore, CA, UCID 18496—Part 2, Jan. 16, 1980, p. 151.

25. B. W. Stallard, F. H. Coensgen, W. F. Cummins, C. Gormezano, B. G. Logan, A. W. Molvik, W. E. Nexsen, T. C. Simonen, and W. C. Turner, "Plasma Wall Charge Exchange Interactions in the 2XIIB Magnetic Mirror Experiment," *Proc. Int. Symp. on Plasma Wall Interaction, Juelich, Federal Republic of Germany, Oct. 18–22, 1976* (Pergamon Press, New York, 1977) p. 63.

26. D. L. Correll and R. P. Drake, Editors, *Results of TMX Operations: January–July 1980*, Lawrence Livermore National Laboratory, Livermore, CA, UCID-18803 (1980).

APPENDIX B
TMX DIAGNOSTICS INSTRUMENTATION

(S. L. Allen, C. A. Anderson, W. L. Barr, G. A. Burginyon, J. F. Clauser, P. Coakley, R. Crabb, W. F. Cummins, G. E. Davis, D. Dietrich, J. H. Foote, R. Fortner, A. M. Frank, C. E. Frerking, A. H. Futch, D. A. Goerz, R. K. Goodman, D. P. Grubb, G. A. Hallock,† R. L. Hickok,† E. B. Hooper, Jr., R. S. Hornady, A. L. Hunt, C. V. Karmendy,** H. A. Koehler, G. W. Leppelmeier, M. E. McGee, R. H. Munger, T. Nash, W. E. Nexsen, L. B. Olk, M. P. Paul,†† G. D. Porter, P. Poulsen, T. C. Simonen, D. R. Slaughter, H. D. Snyder, J. P. Stoering, O. T. Strand,‡ and A. Toor)*

*University of Iowa, Iowa City, IA.
†Rensselaer Polytechnic Institute, Troy, NY.
**Deceased.
††Alcorn State University, Lorman, MS.
‡Johns Hopkins University, Baltimore, MD.

Appendix B.
TMX Diagnostics Instrumentation

B1. INTRODUCTION

This appendix describes the various diagnostic systems that were employed on TMX. Table B-1 lists these diagnostic systems and Fig. B-1 shows the locations of most of them. The fabrication, installation, and improvement of diagnostics has continued throughout the life of TMX. A total of 377 diagnostic channels was used; however, because of various limitations and experimental requirements, not all of these channels were used on a given experiment. The data from as many as 297 channels of these instruments was read directly by the TMX computer system.

B2. DIAGNOSTICS SYSTEMS

B2.1 Thomson Scattering *(R. K. Goodman)*

Thomson scattering of ruby-laser light (6943 Å) was used on TMX to measure the electron temperature and density in a small volume (about 30 mm^3) of the plasma. In Thomson scattering the laser light is scattered by the plasma electrons and also shifted in wavelength by the electron velocity (Doppler effect). The electron temperature is determined from the width of the scattered wavelength spectrum, and the electron density from the total amount of scattered light. A calibration for absolute density was done by filling TMX to a known density of N_2 and measuring the total scattered light. In general, both the electron temperature and density measurements have an accuracy of ±20%.

There were two independent Thomson scattering systems on TMX, one located on the midplane of the east plug and the second on the midplane of the central cell (Fig. B-2). Each system used a 10-J ruby laser which was focused at the center of the plasma. The system viewing the east-plug imaged 1-cm segments of the laser path in the plasma, at the radial positions (r) of 0, 5, 10, and 15 cm. This system also had two polychromators, which allowed simultaneous measurements on any two of these radial positions, usually r at 0 and 5 cm radius. The central-cell system imaged only the zero radius position and had one polychromator.

Each polychromator contained a diffraction grating to separate the scattered plasma light into 10 wavelength channels which were coupled by fiber optics to 10 photomultiplier tubes. These tubes were gated to prevent their saturation by background plasma light. A tungsten light-calibration source could be introduced through the polychromator input optics to normalize the gains of the photomultiplier tubes and amplifiers of the various channels. The outputs of the 10 channels, which give the Doppler profile, were read by the TMX computer, which reduced the profile and total signal to electron temperature and density. The statistical variation of each photomultiplier channel signal was determined, after each shot, using the tungsten calibration source. These "standard deviations" were used by the computer to calculate the error bars for the electron temperature and density for that shot.

B2.2 Beam Attenuation *(J. H. Foote)*

Spatial profiles of line-integral densities were obtained for each plug and the central cell of TMX by measuring the attenuation of neutral beams traversing the plasma.[1-4] The neutral beam sampled in each plug was one of those used to fuel the plasma; the beam sampled in the central cell was a special one installed for that purpose. Fifty-four detectors of the secondary-electron-emission type were mounted near the vacuum-chamber walls, where they intercepted a portion of the associated neutral beam passing through the plasma. The beam intensity at each detector was measured with and without the plasma present. The line integral of the density along the detector line-of-sight through the plasma could be calculated from the fraction of the neutral-beam particles attenuated by the plasma, using

$$T = \exp(-\sigma_{eff} \int n dl) \quad ,$$

where T is the particle fraction transmitted (1 − fraction attenuated) and σ_{eff} is the average cross section for the loss of neutral particles from the beam because of interactions with the plasma,

TABLE B-1. TMX diagnostic instrumentation.

Plasma parameters	Diagnostic systems	No. of diagnostic channels		
		East plug	Central cell	West plug
Electron temperature and density	Thomson scattering	4	1	–
Plasma density profiles	Beam attenuation detector	23	7	24
Electron line density	Microwave interferometers	4	2	2
Plasma energy and δ	Diamagnetic loops	2	6	2
Axial loss current, energy and ϕ_p	End-loss analyzer (ELA)	2	–	2
Central-cell plasma potential	Heavy-ion beam probe (HIBP)	–	1	–
End-loss current profile	Faraday cups, button probes	20	–	13
Exterior density and temperature	Emitting and collecting probes	4	–	–
Potential fluctuations	rf probes	16	28	13
Density fluctuations	Microwave scattering	3	2	1
Charge-exchange flux	Secondary emission detector (SED)	1	2	1
Neutron production rate	Neutron detectors	1	–	1
Neutral-gas pressure	Fast vacuum gauges	1	2	2
Impurity concentration	EUV spectrometers	22	22	1
Ion energy	UV and visible spectrometers	–	3	–
Visible light	Light monitor	2	1	–
Electron energy	X-rays	5	1	1
Power losses	Calorimeters	17	8	16
Power losses	Pyroelectric probe	–	1	–
Wall interaction	Surface probes	1	1	–
Neutral-beam power and focus	Neutral-beam calorimeters	1	–	1
Magnetic field strength	Magnet currents	6	6	6
Neutral-beam power	Beam voltage and current	24	–	24
Plasma-gun output	Gun current	2	–	2
Gas-feed current	Gas-valve timing and output	4	2	4
		165	96	116

calculated for the existing plasma conditions. The value of σ_{eff} typically used for the east plug with deuterium was 1.54×10^{-15} cm^2.

We measured radial and axial profiles in the east and west plugs with arrays of up to 24 detectors in the shape of a cross. These detectors sampled at 4-cm intervals along the magnetic axis, and at 2-cm intervals along chords through the plasma in the direction normal to the axis, each with a field-of-view full width at half maximum (FWHM) of 1 cm at the plasma. Figure B-3 shows these sampling intervals and directions. We regularly measured radial (or vertical) plasma profiles extending 12 cm above and below the magnetic axis. The measured axial profile in the east plug covered the axial range of 19 cm from the plug midplane toward the central cell to 12 cm toward the end wall. In the west plug, the measured axial range was 12 cm toward the central cell and 23 cm toward the end wall. The axial detector array in the west plug thus measured plasma densities up to 11 cm farther toward the end wall than did the east array, while the east-plug array measured 7 cm farther toward the central cell.

The central-cell vertical array had seven detectors to give a radial plasma profile near the central-cell midplane extending from 11 cm below the magnetic axis to 37 cm above.

The output from the various detectors was read and stored by the TMX computer system, which fitted the radial profiles of fndl data with a Gaussian curve at selected times during a shot and

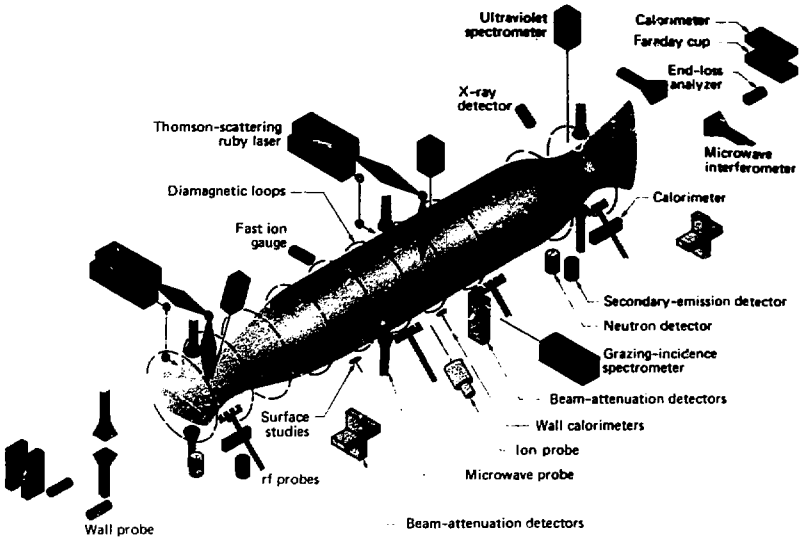

FIG. B-1. Locations of most of the diagnostics on TMX.

plotted the data and fitting curve. Figure B-4 is an example of these results for the west plug. Values of peak density and 1/e radius for the Gaussian fit were printed out on each plot. From the Gaussian fitting of the radial data, plots of peak density and 1/e radius versus time could be conveniently obtained for the plugs and central cell. Axial fndl results for the plugs, at selected times, were also plotted. In addition, there was a computer program that calculated Gaussian and quadratic fits to the axial-profile data.

Plots such as those described above were usually obtained during the between-shot processing, so they were quickly available during a run for determining plasma conditions.

B2.3 Microwave Diagnostics *(A. H. Futch)*

B2.3.1 Microwave Interferometers. The TMX microwave diagnostics are shown in Fig. B-5. The interferometers include three 2-mm interferometers, two 4-mm interferometers, and two x-band interferometers. The locations and several characteristics of these interferometers are given in Table B-2. Superheterodyne detection circuits were used for the 2- and 4-mm interferometers, and simple homodyne detection circuits were used for the x-band interferometers. Figure B-6 shows the sin θ and cos θ output for the central-cell interferometer and compares beam-attenuation line density with microwave line density.

To experimentally investigate the radial transport of Yushmanov-trapped particles and other plasma effects in the magnetic field fans, the 4-mm (1 fringe = 5×10^{13} cm^{-2}) microwave interferometer was installed in the east transition region. Horns were placed in the fan on the central-cell side of the east plug, at the peak field of the inner east mirror, and in the fan region of the east plug. The locations and plasma parameters are summarized in Table B-2. The microwave equipment could be used on any one of the horns at any time.

B2.3.2 Microwave Scattering. The perturbed plasma density may be calculated by a

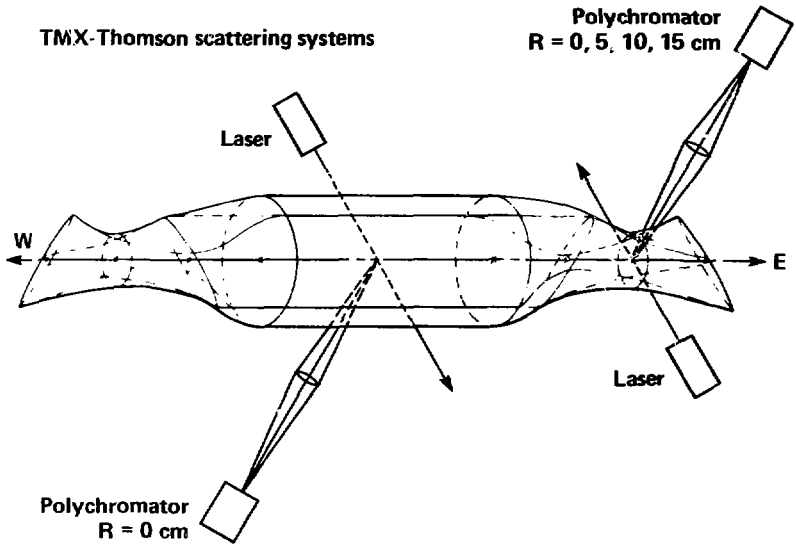

FIG. B-2. Locations of the Thomson-scattering systems on TMX.

procedure developed by Powers and Simonen.[5] The procedure is to mix the intermediate frequency (i.f.) signal of the plasma with the i.f. reference signal. After mixing, the signal is split; half of the power is sent through a low-pass filter to produce low-frequency fringes while the other half is amplified before passing through a band-pass filter. The perturbed density is then calculated as in Ref. 5. Using the appropriate terms from the dispersion relation for the DCLC instability gives

$$4\pi\ e\tilde{n}_e = \left(\frac{\omega_{pe}^4}{\omega_{ce}^2 c^2} + \frac{\omega_{pe}^2 k}{\omega \omega_{ce} R} \right) \tilde{\phi} \quad . \quad \text{(B-1)}$$

Here ω_{pe}, ω_{ce}, and ω refer to the plasma frequency, electron-cyclotron frequency, and wave frequency (due to the plasma instability) respectively, and R is the plasma radius. Substituting and solving for the perturbed potential $\tilde{\phi}$, one obtains

$$\tilde{\phi} = \frac{\tilde{n}_e/n}{2.0 \times 10^{-11}\ n/B_c^2 + 220/B_p B_c} \quad . \quad \text{(B-2)}$$

The first term of Eq. (B-1) was neglected in the analysis in Ref. 5, but is much larger for the central cell of TMX and cannot be neglected. The perturbed potentials measured by this method are several times larger than those measured by probes at the plasma boundary, but generally show similar time dependencies.

B2.4 Diamagnetic Loop Measurements

(W. E. Nexsen, Jr.)

An array of diamagnetic loops is used to measure the plasma diamagnetism of the end plugs and central cell of TMX. At first, two loops were located in each plug and one was located 28 cm west of the center plane of the central cell. In December 1979, an additional five loops were added to the central cell: one in a symmetric position 28 cm east of center line, one in each transition region, and two at intermediate values of the magnetic field.

The plug plasma dimensions are small compared to the plug loop dimensions; consequently, the flux, caused by plasma currents, that links the

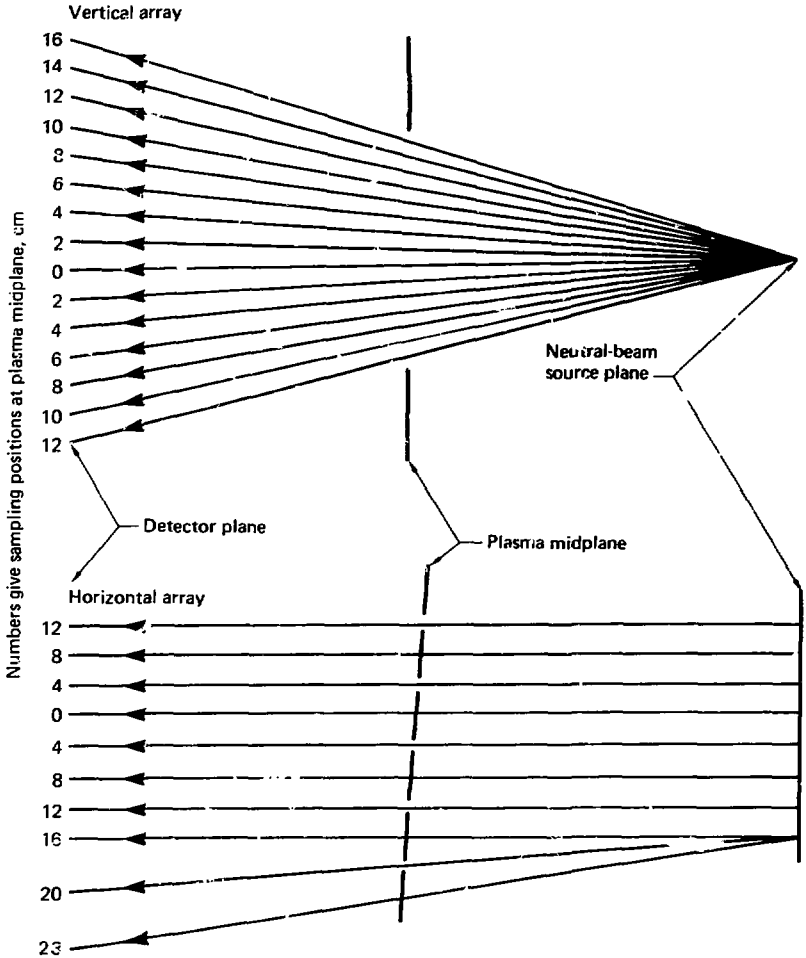

FIG. B-3. Sampling intervals and directions for the array of beam-attenuation detectors in the plugs.

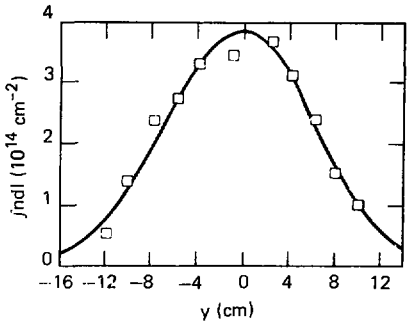

FIG. B-4. Example of west-plug radial profile data fitted with a Gaussian curve (peak line density = 3.89×10^{14} cm^{-2}, 1/e radius = 9.14 cm). The negative values are below the centerline, the positive values above it.

loop can be approximated by the flux from a dipole of magnetic moment m. The plug loops were calibrated *in situ* with a small pulse coil of known magnetic moment located in the plasma position.

The assumptions made to calibrate the plug loops cannot be used for the central-cell loop because the central-cell plasma is long compared to the diameter of the loop; therefore for this case a solenoidal approximation to the plasma's diamagnetic currents was used to calculate the response of the loop to the plasma and to currents induced in the walls by the plasma.

Following the shutdown of TMX, the response of the central-cell loops to a small coil of known magnetic moment was measured as a function of the z position of the coil. When the measured response function of one of the loops near the center plane was convoluted with the axial distribution of the plasma magnetic moment m(z), assuming a Maxwellian central-cell plasma for

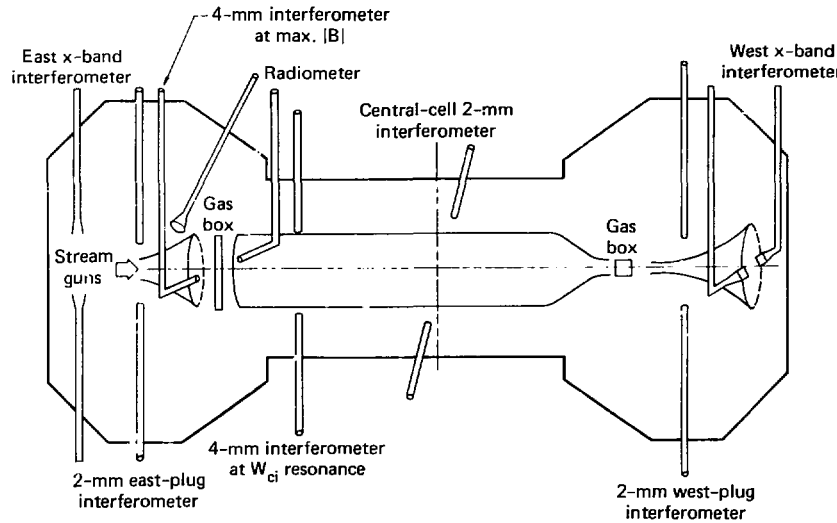

FIG. B-5. The location of the microwave diagnostics in TMX.

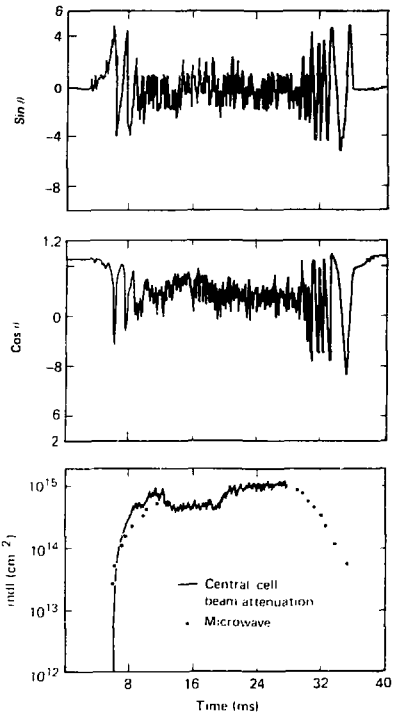

FIG. B-6. Sin θ and cos θ outputs for the central-cell interferometer and a comparison of the line densities measured by microwave interferometers and by beam attenuation detectors.

which $m(z) \propto 1/B^2(z)$, the agreement with the calculated loop response was within 10%.

The magnetic moment measurements can be combined with measurements of the plasma dimensions and densities to obtain values of plasma β ($= 8\pi n W_\perp / B^2$) and the average energy of an electron-ion pair. For the plug plasmas, which are quite similar to those of 2XIIB, we assume that the diamagnetic signal is due to ions only and that, as in 2XIIB, the ion energy is independent of radius and z. Then, for low β (<50%) and assuming that both radial and axial density profiles are Gaussian, we find

$$\beta_p = \frac{0.45\ m}{L_p B_p r_p^2} \quad , \tag{B-3}$$

where L_p and r_p^2 are the 1/e half-length and the radius of the plasma, B_p is the plug field at its center (in gauss), and m is the measured magnetic moment in A/cm^2. The average perpendicular ion energy $\overline{W}_\perp$, is given by

$$\overline{W}_\perp = \frac{2 \times 10^{10}\ m B_p}{L_p r_p \overline{nl}}\ (eV) \quad , \tag{B-4}$$

where $\overline{nl}$ is the line density through the plug diameter in units of cm^{-2}.

For the central cell, further assumptions are required to reduce the data. If we assume that the ions and electrons both have Gaussian profiles with temperature scale length r_w and density scale length r_c, we calculate

$$W_\perp = \frac{3.55 \times 10^{10}\ m B_c}{\overline{nl}\ r_c} [1 + (r_c/r_w)^2] \quad , \tag{B-5}$$

and

$$\beta_c = \frac{0.8\ [1 + (r_c/r_w)^2]}{B_c\ r_c^2} \quad . \tag{B-6}$$

Because we have neither a measured value or a good model for r_w at present, we have assumed that $r_w = r_c$ for the purposes of data reduction.

B2.5 End-Loss Analyzers *(D. P. Grubb)*

In a tandem mirror machine, the central-cell ions are confined as they scatter in pitch angle and energy until they enter the loss region of phase space, and are then lost axially along field lines (through the plugs) to the end walls. Analysis of the ion energy at the end wall thus provides information about the plug potential and the central-cell ion temperature. Electrostatic end-loss ion analyzers (ELA's), shown in Fig. B-7, can be used to determine these parameters. In addition, the current density measured by ELA's can be used in particle and power-balance calculations, and can be

TABLE B-2. Location and several characteristics of TMX microwave interferometers.

Name	Location	Frequency	$\int n dl$ for $\Delta\phi = 2\pi$ (cm^{-2})	Distance between horns (cm)	l_p, plasma path length (cm)
East x-band	147 cm from wall	10 GHz	7.4×10^{12}	35	32
West x-band	142 cm from wall	10 GHz	7.4×10^{12}	35	32
East plug, 2 mm	Midplane of east plug	140 GHz	1.04×10^{14}	71	14
Yushmanov	Between east mirror and center of east plug	70 GHz	5.02×10^{13}	12	3.5
East-plug mirror	At mirror between east plug and central cell	70 GHz	5.02×10^{13}	12	1.9
Central cell, resonance point	At 1-T point between east plug and central-cell midplane	70 GHz	5.02×10^{13}	30	3.5
Central cell, 2 mm	Midplane of central cell, through center	140 GHz	1.04×10^{14}	86	44
West plug, 2 mm	Midplane of west plug	140 GHz	1.04×10^{14}	71	14

NOTE: Plug l_p's are scaled for l_p(central) = 44 cm.

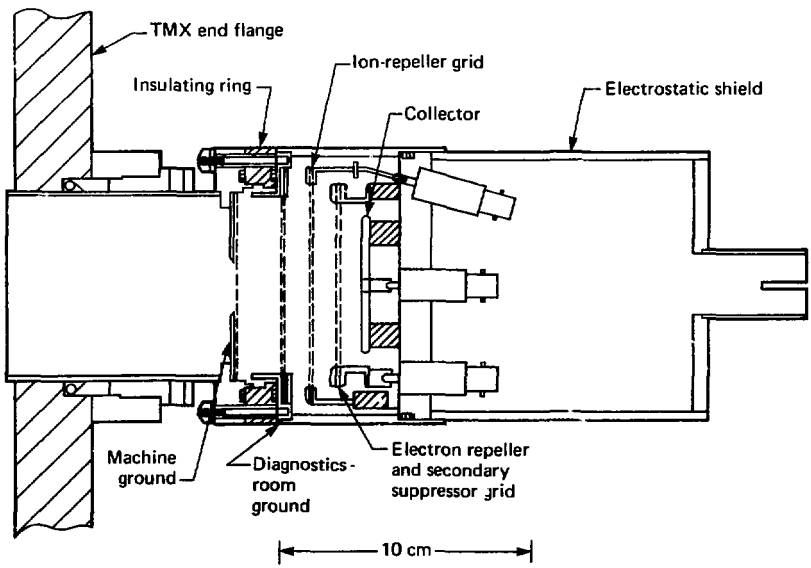

FIG. B-7. An electostatic end-loss analyzer (ELA).

compared with the result of quasi-linear calculations of the stream requirements of the drift-cyclotron loss-cone (DCLC) mode. The ELA's used on TMX were essentially the same as the one used on 2XIIB, but the types and numbers of grids used in the analyzers had to be changed because of the major differences between the two experiments. Table B-3 summarizes some of the differences between the end-loss ions in TMX and those in 2XIIB.

There were four ELA's installed on TMX, two on each end wall. Those on the east end were located at positions, in the direction of the long axis of the fan, that mapped to x = −1.5 and x = +4.5 cm in the midplane of the plug. Measurements have indicated that the center of the plasma fan, in the direction of the thin axis, was not on the geometrical axis of the machine. Thus, in the thin axis, the locations of both of these analyzers map to radii of 3.1 and 5.2 cm from the axis at the midplane of the plug. On the west end, a movable ELA, which could traverse the fan through its thin section, was located on the vertical midplane of the fan. The second ELA was fixed at a position on the long axis of the fan that mapped to y = −1.5 cm from center in the midplane of the plug. Because of the displacement of the plasma fan, the position of this analyzer mapped to a radius of 3.8 cm from center, in the orthogonal direction, at the midplane of the plug.

In one mode of ELA operation, the ion-repeller grid is set at a zero bias so that all of the incident ions are collected. In this mode, the total end-loss current as a function of time can be measured. In a second mode of operation, the ion-repeller grid is biased positively with respect to machine ground and thereby repells ions with energies lower than the ion-repeller grid voltage. In order to avoid problems with shot-to-shot variations, a ramping circuit was used together with a programmable, high-voltage power supply to ramp the ion-repeller voltage over a specified range. Figure B-8 shows the ELA current (I) as a function of the ion-repeller voltage (V) for the ideal case of a perfectly quiescent plasma. Since all of the ions from the central cell must pass through the plug to reach the analyzer, they will arrive at the wall with energy greater than or equal to ϕ_p (the potential drop from the plug to the wall). Therefore, the flux of the end-loss ions will not be attenuated until the ion-repeller voltage is greater than ϕ_p. For higher voltages, the current versus voltage curve is a measure of the energy distribution of the end-loss ions. The exact relationship between the slope of the curve and the assigned ion energy, W_i, depends upon the assumed distribution function of the central-cell ions. At present, the central-cell ions are assumed to have a Maxwellian distribution, and

TABLE B-3. Comparison of TMX and 2XIIB end-loss analysis.

	TMX	2XIIB[a]
Major source of end-loss ions	Central cell	Ionized neutral-beam current and stream-gun current
Average current density at center of mirror	0.5 A/cm^2	0.1 A/cm^2
Current density at analyzer	3 mA/cm^2	30 mA/cm^2
Pitch angle of end-loss ions	3°	22°
B at analyzer	65 G	2 kG

[a]Data is for plasmas during stream-gun and neutral-beam operation only.

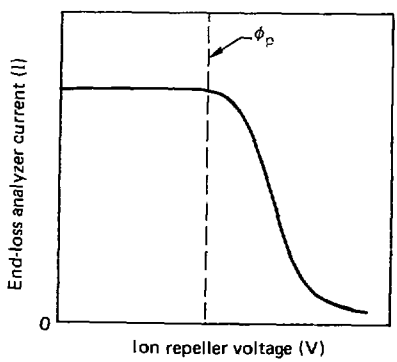

FIG. B-8. End-loss current-voltage characteristics. The break point is a measure of the plug plasma potential, ϕ_p; the fall-off rate is an indication of the ion temperature.

the analysis of the curves is based on this assumption.

A complication is caused by the presence of fluctuations at the plug ion-cyclotron frequency. Since the central-cell ions must pass through the plug to reach the analyzer, they pass through resonance points. Sufficiently strong fluctuations can heat the escaping central-cell ions and alter the observed end-loss spectrum. The presence of fluctuations in the end-loss current gives rise to an uncertainty in the values of ϕ_p and W_i measured by the ELA's. The plug potential can usually be determined within ±50 to 75 V. Typical values of ϕ_p have been in the range of 300 to 800 V after the plasma has reached equilibrium. The same data yields values of W_i in the range 100 to 1200 eV.

The output from the ELA's was reduced by a computer code. This code determined the end-loss current density j, in A/cm^2, the plug potential ϕ_p, in V, and the mean energy of the end-loss ions W_i, in eV. Some typical end-loss current results are shown in Fig. B-9. The quality of the fit to the data depended on the fluctuations in the end-loss current. In Fig. B-9, the fluctuation of the current around the fit line is due to fluctuations that occur on a shorter time scale than the voltage-ramping time.

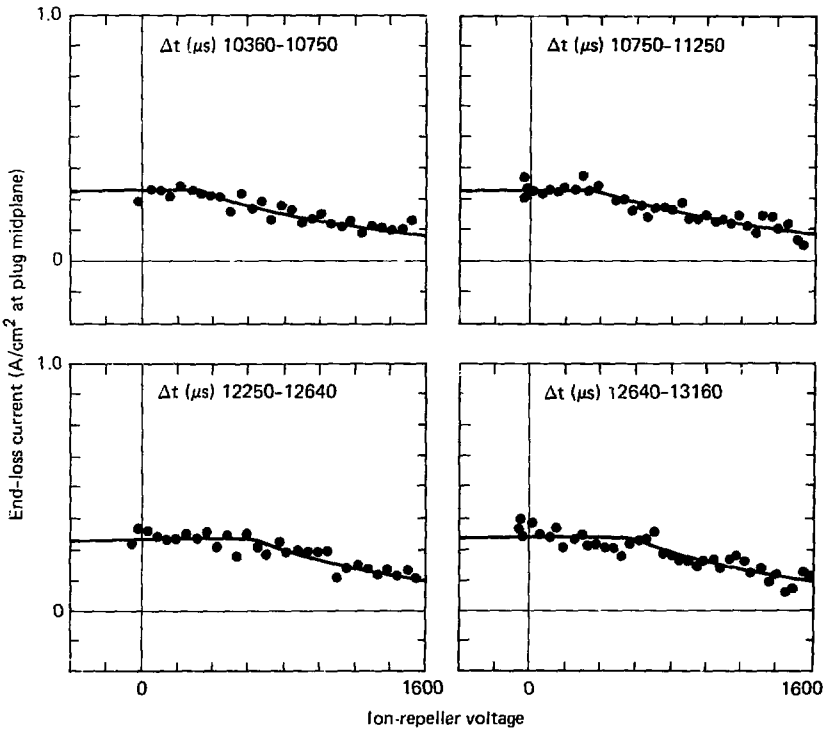

FIG. B-9. West end-loss spectra at four different times.

B2.6 Heavy-Ion-Beam Probe

(G. A. Hallock, R. L. Hick[illegible] *and R. S. Hornady)*

The TMX central-cell space potential was measured by actively probing the plasma with a heavy-ion-beam probe (HIBP) developed by Rensselaer Polytechnic Institute. Measurements were made within a small sample volume, about 1 cm^3. The depth of the confining-potential well in the central cell was obtained by comparing these data to the plug potential obtained from the energy spectra of end-loss ions. The ion-beam probe technique uses the change in the charge state of injected ions that is caused by electron-impact ionization. No significant momentum change occurs during the collision. Ions leaving the plasma in the new charge state have an increased energy equal to the potential at the collision point times the change in charge.

Figure B-10 shows the HIBP used on TMX. Varying the voltages applied to the ion gun and the θ-sweep plates allows the observation point to scan the plasma cross section (Fig. B-11). Diameter scans of the plasma could be made during a single shot by sweeping the θ-deflection voltage. The injection parameters could also be held fixed to provide continuous temporal profiles. Beam chopping with the z-sweep plates allowed noise reduction. The diagnostic system included a monitor to locate the primary beam and its current.

The HIBP control system was based on standard CAMAC modules, commercial high-voltage power supplies, and a microcomputer. The system stood alone, with the microcomputer handling setup, data acquisition, status monitoring, and data storage on floppy disk. This system also processed raw data through interactive graphics and high-level programming. Speed limitations, however, required off-line processing; advanced data reduction was facilitated by a larger computer.

The beam probe consisted of a beam line, which injected singly ionized alkali-metal atoms (the primary beam), and an energy analyzer to monitor the particles leaving the plasma. The particle trajectories were determined from their mass, charge, and injection parameters and the magnetic field. The measurement was based on monitoring the 1+ to 2+ reaction products of primary beam ionization by the impact of plasma electrons,

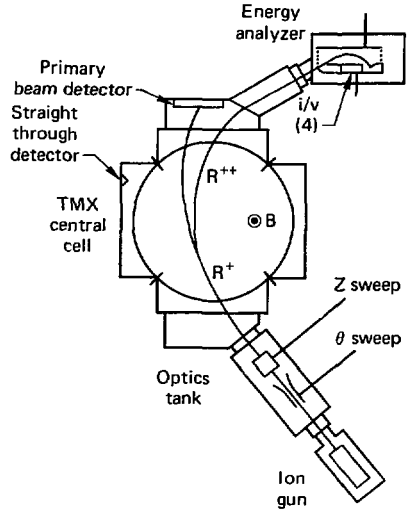

FIG. B-10. The heavy-ion-beam probe (HIBP) used on TMX.

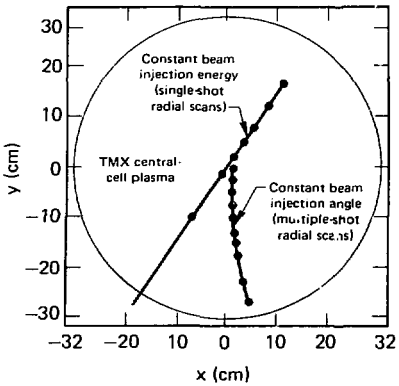

FIG. B-11. Radial scan lines obtained by the HIBP in the central cell.

*Rensselaer Polytechnic Institute, Troy, NY

$$R^+ + e^- \rightarrow R^{++} + 2e^- \quad . \tag{B-7}$$

The 2+ ions (secondaries) left the plasma with an increase in energy proportional to the space potential at the reaction point,

$$E = E_0 + e\phi \quad . \tag{B-8}$$

The imposed magnetic field separated the secondaries from the primary beam. Spatial resolution was determined by the primary-beam diameter and the energy-analyzer aperture. Fluctuations to 40 kHz (1 MHz for short intervals) could be followed with a resolution of approximately 2 V. Calibration of the system probe allowed space-potential measurement with an absolute accuracy (with respect to the vacuum wall) of approximately 25 V. Spatial resolution was about 0.8 cm.

Temperature measurements were inferred from the secondary current level. The ratio of the secondary current to the primary current is proportional to the plasma density times an effective cross section,

$$\frac{I_s}{I_p} \propto n_e \sigma(T_e) \quad . \tag{B-9}$$

Density profiles from the neutral-beam-attenuation detectors were used in evaluating this expression. Information on the temporal behavior of the electron temperature was also obtained by monitoring higher order transitions 1+ to 3+, and 1+ to 4+. This measurement was based on the significant difference in cross section for these cases.

A variety of profile measurements has been obtained. The observation point (sample-volume location) could be held fixed during the shot, providing a continuous temporal profile, or it could be scanned through the plasma, yielding multiple radial profiles. Scan times of 100 μs to 10 ms were typically used, yielding several to dozens of diameter scans per shot.

A typical profile of the center-line (r = 0) space potential in the central cell of TMX is shown in Fig. B-12(a). Machine conditions for this shot, number 39 on September 26, 1980, are representative of normal tandem mirror operation. The secondary ion current level for the same shot, a function of plasma density and electron temperature [see Eq. (B-9)], is shown in Fig. B-12(b).

Correlation between the plasma space potential, secondary-ion-current level, and machine operation is quite strong. A quasi-equilibrium is reached at about 5 ms, shortly after the stream guns and neutral beams begin plasma buildup. At 6 ms the gas box (the dominant source of particle input) is switched on, and the potential begins to increase shortly thereafter. A peak in the space potential occurs at 8 ms, which is the time the stream guns are turned off. Fluctuations in the secondary-current level rapidly increase at about this time. Buildup continues, with the main equilibrium level reached about 10 ms into the shot. Equilibrium lasts until 22 ms, one ms after the west plug is turned off. The potential then decays, with a time constant of about 1 ms, to about two-thirds of the main equilibrium level. This new equilibrium is maintained until just after the 28-ms east plug turnoff, at which time the potential rapidly decays.

The equilibrium central-cell potential (r = 0) varies from about 300 V up to a maximum of about 500 V, with even lower values during machine cleanup. The potential is a function of fueling method (gas box or puffer), fueling rate, neutral-beam current, and other machine conditions.

Profiles for a typical TMX shot where multiple radial scans of the plasma were obtained are shown in Fig. B-13. These results are for shot 88 on September 26, 1980, and represent typical profiles obtained with gas-box fueling of normal gas feed rates [about 1200 A (atom equivalent)]. A blowup of one of the radial scans during the equilibrium interval is shown in Fig. B-14. A full radial scan is obtained in one direction, but scrapeoff of the injected beam on a vacuum valve limits the radial scan to about 18 cm in the opposite direction (measurement coordinates are described in Fig. B-11).

The plot of plasma potential versus radius is parabolic to about 20 cm, as indicated in Fig. B-14. This yields an electric field that increases linearly with radius, as is shown in the lower diagram of the figure, and rigid-body $\mathbf{E} \times \mathbf{B}$ motion of the plasma. With a 1-kG central-cell magnetic field, the $\mathbf{E} \times \mathbf{B}$ frequency is typically 12 kHz. Plasma fluctuations at this frequency have been observed by the HIBP and other diagnostics.

Beyond a radius of 20 cm, the plasma potential tends to flatten out. However, radial variations in

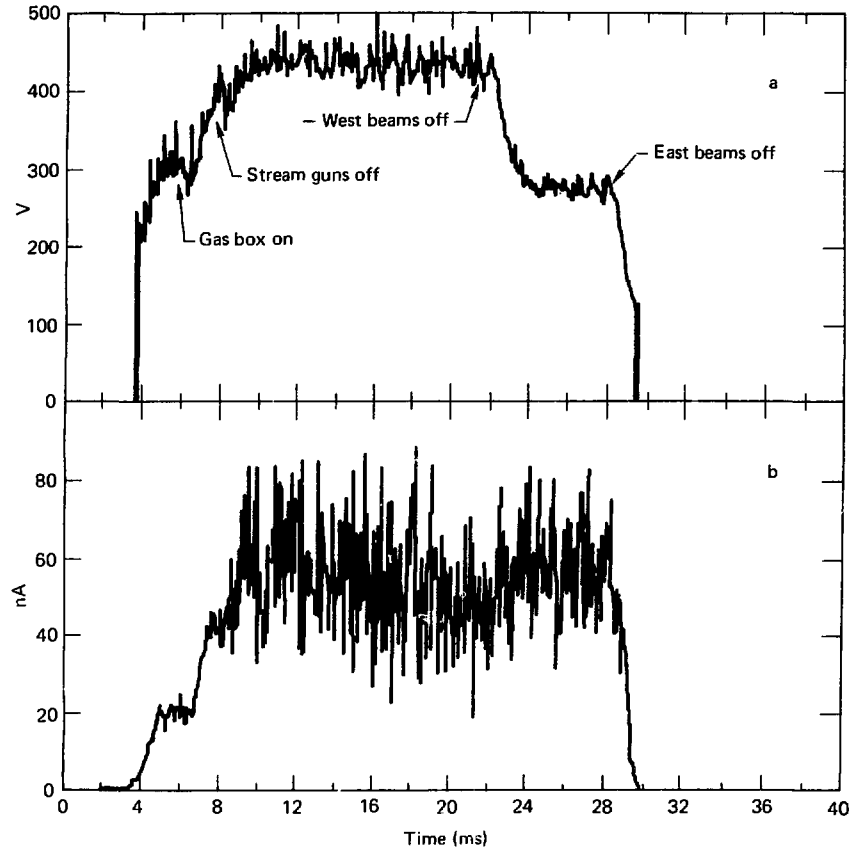

FIG. B-12. Typical HIBP temporal profiles of the central cell at r = 0: (a) space potential, (b) secondary ion current.

calibration parameters, not yet included in the data processing, could introduce an error as large as 100 V at large radii. Separating the spatial and/or temporal behavior of radial oscillations is not possible with the sweep rate used in this shot (about 3.6 cm/100 μs). Data from faster and slower scans as well as the effect of a lower signal-to-noise ratio at the plasma edge is being investigated.

Fluctuations in the central-cell space potential and secondary ion-current level [$\propto nf(T_e)$] are expanded in Fig. B-15. The data are from shot 43 on September 26, 1980; the centerline (r = 0) values were monitored as a function of time. Well-defined oscillations are evident, occurring in bursts with a time scale of about 1 ms. Spectral analysis indicates a large 12-kHz component, as well as other frequencies, with strong coherency within a burst. Fluctuations with similar-frequency components are observed at all radial locations.

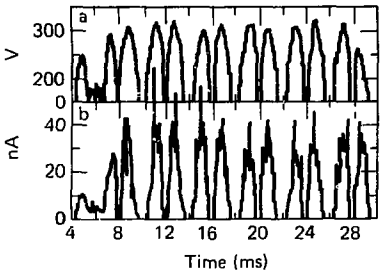

FIG. B-13. HIBP central-cell space potential (a) and secondary ion current (b) for multiple radial scans during a typical TMX shot.

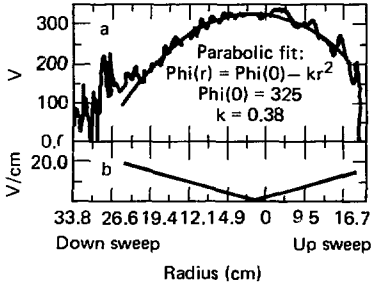

FIG. B-14. A typical HIBP radial profile of the central-cell space potential and electric field at an average time of 19 ms.

The amplitude of potential fluctuations is about 30 V, yielding $\tilde{\phi}/\phi \sim 10\%$ but $e\tilde{\phi}/kT_e \sim 1$. The $nf(T_e)$ fluctuation amplitude is about 50% of the total $nf(T_e)$ signal and is probably dominated by density fluctuations.

B2.7 End-Wall Flux Diagnostics

(C. V. Karmendy, Jr., and E. B. Hooper, Jr.)*

Diagnostics were mounted on the end walls to measure the magnitudes and profiles of the ion flux from the machine, the net current reaching the end walls, and the power density reaching the end walls. The net electron flux to the end walls is obtained by subtracting the net current per unit area from the ion flux. The fluxes are used in determining particle and power balance and in calculating radial transport fluxes.

The diagnostics were mounted in arrays across the narrow part of the end fans. The inner three (of thirteen) Faraday cups (with suppressors) are shown in Fig. B-16. Mounted between the cups are thin copper disks that were used as net-current collectors (disk at ground voltage) and as calorimeters. In Sections 7 and 9, the outputs of these detectors are presented as functions of the radii and areas projected along field lines from the plug centers.

An additional Faraday cup and disk could be mounted on any desired end port to obtain data at other azimuths.

Comparison of the current density measured by a Faraday cup (FC) and by the east ELA yielded $j_{FC}/j_{ELA} = 0.68 \pm 0.15$. The uncertainty includes 0.14 standard deviation, and a possible systematic error of 10% (5% from hole diameter and 5% from load resistor and scope calibration). The statistical and systematic errors are combined as rms.

B2.8 End-Wall Emitting and Collecting Probe Array

(P. Coakley and G. D. Porter)*

The end-wall plasma-diagnostics array (Fig. B-17) consisted of two emitting probes, one 2 cm and the other 10 cm from the east end wall; two collecting probes, also at 2 and 10 cm from the wall; and seven button collecting probes in the plane of the wall. The probe array was recessed approximately 15 cm from the main-chamber end wall and could be valved off from the machine with a gate valve. The probes were positioned in the midplane of the mirror fan and mapped into a point 4.5 cm from the axis at the plug midplane. The emitting probes, which were designed at the University of Iowa,[6] were used to measure the local plasma potential and the collecting probes were used to measure the electron distribution (a localized measurement if the potential of the surrounding plasma is relatively uniform). The magnetic field at the wall where the probes were located was 70 G.

*Deceased.

*University of Iowa, Iowa City, Iowa.

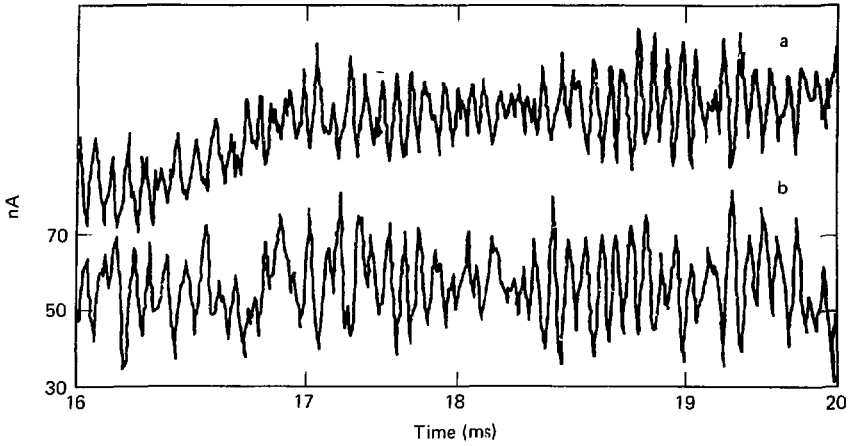

FIG. B-15. Temporal fluctuations of the central-cell (a) space potential and (b) secondary ion current, nf(T_e), at r = 0 measured by HIBP. A dc offset is present in both of these plots. The strongest frequency component is 12 kHz.

The emitting probes consisted of 0.0025-cm-diameter tungsten filaments, approximately 2 cm long, that were heated white hot (to a wire temperature, T_w, of about 0.3 eV) to boil off electrons. Each emitting probe had a getter shield, with the filament extended 0.4 cm beyond it. The shields were biased at various negative and positive voltages within ±20 V of ground. In general, when the probe is negative with respect to the local plasma potential, it emits electrons into the plasma; when the probe is positive with respect to the local plasma potential, it does not emit electrons. The current-voltage characteristics of a swept emitting probe provide a definitive way to determine the local plasma potential. If the floating potential (the potential at which a probe draws no net current) of a cold probe is more negative than the local plasma potential, then a floating hot probe will provide a measure of the plasma potential to within several wire temperatures, about 5 T_w/e, where e is the electron charge. The emitting probes were heated and allowed to float, and the potentials at which they floated were monitored.

Two types of collecting probes were used at the positions 2 and 10 cm from the wall: 2-cm-long, 0.09-cm-diameter cylindrical probes (shown in Fig. B-17) and 0.95-cm-diameter disk (button) probes, with the plane of the disk oriented normal to the local magnetic field lines. The collecting probes also had getter shields.

The cylindrical probes' small size (the cylinder's radius was less than the local Debye length) allowed relatively nonperturbing measurements of the local plasma characteristics, but it also resulted in large uncertainties in plasma parameters. The disk probes provided better current-voltage characteristics because they were larger, but had the disadvantage that they shadowed the wall. The disk probe radius was 0.47 cm; the cold-electron and hot-ion gyroradii were 0.09 and 1.7 cm, respectively. Thus the region between the disk probe and the wall is filled with hot ions and, perhaps, secondary electrons with approximately the same density. The disk probes therefore permitted more detailed measurements of the plasma flowing from the plug, but provided poorer information about the plasma coming from the wall.

To simplify the interpretation of data collected by the disk probes, each of them was coated with ceramic on one side. The disk probe at 2 cm was

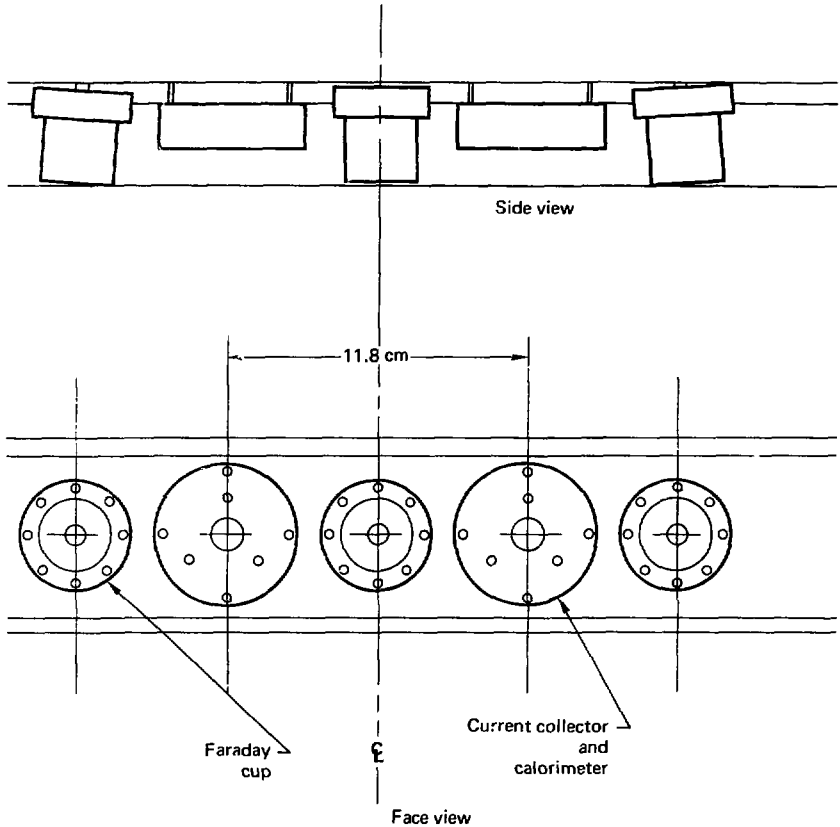

FIG. B-16. An array of end-wall-flux diagnostics showing the center three (of thirteen) Faraday cups and the center two (of twelve) disks used for net current collection and power collectors. The Faraday cups are oriented along the magnetic field lines. The entire array is enclosed within a metal shield to exclude currents leaking from the plasma and to protect against gettering.

coated on the side that faces the wall so that it detected only the plasma that flowed from the plug; the disk probe at 10 cm was coated so that it detected only plasma coming from the wall.

The emitting probes indicated a plasma potential with a characteristic value of approximately 8 V, measured at 2 and 10 cm from the wall. The wall was at zero volts and the potential in the plug varied from 300 to 1000 V. The collecting probes indicated a cold plasma present near the wall, with an electron temperature of about 5 eV and a cold-electron density of about 2×10^9 cm^{-3}, while the hot-ion density at the wall was about 6×10^8 cm^{-3}. The density of electrons in the plug was about 2 ×

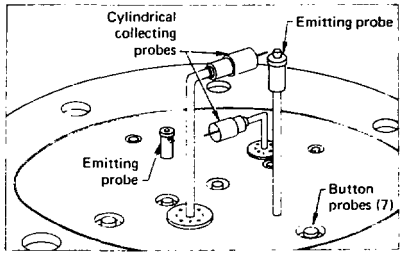

FIG. B-17. The end-wall emitting and collecting probe array.

10^{13} cm^{-3}. The electron temperature measured at the wall was decoupled from the temperature of electrons in the plug and the central cell. The plasma wall sheath was established to balance the flux of hot ions and cold electrons. An additional species of electrons, secondary electrons produced at the end wall, was also identified. These secondary electrons had a directed energy comparable to the local plasma potential, an energy spread of less than 7 eV, and a density of about 4×10^8 cm^{-3}.

B2.9 Radio-Frequency (rf) Probes

(T. A. Casper, D. P. Grubb, and P. Poulsen)

The TMX diagnostics for rf studies are shown in Fig. B-18. This complex diagnostics array reflects the diversity of frequency, wave number, and location of the plasma instabilities that might exist in TMX.

The west end-cell probe was a 5-tip array of high-impedance probes identical to the east-plug array except that the separation between the fourth and fifth tips (4 cm) was greater than that between the first four tips (1 cm). This gave a maximum spacing of 7 cm (tip 1 to 5) for resolution of $|k|$ due to long wavelength perturbations. This probe's location was approximately equivalent to that of the east probe, which allowed for a direct comparison of the relative stability of the end-cell plasmas. The two central-cell probes consisted of eight tips each—six high-impedance probes to observe electrostatic fluctuations and provide perpendicular wave number measurements, and two magnetic pickup loops oriented to be sensitive to $\dot{B}_\theta$ and $\dot{B}_r$. These probes were located at $z = \pm 150$ cm and could move radially along the $\theta = 45°$ azimuthal line on the upper north side of the central cell. The central-cell probes observed fluctuations near the plug cyclotron frequency, and were intended to provide perpendicular wave number measurements, $k_{\perp}$, for comparison with plug values. Their axial locations were intended to give rudimentary information concerning the mode structure of parallel waves in the central cell. A magnetic pickup probe consisting of three loops, $\dot{B}_r$, $\dot{B}_\theta$, and $\dot{B}_z$, was installed to investigate the electromagnetic character of modes observed in the east end-cell.

If every detector shown in Fig. B-18 was monitored, a minimum of 57 data records on every shot (about 225K words of data per shot) would be generated. However, because of limitations in electronic equipment, we were able to monitor only a few selected channels for most of the experiments. Table B-4 lists the probes normally monitored. The signals from these diagnostics were amplified (from bandwidth 3 kHz to 300 MHz) before they were analyzed. Each signal was fed into a peak-envelope detector so that the fluctuations in power could be measured as a function of time. This signal was sampled every 0.01 ms for the duration of the plasma. A shorter record of each of the signals was also stored in faster transient recorders, this allowed us to analyze the frequency of the recorded signals from 3 kHz to 25 MHz.

B2.10 Secondary Emission Detectors

(T. C. Simonen)

Secondary-emission detectors (SED's) were located at the midplane of each end plug. These simple and reliable detectors were used to guide machine operation, monitor system timing, estimate plug density, and estimate neutral density surrounding the plasma.

The SED design is shown in Fig. B-19. Charge-exchange atoms that strike the detector cone release secondary electrons. Ultraviolet light also releases secondary electrons, but tests on 2XIIB indicated that the charge-exchange component dominated. The charge-exchange current incident on the detector was proportional to the product of neutral-atom density, ion density, and angular distribution function in the direction of the detector. These detectors viewed a cone that is perpendicular to the magnetic axis. During neutral-beam injection, most of the neutral particles present were the atoms of the beam. In this case the SED signal was

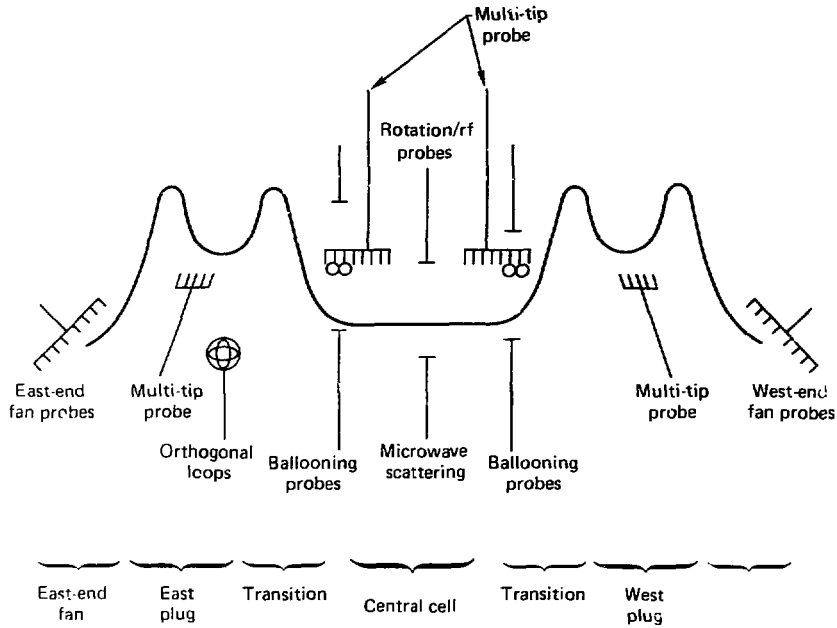

FIG. B-18. Location of the rf probes.

TABLE B-4. Radio-frequency diagnostics usually monitored.

Diagnostic	Parameter measured	Information gained
2 tips of east 5-tip probe	$\tilde{\phi}$	(1) rf envelope at ω_{cip}, $2\omega_{cip}$, and broadband for 41 ms (2) frequency spectra for 41 μs (3) wavelength estimate
2 channels of east-end-fan probe array	$\tilde{\phi}(r)$	Broadband rf envelope for 41 ms at two selected radial positions and frequency spectra at these positions for 41 μs
2 channels of central-cell probe array	$\tilde{\phi}$	Frequency spectra for 41 μs, and low frequency (<1 MHz) spectra for 512 μs
1 central-cell midplane, pick-up disk probe	$\tilde{\phi}$	Broadband rf envelope for 41 ms and frequency spectra for 41 μs
3 channels of central-cell pickup disks	$\tilde{I}$	Low frequency ($f < 30$ kHz) oscillations in central cell near midplane for 41 ms
4 channels of ballooning pickup disks	$\tilde{\phi}_{transition}$	Low frequency ($f \lesssim 30$ kHz) oscillations in these regions
1 tip of west 5-tip probe	$\tilde{\phi}$	(1) rf envelope at ω_{cip}, $2\omega_{cip}$, and broad band for 4 ms (2) frequency spectra for 41 μs
2 channels of west-end-fan probe array	$\tilde{\phi}(r)$	Same as east-end-fan array

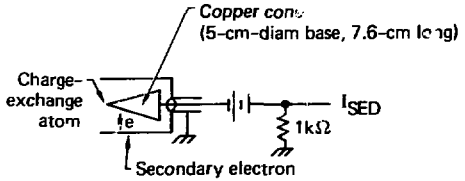

FIG. B-19. Secondary-emission detector (SED).

proportional to the product of neutral-beam current and ion density. When the neutral beams were turned off, most of the neutrals present came from background gas impinging on the plasma surface. In this case the signal was proportional to the background gas density. By turning the neutral-beams off rapidly, we could determine the amount of charge-exchange current due to background gas by normalizing the SED signal to the value obtained during beam injection, when the charge-exchange current could be calculated fairly well.

B2.11 Neutron-Yield Measurements

(D. R. Slaughter)

Two time-resolved neutron-yield monitors were installed on TMX, one on each end plug (Fig. B-20). The design and calibration of these detectors (Fig. B-21) are described in Ref. 7. Each recoil proton detector consists of a liquid-hydrocarbon scintillator (NE213). The difference in their fluorescence decay time was used to discriminate neutron- and photon-induced scintillations. The light output was also pulse-height analyzed during some runs to obtain the energy spectrum of recoil protons. These data were then unfolded to obtain the neutron-energy spectrum at the detector location. That allowed us to determine the contribution of scattered neutrons at the monitor location and thus determine the background under plasma-source conditions. As a result, absolute neutron yield could be measured on each end plug with estimated errors of ±15%.

Each monitor was calibrated absolutely by using a 2.45-MeV neutron source at the RTNS-I facility at Livermore, and the change in calibration introduced by scattered neutrons in the TMX environment was determined by a neutron-energy spectrum measurement on TMX. In addition, the background radiation (due to nearby neutral-beam-ion dumps) and the charge-exchanged neutrals that strike the vacuum walls have been found equivalent to less than 5×10^9 neutrons per second produced at plasma center.

Absolute neutron-yield measurements have been used in conjunction with line-density and plasma-length data to determine σv in the end-plug plasmas. Since σv is a rapidly rising function of the ion energies (at least 3rd order), $\overline{W}_i$ may be determined from σv with only slight dependence on the model assumed for the ion-energy distribution. This calculation was carried out for selected shots on both end plugs.

Figure B-22 shows neutron spectra measured on July 17, 1980, at the east and west plugs. Spectral intensity in these data shows that scattered neutrons contribute approximately 40% of the neutron intensity above 1.0 MeV. The energy threshold established for counting was normally 1.0 MeV, in order to partially suppress the monitor's response to scattered neutrons.

The dispersion in the peak of a fusion-neutron spectrum is due to the Doppler effect resulting from center-of-mass motion of the reacting ions. For D-D fusion, the spectral width due to Maxwellian motion is E_n (FWHM) = $82.7\sqrt{T_i}$ (keV), where T_i is the ion temperature in keV. Since the instrument line shape has a width FWHM of approximately 200 keV in these data, the broadening due to $\overline{W}_i$ in the range 4 to 7 keV is not sufficient to provide an unambiguous measurement of $\overline{W}_i$ directly. However, the observed spectral width is consistent with $\overline{W}_i$ inferred from the yield.

B2.12 Vacuum Gauges

B2.12.1 Fast Ion Gauges. *(A. L. Hunt)* The fast ion gauges were of the now-conventional Bayard-Alpert, nude-ion gauge design. The term "fast" refers to the speed or frequency response of

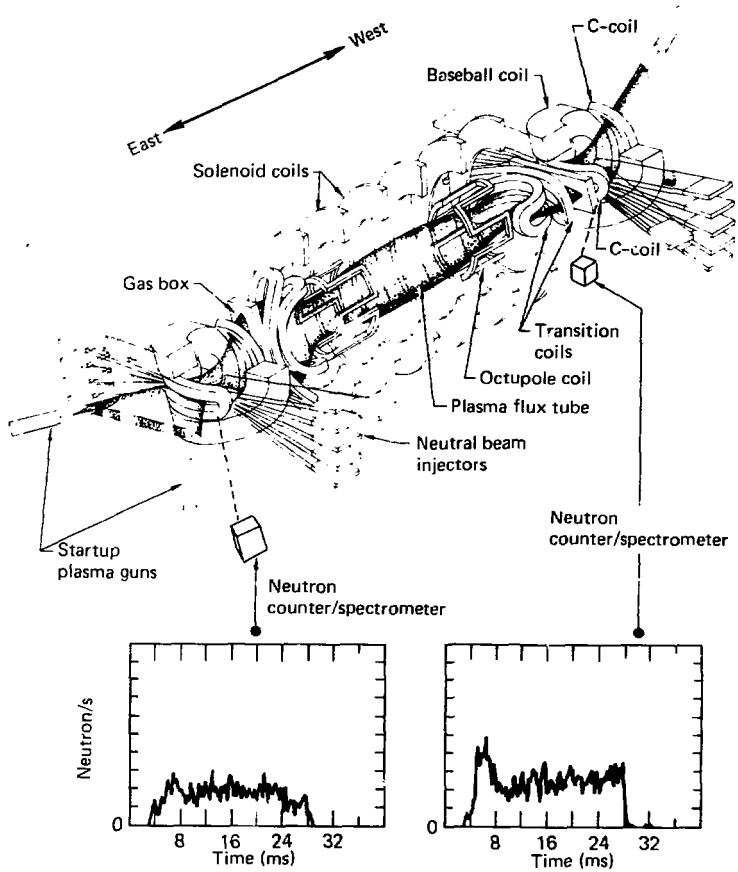

FIG. B-20. Location of the neutron diagnostics in TMX and some typical results of neutron yield measurements.

the collected ion-current amplifiers. The high-speed or during-shot-time resolution resulted in a low pressure sensitivity, so measurements were not possible at pressures much less than 10^{-5} Torr. These gauges were installed in the central-cell region, at locations depending on the central-cell configuration. The gauges were operated with the central-cell fields nominally at 5×10^{-2}, 10^{-1}, and 2×10^{-1} T. The gauges were very sensitive to the 2×10^{-1} T field but the results were usable at the lower central fields of 5×10^{-2} and 10^{-1} T.

B2.12.2 Penning Discharge Gauge. *(G. W. Leppelmeier and G. E. Davis)* A Penning discharge gauge was installed on the west end of TMX. The basic gauge consists of a cylinder with two plates slightly separated from the ends of the

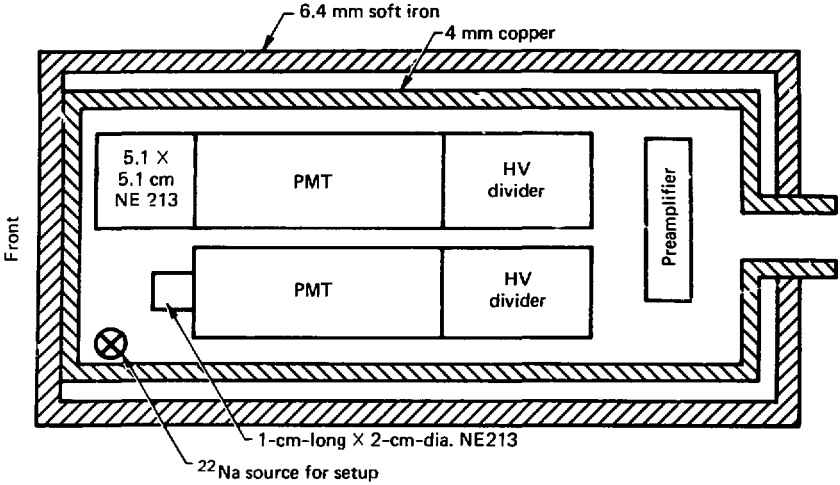

FIG. B-21. A TMX neutron monitor. The neutron detectors are enclosed within a copper rf shield and a soft iron magnetic shield so that the stray 0.01-to-0.02-T magnetic field and the transient rf fields do not affect the enclosed photomultiplier tube (PMT).

cylinder. The cylinder is held at a positive voltage (about 3700 V) with respect to the end plates. A plasma discharge is created (by stray electrons) along the axis of the cylinder. The plasma density is proportional to the gas density in the discharge region. Diffusion across the magnetic field lines, which are parallel to the axis of the cylinder, supplies a current flow between the end plates and the cylinder. The current measured at an instrument some distance away will include this ion-drift current. There are a number of spurious effects that can also contribute to the measured current.

Once formed, the plasma may oscillate in a number of modes that may have discrete or continuous frequency distributions. Any change in modes can cause a change in ionization efficiency because of changes in the spatial distribution of current density. In the present gauge design, the inhomogeneous magnetic field of the C magnet employed appears to have eliminated the pressure-dependent mode effects that are present in uniform fields.

The gauge was constructed by modifying a 2-l/s ion pump (Fig. B-23). The pumps come supplied with titanium structures that are sputtered by the discharge onto the interior surfaces of the pumps. These free, active titanium atoms chemically pump active gases. To use these pumps as gauges, it was necessary to remove the titanium, hence reducing the pumping action that would affect the measured ion currents. The modification consisted of removing the magnetron cathode assembly and remachining the endplates to preserve the original geometry. This conversion resulted in a stainless-steel Penning discharge gauge suitable for ultra-high vacuum applications. Tests have shown the current of this gauge to be linear, with pressure in the range 10^{-5} to 10^{-7} Torr. A typical plot is shown in Fig. B-24.

B2.13 Ultraviolet-Spectroscopy

B2.13.1 Normal-Incidence Survey Spectrograph. *(R. Fortner, D. Dietrich, and T. Nash)* Survey spectrographs were used to identify the most important impurities in the plasma. The normal-incidence spectrograph was a commercial vacuum spectrograph equipped with a 35-mm film cassette (see Fig. B-25). It had a 1.0-m focal length

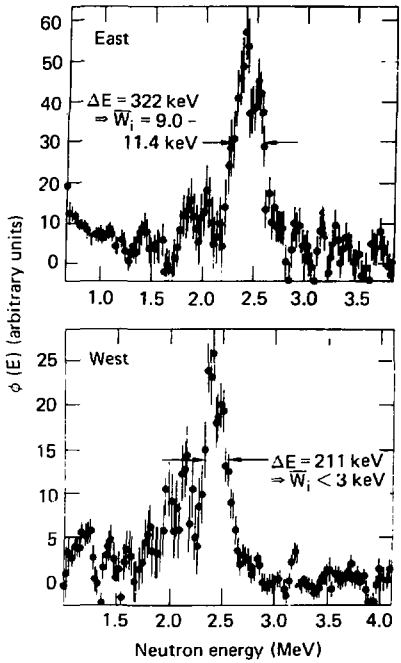

FIG. B-22. Neutron-energy spectra measured at TMX end plugs. The data were accumulated during 30 shots on July 17, 1980.

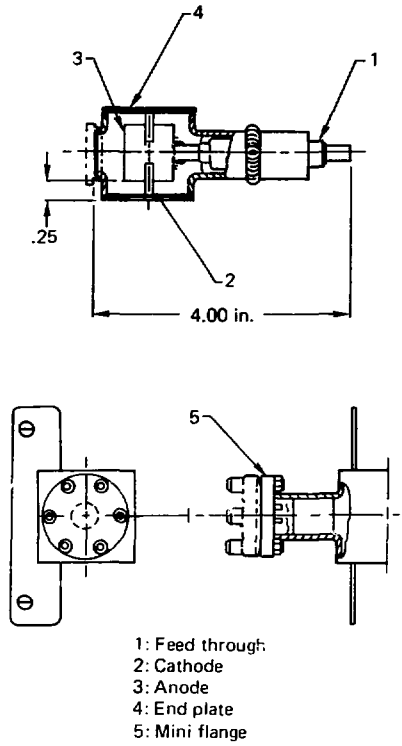

FIG. B-23. The 2-l/s ion pump that was modified for use as a Penning gauge.

and an f/50 (horizontal) by f/11 (vertical) field of view; external baffles and a vacuum beam line permitted a ±12-cm vertical view (along the radius) of the plasma and a ±12-cm horizontal view (along z). This spectrograph was located on the north side of the TMX central cell at z = 0.

Two gratings were used in the survey instrument to cover different wavelength regions. A 1200 gr/mm grating, blazed at approximately 1500 Å (the peak of the efficiency curve is at the blaze wavelength in first order) gave a useful spectral range of 250 Å to 3000 Å with a 0.1 Å resolution; a 600 gr/mm grating, blazed at 5000 Å, covered from 250 Å to 6000 Å with 0.2 Å resolution. UV sensitive film in 35-mm cassettes was used to record the spectrum; typically 800 Å would fit on the film for each exposure. A movable baffle was used to select various sections of the film so that several exposures could be made on a single piece of film.

A hollow-cathode, platinum-lamp source[8] was mounted on the beamline of the instrument; a 45°-mirror could be inserted into the beamline so that the well-known platinum spectrum could be recorded. By moving the baffle, a platinum spectrum could be recorded on the same piece of film as the spectrum from the plasma, thus allowing accurate determination of wavelength and instrumental resolution. (See Table B-5 for a summary of the instrument's parameters.)

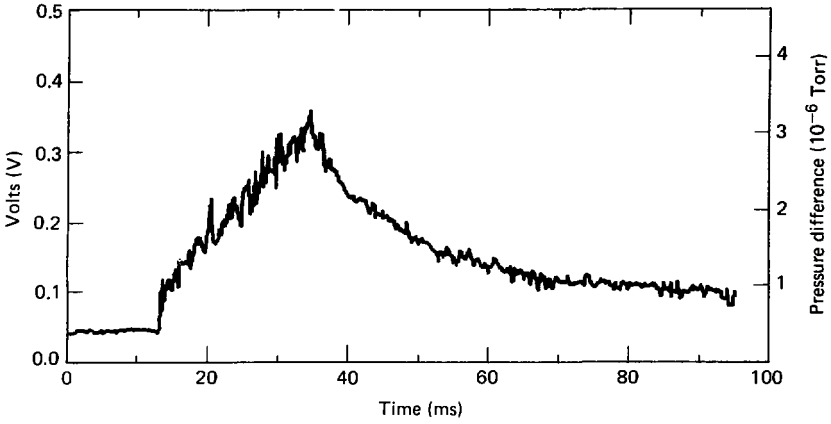

FIG. B-24. Typical data from the Penning discharge gauge during a TMX shot.

B2.13.2 Grazing-Incidence Survey Spectrograph. *(R. Fortner, D. Dietrich, and T. Nash)* A commercial grazing-incidence spectrograph was used to survey the wavelength region from 50 to 2000 Å, with special emphasis on the short wavelength (50 to 250 Å) region not covered by the normal-incidence instrument. A 300 gr/mm grating mounted at an 82° angle of incidence and blazed at 400 Å was used in the 2.0-m-focal-length spectrograph; the f-number was f/50, which provided a 2-cm field of view. The instrument's resolution was approximately 1.0 Å. UV-sensitive plates were used to record the spectrum. This instrument was also located on the central cell (although not at the same time as the normal-incidence survey instrument).

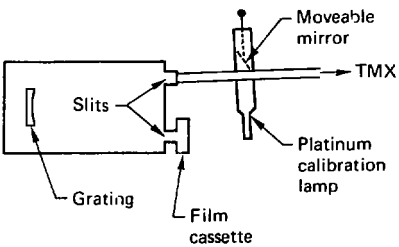

FIG. B-25. Diagram of the normal-incidence UV survey spectrograph.

B2.13.3 Absolutely Calibrated Single-Channel Monochromator. *(O. T. Strand* and S. L. Allen)* An absolutely calibrated, single-channel monochromator was used for initial measurements on the central cell and, later, the west plug. This same instrument was used for impurity studies on the Alcator A Tokamak[9,10] and 2XIIB.[11] It was developed by Johns Hopkins University, and its operation is discussed thoroughly elsewhere.[12] In summary, it is a 0.4-m-focal length, normal-incidence monochromator that has been absolutely calibrated in both wavelength and flux. The absolute calibration was performed at Johns Hopkins University and is traceable to the National Bureau of Standards. The 510-W, windowless photomultiplier is used in the analog mode, with a practical time resolution of 70 μs. The instrument's resolution is approximately 0.2 Å, but most experimental conditions required only 1 to 2 Å resolution. The system was equipped with

*Johns Hopkins University

TABLE B-5. Diagnostic instruments for measuring plasma UV in TMX.

	Normal-incidence survey	Grazing-incidence survey	Single channel	22 Channel (two)
Spectral region (Å)	250–3000[a] 250–6000[b]	50–2000	300–1700	300–1700[c] 300–1200[d]
Spectral resolution (Å)	0.15	1.0	0.15[e] 1[f]	0.2[e] 1[f]
Time resolution	–	–	70 μs	125 μs
Spatial scanning	–	–	Shot-by-shot	Single-shot
Spatial resolution (radial)	–	–	–	1.6 cm[c] 0.7 cm[d]
Calibration	(g)	(g)	Absolutely calibrated	Absolutely calibrated
Detector	Film	Film	Photomultiplier	Microchannel plate
Location	Central cell	Central cell	West plug	Central cell/east plug

[a]1200 gr/mm grating.

[b]600 gr/mm grating.

[c]Central-cell instrument.

[d]East plug instrument.

[e]Maximum instrumental resolution.

[f]Typical resolution used in experiment.

[g]Estimated by cross calibration with calibrated instruments.

magnetic, electric, and radiation shielding and has its own pumping system capable of maintaining a pressure of less than 10^{-8} Torr. A remote-control tilting mechanism allows shot-by-shot spatial scanning of a single spectral line.

B2.13.4 Absolutely Calibrated 22-Channel Monochromator. *(O. T. Strand* and S. L. Allen)* A 0.4-m monochromator similar to that discussed in the previous section was modified, and a spatial imaging detector system[13] (SIDS) developed by Johns Hopkins University was added, so that 22 chords of the plasma could be observed simultaneously (see Fig. B-26). The SIDS allows acquisition of a UV image of the plasma every 125 μs. It should be noted that other imaging systems used on pulsed-plasma machines have used a rotating mirror, which requires about 5 ms for a spatial scan. Because the total duration of the TMX plasma is approximately 25 to 30 ms, only a few spatial scans could be performed with this technique. In addition, these chords are not measured simultaneously, so this method is useful only in steady-state situations.

Because the SIDS system has been thoroughly described elsewhere,[13,14] only a short general description will be presented here. Imaging is accomplished by using the entrance slit as a one-dimensional analog of a pinhole camera; each position A in the plasma has a corresponding point

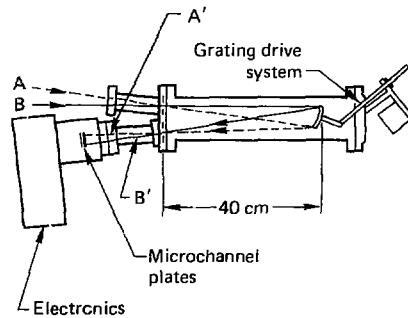

FIG. B-26. Diagram of the 22-channel, grazing-incidence, UV spectrograph.

*Johns Hopkins University

A′ on the detector. The desired wavelength is selected by rotating the grating (using a remote-control grating drive), directing a monochromatic image of the plasma onto the detector.

The SIDS detector system consists of a pair of microchannel plates (MCP's) in a chevron configuration. The MCP's are in essence millions of photomultipliers. Twenty-two discrete anodes are placed behind the MCP's to collect the charge. Each anode has a pulse-amplifier discriminator (PAD) and a counter. The data are stored by transferring them from the counters to a computer via direct memory access. Two such instruments were used on TMX, and a system was developed so that both instruments could be controlled from a single computer. Data from both instruments were displayed and recorded on magnetic tape between shots. In addition, Abel or matrix inversions of the radial brightness profiles could be performed.

Table B-5 summarizes the major characteristics of the instruments.

B2.13.5 Location of the UV-Spectroscopy Instruments on TMX. *(O. T. Strand* and S. L. Allen)* Figure B-27 shows the location of spectroscopic instruments on TMX. Each survey spectrograph was located on the north side of TMX at z = 0 in the central cell and viewed a horizontal chord.

The single-channel monochromator was used from July 1979 to January 1980 to measure the central-chord brightness of impurity emissions in the central cell. In January of 1980, a 22-channel monochromator was mounted on the east plug. In March of 1980, this instrument was moved to the central cell, where it viewed the plasma from above. (At the same time, the single-channel instrument was moved to the west plug.) Approximately 37 cm of the plasma were imaged on a single shot with 1.65-cm spatial resolution; two shots were required to obtain a complete radial scan of both halves of the plasma. Typically, more shots (3 to 4) were used with overlap between the radial scans to insure reliable data and to detect any shot-to-shot variations. Both halves of the plasma were measured to determine if asymmetries in the emission were present.

In April of 1980, a second 22-channel instrument was supplied by Johns Hopkins University. This instrument was similar to that owned by LLNL but was designed for the high counting rates encountered in tokamaks, hence it was suited for use on the plug where the brightnesses are usually greater. Figure B-27 shows the placement of the four instruments in the final configuration of the experiment: (1) a 22-channel (high count rate) instrument on the east plug, capable of imaging the plug plasma in one shot; (2) a 22-channel instrument on the central cell, capable of imaging half of the plasma; (3) a single-channel instrument on the west plug, capable of shot-to-shot scanning and (4) a survey instrument on the central cell, which integrates several shots.

B2.14 Visible-Light Spectroscopy

B2.14.1 Spectral Survey of the Central-Cell Plasma. *(A. M. Frank, C. A. Anderson, and M. P. Paul*)* An electronic spectrograph covering the range 370 to 690 nm was used to survey the visible-light spectra of the TMX central cell. The plasma was viewed through a 6-in.-diam achromatic lens directed up through the central cell one pitch west of center. The spectrometer used a modified half-meter monochromator, and the signal was detected with a microchannel-plate (S-20 photo cathode) coupled through a phosphor to a linear array of 1024 silicon diodes. The array was read in 5 ms by a microprocessor with a 10-bit A/D converter. Background levels were subtracted by the microprocessor and data were sent to a video display. Data could also be sent to an x-y plotter or to punched tape. Punched-tape data were smoothed and plotted by another computer system.

Using a 600-gr/mm grating in the first order, the system covered 500 Å with a resolution (intensifier-limited) of 30 Å. Wavelength calibration with a mercury source and known deuterium lines allowed spectral calibration to better than ±5 Å.

Figure B-28 shows a composite of 10 spectra covering the spectral range of the instrument. Integration time was 25 ms when the data were taken. Note that the double peaks of D_α at 464 nm are fluctuations from the computer smoothing of the saturated detector. Also note that the individual spectra used in the composite were taken over two

*Johns Hopkins University

*Alcorn State University, Lorman, MS.

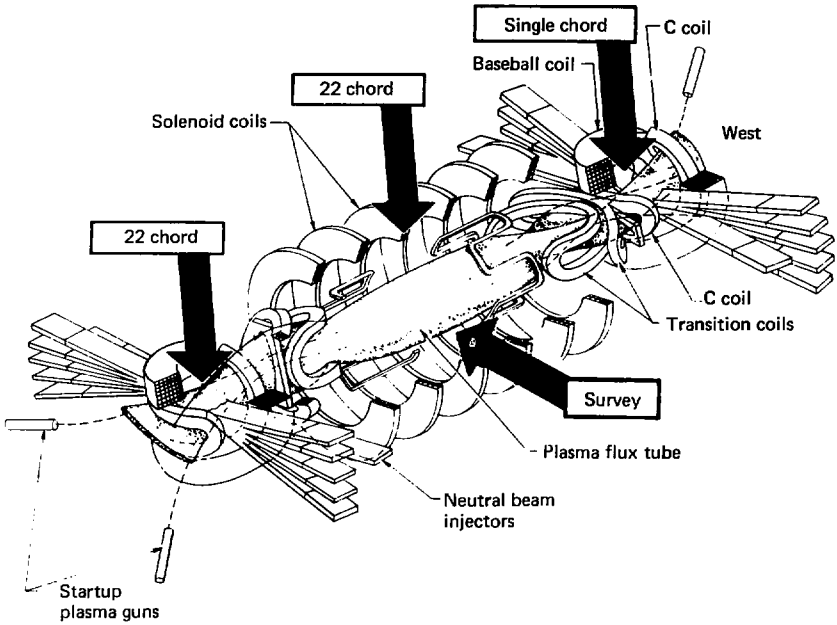

FIG. B-27. Location of UV diagnostics on TMX.

days running of TMX with varying machine conditions. Consequently the intensities of lines in the composite can only be compared when they occur in the same individual spectrum.

The results of the survey indicate the presence of molecular N_2 bands at λ = 646.8 and 678.8 nm. The brightness of these lines was correlated with the N_2 level of the residual-gas analyzer (RGA). The band at 646.8 nm was the strongest, up to 10% of the D_α emission. The D_α and total light emissions from the east-plug plasma were also monitored through the optics of the Thomson-scattering system.

B2.14.2 Doppler Broadening of Visible Light. *(A. M. Frank)* The instrument for measuring Doppler broadening of visible light sampled the central cell 60 cm west of center. A 300-mm-diam lens focused the plasma light through a spectral line filter onto a 1-mm field stop. A second lens collimated the light before it passed through the Fabrey-Perot etalon into the photomultiplier tube as shown in Fig. B-29. The etalon was scanned piezoelectrically at a rate of 2.5 to 3 ms per free-spectral range. The plate spacing of the etalon was 0.2 mm, giving a free-spectral range of 5.49 Å at 4686 Å. The instrument line width was determined by scanning the 4880 Å line of an argon laser. The line width was dependent on aperture and scan rate, and degraded rapidly at sweep times less than 2 ms. At 3 ms per free-spectral range and for a 1-cm aperture, the finesse of the etalon was 8.25, giving an instrument line width of 0.67 Å. The instrument width was subtracted in quadrature from the measured line widths. The minimal resolvable Doppler temperature for the helium He II line width was 15 eV and for the hydrogen H_β line width was 7 eV.

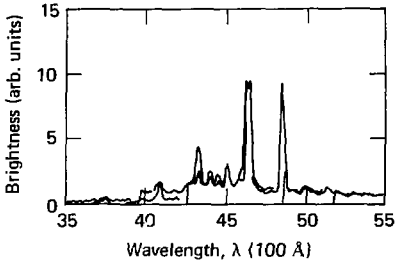

FIG. B-28. Composite spectrum of visible emission from the central cell taken over two days of running.

The Doppler full width between the two half-maximum-intensity points (FWHM) of the spectral emission line is given by:

$$\Delta\lambda_{1/2} = 7.16 \times 10^{-7}\ \lambda(T_i/A)^{1/2} \quad ,$$

where

λ = wavelength of the observed transition in Å,

T_i = temperature of radiating species in K,

A = atomic weight (2 for deuterium).

The Doppler width was measured in the TMX center cell by scanning across an emission line with the Fabrey-Perot etalon. Measurements of helium 4686 Å, He II (He II ionization potential, 54 eV) line widths gave temperatures up to 95 eV (November 29, 1979), whereas deuterium 4861 Å, D (deuterium ionization potential, 13.6 eV) gave 33 eV (December 5 and 6, 1979). These temperatures are in the expected range.

B2.15 X-Ray Instruments

B2.15.1 Time-Integrated X-Ray Cameras. *(C. A. Anderson)* Time-integrated photon images were obtained with multiple-image pinhole cameras located on the west plug and central cell. Schumann-type film in these cameras recorded up to eight images per shot through different filters.

The contour plot of the brightness of the west plug shown in Fig. B-30 is as expected and agrees with similar data from 2XIIB. The radial profile (inverted brightness) of the central cell also shows the expected hot core. These data were obtained from images which were recorded through 4000-Å to 10,000-Å beryllium and carbon filters. The relative brightness of the images through the different filters indicates that they were produced by 50-eV to 100-eV photons. Other TMX diagnostics indicate that these images may be produced by line radiation from O_V and O_{VI}. These data provide information about the symmetry and uniformity of the hot plasma.

B2.15.2 Time-Resolved X-Ray Camera. *(H. A. Koehler, L. B. Olk, and C. E. Frerking)* An imaging system that provides high sensitivity, time resolution with a 1-ms frame rate, and instant data display was used on the central cell. This system consisted of a camera with a 50 × 50 array of photodiodes, high-speed memory, and a microprocessor. It had a pinhole, filter fiber-optic (FO) coupler, microchannel plate intensifier (MCPI), and FO reducer (reduction was 2.5:1). The 15-mil-diam pinhole provided 1.9-cm resolution at the plasma location (pinhole-limited). The camera (Fig. B-31) had a 55-cm-diam field of view located slightly west of the midplane of the central cell of TMX.

The spectral region recorded could be selected by installing Be (0.4, 0.8 μm), Al (0.2, 0.4 μm), or LiF filters in the filter wheel (five locations were available). A light-emitting diode (LED) was used in dry runs to check the proper operation of the system; it occupied one of the openings in the filter wheel. A layer of sodium salicylate on the FO coupler converted x rays and UV photons to visible photons (approx 4500 Å) at a relatively high and uniform quantum yield (10%). The MCPI, with an S-25 photocathode and P-46 anode, provided a gain of approximately 150 with no loss of spatial resolution. The FO reducer coupled the 18-mm-diam MCPI to the 0.5 × 0.5-cm, Si-photodiode array. The variable gain of the MCPI (1 to 10^6) greatly enhanced the UV/x-ray sensitivity of the imaging system.

The camera was calibrated in digital values (counts) versus energy per pixel or resolution element. Also, the exact field of view of the camera was measured for the central cell.

The images obtained with the camera were digitized (3.3 MHz) and stored in a large, high-speed memory. Exposure time, number of exposures, and the start of the first exposure could be

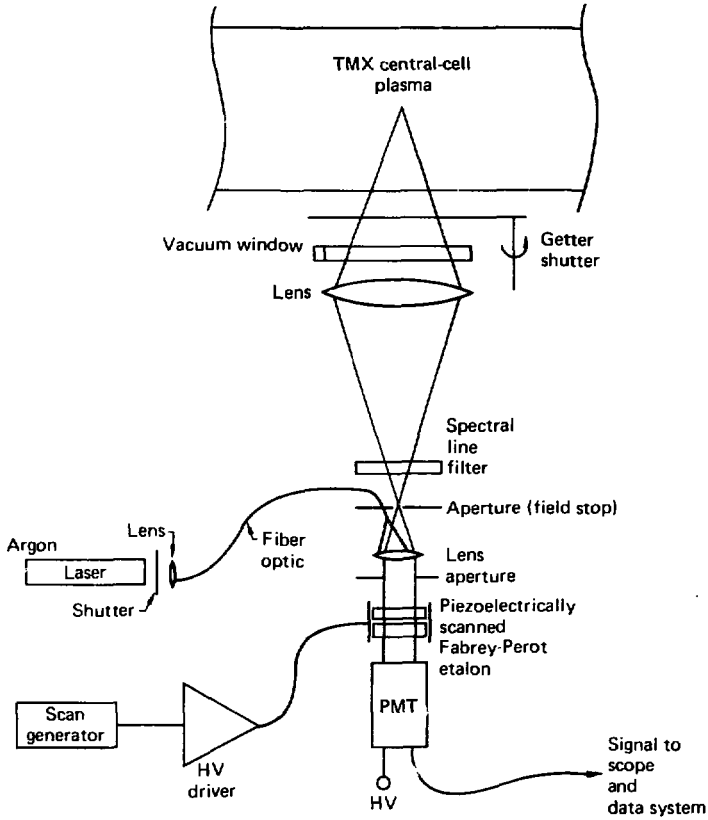

FIG. B-29. Diagram of the diagnostic for Doppler broadening of visible-light.

varied. The minimum exposure time (temporal resolution) was determined by the time gate of the MCPI. The minimum framing time and thus the maximum number of frames was fixed by the readout time of the photodiode array, i.e., 0.9 ms. The memory could store 45 images.

A local microprocessor could process and display the data instantly. Raw data and data with the background subtracted (background frame taken at −5 ms) could be presented as dot plots, frequency plots (histograms), and intensity plots (row/columns). Ordinarily, the intensity was scaled automatically in 36 steps. Any one to four frames could be selected from memory and stored on a floppy disk for future reference. The data stored on floppy disks could then be further processed on another computer system. Pseudo-color plots, color contour plots, and three-dimensional plots could be obtained from the raw data, as well as from any desired arithmetic transformation of the data. An Abel inversion could also be made on the processed data.

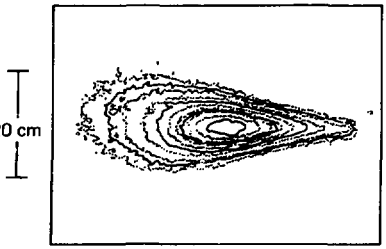

FIG. B-30. Contour plot of the x-ray brightness of the west plug.

Figure B-32 shows cross sections of plasma images obtained with and without a 4000-Å Be filter, which blocks off x rays with energies less than about 50 eV. The differences between the cross sections suggest strong UV emission from the boundaries of the plasma and a shell surrounding a hot central core. The 1/e radii of these two images are 13 and 17 cm respectively. For comparison, the radius of the central-cell plasma measured by beam-attenuation detectors was 21 cm. These measurements indicate good up-down symmetry and that the central-cell plasma is centered about 2 cm below the geometrical center of the machine.

B2.15.3 X-Ray Spectrometer. *(J. P. Stoering, G. A. Burginyon, H. D. Snyder, A. Toor, C. Anderson, R. Crabb, M. E. McGee, and P. Poulsen)* A medium-resolution (about 0.1 keV), reflection-refraction spectrometer,[15] which allowed spectral diagnosis of bursts of x rays from about 0.5 keV to 8.0 keV, was used to measure x rays from the east-plug plasma.

The spectrometer is illustrated in Fig. B-33. Incident x-rays accepted by the collimator-slit system pass through a selected filter and a thin light barrier before being reflected at grazing incidence from a polished vitreous-carbon mirror to the face of a fluor-photomultiplier tube detector. The photomultiplier tube was optically bonded to a thin (about 0.3 mil) NE102 fluor. A thin scintillator was chosen to minimize neutron background. The angle of the detector was kept small enough (less than 9° with respect to the reflected beam) to guarantee 100% absorption of all x rays of less than 1.5 keV reflected by the carbon mirror. Any x rays below about 0.17 keV were reflected from the detector and undetected. The current from the photomultiplier was a direct time-dependent measure of the contents of a selected energy band from the incident spectrum into the scintillator. The lower- and higher-energy cuts of the x-ray band were determined by the appropriate filter selection and carbon-mirror angle, respectively.

As Fig. B-33 shows, the carbon mirror and detector were mounted on separate goniometers (rotation stages). The detector's goniometer rode on a translation stage to maintain the proper θ to 2θ geometry for various settings of carbon-mirror angle. In addition, this translation stage could move the detector in and out of the x-ray beam to determine background emissions. Both goniometers, as

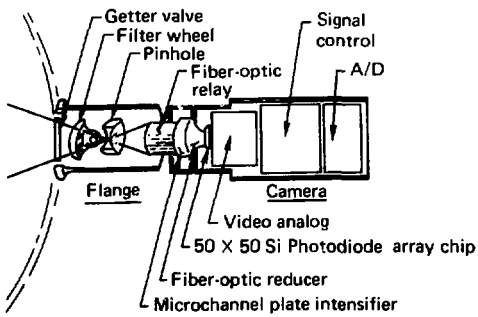

FIG. B-31. Diagram of the time-resolved x-ray camera.

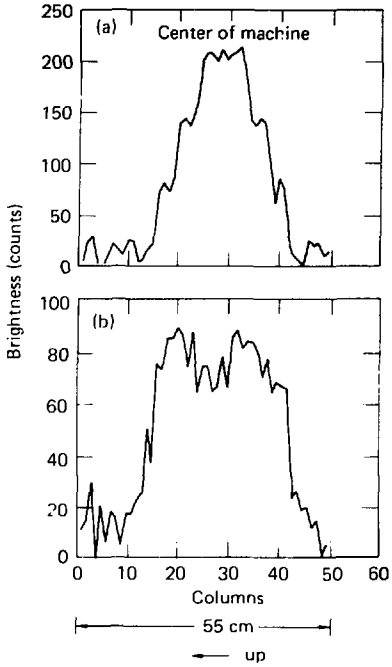

FIG. B-32. Plasma-image cross section with a 4000-Å Be filter (a) and without a filter (b).

well as the translation stage and filter wheel, were remotely controlled. Angular settings were accurate to ±0.01°, and the translation stage could be set to within 0.02% of full travel (about 12 μm).

Early TMX experiments confirmed that our measured signals were indeed x rays, with no optical or UV contribution. The possibility of a UV contribution was eliminated by experiments using a LiF filter opaque to x rays but transparent to UV below 10 eV. In combination with an experiment in which one x-ray bin was gradually closed to x rays by increasing the carbon-mirror angle, these experiments provided final confirmation.

All spectrometer measurements were normalized to signals from a four-channel x-ray detector. Three x-ray channels incorporate filters having lower-edge-transmission half values at 0.65, 0.75, and 0.95 keV. The remaining channel, having a thick filter (black to x rays) was used as a shot-to-shot neutron monitor.

B2.16 Plasma Calorimeters *(R. S. Hornady)*

Calorimeters were used at a number of places in TMX to measure power loss. Each of these calorimeters was a 16-cm^2 copper disk, 0.025-cm thick, with a precision thermistor and calibration resistor affixed to the back side with thermally conducting epoxy (Fig. B-34). The calorimeters were all calibrated by discharging a capacitor storing a known energy. The resistance of the calibration resistor was large compared to line resistance, so line losses were negligible. The discharge time was short compared to the thermal time constant of the calorimeter, so the thermal loading was similar to that from the plasma. The reflectance of the surface for charge-exchange atoms and radiation was unknown and varied, because the surface was not shielded from the getters, which covered the surface with sublimed titanium. The calorimeter system was calibrated frequently, since the thermistors are nonlinear devices and calorimeter temperature varies when getters and liquid nitrogen liners are used nearby. The sensitivity was adequate to measure approximately 0.01 J/cm^2. It is expected that the error is on the order of 30% to 50%.

Energy loss to the central-cell walls of TMX was measured with an array of eight calorimeters. Four were located 52 cm west of the midplane and equally spaced azimuthally at 52-cm radius. Three more were located on the same radius but 21 cm, 122 cm, and 193 cm east of the midplane. The last calorimeter was 13 cm above the centerline and 198 cm east of the midplane, above the flat part of the plasma fan.

Another series of calorimeters was located on the jaws (facing the plugs) of the east and west gas boxes (Fig. B-35). A single calorimeter viewed the Yushmanov region of the east plug. An array of 12 calorimeters was located on each end wall to measure the radial distribution of end-loss power.

From these calorimeters the energy-loss rate from the plasma to the central-cell walls, to the gas-box jaws, and to the end walls was determined. Most of the injected power was found on the end walls. The loss to the central-cell walls depends strongly upon the nature and amount of gas fueling

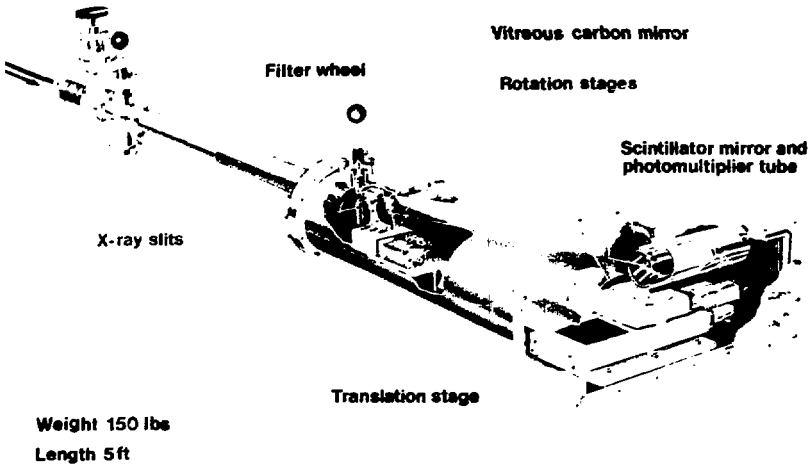

FIG. B-33. Double-reflection x-ray spectrometer (DREX).

used (i.e., gas box or puffer). In recent gas-box operation, approximately 20 kW was lost to the walls of the central cell, 2.5 kW to the gas-box jaws, and 100 kW to each end wall. The total trapped beam power was approximately 300 kW.

B2.17 Pyroelectric Detector (*W. L. Barr*)

The pyroelectric detector measured the absorbed fraction of the total incident power flux which consisted of photons and charge-exchange neutrals. Because of the black chrome plating on the detector, the absorption of photons should be nearly complete (about 80%). The energy absorption from D^0 depends on incident energy. (For H, T, or He on Cu, energy absorption varies from 60% at 50 eV to 80% at 400 eV.) The pyroelectric has fast response and is rugged, simple, and not affected by magnetic field or gravity; its weak points are that it is very sensitive to microphonics, to charge-up of its surfaces, and to capacitive coupling to its surroundings.

The detector was mounted on the bottom of the central cell about 1.68 m from the axis of the machine, and viewed about a 30-cm length and width of plasma. Calibration with a high-intensity lamp that produced 5 W/cm^2 showed that the lead-zirconate–lead-titanate (PZT) ceramic detector gave 10 nA per absorbed W/cm^2. The current-to-voltage (I-V) converter had a gain of 2×10^6 V/A, giving a final calibration factor of 0.02 V/W cm^{-2}.

The equivalent circuit of the detector is a current source in parallel with the capacitance, C, of the detector. An I-V converter produces a voltage proportional to the heat flux. The advantage of the I-V converter is that its low input impedance allows it to be located far from the detector. Then, a series resistor, R, at the input to the

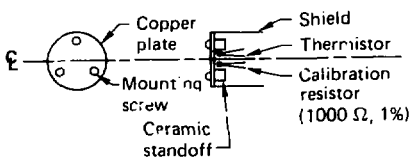

FIG. B-34. A typical TMX calorimeter.

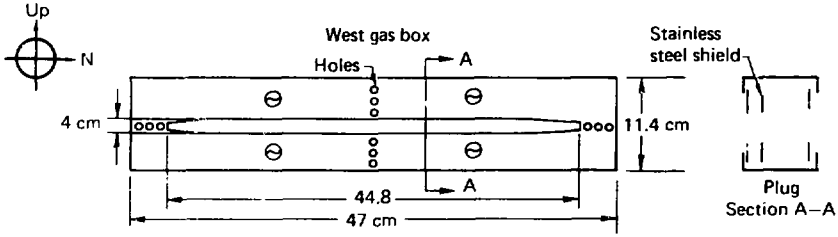

FIG. B-35. **Locations of the four gas-box calorimeters, showing small holes for thermal isolation and stainless steel shields.**

I-V converter can provide filtering by controlling the response time $\tau = RC_{in}$. On TMX, C_{in} was almost entirely due to the cable since $C = 150$ pF for the detector. The series resistor also served to isolate the I-V converter from C_{in}, which would tend to cause the converter to oscillate.

The cylindrical detectors were cemented to BNC connectors with silicon rubber, which gave mechanical isolation and also shielded the signal lead from stray currents. Since the signal current amounted to only 10^{-9} A W^{-1} cm^{-2}, the signal lead had to be well shielded from plasma. Also, the sides of the cylinders tended to become charged and produce noise. This charging was apparently the reason that the detector did not work on the end wall. Solid shielding of the sides makes a mechanical coupling and gives much more microphonic noise.

Normally the signal was not detectable on the pyroelectric detector (less than 0.4 W cm^{-2}). Detectable signals were usually obtained on the first few shots of the day or before cooling the liquid nitrogen (LN) liners. Because the vacuum improved on July 15, 1980, we were able to observe that the pyroelectric signal decreased into the noise level as indicated in Table B-6. This behavior indicates that the pyroelectric detector signal is related to machine vacuum conditions.

B3. TMX OPERATING PARAMETERS

B3.1 Neutral-Beam Calorimeter

(R. H. Munger)

Calorimeters were raised to the center of each plug when needed to determine the delivered power, focus, and aim of each neutral beam. Figure B-36 shows a face of one of these calorimeters.

Incident neutral-beam power was indicated by the temperature rise of a rectangular copper plate (10 by 40 cm) facing each group of beams. Cooling-water flow was stopped before calorimeter shots, and the temperature rise was measured. The calorimeter was divided into two sections, an inner plate and an outer plate. The ratio of incident power on these two plates was used as a figure of merit for beam focus.

The distribution of the beam over the plate was monitored by a fast-scan beam-profile monitor[16] that scanned the signals from 45 secondary-electron-emission buttons located behind beam-sampling holes in the copper calorimeter plates. This scan was repeated at frequent intervals during the beam pulse. The calorimeter plate was accurately positioned in the plug by means of a lead screw turned by a stepping motor controlled by a digital counting unit.

TABLE B-6. Pyroelectric-detector data on July 15, 1980.

Shot	LN liners	Central-cell pressure (Torr)	Pyroelectric-detector signal (W/cm^2)
17	Warm	4.2×10^{-7}	2.5 to 2.0
27	Warm	3.7×10^{-7}	0.7
36	Cool	1.0×10^{-7}	0.2

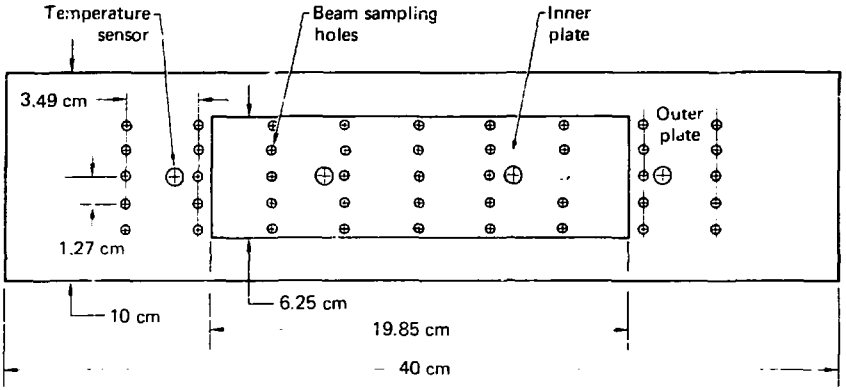

FIG. B-36. A neutral-beam calorimeter.

B3.2 Neutral-Beam Voltage and Current

(R. H. Munger)

Two neutral-beam operating parameters were read by the TMX diagnostic computer: acceleration voltage (V_{accel}) and acceleration current (I_{accel}).

The V_{accel} signal was obtained from a 5000-to-1 voltage divider connnected to the cathode of the series-regulator tube. Current from that point was fed to the first accelerating grid of the injector by way of the leads to the ion-source filament.

The I_{accel} signal came from a current transformer through which the accel lead passed. The transformer core, as used on TMX at 250 A, V was adequate for the 25-ms pulse but not for a longer pulse.

B3.3 Magnet Current *(D. A. Goerz)*

The coil current was measured by noncontacting dc current transductors at the power supplies. The representative voltage signals were sent over foil-shielded twisted-pair cables to the control room, where they were electrically isolated from other control-room signals. The limit of the frequency bandwidth was set at 100 Hz at the analog-voltage isolation stage. The current signals were recorded by the magnet control computer and were monitored by the magnet safety chassis to ensure proper operation of the magnet system. The signals were then passed through another isolation chassis before being digitized in a data logger.

B4. TMX COMPUTER SYSTEM

(W. F. Cummins and J. F. Clauser)

A distributed computer facility acquired, managed, and analyzed the data from the TMX experiment. The system consisted of three computers (as shown in Figs. B-37 and B-38) with the following responsibilities:

- TMX Exec processor. This computer was the system executive or supervisor and performed tasks of data reduction and data-base management. Other computers in the TMX system sent their data to the Exec for storage, processing, and output.
- TMX diagnostics. This computer was responsible for acquiring and archiving diagnostic data. The data was sent to the Exec via a high-speed parallel link.
- TMX off-line development and analyses. This processor is used for software development and data analyses. The TMX system was also linked to the Beta II computer to provide both experiments with a degree of equipment backup and to provide extended processing capability in case overloads occur on one of the systems.

B4.1 Data-Base Management System

Drawing on our experience with the 2XIIB experiments, we designed a data-base management

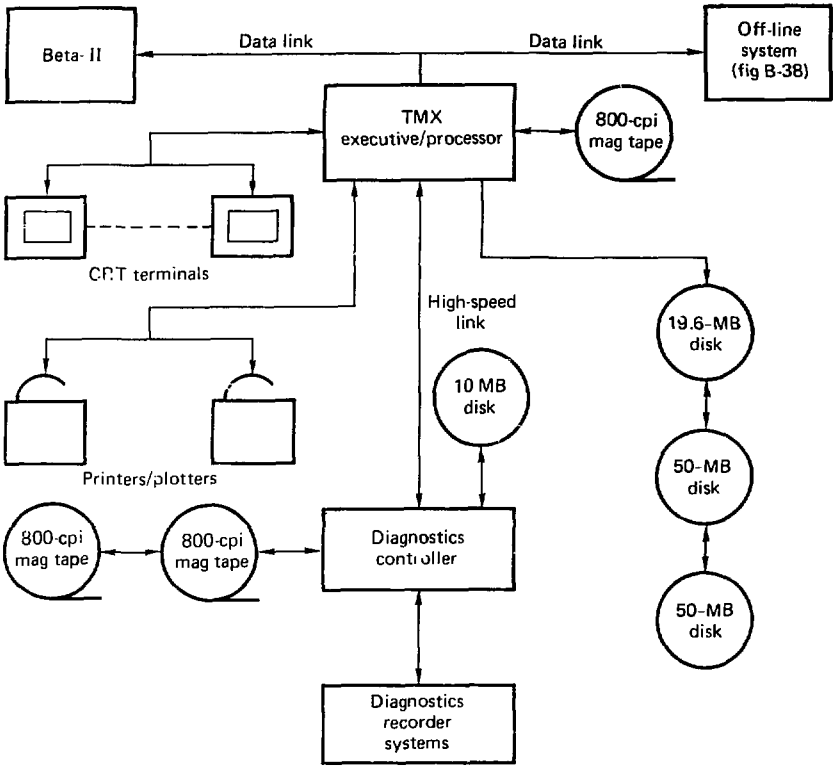

FIG. B-37. Schematic of the on-line computer system for TMX.

system for TMX/Beta II that performed the following tasks:

- Retrieved data from satellite computers, stored it on large disk volumes, and generated a permanent tape archive.
- Provided user control of the data-base management system.
- Provided for access to and use of the data base through a system of internally linked journal, raw-data, and processed-data file structures, and a library of programs and utility subroutines (particularly graphics).
- Provided for automatic intershot data analysis and display.
- Supported a data-input rate of 1.7×10^6 bytes per shot.

The principal components of this system were:

- Data acquisition system responsible for acquiring and archiving all data.
- Automatic data-processing system, responsible for automatically reducing and displaying data between shots.
- Processors—individual programs that reduce and display data, run by the automatic

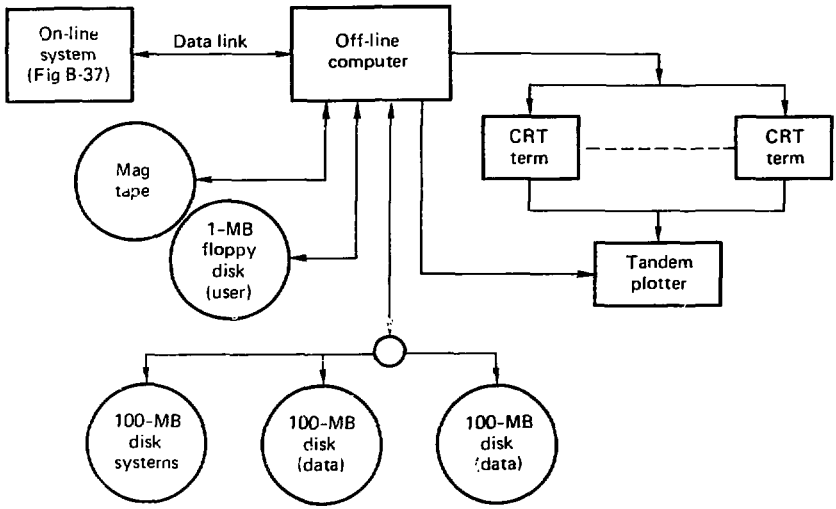

FIG. B-38. Schematic of the off-line computer system for TMX.

processing system or in off-line, interactive, or batch modes.

- Data retrieval and analysis system, for interactive data retrieval, analysis, and graphics.

User programs and subroutines are provided to retrieve data from journal, processed-data, and raw-data files. Using appropriate system controls, the journal and processed-data files may be modified.

This data-base system was designed to be relatively "open," with security measures applied only where necessary to protect the prime data.

B4.2 Configuration of the System's Software

The TMX computer system was set up to provide for rapid data acquisition and intershot processing, as well as to provide convenient access to the data base. Through experience, we evolved a system for data flow to effect these features. The data base is composed of three types of files: raw-data files, processed-data files, and journal files.

The data-acquisition system acquired the data at direct-memory-access (DMA) speed via a CAMAC parallel-branch highway (and a variety of other interfaces), and wrote the raw diagnostic data directly onto the raw-data file, along with the associated diagnostic parameters. The subsequent processing of the data occurred on several levels. First a series of programs called primary processors read data from the raw-data files for each diagnostic and produced numbers in physical units that were representative of a given diagnostics measurement of the plasma. These results were then written to the processed-data file. Next, several layers of secondary processors read data from the processed-data files. These results were accumulated onto the processed-data file. Therefore, the system was modular, so complex calculations that required data from more than one diagnostic and/or preceding calculation could be made. In this way, calculations could be performed to any degree of complexity, and the results could be available between shots. Moreover, additional processing could be performed later and the results added to the processed-data files. Once the raw and processed files were in some sense complete, they were archived on magnetic tape.

B4.3 Computer Graphics

The following types of graphics output were available on TMX:

(1) A certain amount of graphics hard-copy output was required during intershot processing. Speeds of plotting hardware (video terminals and hard-copy units) limited the number of graphical outputs at any one time, so outputs were selected to suit the current experiment.

(2) Both hard- and soft-copy graphics were available between shots upon a user's request to the computers. These were displayed on different graphics terminals, and could be used to obtain graphical outputs not included in (1) above. Graphical outputs could be thus produced from raw or processed data files that were still on disk (typically the preceding 20 shots).

(3) A complete set of graphical outputs and data tabulated in "standard form" was available (usually by the day after it was acquired), bound in notebooks. These books are useful for quick access to data for any shots in the history of the machine. Additional "non-standard" graphical and tabulated data can be added to this reference library upon a user's request. This library is essentially a completion of (1) above.

REFERENCES

1. W.C. Turner, A.W. Molvik, and J. Williams, "Beam Probe Measurements of Plasma Density Profiles in 2XIIB," *Bull. Am. Phys Soc.* 21, 857 (1976).
2. W.C. Turner and T.B. Kaiser, "Neutral Beam Trapping by Mirror Confined Plasma," *Bull. Am. Phys. Soc.* 23, 754 (1978).
3. M.A. Harrison, Scientific Editor, *Magnetic Fusion Energy Annual Report—July 1975 through September 1976*, Lawrence Livermore National Laboratory, Livermore, CA, UCRL-50002-76 (1976), p. 24.
4. J.H. Foote, "Plasma-Density Measurements in TMX from Neutral-Beam Attenuation," *Bull. Am. Phys. Soc.* 24, 1018 (1979).
5. E.J. Powers and T.C. Simonen, "Microwave Measurement of Plasma Density Fluctuation Amplitudes," *J. of Appl. Phys.* 47, 3911 (1976).
6. J.R. Smith, N. Hershkowitz, and P. Coakley, "Inflection-point Method of Interpreting Emission Probe Characteristics," *Rev. Sci. Instrum.* 50, 210 (1979)
7. D.R. Slaughter, *Neutron Yield Measurements on a TMX Endplug*, Lawrence Livermore National Laboratory, Livermore, CA, UCRL-52923 (1980).
8. G. Mount, G. Yamasaki, W. Fowler, and W.G. Fastie, "Compact Far Ultraviolet Emission Source with Rich Spectral Emission 1150–3100 Å," *Applied Optics* 16, 591 (1977).
9. J.L. Terry, K.I. Chen, H.W. Moos, and E.S. Marmar, "EUV Impurity Study of the Alcator Tokamak," *Nucl. Fus.* 18, 485 (1978).
10. K.I. Chen, J.L. Terry, H.W. Moos, and E.S. Marmar, "Spatial Profiles of Light Impurity Ions in the Alcator A Tokamak Plasma," *Nucl. Fus.* 20, 189 (1980).
11. R.P. Drake and H.W. Moos, "Evidence for Neutral-Beam-Injected Oxygen Impurities in 2XIIB," *Nucl. Fus.* 19, 407 (1979).
12. H.W. Moos, K.I. Chen, J.L. Terry, and W.G. Fastie, "Construction, Calibration, and Application of a Compact Spectrophotometer for EUV (300–2500-Å) Plasma Diagnostics," *Applied Optics* 18, 1209 (1979).
13. R.K. Richards, H.W. Moos, and S.L. Allen, "Spatial Imaging Detector System for Pulsed Plasma Extreme Ultraviolet Diagnostics," *Rev. Sci. Instrum.* 51, 1 (1980).
14. S.L. Allen, *A Study of Impurity Transport with an EUV Spatial Imaging Detector System on the Alcator A Tokamak*, Ph.D. Thesis, Johns Hopkins Univ., Baltimore, MD (1980).
15. G.A. Burginyon, J.P. Stoering, R.W. Hill, and L.V. Singman, "A Low-Energy High-Fluence Reflection-Refraction X-ray Spectrometer," *J. Appl. Phys.* 49, 513 (1978).
16. A.F. Waugh, "Fast-Scan, Beam-Profile Monitor," in *Proc. 7th Symposium on Engineering Problems of Fusion Research, Knoxville, Tennessee, October 25-28, 1977* (Institute of Electrical and Electronics Engineers, New York, IEEE Pub. No. 77CH 1267-4 NPS, 1977) and Lawrence Livermore National Laboratory, Livermore, CA, UCRL-79680 (1977).

Appendix C.
Predicted Central-Cell Confinement in TMX

C1. SUMMARY

This appendix contains formulas used to evaluate TMX experimental data on central-cell confinement described in the main part of this report.

An expression for $(n\tau)_c$, accurate to ±25% for all TMX plasmas with $\phi_c/T_{ic} \gtrsim 1$, is (in $cm^{-3}\cdot s$):

$$(n\tau)_c = \left\{7.4 \times 10^{10}\ T_{ic}^{1/2}\ \phi_c \left(\frac{A}{2}\right)^{1/2} + 10^{-8}\ \frac{2n_cL_cR_c}{(T_{ic}/A)^{1/2}}\right\} \exp\frac{\phi_c}{T_{ic}} \quad . \quad (1)$$

A more complete and accurate expression is

$$(n\tau)_c = \left\{2.45 \times 10^{10}\ T_{ic}^{3/2} \left(\frac{A}{2}\right)^{1/2} \times H(R_c)\, K\left(\frac{\phi_c}{T_{ic}}\right) + 10^{-8}\ \frac{2n_cL_cR_c}{(T_{ic}/A)^{1/2}}\right\} \exp\frac{\phi_c}{T_{ic}} \quad , \quad (2)$$

in which

$$K(x) = \frac{x^2 + 0.25}{x + 0.5} \quad , \quad (3)$$

and

$$[H(R_c)]^{-1} = [G(R_c)]^{-1}\ 2\ K\left(\frac{\phi_c}{T_{ic}}\right) \exp\left(-\frac{\phi_c}{T_{ic}}\right) + \left[G\left(\frac{R_c}{R_p}\right)\right]^{-1} \left[1 - \exp\left(-\frac{\phi_c}{T_{ic}}\right)\right] \quad , \quad (4)$$

with

$$G(x) = \frac{x + 1}{x} \ln(2x + 2) \quad . \quad (5)$$

In the above equations,

T_{ic} = central-cell ion temperature (keV),
A = central-cell ion mass (AMU),
R_c = full central-cell mirror ratio (B_m/B_c),
ϕ_c = electrostatic-well depth (keV),
n_c = central-cell density (cm^{-3}), and
L_c = central-cell effective length (cm).

Equation (5) assumes $R_p = 2$, where R_p is the ratio of the magnetic field at the mirror to that at the end-cell midplane (B_m/B_p). The following sections trace the historical development of the confinement formulas.

C2. TMX PROPOSAL

The TMX proposal[1] gives an expression for the Pastukhov confinement parameter:

$$(n\tau)_p = 10^{11}\ T_{ic}^{1/2}\ \phi_c \exp\frac{\phi_c}{T_{ic}} \quad . \quad (6)$$

The units are keV and $cm^{-3}\cdot s$. This expression does not include short-mean-free-path effects. It also neglects mirror-ratio effects and is inaccurate for $\phi/T \lesssim 4$.

C3. THE PASTUKHOV TERM

A complete Pastukhov-type solution to the tandem mirror problem is given by Cohen, et al.[2] Neglecting impurities, the expression they obtain (in cgs units) is

$$(n\tau)_p = (n\tau)_0 \frac{\sqrt{\pi}}{2}\, G(R) \frac{e\phi_c}{T_{ic}} \frac{\exp\left(\frac{e\phi_c}{T_{ic}}\right)}{I\left(\frac{T_{ic}}{e\phi_c}\right)} \quad . \quad (7)$$

In this expression,

$$(n\tau)_0 = \left(\frac{m_i}{2}\right)^{1/2} \frac{T_{ic}^{3/2}}{\pi e^4 \ln \Lambda_{ii}} \quad . \tag{8}$$

The value of $\ln \Lambda_{ii}$ used in current Fokker-Planck codes is[3]

$$\ln \Lambda_{ii} = \ln \left[1.212 \times 10^{15} \left(\frac{m_i T_i T_e}{n_e}\right)^{1/2}\right] \quad , \tag{9}$$

where m_i is in AMU, T is in keV, and n_e is in cm^{-3}. The function I is[2]

$$I(x) = 1 + \frac{1}{2}\sqrt{x}\exp\left(\frac{1}{x}\right)\left[1 - \text{erf}\left(\frac{1}{\sqrt{x}}\right)\right] \quad . \tag{10}$$

An adequate approximation to I is[4,5]

$$I(x) = \frac{1 + \frac{x}{2}}{1 + \frac{x^2}{4}} \quad . \tag{11}$$

This expression should give accurate results for $\phi/T > \alpha$ with $\alpha \lesssim 1$.

If the peak of the plasma potential occurs at a magnetic mirror, the mirror ratio R enters Eq. (7) directly. Neglecting impurities, G(R) for ions is given by[2]

$$G(R) = \frac{(R + 1)}{R} \ln(2R + 2) \quad . \tag{12}$$

However, in TMX the potential peak is at the end-cell midplane. There is no single mirror ratio that corresponds to the Pastukhov losses. These losses include angular scattering (mirror ratio R_c) and diffusion in energy (mirror ratio $R_c/2$ for $R_p = 2$). Cohen[5] has derived a physically plausible expression for G(R) in TMX:

$$[H(R)]^{-1} = [G(R_c)]^{-1}\, 2K\left(\frac{\phi_c}{T_{ic}}\right)\exp\left(\frac{\phi_c}{T_{ic}}\right) + \left[G\left(\frac{R_c}{R_p}\right)\right]^{-1}\left[1 - \exp\left(\frac{\phi_c}{T_{ic}}\right)\right] \tag{13}$$

[The designation H(R) is used to avoid confusion with G(R).] Figure C-1 shows H(R) as a function of ϕ_c/T_{ic} for several values of R_c.

To evaluate Eq. (7), we note that $\ln \Lambda_{ii} = 18$ for TMX to within 5% [Eq. (9)] over the range of normal TMX parameters. This gives (keV, AMU, cm^{-3}·s)

$$(n\tau)_0 = 2.76 \times 10^{10} \left(\frac{A}{2}\right)^{1/2} T_{ic}^{3/2} \quad . \tag{14}$$

By combining Eqs. (7) and (14) and replacing G(R) with H(R), we obtain

$$(n\tau)_p = 2.45 \times 10^{10}\, T_{ic}^{3/2} \left(\frac{A}{2}\right)^{1/2} \times H(R_c)\frac{\phi_c}{T_{ic}}\exp\left(\frac{\phi_c}{T_{ic}}\right)\left[\frac{1 + \left(\frac{T_{ic}}{2\phi_c}\right)}{1 + \frac{T_{ic}}{2\phi_c}}\right]^2 \quad . \tag{15}$$

This can be written more simply by defining

$$K(x) = \frac{x^2 + 0.25}{x + 0.5}$$

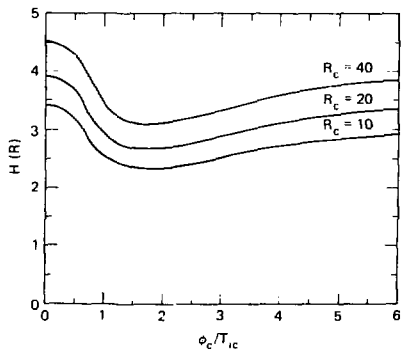

FIG. C-1. H(R) versus ϕ_c/T_{ic} for $R_p = 2$ and $R_c = 10$, 20, and 40.

to obtain

$$(n\tau)_p = 2.45 \times 10^{10}\, T_{ic}^{3/2} \left(\frac{A}{2}\right)^{1/2} \times H(R_c)\, K\left(\frac{\phi_c}{T_{ic}}\right) \exp\left(\frac{\phi_c}{T_{ic}}\right) \quad . \quad (16)$$

Figure C-2 shows $K(\phi_c/T_{ic})$ versus ϕ_c/T_{ic}. The product $H(R)\,K(\phi_c/T_{ic})$ is shown in Fig. C-3.

For approximate purposes, since $H \times K = 3\,\phi_c/T_{ic}$ to within 25% for $1 \leq (\phi_c/T_{ic} < 5$, we obtain

$$(n\tau)_p = 7.45 \times 10^{10}\, T_{ic}^{3/2} \left(\frac{A}{2}\right)^{1/2} \frac{\phi_c}{T_{ic}} \exp\left(\frac{\phi_c}{T_{ic}}\right). \quad (17)$$

This is accurate to ±25% for all relevant TMX data. A more precise evaluation must use Eq. (11).

C4. COLLISIONAL EFFECTS

As Rognlien and Cutler have shown,[6] collisional effects are also important in TMX. The collisional confinement (in cgs units) is

$$(n\tau)_F = \frac{\sqrt{\pi}\, n_c L_c}{(2kT_{ic}/m_i)^{1/2}} \frac{R_c}{R_p} \exp\left(\frac{e\phi_c}{kT_{ic}}\right) \quad . \quad (18)$$

Using keV, AMU, cm^{-3}, and cm, Eq. (18) is:

$$(n\tau)_F = 10^{-8} \frac{2n_c L_c R_c}{(T_{ic}/A)^{1/2}} \frac{2}{R_p} \exp\left(\frac{\psi_c}{T_{ic}}\right) \quad . \quad (19)$$

As also shown in Ref. 6, the sum of Eqs. (16) and (19) gives $(n\tau)_c$ in all confinement regimes. This expression is used in the summary above.

In the presence of a potential, Eq. (19) is correct. However, as ϕ_c/T_{ic} approaches zero, the effective mirror ratio doubles for $R_p = 2$. In Eq. (19), R_c/R_p should be replaced by an effective mirror ratio given approximately[7] by

$$R_{eff} = \frac{R_c}{R_p}\left[1 - \left(1 - \frac{1}{R_p}\right) \times \exp\left(\frac{-2\,\phi_c}{T_{ic}\,(R_p - 1)}\right)\right]^{-1}$$

For all cases of interest in TMX, we may take $R_{eff} = R_c/R_p$.

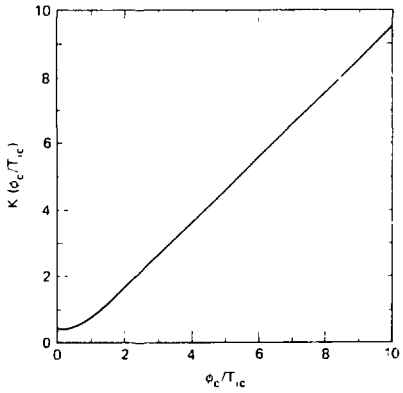

FIG. C-2. $K(\phi_c/T_{ic})$ versus ϕ_c/T_{ic}.

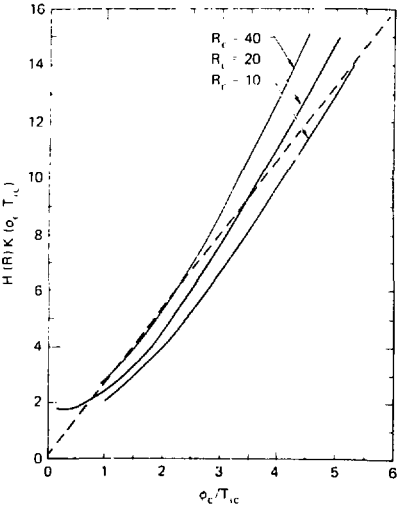

FIG. C-3. The product $H(R)K(\phi_c/T_{ic})$ versus ϕ_c/T_{ic} for $R_p = 2$ and $R_c = 10$, 20, and 40. The dashed line represents $HK = 3\,\phi_c/T_{ic}$.

REFERENCES

1. F. H. Coensgen, *TMX Major Project Proposal*, Lawrence Livermore National Laboratory, Livermore, CA, LLL-PROP-148 (1977), p. 43.
2. R. H. Cohen, M. E. Rensink, T. A. Cutler, and A. A. Mirin, "Collisional Loss of Electrostatically Confined Species in a Magnetic Mirror," *Nucl. Fusion* 18 1229 (1978).
3. M. E. Rensink, Lawrence Livermore National Laboratory, Livermore, CA, private communication (September 1980).
4. R. H. Cohen, I. B. Bernstein, J. J. Dorning, and G. Rowlands, "Particle and Energy Exchange Between Untrapped and Electrostatically Confined Populations in Magnetic Mirrors," *Nucl. Fusion* 20, 1421 (1980).
5. R. H. Cohen, Lawrence Livermore National Laboratory, Livermore, CA, private communication, September 1980 MFE/TC/80-0099/1914u memo,* October 10, 1980.
6. T. D. Rognlien and T. A. Cutler, "Transition from Pastukhov to Collisional Confinement in a Magnetic and Electrostatic Well," *Nucl. Fusion* 20, 1003 (1980).
7. R. P. Drake, Lawrence Livermore National Laboratory, Livermore, CA, notes on collisional confinement, available privately (1979).

*Readers outside the Laboratory who desire further information on LLNL internal documents should address their inquiries to the Technical Information Department, Lawrence Livermore National Laboratory, Livermore, CA 94550.

Appendix D.
Radial and Axial Weighting Functions

D1. INTRODUCTION

This appendix describes some calculations that were too lengthy to be included in Sec. 5: the radial and axial averaging needed for physical and diagnostic reasons; the equations used to evaluate the axial weighting factors f_1 and f_3 in Eq. (1) of Sec. 5; and finally, the neutral beam density, which was important for Fig. 5-8. The weighting factor f_4 converts a known gas flux into a loss rate, but will not be considered here, since it is not needed.

The plasma ions have a significant Larmor radius ($r_L \sim 2$ cm). In addition, they bounce back and forth between the magnetic mirrors. The actual ion confinement results from the interactions that occur throughout the volume traversed by the ion. For this reason, one should average the processes of fueling and loss axially over a distance that includes the turning points of most of the ions, and radially over at least one orbit diameter. In addition, the plasma-density diagnostics determine the average density within the plasma core more accurately than they determine the density on centerline, and this also encourages radial averaging. In the following, we averaged axially over the plasma density e-folding length and radially over a 6-cm radius. We assumed the radial average was independent of the axial average. In addition, the radial line-density profiles permit the plasma-density profile within a 6-cm radius to be flat, slightly peaked, or slightly inverted. We assumed that the plasma-density profile is flat for purposes of averaging.

The axial weighting factors were computed by integration over the plasma length. The application of these factors is to evaluate the Coulomb density *limit, which is logarithmically* insensitive to their exact values. We express the axial plasma-density profile as $n_p g_1(z)$ and the neutral-beam density profile as $n_b g_2(z)$. We have measured both axial profiles. The data fit well if we assume $g_1(z) = \exp(-z^2/\ell^2)$, in which ℓ is approximately 13 cm for the east end cell and 18 cm for the west end cell. The function $g_2(z)$ is defined in Eq. (7). With these definitions, we have

$$f_1 \langle \sigma v \rangle_{ion} n_b n_p = \langle \sigma v \rangle_{ion} n_b n_p \frac{1}{2\ell} \times \int_{-\ell}^{\ell} g_1(z)\, g_2(z)\, dz \qquad (1)$$

and

$$f_3 \frac{\langle \sigma v \rangle_{cx} n_b n_p}{\exp\left(\frac{\tau_d}{\tau_{cx}}\right) - 1} = \frac{\langle \sigma v \rangle_{cx} n_b n_p}{2\ell} \times \int_{-\ell}^{\ell} \frac{g_1(z)\, g_2(z)\, dz}{\exp\left[\frac{\tau_d}{\tau_{cx}} \frac{g_2(z)}{g_1(z)}\right] - 1} \qquad (2)$$

We evaluated f_1 and f_3 for the data plotted in Fig. 5-8 to obtain $f_3 f_1 = 0.7$. The uncertainty in the Coulomb density limit resulting from the uncertainty in $f_3 f_1$ is small compared to the other uncertainties.

The neutral-beam density along the radius and the axis must be evaluated, and the radial average taken, to obtain the Coulomb density limit described above. In the absence of plasma, the density of neutral-beam atoms as a function of height (y) and (z) [$n_b(y, z)$] is

$$n_b(y, z) = \frac{I_b}{e\pi\, wq\, v_b} \times \exp\left(-\frac{y^2}{w^2}\right) \exp\left(-\frac{z^2}{q^2}\right) \qquad (3)$$

In TMX, we found $w \simeq 3$ cm and $q \simeq 18$ cm. The neutral-beam current, I_b, is in equivalent A, and the velocity of the beam atoms, v_b, is 1.1×10^8 cm/s. The peak density of neutral-beam atoms is

$$n_b = \frac{I_b}{e\pi\, v_b\, wq}.$$

If a plasma is present, the local density of neutral-beam atoms has been attenuated by the plasma along the line-of-sight of the beam. It is

$$h(x, y, z) = \exp\left(-\frac{y^2}{w^2}\right) \exp\left(-\frac{z^2}{q^2}\right) \times \exp\left(-\int_{-\infty}^{x} n_e(x)\, dx\sigma\right) \quad . \quad (4)$$

In this equation $n_e(x)$ is the electron density along the beam path to the point, and σ is the effective cross section for neutral-beam attenuation. (For TMX, $\sigma = 1.54 \times 10^{-15}$.) We have evaluated the radial average of the neutral-beam density at z = 0 as

$$n_b = n_b \exp\left(-\frac{\int ndl\sigma}{2}\right) F \quad . \quad (5)$$

The quantity $\int ndl$ is the line density along a central chord through the plasma, and F is given by

$$F = \exp\left(\frac{\int ndl\sigma}{2}\right) \frac{1}{\pi a^2} \times \int_{-a}^{a} \int_{-(a^2-y^2)^{1/2}}^{(a^2-y^2)^{1/2}} h(x, y, o)\, dx\, dy \quad . \quad (6)$$

In this equation, the integral is taken over a circle of radius a in the x-y plane. To evaluate Eq. (6), we approximated the line density profiles as parabolas (Figs. 5-3 and 5-4) and Abel-inverted to obtain the density profiles. For the TMX geometry we found F = 0.54 to within five percent for the entire range of TMX parameters and including the uncertainties in the geometry. [If the beam width, w, changes, the changes in n_b and F(a) compensate.]

On the basis of the above discussion, we can write the function $g_2(z)$, which describes the axial variation of n_b in Eqs. (1) and (2), as

$$g_2(z) = \exp\left(-\frac{z^2}{q^2}\right) \times \exp\left[\frac{\int ndl\sigma}{2}\left(1 - e^{-z^2/q^2}\right)\right] \quad . \quad (7)$$

This equation was used to evaluate f_1 and f_3.

Appendix E.
Power Balance Formulary

E1. INTRODUCTION

In this Appendix we present the formulas, approximations, and conventions used in the analysis of the power balance and power flow in TMX. In Table E-1 we list the symbols with appropriate units for all of the equations used in the power balance formulary. *Please note that the symbols* and units presented in Table E-1 are not necessarily consistent with conventions used by other authors in other sections of this document or in other reports or publications.

The formulas presented in this section are designed for use in a global (volume-integrated) power balance. The value of several of the terms in the power flow was obtained from analysis of experimental data using computer codes. Where simple analytic approximations to the code results exist, they are included in the text of this appendix. Where such expressions are not available, the reader is referenced to the proper code.

- Plasma profiles

In order to obtain the most accurate interpretation of the measured radial profiles of the line density from the beam attenuation diagnostic, we have fit two different model profiles to the data: Gaussian and polynomial.[1] The power balance is then calculated using the profile which best fits the data. The formulas used in the power balance calculations depend upon the model profiles used. The sets of equations for both model profiles are summarized in Tables E-2 and E-3. For the sake of clarity, the text of this appendix will refer only to Gaussian profiles. Simply substitute the appropriate formula from Table E-3 to perform a power balance when the line density profile is best fit by a polynomial profile.

E2. PLUG IONS

- Net power input by neutral beams

The total trapped neutral beam power is given by

$$P_\beta = I_b \bar{E}_b (f_i + f_{cx}) \qquad (1a)$$

where I_b is the incident neutral beam current in atom-amps, $\bar{E}_b$ is the current weighted mean injection energy, and f_i and f_{cx} are the fraction of the beam which is trapped by ionization and by charge exchange, respectively. The net power input to the end cells, however, is less than the value calculated using Eq. (1a). This occurs because charge exchange between an energetic beam neutral and an end cell ion results in the loss of the end cell ion which carries with it energy; $\overline{W}$. (Reionization of charge exchange products has already been included in the calculation of f_i and f_{cx}.) The net power input by the neutral beams is, therefore,

$$P_{net} = I_b f_i \bar{E}_b + I_b f_{cx} (\bar{E}_b - \overline{W}) \qquad (1b)$$

The trapping fractions, f_i and f_{cx}, used in this report were calculated using a beam trapping code developed by Turner.[2] This code includes effects such as finite plasma size, beam footprint dimensions, and reionization of charge exchange products. It has been shown by Correll[3] that for typical TMX parameters the values calculated by the beam trapping code can be approximated by

$$f_i \cong 0.28 \times 10^{-15} \int \hat{n} dl$$

$$f_{cx} \cong 2.5\, f_i \qquad (2)$$

For the power balances presented in Sec. 7D exact code results were used.

The current weighted, mean neutral beam accelerating voltage is calculated according to

$$\overline{V}_{Accel} = \sum_i \frac{I_i \cdot V_{Accel.\,i}}{\sum_i I_i} \qquad (3)$$

The values used for the ith neutral-beam current, I_i, are obtained from calorimetry performed just prior

TABLE E-1a. Symbols and appropriate units for equations in Appendix E.

Parameter	Description	Units
$\int nd\ell$	Line density	cm^2
n	Density	cm^3
T_e	Electron temperature	eV
T_{ic}	Central cell ion temperature	eV
W	Plug ion energy	keV
r_p	Gaussian (plug) radius	cm
l_z	Gaussian (plug) axial scale length	cm
l_c	Effective length of central cell (314)	cm
J	End Loss current density	A/cm^2 at 10 kG
ϕ	Plasma potential	Volts
W_{EL}	End loss ion energy	eV
R	Max. radius of parabolic function	cm
I	Equivalent current	Atomic Amperes
f_i	Ionization fraction	–
f_{cx}	Charge exchange fraction	–
E	Energy	keV
B_{ci}	Plug vacuum field strength at minimum of magnetic well	Tesla
B_c	Central cell solenoidal magnetic field strength	Gauss
r_{max}	Maximum radial extent of Gaussian profile	cm
M	Magnetic moment	$A\text{-}m^2$
l_s	Axial scale length of plug magnetic field (55 cm)	cm
β	Beta	–
P	Power	kW
ϕ_e	Central cell plasma potential	Volts
λ	Secondary electron multiplication factor	–
α	Constant	
	Used in thermal barrier calculations	
I	$I = \dfrac{1 + \dfrac{T_p}{2q\phi}}{1 + \left(\dfrac{T_p}{2q\phi}\right)^2}$	
C_c	$C_c = w/n \dfrac{w + 1}{w - 1}$	
w	$w^2 = 1 + \dfrac{1}{RZ}$	
R	Parallel mirror ratio	
Z	$Z_{effective}$	

to or just after the experimental run. If this data is not available the current drain from the accelerating power supply; $I_{accel.}$ is used.

The mean injection energy is calculated according to

$$\bar{E}_b = \frac{\bar{V}_{Accel}}{1.4} \quad . \tag{4}$$

The factor 1.4 is derived from the observation that a TMX (LBL) neutral beam running on density at 20 kV produces 70% atomic deuterium, 20% diatomic deuterium and 10% triatomic deuterium[4] $(1 \times 0.7) + (2 \times 0.2) + (3 \times 0.1) = 1.4$. However, if the beam is not running exactly on density (the usual case) the fraction of diatomic and triatomic species is increased. Eq. (4), therefore, tends to over estimate the mean injection energy.

The total incident neutral beam current (per plug) was calculated according to

$$I_b = \frac{1}{2} \sum_i I_{Accel.\ i} \quad . \tag{5}$$

TABLE E-1b. Subscript and superscript meanings for the equations in Appendix E.

E	East plug
W	West plug
cc	Central cell
c	Central cell
P	Plug
$\bar{}$ (Bar)	Average
$\hat{}$ (Hat)	Value at, r = o
$\perp$	Perpendicular to B_z
$\parallel$	Parallel to B_z
e	electron
i	ion
EL	End loss
H	Hot ions
rf	Ion cyclotron fluctuations
b	Beam
Accel	Neutral Beam accelerating voltage (current)
D	Drag
cx	charge exchange
V	see Ref. 7
s	secondary electron
scl	space charge limit

The assumption in Eq. (5) is that the net electrical efficiency, defined as the current delivered to the plasma divided by the accel drain current, is 50%. Calorimetry in TMX has shown that—on the average—50% is an acceptable number. However, the electrical efficiency of individual beams ranges from 20 to 70%.

- Mean plug ion energy

The mean (volume average) plug ion perpendicular energy is calculated from the total plasma diamagnetism according to

$$M_p B_o = \int_{-\infty}^{\infty} \int_0^{r_{max}} n\,(r,z) \times W_\perp\,(r,z)\, 2\pi r dr dz$$

TABLE E-2. Gaussian radial profiles.

- Plug density[a]

$$n_p(r,t) = \int \frac{ndl}{\sqrt{\pi} r_p} e^{-(r-r_p)^2} e^{-(z-L_z)^2}$$

- Plug ion mean perpendicular energy

$$\bar{W}_\perp = \frac{1.14 \times 10^{15} M_p B_o}{n\, r_p^2\, L_z\, [1 - e^{-(r_{max} - r_p)^2}]}$$

- Plug beta

$$\beta_p = \frac{0.45\, M_p}{r_p^2\, L_z\, B_o}$$

- Plug ion to electron drag power

$$P_{ID} = 2.8e \times 10^{-20} \frac{n^2 \bar{W}}{T_{ep}^{3/2}} r_p^2 L_z [1 - e^{-(r_{max}/\sqrt{2} r_p)^2}]$$

- Plug ion to end loss ion power transfer (per plug)

$$P(H - EL) = 10^{-3} \frac{\pi}{2} r_p^2 \left| \hat{W}_{EL} - (\phi_p + kT_{ic}) \right|$$

- Central cell electron axial loss power

$$P_{EL}\,(cc\ e^-) = 10^{-3} \sum_{E,W} \frac{\pi r_p^2}{2} \left| \phi_e + kT_{ec} \right|$$

- Power loss due to secondary electron emission from end walls

$$P(2^{nd}\ e^-) = 10^{-3} \sum_{E,W} \frac{\pi r_p^2}{2} \frac{\left| T_{ec} \right|_{EL}}{1 - \lambda_{scl}}$$

- Power transferred by rf from plug ions to central cell ions

$$P_{rf} = \sum_{E,W} 1.6 \times 10^{-17} \bar{E}_{rf}^2\, n_c\, r_c^2$$

- End Loss ion axial power loss

$$P_{EL}\,(cci) = 10^{-3} \sum_{E,W} \frac{\pi r_p^2}{2} \left| \phi_c + kT_{ic} \right|$$

[a] All parameters are assumed to have radial profiles of the form $F(r) = F\, e^{-(r/r_f)^2}$. (Exception is plug ion energy.)

TABLE E-3. Polynomial r. al profiles.

The line density is assumed to have the form

$$\int n\,dz(r) = \int n\,dz\,|_0\,[1 + (r/R_p)^2 + B(1 + (r/R_p)^4)]$$

therefore

$$n(r) = \frac{2}{\pi R_p^2} \int_r^{R_p} n\,dz\,|_0 \sqrt{1 - (r/R_p)^2}\,[a + 2(a+b) + 4(a+b)(r/R_p)^2]$$

The plug density is assumed to have an axial dependence of the form $n_p(z) = n_e^{-(z/L_p)^2}$. All other parameters are assumed to have a radial profile described by $f(r) = [1 + (r/R_p)^2]$. (Exception is plug ion energy.)

- Plug ion mean perpendicular energy

$$W = 6.25 \times 10^{15} \frac{M_p B_0}{N} \quad \text{where}$$

- N is the total number of ions in the plug

$$N = \pi \int n\,dz\,|_0 R_p^2 L_p (A + 0.5 B)$$

- Plug beta

$$\beta = \frac{0.22 \times 10^{-12} N_p}{R_p^2 L_p B_0}$$

- Plug ion to electron drag power

$$P_{ie} = 1.2 \times 10^{-25} \int_0^{R_p} \int_{-L_p}^{L_p} \frac{n_p^2(r,z)\,W}{T_e^{3/2}(r)}\,2\pi r\,dr\,dz$$

where

$$I_1 = \begin{cases} \int_{10}^{T_e(r)} T_e(r) - 10\ \text{eV} \\ \int_{10}^{T_e(r)} 10\ \text{eV} \end{cases} \quad \text{Integration performed numerically}$$

- Plug ion to end loss ion power transfer (per plug)

$$P_{ii} = 1.6 \times 10^{-19} \frac{\pi}{4} R_p^2 \left| W_{ii} - (n_p + \tfrac{1}{2} kT_{ic}) \right|$$

- Central cell electron axial power loss

$$P_{ll}(e,c) = 10^{-3} \sqrt{\frac{N}{EW}} \frac{\pi R_p^2}{3} [\varepsilon_e (n_e + kT_{ec})$$

- Power loss due to secondary electron emission from the end walls

$$P(2^{nd}\ e) = 10^{-3} \sqrt{\frac{N}{EW}} \frac{\pi R_p^2}{3} T_{es} \left| 1 - \frac{1}{\gamma_{sc}} \right|$$

- End loss ion axial power loss

$$P_{ll}(ion) = 10^{-3} \sqrt{\frac{N}{EW}} \frac{\pi R_p^2}{3} [\varepsilon_L + kT_{ic}]$$

For a Gaussian density profile in r and z and $W_\perp(r,z) = \overline{W}_\perp$ we can solve this equation for $\overline{W}_\perp$. We find

$$\overline{W}_\perp = \frac{1.4 \times 10^{13} \; M_p \; B_o}{n \; r_p^2 \; L_z \left[1 - e^{(-r_{max}/r_p)^2}\right]} \qquad (6)$$

The total mean ion energy is obtained from the perpendicular energy and the measurement of the plasma length:

$$W = \left[1 + \left(\frac{W_\parallel}{W_\perp}\right)\right] \overline{W}_\perp \qquad (7)$$

where

$$\left(\frac{W_\parallel}{W_\perp}\right) = \frac{1}{2}\left(\frac{L_z}{L_m}\right)^2 \qquad (8)$$

and

$$\frac{1}{(L_m)^2} = \frac{1}{L^2} + \frac{1}{\beta_i}\left(\frac{\beta_i}{2L_z} + \frac{1}{L_z}\right) \qquad (9)$$

Eqs. (8) and (9) are from Smith.[3]

$$\beta_i = \frac{0.45 \; N_p}{r_p^2 \; L_z \; B_o} \qquad (10)$$

Eq. (10) is correct for β small. Since the beta in the TMX end cells was typically 5% to 10% this is an acceptable approximation.

- Radial Scale Length

A least-squares best fit of the radial density profile as determined by the beam-attenuation profile was performed to calculate n and r_p according to

$$\int_0^\infty n d\ell(r) = \int_0^\infty n d\ell \; \exp[-(r/r_p)^2] \qquad (11)$$

and

$$n = \frac{\int \widehat{n d\ell}}{\pi r_p^2} \qquad (12)$$

- Axial Scale Length

The length of the hot plasma was determined by a least-squares best fit of the axial-beam attenuation profile according to

$$\int^* n d\ell(z) = \int \widehat{n d\ell} \; \exp[-(z/L_z)^2] \qquad (13)$$

The asterisk in Eq. (13) means that the measured value of the line density has been multiplied by a term which corrects for the change in path length as a function of z which is caused by the quadrupole fanning of the field lines.

In actuality the axial variation of the plug plasma can be more accurately described by two scale lengths: one L_z for the plasma on the end fan side of the plug midplane and one L_z' for the plasma on the central-cell side. The reason for this is that the cold plasma from the central cell leans in on the hot plasma. This result is a longer scale length on the central-cell side. The neutral-beam interaction with this cold plasma is distinctly different than the interaction with the hot-plug plasma. Power input by interaction with cold plasma is large because the term $\overline{W}$ in Eq. (1) is approximately equal to zero. A charge exchange event therefore inputs energy E_p. Since $L_z' > 2.5 L_z$ this interaction has the potential to significantly increase the power input to the plugs. In addition charge exchange of an energetic neutral with a cold ion is a source of energetic ions. Because these ions are born away from the center of the plug they are in essence sloshing ions which may aid the stability of the plugs.

It should be noted that the effects of neutral-beam interaction with the cold plasma leaning in on the plug plasma is accentuated in the west plug by the fanning of the field lines and deaccentuated in the east plug by the same mechanism. The reason for this is that the field lines entering the central-cell fan from the west plug are in the plane of the neutral beams. This increases the effective line density of the plasma and so increases the trapping. In the east plug the fanning is perpendicular to the plane of the beams so the path length is decreased and, therefore, so is the trapping. The combination of increased particle input and a possibly more stable distribution in the west plug may, in part, explain the observation that a higher line density is

usually obtained in the west plug for a given neutral-beam current than is obtained in the east plug for the same current.

- Maximum plug plasma radius, r_{max}

In TMX the gas box jaws were cut so that they formed a radial limiter equivalent to $r_{max} = 15$ cm at the plug midplane. Thomson scattering measurements at $r = 15$ cm indicate low density plasmas ($n_e < 5 \times 10^{11}$ cm^{-3}) with low electron temperature ($T_e < 10$ eV). For this reason $r_{max} = 15$ cm was used in these calculations.

- *Drag Power*

The total (volume integrated) power transferred from the plug ions to the plug electrons by Coulomb drag is given by

$$P_D = K \int_{-\infty}^{\infty} \int_{0}^{r_{max}} \frac{n_e(r, z)\, n_i(r, z)\, W_i(r, z)}{T_e^{3/2}(r, z)} \times 2\pi r dr dz \quad .$$

For the assumed profiles this becomes

$$P_D = \frac{2.86 \times 10^{-26}\, \bar{n}^2\, \bar{W}\, r_p^2\, L_z}{T_{ep}^{3/2}} \times [1 - e^{-(r_{max}/r_p)^2}] \qquad (14)$$

- Plug-ion axial loss

In the presence of charge exchange on neutral beams and background gas there is no simple formula for the axial-loss power of the plug ions. This information is obtained from the RFP code.

- Plug-ion charge exchange loss on background gas

We are still studying the details of this loss mechanism using the RFP code and a gas-fueling code. Values presented in the text come from these studies

We can use the secondary electron detector (SED) signals to estimate the power lost by this mechanism. Before neutral-beam turnoff the SED signal, V_i, is proportional to the sum of the power lost by charge exchange between plug ions and energetic neutral beam particles ($I_b f_{cx} \bar{W}$) and the power lost by charge exchange (cx) with background gas (P_{cx}). Soon after the beams are turned off the remaining SED signal, V_f, is proportional to the charge exchange with background gas and only the beam-attenuation-diagnostic (BAD) beam. We can, therefore, relate the power lost by cx on gas, P_{cx}, to the power lost by cx with beam particles, P_b, according to

$$P_{cx} = \left(\frac{\epsilon - \frac{I_{BAD}}{I_b}}{1 - \epsilon} \right) P_b \qquad (15)$$

where

$$\epsilon = \frac{V_f}{V_i}$$

and

$$P_b = I_b\, f_{cx}\, \bar{W} \quad .$$

- RF heating of central-cell ions

In our power balance calculations we allow power to be transferred from the plug ions to the central-cell ions by means of the plug driven ion cyclotron fluctuations. This term will be described when we consider the central-cell ion power balance.

- Power transferred to the end-loss ions

Most of the power taken to the end walls is carried by ions which escape the central cell. These ions escape the central cell with their kinetic energy; then fall down the potential hill created by the electrons such that they arrive at the end wall with a total kinetic energy equal to $(\phi_p + \alpha k T_{e_i})$. We have found that the ions reaching the end walls of TMX have energy in excessive of this value. This difference in energy is attributed to rf heating of the end-loss ions as they pass through the plugs. For this reason we include a power drain on the plug ions given by

$$P(H - EL) = \int_{0}^{r_p} J_i(r)\, [W_{EL}(r) - (\phi_p(r) + \alpha k T_{e_i}(r))]\, 2\pi r dr$$

When detailed measurements of these profiles are unavailable we may approximate this term by

$$P(H - EL) \simeq 10^{-3}\, \frac{\pi}{2}\, r_p^2\, J_i \times [\bar{W}_{EL} - (\phi_p + \alpha k T_{e_i})] \qquad (16)$$

E3. PLUG ELECTRONS

The drag power from the plug ions to the electrons was presented in the previous section. Power lost by impurity radiation was measured by EUV spectrometers. The power lost by this mechanism is small. Power is also lost due to the ionization of the background gas on the edge of the plug plasma. Present calculations of this power loss obtained from the gas-fueling code indicate that it is also a small power loss.

The bulk of the power lost by the plug electrons is caused by the interaction between the plug electrons and the passing electrons from the central cell. The power exchanged between these two classes of particles is given by Cohen, et al.[6] Cohen's formula for the time derivative of the total energy content of the plug electrons reduces to

$$\frac{3}{2}\frac{d}{dt}(n_p T_{ep}) = \frac{2lR}{C}(n\bar{T})_x \quad (n\bar{T})_x + P \qquad (17)$$

where

$$(n\bar{T})_x = 4.53 \times 10^{-24} \frac{n_p}{T_p}\frac{n_c}{\ell n\left[\frac{T_p}{n_c\sqrt{T_c T_p}}\right]} \times \left(\frac{T_p}{T_c}\right)\left(\frac{T_p - T_x}{T_p^{3/2}}\right) \qquad (18)$$

in W cm^{-3}. $P = P_{ip}$ in the TMX plug.

When the power transferred according to Eq. (19) exceeds the total drag power input to the plug electrons, we can use Cohen's code to estimate the barrier density, n_b, necessary to satisfy $P_{ep,ec} = P_{ip}$.

E4. CENTRAL-CELL ELECTRONS

There is drag power exchanged between the electrons and ions in the central cell. However, for typical TMX parameters $T_{ec} \approx T_{ic}$ so that the drag power exchanged between these two classes of particles is generally small.

$$P_{ei}(e - i) = 3.8 \times 10^{-30}\,\pi r_c^2 L_c n_c^2 \frac{(\bar{T}_e - \bar{T}_i)}{\bar{T}_e^{3/2}} \times \left[1 - e^{-3.2(t_m/\tau_c)^2}\right]$$

The dominant power input to the central-cell electrons comes from the plug electrons as presented in the previous section. The dominant power loss is by axial loss of the electrons:

$$P_{EL}(ece) = \sum_{E,W}\int J_e(r) \times [\phi_p(r) + kT_{ec}(r)]\,2\pi r dr$$

where the summation is performed over the east- and west-end losses. Note that we have allowed for the fact that $J_e(r)$ is not necessarily equal to $J_i(r)$. When detailed profiles of these parameters are not available we approximate this loss by

$$P_{EL}(ece) = 10^{-4}\sum_{E,W}\left[\pi\frac{r_p^2}{2} J_e \times (\phi_p + kT_{ec})\right] \qquad (19)$$

The power lost by the central-cell electrons due to ionization of the gas which is introduced to fuel the central cell is calculated from the gas fueling code. The additional power lost in Lyman alpha radiation associated with the fueling process is obtained from EUV spectrometry.

The emission of secondary electrons from the end walls also represents an electron power loss. During some of the TMX running we used emissive probes near the end wall to estimate the magnitude of the secondary electron current. The power loss is given by

$$P(2^{nd}\ e-) = 10^{-4}\int J_e(r)\,T_{ec}(r)\,2\pi r dr$$

When measurements of the secondary electron current are not available we estimate this power loss by assuming that the emission of secondary electrons is limited by space charge limited flow from the end walls[5]

where

$$J_e(r) = \frac{1}{1 - \lambda_{ei}(r)} J_{EL}(r)$$

and

$$\lambda_{sc}(r) = 10.15 / (n\ B(r) + 0.65\sigma)^{1.4}$$

with

$$B(r) = \frac{I_{cc}(r)}{\phi_c(r) + \phi_i(r) + T_e(r)}$$

For TMX parameters $B(r) \approx B$ so

$$I_{cc}(r) = 1 - \frac{1}{\lambda_{sc}} \int_0^r I_{ii}(r)$$

The power loss associated with secondary electrons is then

$$P_{LOSS}(cc) \approx 10^{-4} \sum_{E,W} \frac{\pi}{2} r_p^2 \frac{T_{ec}\ I_{ii}}{1 - \lambda_{sc}} \qquad (20)$$

Detailed measurements (Sec. 15) in TMX have shown that the emission of secondaries is *limited* by wall conditions and not space charge buildup, so the above equation is known to overestimate the power loss by secondary electron emission in TMX.

E5. CENTRAL-CELL IONS

As noted earlier, the central-cell ion and electron temperatures were generally equal in TMX so that the power exchanged between the central-cell ions and electrons by drag was, typically, small. The primary power input to the central-cell ions, therefore, appeared to be rf heating by the plug ion cyclotron fluctuations.[9,10] The rf heating power is given by

$$P_{rf} = \sum_{E,W} 1.6 \times 10^{-17}\ \hat{E}_{rf}^2\ n_c\ r_c^2 \quad . \qquad (21)$$

where the summation is performed over the east and west resonance zones.

The dominant power loss by the central-cell ions comes from the axial loss of the electrostatically confined ions. The total power lost by this mechanism is

$$P_{ll}(ii) = \sum_{E,W} \int J_i(r)\ [\phi_c(r) + \alpha k T_{ic}(r)]\ 2\pi r dr \quad ,$$

where

$$\alpha = \begin{cases} 1 & \text{collisionless losses} \\ 2 & \text{collisionless losses} \end{cases} \qquad (11)$$

If detailed profiles of the parameters are not available we can approximate this loss term by

$$P_{ll}(cc) \approx 10^{-4} \sum_{E,W} \frac{\pi}{2} r_p^2\ J_i[\phi_c + \alpha k T_{ic}] \qquad (22)$$

Gas fueling of the central cell also causes a loss of ion power. This loss is predominantly due to charge exchange between the gas atoms and the ions at the boundary of the plasma. The details of this loss depend upon the mechanism of fueling (gas box versus puffer valve) and the electron temperature and density at the edge of the plasma. For this reason the gas fueling code is used to calculate the power lost by this mechanism.

REFERENCES

1. E.B. Hooper, "Center Cell Density Profiles: Non-Gaussian Fits and Consequences for Ion Temperature, and Confinement," Memorandum MFE/CP/80-2300, Oct. 1980.
2. W.C. Turner and T.B. Kaiser, *Bull. Am. Phys. Soc.* 23, 754 (1978).
3. D.L. Correll, "TMX Power Balance," Physics Basis for MFTF-13 (part I), UCID-18496, Jan. 1980.
4. Klaus Berkner, Lawrence Berkeley Laboratory, private communication.
5. G.R. Smith, "Anisotropy-Driven Instability in Tandem-Mirror End Cells," Memorandum MFE/TC/80-1739, 1980.

6. R.H. Cohen, et al., *Nucl. Fus.* **20**, 1421 (1980).
7. R.P. Drake, Lawrence Livermore National Laboratory, private communication.
8. B.G. Logan, "TMX Upgrade Operating Parameters with Thermal Barriers," *TMX Major Project Proposal*, LLL-PROP-172, April 1980.
9. T.D. Rognlien and Y. Matsuda, "Tandem Mirror Confinement in the Presence of Ion Cyclotron Fluctuations," UCRL-84571, July 1980.
10. R.P. Drake, et al., "The Effect of End-Cell Stability on the Confinement of the Central-Cell Plasma in TMX," UCRL-84558 (Rev. 1), Dec. 1980.
11. R.S. Devoto, Sec. IIA, *Physics Basis for MFTF-B*, UCID-18496 (part 1) Jan. 1980.

APPENDIX F
AN ORBIT-AVERAGED COMPUTER CODE FOR RADIAL PLASMA BUILDUP IN THE TANDEM MIRRORS

(M. Campbell and A. H. Futch)

Appendix F.
An Orbit-Averaged Computer Code for Radial Plasma Buildup in the Tandem Mirrors

F1. INTRODUCTION

This appendix describes an orbit-averaged computer code for plasma buildup in tandem mirrors (TOARBUC). The introduction starts with a brief description of other numerical codes which have been used to model different attributes of the TMX plasma.

The TAMRAC[1] code, which was used in the design of the TMX experiment, also provided an initial comparison with experimental results. TAMRAC solves for the time-dependent plasma parameters on the magnetic axis in both the central-cell and plug regions. Heating of the central-cell ions by rf activity was added to model the effect of the ion cyclotron instability on the central cell confinement. With this addition, parameters calculated by TAMRAC on-axis agreed with experimental results to within a factor of 2.

A second code, TANDEM,[2] has been used to calculate global parameters by averaging plasma parameters over the plasma radius, using analytical models for various radial profiles. Rognlien and Matsuda[3] used a Monte Carlo code to more accurately model the effect of an electrostatic ion cyclotron wave on central-cell confinement. They derived diffusion coefficients for use in Fokker-Planck codes and a simple formula for modeling rf effects in particle codes. A radial-transport code TMT[4] has been developed to accurately describe resonant-neoclassical transport. Code results indicate a radial ion flux of about 5×10^{15} cm^{-2} s^{-1} at the plasma edge in the central cell.

TAMBAR and TOARBUC are two general-purpose radial codes. TAMBAR[5] is a particle buildup code that includes much of the general physics needed for studying tandem plasmas, as discussed in Section 3.

TOARBUC (for Tandem Orbit-Averaged Radial Buildup Code) was developed to model tandem physics plasmas when the approximate treatment provided by existing particle and fluid codes is inadequate. For example, an adequate description of radial transport in the plug requires an orbit-averaged code. Both the TOARBUC code and measurements in TMX show that 80% of the hot ions deposited are lost from the plasma core by charge-exchange diffusion. Central-cell confinement and radial profiles tend to follow the pattern established in the plug because of the exponential dependence on the plug potential. Calculations of non-Maxwellian plasmas in the central-cell resulting from beam injection, ion cyclotron heating (either externally induced or resulting from instability fluctuations), etc., may require a code that includes the distribution function, such as TOARBUC.

The TOARBUC model is based on the finite orbit, Fokker-Planck model RFP developed by A. Futch to study conventional mirrors.[6] The two major changes made to the RFP code are: (1) the central cell has separate electron and ion confining potentials and the sign of the ion potential is opposite that in a conventional mirror, and (2) a two-electron temperature treatment derived by R. Cohen[7] is included to allow the plug and central cell to have different T_e's as they were observed to

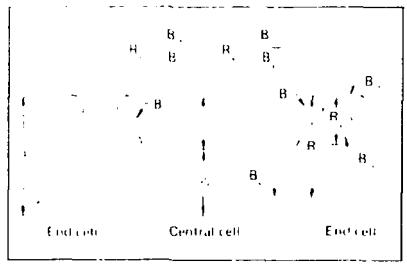

FIG. F-1. The TMX magnetic field (B), electrostatic potentials (φ), and mirror ratios (R).

have in the experiment. The following sections explain these changes in greater detail.

The modifications to the RFP code allow the plug and central cell plasma parameters of a tandem mirror to be calculated during alternate iterations. At each time step the plug ion parameters are generated first followed by those of the central-cell ions. Then the self consistent potentials and the number of electron particles and energy between the two regions are determined. New values for the ion densities in the plug and central cell (n_p, n_c), the electron and ion temperatures in these regions (T_{ep}, T_{ip}, T_{ec}, T_{ic} respectively), and the ion and electron electrostatic potentials in the central cell (ϕ_c, ϕ_e) and plug ($\phi_p = \phi_c + \phi_e$) are found for use in the next time step. The magnetic field strengths electrostatic potentials, and mirror ratios used in these calculations are shown in Fig. F-1. (R_c and R_p are the central cell and plug mirror ratios, respectively.)

The TOARBUC code differs from a particle-buildup code in several important respects; some of the basic differences between TOARBUC and the particle-buildup code TAMBAR[1] are listed in Table F-1.

In an orbit averaged code such as TOARBUC, the particle deposition, loss, and energy-exchange rates are calculated by averaging them around an orbit. These orbit-averaged quantities are then used to calculate a time-dependent distribution function self consistently. Particle codes, such as TAMBAR,[1] assume the form for the distribution function, and do not average around the orbit since the orbit is unknown; consequently, particle deposition, loss, and energy-exchange rates are approximate. Figure F-2 illustrates this effect. Consider the loss of a particle due to a charge-exchange collision at x. This charge-exchange collision results in a loss in density over the range $R - \rho$ to $R + \rho$, which is correctly calculated by an orbit-averaged code (Fig. F-2a) since the guiding center is

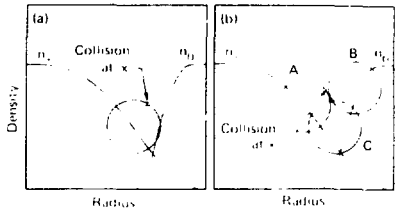

FIG. F-2. Graphic comparison of density loss for a collision at x for (a), a particle with a known orbit as in TOARBUC, and (b) a particle with an unspecified orbit as in TAMBAR. Several orbits passing through x are indicated—each results in a different radial loss.

TABLE F-1. Basic differences between the orbit-averaged code for the distribution function (TOARBUC) and the particle-buildup code TAMBAR.

TOARBUC	TAMBAR
1. Rate equations used for calculating atomic physics includes secondary neutrals (Stallard model).	1. Three-dimensional Monte Carlo calculation of neutral reactions.
2. Orbit averaged.	2. Finite-orbit effects generally neglected except for beam deposition.
3. Distribution function: a. Plug—calculated b. Central cell—calculated.	3. Distribution function: a. Plug—assumed b. Central cell—assumed.
4. Ion end loss: a. Coulomb end losses b. Quasi-linear end losses. $\hat{\phi}^a$ is an input parameter which may be set equal to 0 for classical processes only.	4. Ion end loss: a. Spitzer drag with decreased plug lifetime to satisfy quasi-linear requirements.
5. Ion energy—calculated.	5. Ion energy—assumed E_{inj}

[a] *$\hat{\phi}$ is the perturbed potential resulting from the ion cyclotron instabilities.*

known. For a particle code the guiding center is unknown; therefore, the charge-exchange collision could result in the loss of a particle having orbit A, B, or C (Fig. F-2b), for example, and there is a corresponding uncertainty in the charge-exchange loss rate. Radial transport due to charge exchange will be more uncertain for a particle code, since it is the difference between trapping and loss rates of approximately the same magnitude. Similar considerations apply to end loss, electron drag, and other parameters. The importance of orbit effects depends on the spatial gradients of parameters such as the plasma density and the thermal gas density compared to the orbit size.

TAMBAR assumes that the plug ion energy is fixed at the injection energy, whereas, TOARBUC calculates the ion energy self-consistently from the time-dependent distribution function.

Three-dimensional transport of neutral gas and neutral beams is calculated by a Monte Carlo code[9] in TAMBAR. In TOARBUC, atomic physics processes are described by rate equations including the modeling of secondary beams.[10]

At present both codes require approximately the same computer time for a run. The more detailed atomic physics in TAMBAR appears to compensate for the more complete plasma physics of TOARBUC in the use of computer time.

Table F-2 gives a more general comparison with other numerical codes including TAMBAR.

F2. ALTERATIONS TO THE RFP MODEL

F2.1 Ion Loss Probability

In the plug region the ion loss probability depends on a slowly varying function of the mirror ratio (R_{eff}) given by:

$$R_{eff} = R \Big/ \left(1 + \frac{|q\phi_p|}{W_i}\right) \quad ,$$

or

$$R_{eff} = 1 \quad . \tag{1}$$

whichever is larger. Here R is the mirror ratio, q is the charge, ϕ_p is the plug plasma potential, and W_i is the ion energy. In the central cell the ions are confined by a negative potential, ϕ_c, and the loss probability is zero for all ions with $W_i < |q\phi_c|$ and affects R_{eff} to give:

$$R_{eff} = \infty, W_i \leq |q\phi_c| \quad ,$$

$$R_{eff} = R \Big/ \left(1 - \frac{|q\phi_c|}{W_i}\right), W_i > |q\phi_c| \tag{2}$$

TABLE F-2. Tandem mirror/thermal-barrier experimental modeling codes.

	TAMRAC	TANDEM	Monte Carlo	TMT	TAMBAR	TOARBUC
Time dependent	Yes	Yes	No	Yes	Yes	Yes
Radial profiles	No	Radial averaged	No	Yes	Yes	Yes
Axial profiles	No	No	Yes	No	No	No
Beam trapping	No	Yes	Yes	Fixed profile input	Yes	Yes
Cold-gas fueling	No	No	No	FC neutrals	Yes	Yes
Neutral transport	No	No	No	Yes	Yes	Yes
ECRH	No	Yes	Yes	M[a]	M	M
Orbit averaged	No	No	No	No	No	Yes
Thermal barrier physics	No	Yes	No	No	Yes	M

[a]M means "Could be modified."

In addition to its effect on the ion loss probability, ϕ_c affects the turning-point mirror ratio. For $|q\phi_c| > W_i$, the turning point for potential-confined ions is near the minimum-B in the plug (where the potential is largest), but magnetically confined ions are reflected at the inside plug mirror. In order to facilitate a smooth transition between these two modes, the mirror ratio R in Eq. (2) is replaced by the expression

$$R = \frac{R_c}{R_p}\left\{1 - \left[1 - \frac{1}{R_p}\right] \exp\left(\frac{-2q\phi_c}{T_{ic}(R_p - 1)}\right)\right\}^{-1} , \qquad (3)$$

where R_c is the central-cell mirror ratio, R_p is the plug mirror ratio and T_{ic} is the central-cell ion temperature (see Fig. C-1).

F.2.2 Electron Balances

Because different electron temperatures have been observed in TMX, the two-electron-temperature formulas developed by R. Cohen[8] were incorporated into the TOARBUC model. Cohen's formulas provide for a group of "trapped" electrons, confined by the potential ϕ_c and residing in the plug, and a group of "passing" electrons, confined by ϕ_c and occupying the entire tandem system. These groups, with densities of n_p and n_c respectively, can have different mean temperatures (T_p, T_c, where the "e" subscript has been dropped). These groups are connected by the fraction of "passing" electrons that occupies the plug region during a fraction of their bounce period (density designated by n_μ) and allows scattering and direct energy transfer between the two groups. The formula given by Cohen for the particle (density) balance in the plug is

$$\frac{dn_p}{dt} = -\frac{n_p}{\tau_p}\left[1 - (T_p/T_c)^{1/2}\,\frac{n_c}{n_p}\,\exp\left(\frac{q\phi_c}{T_p}\right)\right] + J_p , \qquad (4)$$

where the "e" subscript on the temperatures is again omitted, J_p is the total source of plug electrons, and τ_p is the Pastukhov time in the plug (Ref. 3), which is given functionally as

$$\tau_p = \frac{1}{2} K \tau_{ee} \cdot G(R) \cdot \left(\frac{\phi_c}{T_p}\right) \exp\left(\frac{\phi_c}{T_p}\right) , \qquad (5)$$

where τ_{ee} is the time between electron collisions, G(R) is a slowly varying function of the mirror ratio, and K contains the Coulomb terms.

The electron energy (power) balance in the plug is given by

$$\frac{3}{2}\frac{d(n_p T_p)}{dt} = -\frac{n_p}{\tau_p}\left[(q\phi_c + T_p) - (T_p/T_c)^{1/2}\,\frac{n_c}{n_p} \cdot \exp\left(\frac{q\phi_c}{T_p}\right) \cdot (q\phi_c + T_c)\right] - (\dot{n}T)_{ee} + (\dot{n}T)_{ei} + P_{aux} + J_p E_{cp} , \qquad (6)$$

[1] [2] [3] [4] [5]

where the terms are as follows:

[1] the interchange between trapped and untrapped groups times the energy carried by an electron transferring from one group to the other (measured in the plug).

[2] the collisional (drag) energy transfer between the trapped and passing groups in the plug;

[3] the energy transfer from ions to the trapped electrons (because n_μ is small, energy transfer from ions to passing electrons is negligible);

[4] auxiliary heating, if any; and

[5] the energy input from the trapped-electron source.

Other terms such as radiation losses and anomalous cooling can be added as desired.

The electron energy transfer rate of [2] is given by Cohen as:

$$(nT)_{ee} = \frac{n_c\,(T_p/T_c)^{1/2}(T_p - T_c)}{\tau_v} , \qquad (7)$$

where τ_v is the volumetric temperature equilibrium time, and

$$\tau_v^{-1} \simeq \frac{2T_p}{\sqrt{\pi}\, R \tau_{ee}(q\phi_i)} \quad .$$

Here R is the plug mirror ratio and τ_{ee} is the electron collision time in the plug. Since the primary source of energy to the central-cell electrons comes from the plug ($T_{ep} > T_{ec}$), a negative sign is attached to this term in Eq. (6).

The electron particle and energy balances in the central cell are only slightly more complex and, while not given by Cohen, are readily derived. The particle (density) balance is:

$$\frac{dn_c}{dn} = C \left\{ J_c V_c + \frac{2n_p V_p}{\tau_p} \right.$$

[1]

$$\left[1 - (T_p/T_c)^{1/2} \frac{n_c}{n_p} \cdot \exp\left(\frac{q\phi_c}{T_p}\right) \right]$$

[2]

$$\left. - \frac{n_c V_c}{\tau_c} - \frac{2n_\mu n_p V_p}{n_c \tau_c} \right\} \quad , \qquad (8)$$

[3] [4]

where V_c and V_p are the volume of the central cell and the plug and τ_c is the Pastukhov time in the central cell, with ϕ_e being the confining potential. The coefficient C is

$$C = \frac{n_c}{2n_\mu V_p + n_c V_c} \quad , \qquad (9)$$

and represents the weighting given to the portion of the passed fraction of electrons occupying only the central cell, on the average. Particle bookkeeping is done so that only the fraction of passing electrons occupying the central-cell constitutes the density n_c. The passing-electron density in the plug is designated by n_μ (on the average) and for a square-well approximation the total number of passing electrons (N_μ) is

$$N_\mu = n_c V_c + 2n_\mu V_p \quad . \qquad (10)$$

Thus C accounts for the fractional change in electron density in the central cell due to a change in the total number of passing electrons, the remainder affecting n_μ. [It should be noted that a factor of V_c was divided through in the particle balance to obtain the "density" balance of Eq. (8), giving the expression for C in Eq. (9).]

The various terms in the central-cell particle balance, Eq. (8), are as follows:

[1] the total central-cell electron source (local);

[2] the trapped-passing interchange term;

[3] the scattering loss rate for passing electrons in the central cell; and

[4] the scattering loss rate for passing electrons in the plug (primarily off of trapped plug electrons). The loss time (τ_c) is approximate for this term, which usually represents a small loss contribution.

The energy (power) balance in the central cell is given similarly:

$$\frac{3}{2} \frac{d(n_c T_c)}{dt} = V_R \cdot \left(2V_p \cdot \left\{ \frac{n_p}{\tau_p} \left[T_p - (T_p/T_c)^{1/2} \frac{n_c}{n_p} \right. \right. \right.$$

[1]

$$\left. \left. \cdot \exp\left(\frac{q\phi_c}{T_p}\right) \cdot T_c \right] \right.$$

$$\left. + (nT)_{ee} \right\} - V_c \cdot (nT)_{ei} + J_c V_c E_{ic}$$

[2] [3] [4]

$$- \left(\frac{n_c V_c}{\tau_c} + \frac{2n_\mu n_p V_p}{n_c \tau_c} \right) \cdot (q\phi_e + T_c) \Big) \quad , (11)$$

[5]

where [1], [4], and [5] are terms already discussed in relation to the particle balance, multiplied by the respective average energies transferred by each electron (as measured in the central cell). Term [2] is the energy transfer between trapped and passing electrons, as discussed previously, and term [3] is

the energy transfer from ions to trapped electrons in the central cell. All terms are weighted by C as explained earlier.

The passing-electron density in the plug used in both balances is found using Cohen's formula:

$$n_\mu = n_c \exp(Y) \cdot \left\{ \operatorname{erfc}(\sqrt{Y}) - \left(1 - \frac{1}{R}\right)^{1} \cdot \exp\left(\frac{Y}{R-1}\right) \cdot \operatorname{erfc}[(RY/R-1)^{1/2}] \right\} \quad (12)$$

where $Y = q\phi_c / T_c$, R is the plug mirror ratio, and erfc is the complementary error function.

$$\operatorname{erfc}(x) = \frac{2}{\sqrt{\pi}} \int_x^\infty \exp(-x^2)\, dx \quad (13)$$

F3. SOLVING THE TIME-DEPENDENT EQUATIONS

For times longer than τ_{ee}, the plasma may be assumed to satisfy conditions of quasi-neutrality, particularly in the rapidly varying plug (if this is not true, the potentials readily become unrealistically large). The tandem's least-confined particles are plug electrons, but changes in the plug ion density generally determine quasi-neutrality conditions in this region, because the ion loss rate in the plug is not very sensitive to changes in ϕ_c (provided $\phi_c << \phi_p$), which largely determine the electron transport.

In the TOARBUC model, the rate of change for plug ion density is set equal to the rate for electron density to enforce quasi-neutrality over time intervals $\Delta t > \tau_{ee}$:

$$\frac{\Delta n_i}{\Delta t} = \frac{\Delta n_e}{\Delta t} \quad (14)$$

the value of $\Delta n_i/\Delta t$ being determined by beam trapping and various loss rates in the plug (using the previous time step ϕ_p). For Eq. (4), this gives the formula

$$\frac{dn_p}{dt} \simeq \frac{\Delta n_i}{\tau} = -\frac{n_p}{\tau_p} \left[1 - (T_p/T_c)^{1.2} \frac{n_c}{n_p} \exp\left(\frac{q\phi_c}{T_p}\right) \right] + J_p \quad (15)$$

This expression can be solved for $q\phi_c$ by letting $J_p' = J_p - \Delta n_i/\Delta t$. Then

$$q\phi_c = T_p \ln \left[(T_c/T_p)^{1.2} \left(\frac{n_p - J_p' \tau_p}{n_c} \right) \right] \quad (16)$$

This expression for $q\phi_c$ can be substituted into Eqs. (6), (8), and (11) to simplify them. The energy balance in the plug then becomes

$$-J_p'(q\phi_c + T_c) - \frac{n_p}{\tau_p}(T_p - T_c) - (n\dot{T})_{ei} + (n\dot{T})_{ei} + P_{aux} + J_p E_{ap} = 0 \quad (17)$$

from which, by using $n_p = n_i$, the ion density (local) can be solved approximately for T_p, the new plug electron temperature, in terms of T_c and ϕ_c. The central-cell particle and energy balances become:

$$\frac{dn_c}{dt} = C \left(J_c' V_c + 2 J_p V_p - \frac{n_c V_c}{\tau_c} - \frac{2 n_\mu n_p V_p}{n_c \tau_c} \right) \quad (18)$$

and

$$\frac{3}{2}\frac{dn_c T_c}{dt} = C \left\{ 2V_p \right.$$

$$- \left[\frac{n_p}{\tau_p}(T_p - T_c) + J_p T_c + (nT)_{ec} \right]$$

$$V_c (nT)_{ec} + I_c V_c E_{ic}$$

$$\left. \left(\frac{n_c V_c}{\tau_c} + \frac{2n_p n_c V_p}{n_c \tau_c} \right) [q\phi_c + T_c) \right\} \quad (19)$$

Equations (18) and (19) can be solved iteratively with Eqs. (17), (12), and (7) to find T_{ep}, T_{ic}, and n_c (n_p is already determined by the plug ion density). Convergence of the solution is very rapid for Δt << least of $\{\tau_p, \tau_c, \tau_i\}$.

F4. COMPARISON OF TOARBUC RESULTS WITH TMX DATA OF SEPTEMBER 24, 1980

An extensive analysis of the TMX data for September 24, 1980, is described and compared with results from the TAMBAR code in Section 9. Figure F-3 and Table F-3 show an extension of this analysis which includes TOARBUC code results. Except for the end-loss current I_c and the plug density n_p, both codes match the experimental data reasonably well. TOARBUC gives a plug density value that agrees with experimental data, but gives a value for the end-loss current that is too low by approximately a factor of 2, whereas TAMBAR gives an end-loss current that agrees with experimental data, but gives a value for the plug density that is too low by almost a factor of 3. In addition both codes give somewhat higher electron temperatures, especially for the central-cell.

Some additional observations on the radial density profiles should be made. The comparisons of line densities, Indl given in Fig. F-3 obscure the large differences between the experimental data and TOARBUC (as compared with TAMBAR) for the density profiles vs radius. In the end plugs, the measured profiles correspond to plasmas that are slightly hollow in the core, which agrees with the

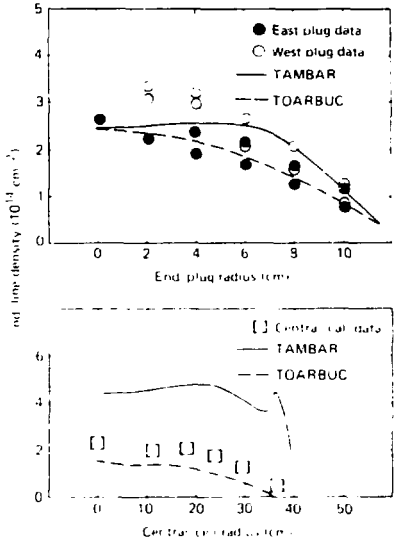

FIG. F-3. *Line density profiles from the* TAMBAR and TOARBUC codes compared with experimental data from the TMX.

TOARBUC results (Fig. F-4). In the TAMBAR results, the plasma density is very hollow, with a peak-to-valley density ratio of about 5 vs 1.2 or less for both TOARBUC and the experimental

TABLE F-3. Comparison of results of plasma-buildup codes with TMX results.

Parameter (r = 0)	Results: TMX 9-24-80 (shots)	TOARBUC	TAMBAR
T_{ep} (eV)	80	98	107
$T_{ep} + T_{ic}$ (eV)	80	110	120
T_{ep} (eV)	41	84	93
J (A/cm^2)	0.21	0.11	0.25
ϕ_p (V)	510	485	500
ϕ_e (V)		348	510
n_c (10^{12} cm^{-3})	2.5	2.7	2.5
n_p (10^{12} cm^{-3})	18	16	6.7

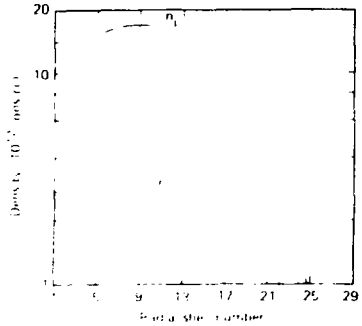

FIG. F-4. TMX plug and central-cell densities modeled by the TOARBUC computer code.

TABLE F-4. TOARBUC computer-code input parameters for comparison with TAMBAR and TMX data.[a]

Plug	Central cell
E_{inj} = 18, 18.6 keV	E_{inj} = 3, 0.08 eV
I_{inj} = 122 A	I_D = 180 A, 17 A
$\hat{\phi}$ = 34 eV (for Δ_w = 0.1 a_{cc})	$\hat{\phi}$ = 0
n_0^j = 1 × 10^{10} $J_{trapped}/J_{norm}$ (atoms cc)[b]	B = 1 × 10^6 cm^{-3} s
= 0 × 10^9 (atoms cc)	

[a] See Fig. 3 for results of comparison

[b] J = neutral-beam current density

In the plug region, as both the measured data and TOARBUC (Fig. F-4) have relatively flat profiles in the plasma core and a Gaussian fall off in the radial boundary. TAMBAR predicts a hollow profile with a second density peak near the plasma boundary. This second peak is presumably due to the formation of cold molecular hydrogen ions. In the TOARBUC runs it was assumed that these ions would be neglected because of their very short lifetimes. The neutral gas is modeled by Franck-Condon atoms which have a longer mean free path resulting in density profiles without peaks. A small amount of low-energy atoms (17 A at 0.08 eV) is also included as a source impinging on the plasma.

The TOARBUC input parameters for the comparison of Fig. F-3 and Table F-3 are given in Table F-4. Full- and half-energy neutral beams were injected into the plug. The half-energy component was reduced slightly to account for a small one-third-energy component. An enhanced loss rate was introduced in both TOARBUC and TAMBAR. In TAMBAR the classical loss rate was increased by a factor of 10. In TOARBUC the radial transport term was calculated by a term

$$\frac{1}{R}\frac{\partial}{\partial R}\left(B\frac{\partial D}{\partial R}\right)$$

where D is the guiding-center distribution function and B was taken to have the constant value of 1×10^6 cm^{-3} s.

Cold ions resulting from background gas ionization have historically been neglected in many buildup codes modeling plug densities. It has been assumed that these ions would be expelled from the plasma immediately by the plasma potential since they are born within the loss cone as modified by the potential. It has also been suggested that if these cold ions were included as a source and given a lifetime determined by the transit time to the mirrors, a cold plasma or halo surrounding the hot plasma would be created. The halo would shield the hot plasma from the thermal gas enabling the plasma to build up with less beam injection or with higher background gas pressure.

To test this thesis, TOARBUC was modified by including the cold ions as a source (the associated electrons were included previously) with a transit lifetime. TOARBUC was then run with this modification using the same input data (Table F-3). Table F-5 compares some important parameters for these two runs. The retention of the cold ions in TOARBUC modified the plasma parameters by only a small amount. Figures F-4, F-5, and F-6 show the particle densities and temperatures vs radius for both the central-cell and plug when the cold ions are retained.

TABLE F-5. Comparison of values of several plasma parameters for the TMX plug, modeled by two versions of the TOARBUC code, one ignoring the cold-ion effect and the oth including it.

Parameter	Cold ions ignored (no halo)	Cold ions included (halo)
Plug $\int n\,dl$	I[a] 1.2 35 × 10^{14}	2.5 × 10^{14}
	I 10 2.14 × 10^{14}	2.29 × 10^{14}
	I 20 0.61[7] × 10^{14}	0.663 × 10^{14}
T_{ep} (r 0)	98 eV	104 eV
T_i (r 0)	11.0 keV	11.1 keV
p (r 0)	489 V	490 V
n_p (at peak density)	1.0 × 10^{13}	1.7 × 10^{13}

[a] I is an index measuring the vertical displacement of the chord through the plasma.

Time has permitted only a limited comparison of TMX data with code results. Better agreement is to be expected in the future as modifications are made to both TOARBUC and TAMBAR to include additional physics of plug and central cell confinement. Several processes included in the TOARBUC code which tend to lower the electron temperature are:

1. The cooling effect resulting from ionization of oxygen impurity in the neutral beams.
2. The penetration of neutral gas into the ion regions which increases the number of cold electrons created along field lines through the plasma core.
3. The reflux through the plasma of cold secondary electrons from the end walls.

Additional runs are being made to determine the relative importance of these processes.

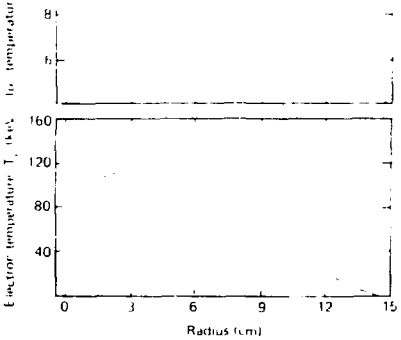

FIG. F-5. TMX plug temperatures vs radius, modeled by TOARBUC code modified to include cold ion effects.

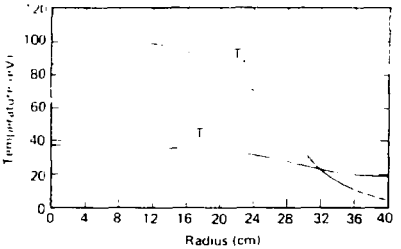

FIG. F-6. TMX central-cell temperatures vs radius modeled by the TOARBUC code.

REFERENCES

1. R. H. Cohen, "Time-Dependent Tandem Mirror Confinement Studies," *Nucl. Fusion* **19**, 1295 (1979).
2. R. S. Devoto, Computation of MFTF-B Properties with A-Cell Barriers (abstract), *Bull. Am. Phys. Soc.* **25**, 956 (1980).
3. T. D. Rognlien and Y. Matsuda, Tandem Mirror Confinement in the Presence of Ion Cyclotron Fluctuations, *Nucl. Fusion* **21**, 345 (1980).
4. M. J. Rensink, *Radial Transport in Tandem Mirrors* (abstract) *Bull. Am. Phys. Soc.* **25**, 880 (1980).
5. G. E. Gryczkowski and J. M. Gilmore, *Buildup Studies of a Tandem Mirror Reactor with Inboard Thermal Barriers*, Lawrence Livermore National Laboratory, Livermore, CA, UCRL-84233 (1980).
6. A. H. Futch and D. Freeman, *Bull. Am. Phys. Soc.* **23**, 776 (1978).
7. A. H. Futch, "A Computer Model for Plasmas Confined by Magnetic Mirror Fields," to be published.
8. R. H. Cohen, I. B. Bernstein, J. J. Dorning, and G. Rowlands, *Particle and Energy Exchange Between Untrapped and Electrostatically Confined Populations in Magnetic Mirrors*, Lawrence Livermore National Laboratory, Livermore, CA, UCRL-84147 Rev. 1 (1980) (submitted to *Nucl. Fusion*)
9. G. E. Gryczkowski, unpublished results (1980).
10. B. W. Stallard, *Radial Plasma Buildup Code for Neutral Beam Injection into a Mirror Machine*, Lawrence Livermore National Laboratory, Livermore, CA, UCRL-51784 (1975).

BRS

U. S. Government Printing Office: 1981/12–587-002/4026